



IRE Convention Record

Part 3— Electron Devices and Component Parts

SESSIONS ON . . .

- Electron Devices I — Tubes
- Electron Devices II — Microwave Tubes
- Electron Devices III — Cathode-Ray Type Tubes
- Component Parts I — Electromagnetic Devices
- Electron Devices IV — Transistors
- Component Parts II — General

SPONSORED BY

IRE PROFESSIONAL GROUPS ON . . .

- Component Parts
- Electron Devices

Presented at the IRE National Convention, New York, N.Y., March 21-24, 1955
Copyright 1955, by The Institute of Radio Engineers, Inc., 1 East 79 Street, New York 21, N.Y.

The Institute of Radio Engineers

Additional Copies

Additional copies of 1955 Convention Record Parts may be purchased from The Institute of Radio Engineers, 1 East 79 Street, New York 21, N.Y., at the prices listed below.

PART	TITLE	PRICES FOR MEMBERS (M) COLLEGE & PUB. LIBRARIES (L) NON-MEMBERS (NM)		
		M	L	NM
1	Antennas & Propagation Sessions: 2, 10, 33, 40	\$1.00	\$2.40	\$3.00
2	Circuit Theory Sessions: 7, 32, 39	1.00	2.40	3.00
3	Electron Devices and Component Parts Sessions: 16, 23, 43, 44, 51, 52	1.50	3.60	4.50
4	Computers, Information Theory, Automatic Control Sessions: 8, 14, 24, 27, 35, 42, 48, 53	2.25	5.40	6.75
5	Aeronautical and Navigational Electronics Sessions: 11, 19, 55	1.00	2.40	3.00
6	Management, Quality Control, and Production Sessions: 18, 29, 37, 46, 50	1.50	3.60	4.50
7	Transmitters, Receivers, and Audio Sessions: 12, 13, 20, 21, 25, 31, 38	2.50	6.00	7.50
8	Communications and Microwave Sessions: 3, 4, 28, 36, 47, 54	2.00	4.80	6.00
9	Ultrasonics, Medical and Industrial Electronics Sessions: 5, 26, 34, 41, 49	1.50	3.60	4.50
10	Instrumentation, Telemetry and Nuclear Science Sessions: 1, 6, 9, 15, 17, 22, 30, 45	2.50	6.00	7.50
	Complete Convention Record (All Ten Parts)	\$16.75	\$40.20	\$50.25

Responsibility for the contents of papers published in the IRE Convention Record rests solely upon the authors, and not upon the IRE or its members.

IRE CONVENTION RECORD
1955 NATIONAL CONVENTION

PART 3 - ELECTRON DEVICES AND COMPONENT PARTS

TABLE OF CONTENTS

Session 16: Electron Devices I - Tubes

(Sponsored by the Professional Group on Electron Devices)

A Gas Discharge Noise Source	W. Honig and P. Parzen	3
Corrections to the Theory of the Grounded-Grid Triode	W. A. Harris	10
Development of a Large-Diameter Dumet Lead for Sealing to Soft Glass (Abstract)	D. L. Swartz and J. C. Turnbull	16
Novel Design Approach for Microwave Tubes	J. E. McLinden and D. Lichtman	17
Magnetron Operation at Very-Long Pulses	Markus Nowogrodski	22

Session 23: Electron Devices II - Microwave Tubes

(Sponsored by the Professional Group on Electron Devices)

Klystron Power Amplifiers for Long-Hop Microwave Relay	N. P. Hiestand	29
Wide-Band, High-Power Traveling-Wave Tubes at S-Band	S. F. Kaisel and W. L. Rorden	39
A-1 KW Pulsed Traveling-Wave Tube Amplifier at X-Band (Abstract)	J. E. Nevins, S. F. Kaisel, and M. Chodorow	46
Noise Analysis of Traveling Wave Tube Video Detector	Glen Wade	47

Session 43: Electron Devices III - Cathode-Ray Type Tubes

(Sponsored by the Professional Group on Electron Devices)

A Time-Sampling and Amplitude-Quantizing Tube	R. P. Stone, C. W. Mueller, and W. M. Webster	56
Cathode-Ray Tube with Single Step Intensifier	Jenny E. Rosenthal	62
A New High Efficiency Parallax Mask Color Tube	M. E. Amdursky, R. G. Pohl, and C. S. Szegho	66
The Tricolor Vidicon—an Experimental Camera Tube for Color Television (Abstract)	P. K. Weimer, S. Gray, H. Borkan, S. A. Ochs, and H. C. Thompson	74

Session 44: Component Parts I - Electro-Magnetic Devices

(Sponsored by the Professional Group on Component Parts)

Blocking Oscillator Transformer Design	P. R. Gillette, K. W. Henderson and K. Oshima	75
Improvements in Pulse-Switching Reactor Design	R. A. Mathias and E. M. Williams	82
Magnetostriction Resonators as Circuit Elements (Abstract)	R. T. Adams	88
Wide-Band Electrically Tunable Oscillators	John L. Stewart and Kermit S. Watkins	89
Fluorochemical Liquids and Gases as Transformer Design Parameters	L. F. Kilham, Jr. and R. R. Ursch	97

Session 51: Electron Devices IV - Transistors
 (Sponsored by the Professional Group on Electron Devices)

Thermal Properties of Semiconductor Diodes	J. N. Carman and W. R. Sittner	105
Grain Boundaries and Transistor Action	Herbert F. Matare	113
Developments in Silicon Junction Diodes and Power Rectifiers	H. Gunther Rudenberg	125
Comparative High-Frequency Operation of Junction Transistors Made of Different Semiconductor Materials	L. J. Giacoletto	133
Characteristics and Some Applications of Fused Junction P-N-P Germanium Transistors for High-Frequency Use	R. D. Greene	138

Session 52: Component Parts II - General
 (Sponsored by the Professional Group on Component Parts)

A Miniature Precision Delay Line	James B. Hickey	144
Criteria and Test Procedures for Electromagnetic Delay Lines	Norman Gaw and David Silverman	152
Evolution of Selenium Rectifier Voltage Ratings	N. Bechtold	157
A Precision Deflection Yoke	Harold J. Benzuly	165
Ceramic-to-Metal Seals for Magnetrons	Leo J. Cronin	171

A GAS DISCHARGE NOISE SOURCE

William Honig and Philip Parzen
The Johns Hopkins University
Radiation Laboratory
Baltimore, Maryland

Summary

A brief review of the theoretical and experimental work in gas discharge noise sources is given. The results of an experimental study of the noise powers available from a gas discharge maintained by a magnetic field is given. Sealed versions of such gas discharge tubes are described together with the results of examinations of the noise output of the tubes.

Introduction

The presence of large amounts of noise power in gas discharges with magnetic fields has been indicated theoretically by Malmfors¹ and Bailey² and experimentally by Bailey and Landecker³. These measurements, however, were made in discharges maintained by a DC voltage and at a high value of DC current (greater than 20 ma). The effect of the DC magnetic field is principally to govern the nature of the propagation of an AC signal. It was felt that greater noise output powers would be realized in DC gas discharges maintained by DC magnetic fields. A practical gas discharge noise source having operating voltages in the 2000 volt range with currents of less than 10 ma would have the obvious advantage of needing relatively small amounts of power for operation. The operation of the gas discharge in the low pressure region (about 1.0 microns of Hg) would allow such a noise source to suffer little degeneration with time.

Theoretical and Experimental Background

The fluctuations in a gas discharge in a magnetic field is an inadequately understood phenomenon. A better starting point for some understanding of fluctuations in a gas discharge in a magnetic field is the study of the fluctuations present in a DC gas discharge.

The radiated and conducted AC power from a DC gas discharge may perhaps be divided into three groups; first the AC power from a DC discharge due to the random collisions of the ions and of the electrons, second the AC power due to sustained plasma oscillations of either ions or electrons, and third AC powers due to oscillations of charged particles about potential minima. The fact that such AC currents may exist in the plasma of a gas discharge does not specify that these AC currents may be coupled from that discharge. The problem of how AC currents may be coupled from the region of the plasma is also a difficult one.

The AC power available in a DC gas discharge due to collisions may be estimated as follows: Consider the collisions of a group of

electrons suddenly injected into a neutral gas. If the electrons are not captured, they will after a short time reach a velocity distribution and temperature corresponding to thermal equilibrium with the gas. If the electrons are assumed to exist in the plasma of a DC gas discharge where the densities of ions and electrons are high and substantially equal, then due to the electric field maintaining the discharge the electrons will begin to gain energy which cannot be very well given up to gas particles in elastic collisions because of the large value of the ratio of molecular to electron mass. In most discharges the velocities gained by the electrons are randomized by collisions and they may be termed thermal velocities. The electrons may then be thought of as possessing an electron temperature which can be much higher than the temperature corresponding to the random velocities of the gas or ion particles in the discharge plasma. Indeed, the graph reproduced in Fig. 1 from Cobine's "Gaseous Conductors" shows this quite clearly for several different gases.

The ratio of electron temperature to gas temperature is plotted against different values of electric field divided by pressure. The abscissa of 1 corresponds, for example, to an electric field of 1 volt per cm and a pressure of 1 mm of Hg. The electron temperature for a discharge in neon is more than 200 times the gas temperature and the gas temperature may be as high as 2000° C.

The operation of a DC gas discharge as a noise source has been described in terms of its apparent noise temperature. Such a gas discharge has been used as a high frequency noise source. Mumford⁴ and Johnson and DeRemer⁵ have described such a noise source and have described the noise power available from such a source in terms of an apparent noise temperature. That is, the noise power has been set equal to the noise available from a resistor at some elevated temperature. It has been suggested by the above writers that this is essentially the electron temperature in the discharge. The measured noise temperature agrees quite well with the noise temperature calculated by V. Engel and Stenback for the conditions of the particular discharge under consideration. A measured noise temperature of 15.5 db above kT where $T = 290^\circ K$ compared favorably with the computed value of electron temperature of 15.1 db above kT ($T = 290^\circ K$) for a Mercury discharge. See Fig. 2 for a value of rp (cm mm Hg) equal to the value existing in a Mercury fluorescent lamp. The abscissa rp is the product of r , the radius of discharge in centimeters and p , the pressure in mm of Hg. Power spectra measurements performed by several

investigators have shown that the noise output is fairly constant in the 2000-25000 mc range so that the output may be looked on as electron thermal noise.

The AC power available in a DC gas discharge due to plasma oscillations may be described as follows: The plasma possesses some similarities to an acoustic medium. It is capable of sustaining and propagating longitudinal waves of electrons and ions. Tonks and Langmuir have described and measured such plasma oscillations of electrons and ions. They were led to investigate this phenomenon by noting that there are a wide range of discharge conditions in which a large number of electrons rapidly acquire velocities whose voltage equivalent is greater than the total drop across the tube. The plasma oscillations which usually accompany an abrupt increase in the energy spread of the beam were related by Tonks and Langmuir with the equation

$$\omega_p^2 = n e^2 / m \epsilon_0 \quad (1)$$

where ω_p is the radian frequency of the plasma oscillation, n the electron density, m the mass of the electron, and ϵ_0 the permittivity of free space. Plasma oscillations have been observed although the powers available at the output terminals of coupling devices inserted into the region of the plasma has not yet been found theoretically. The frequency of electron plasma oscillation is in the 1500 megacycle range for electron densities of 1×10^{16} electron/cm³. Ionic plasma oscillations are for some simple cases approximately equal to

$$\left[\frac{(1950)(\text{atomic weight})}{\text{of the molecule}} \right]^{\frac{1}{2}} \text{ times the electron}$$

plasma oscillation frequency for the same density. That is, if 10^{11} electrons/cm³ have a plasma oscillation frequency of 1000 mc then the nitrogen ionic plasma oscillation frequency is 6.2 mc. In a series of earlier tests, Looney and Brown have shown quite clearly that such oscillations can exist and that they are longitudinal electron pressure waves set up in the plasma. DeRemer in fact has developed a plasma electron oscillator tube capable of delivering sustained oscillations from 30 to 3000 mc.

The AC power due to oscillations of positive ions in a potential minimum are small compared to plasma oscillations and will not be mentioned further.

The problem of fluctuations in a gas plasma in a magnetic field may now be discussed. High intensity fluctuations have been observed in vacuum tubes operating in a magnetic field. This is evident in the fact that appreciable electron densities exist in the region beyond cut-off in a DC magnetron. Large magnitudes of noise have also been observed in other tubes employing crossed electric and magnetic fields such as trochotrons. Efforts to explain these large magnitudes of noise were undertaken by Ballof. He used some ideas of V. A. Bailey who has

determined what electric waves can exist in a plasma subject to static electric and magnetic fields. Bailey showed that frequency bands exist in which initial fluctuations may be amplified so that strong electromagnetic noise can be developed from small random fluctuations. These theories demonstrating the enhancement of initial small current fluctuations have mostly to do with dispersion equations determined by the interaction between charged particles and the electric and magnetic fields. This affects the character of the propagation constant. It is not possible, however, to use these results to compute the magnitude of observed noise power.

An intensive experimental study by Batten and Early¹¹ has shown that the large fluctuations present in a DC gas discharge propagate approximately in the direction of electron drift and that these fluctuations grow as they propagate.

Experimental Work

Since it was felt that even larger amounts of noise power could be obtained from discharges maintained by a magnetic field, structures utilizing Penning gauge geometry were investigated. The purpose of the work was to find a gas discharge noise source capable of generating larger amounts of noise than that available from the gas discharge noise source described by Mumford and Johnson and DeRemer and, if possible, having frequency components in a large band of frequencies.

First tests were made on a modified Phillips Ionization Gauge (see Fig. 3). The metal surfaces are nickel plated and the magnitude of the magnetic field is 150 gauss. In operation, the electrons given off by the cold cathodes, A and B, move in spirals as they approach the center loop anode. The probability of ionizing collisions is increased because of the increase in total electron path length before capture at the anode. The form of the anode permits the electron to make many traversals of the volume of the tube, before anode capture so that ionization may occur at quite low values of pressure (10^{-7} mm of Hg). A coaxial probe was inserted into the ionization gauge with its center conductor extending further into the region of the discharge. The coaxial probe was designed to match the input impedance of receivers used (AFR-1, and MA-2).

The power spectrum of the noise was determined by varying the output of a calibrated signal generator to match the deflection of the output meter of the receiver actuated by the noise. The noise power is then, the input CW signal generator power divided by the noise bandwidth of the receiver. The noise power is specified in terms of power per cycle of bandwidth. The units of noise power used here are db above 1T per megacycle of bandwidth where $T = 293^\circ \text{K}$. This can be easily compared to the Johnson and DeRemer, and the Batten and Early data.

It was found that the optimum noise power spectrum is as shown in Fig. 4. The curve drawn in the diagram is meant to indicate noise maxima; the powers measured in the 30 to 300 megacycles

bands are higher than the 40 to 50 db above KT ($T = 290^\circ K$) measured by Batten and Early for a tube having similar geometry but higher pressures (11-20 microns of Hg). Here the operating conditions were $I = 1.0$ ma, $V = 1500$ v, $p = .2$ microns of Hg, magnetic field 1450 gauss. It should be noted that values of noise power of between 25 and 35 db above KT per megacycle of bandwidth were measured in the 3 band region. Here the noise occurs in bands several megacycles wide. This is 10-20 db above the thermal noise powers observed by Johnson and DeRemer.

A demountable noise gas discharge tube was constructed as shown in Fig. 5. Here the position of the probe could be controlled by the bellows arrangement. DC magnetic fields of 2000-3000 gauss were available. Aluminum, Molybdenum and stainless steel were used as electrodes. Although the aluminum and Molybdenum electrodes gave no lower noise powers than the stainless steel electrode, their use was abandoned because of excessive vaporization and sputtering. This discharge contains 2 disc cold cathodes and an annular anode between them. The discharge is maintained by the magnetic field and vanishes upon the removal of the magnetic field. It was found that higher noise powers were observed (see Fig. 6) than in the case of the modified Phillips gauge. The measurements made on these tubes indicated that in the 30-90 megacycle range powers greater than 50 db above KT per megacycle of bandwidth could be obtained with smaller bands of 5-10 megacycles wide in this range having as much as 70-90 db above KT per megacycle of bandwidth. In the 90-500 mc range noise powers of approximately 1.0 db above KT per megacycle of bandwidth were found to exist in bands 5-10 megacycles wide. Measurements in the 1000-4000 mc range indicated that the noise power did not exceed 35 db above KT per megacycle of bandwidth. The different electrode materials tested did not seem to give radically different noise power spectra. The movements of the position of the probe seemed to change the magnitude of the noise power but because of the small size of the tube no detailed behavior could be noted. There was noted at certain operating voltages and pressures the existence of Barkhausen oscillation but tube operation was confined in the noise power spectrum tests to operating regions where this was minimized.

Gas discharge tubes having oxide coated heated cathodes were also constructed. The cathodes had a short lifetime under the above operating conditions but greater currents were available (20-50 ma) and noise power spectra tests seem to indicate that much smaller magnitudes of noise power were available.

Sealed versions of hot and cold cathode noise discharge tubes were constructed.

The geometry of these tubes was similar to that of the demountable discharge tubes (see Fig. 7). The discharges, however, were in a Mercury vapor. The difficulty that prevented the construction of sealed tubes containing gases such as nitrogen, hydrogen, or argon at pressures of 1 micron of Hg is that a pressure of 1 micron of Hg cannot be maintained during operation.

A getter which will absorb gases liberated during tube operation would also absorb the gas originally put into the tube. Fortunately, sealed tubes containing Mercury reservoirs would operate at pressures of 1 micron of Mercury if the temperature of the Mercury reservoir was kept at $18.1^\circ C$.

The noise power spectra were similar to the demountable gas discharge tubes. The probe here consists of an unshielded wire filament. This was a short length of tungsten wire of 2 mil. diameter welded to the lead through wire and then coupled to the receiver.

An attempt was made to find out whether the power measured in some of the frequency bands where that power was large is truly noise power or whether it contained strong coherent components in some frequency bands. It seemed likely that most of the powers measured were really random fluctuations of power since oscillograms were taken of the output of the IF amplifier of the receiver. Figure 8 shows such an oscillogram where 1 is the IF output signal of the receiver, with no input signal to the receiver; 2 is the output IF signal with the output of the gas discharge tube connected to the input of the receiver; and 3 is the IF output signal with a coherent sinusoidal input signal. Oscillogram 2 seems to give the usual appearance of a noise voltage and the audio signal in a pair of ear-phones gave the characteristic hissing that noise usually gives.

There was available at the laboratory an instrument that presents the amplitude probability distribution function of an input time varying signal on an oscilloscope. This is a device described by Orr¹¹ which plots a function whose abscissa is equal to a portion of the range of the input signal under observation, and whose ordinate is proportional to the amount of time that a signal spends in that small range of amplitude. For example, a sinusoidal wave has an amplitude probability distribution function that is approximately as shown in Fig. 9. The value of this function at the limits of the sinusoidal signal are infinite when the range of amplitude analyzed is differentially small. The finite resolution of this instrument results in the finite values of the amplitude probability distribution function at the maximum range of the signal. If an input time varying voltage in a small frequency interval has a gaussian amplitude probability distribution function then this will be plotted as a gaussian amplitude probability distribution function on this device. Figure 10 shows the amplitude probability distribution function of a GR low frequency noise source. Figure 11 shows the amplitude probability distribution function of the IF output signals for the receiver with the input coupled to the gas discharge probe. Similar amplitude probability distribution functions were taken at receiver settings of 10, 76, 90 and 140 mc. The amplitude probability distribution function shown at 90 mc (see Fig. 12) suggests that a coherent component of oscillation in the discharge may exist. Such a method may be of some aid in determining whether the output of a gas discharge tube has a truly random character or is a sustained

oscillation in some frequency range.

The amplitude probability distribution function curves and the oscillograms taken of the IF output voltage of the receiver in all other portions of the spectrum above 30 mc indicated that the power is of a random nature and that this device can be used as a noise source in these frequency ranges.

An oscillogram of the gas discharge noise signal was taken from the output of several wide band SKL amplifiers connected in tandem and having their output presented to the vertical deflection plate of a Tektronix Type 517 Synchroscope. Here, the low frequency cut-off was less than a megacycle and the high frequency cut-off was above 70 megacycles. With the synchroscope synchronized on input signal the oscillogram shown in Fig. 13 was taken. A strong coherent 25 mc component is evident. This may be Barkhausen oscillation or sustained coherent plasma oscillations but the fuzziness of the signal indicates also the random components of the signal.

Conclusions

Large magnitudes of noise power can be extracted from a gas discharge maintained by a magnetic field. It is felt that these high noise power levels are due to amplified random plasma oscillations whose level is a function of oscillation frequency and discharge conditions.

lating frequency distribution are widened by the presence of a magnetic field.

References

1. W. G. Malmgren, Arkiv Fur Fysik, 1, 564, (1950)
2. V. L. Bailey, Phy. Rev., 73, 129, (1950)
3. Bailey and Landecker, Nature, 121, 259, (1950)
4. Mumford, I.T.V., 23, 604, (1949)
5. Johnson and Deener, I.R.S., 39, 908, (1951)
6. Tonks and Lamuvir, Phy. Rev., 33, 195, (1929)
7. Looney and Procn, Phys. Rev., 93, 965 (1951)
8. Mehner, J.A.P., 761, June, 1951
9. Linder, I.R.S., 26, 316, (1936)
10. "Theory and Applications of Trochotrons", Engl. Technische Hochschulen Hardinger, No. 22, 1948
11. V. L. Bailey, J. Royal Soc., 20, 82, 107, (1942)
12. Gross, Phys. Rev., April, 1951
13. Batten and Early, "Plasma Fluctuations in Crossed Electric and Magnetic Fields", Tech. Rep. No. 2, E.R.I., Univ. of Mich., May, 1951
14. Orr, "Wide Band Distribution Analysis of Voltage Sources", Tech. Rep. No. 22, E.R.I. Univ. of Mich., October, 1953

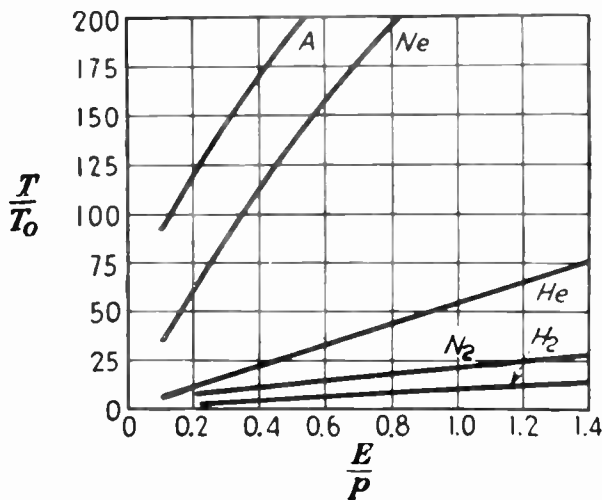


Fig. 1

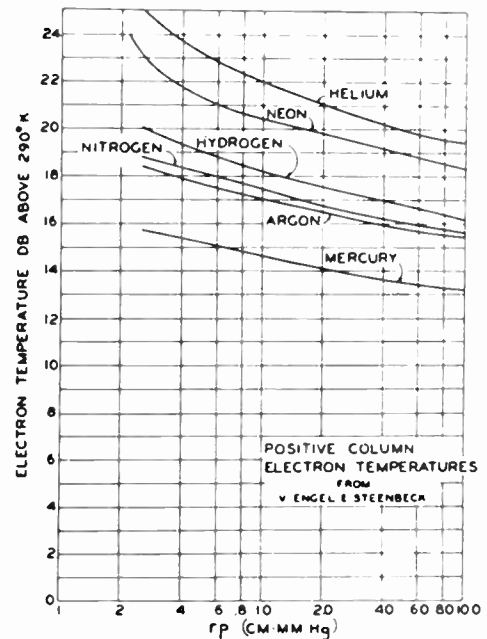


Fig. 2

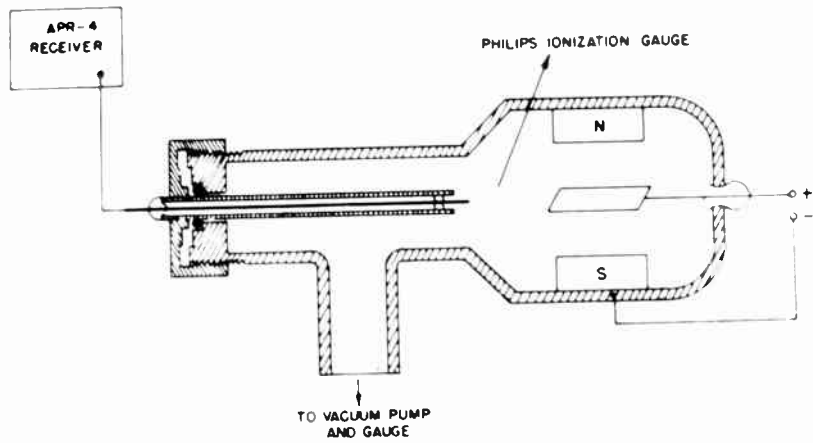


Fig. 3

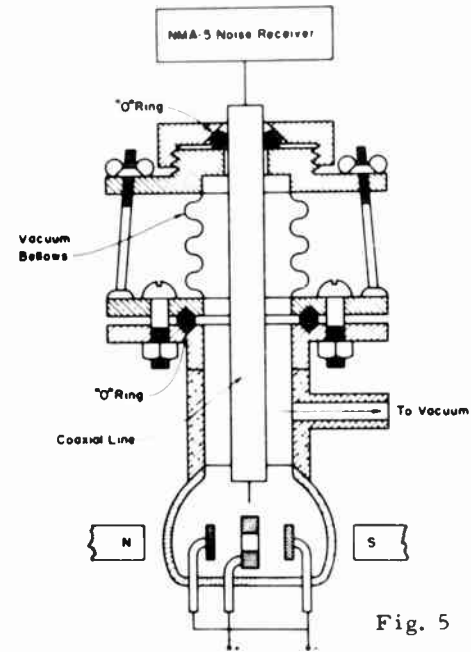


Fig. 5

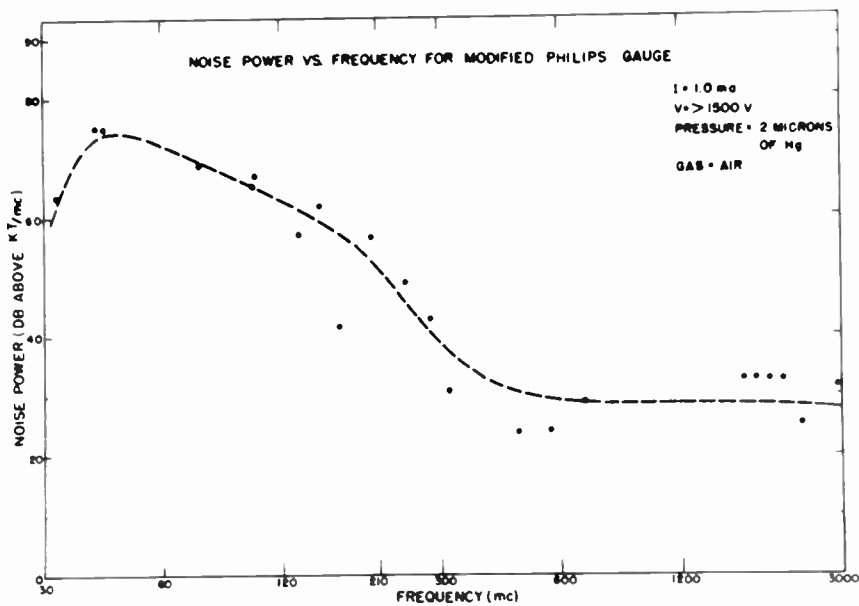


Fig. 4

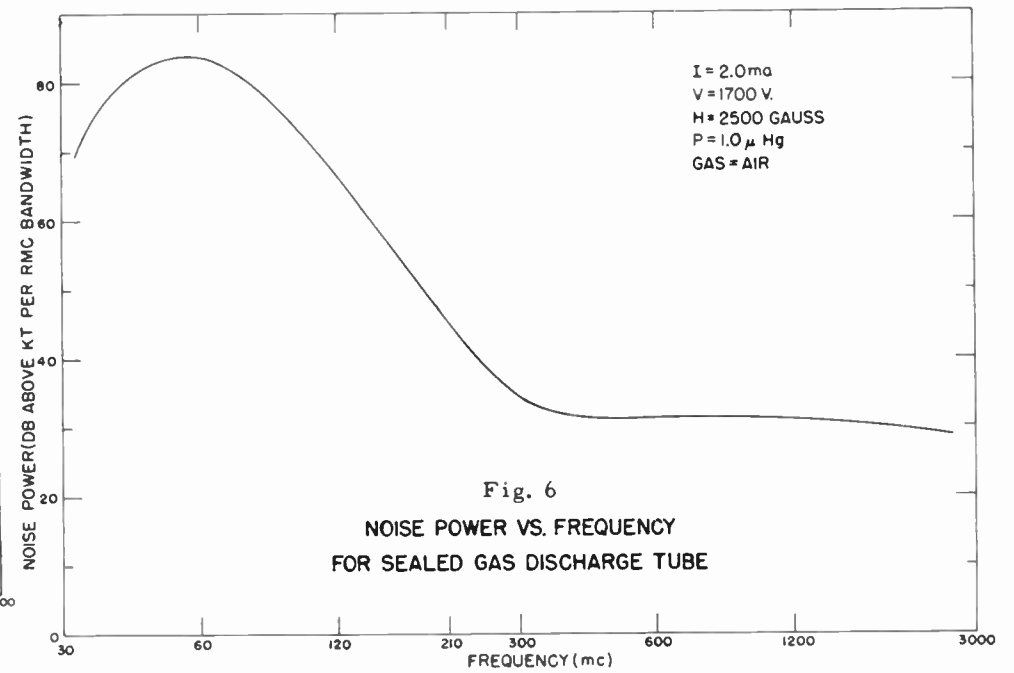


Fig. 6

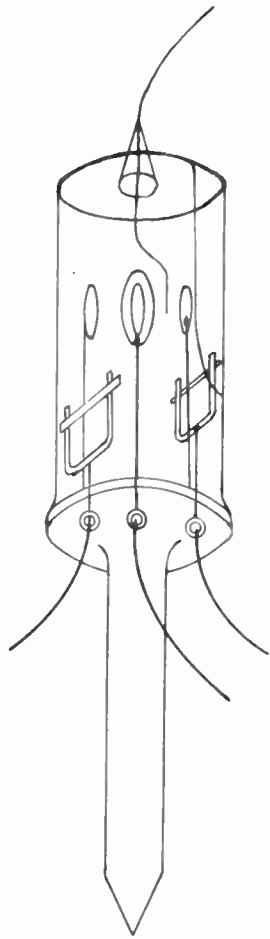


Fig. 7

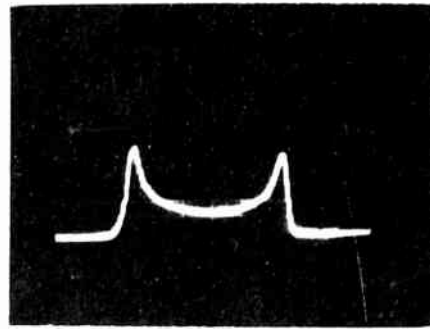


Fig. 9

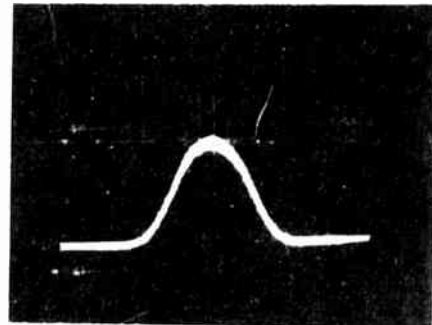


Fig. 10

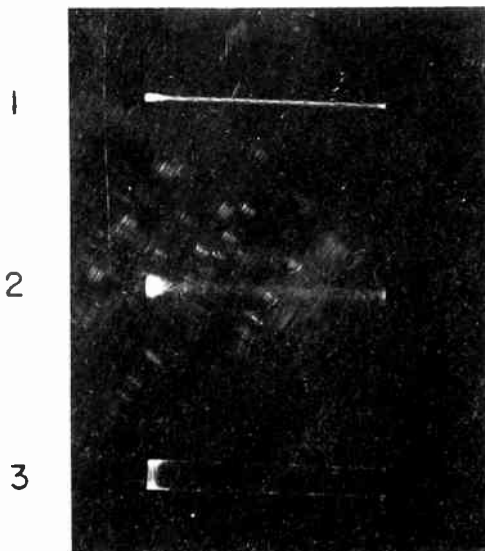


Fig. 8

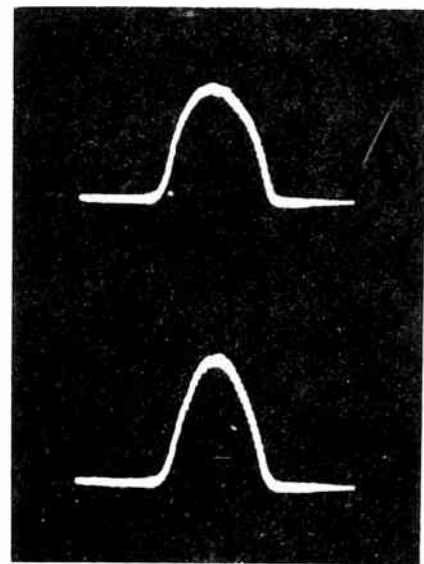


Fig. 11

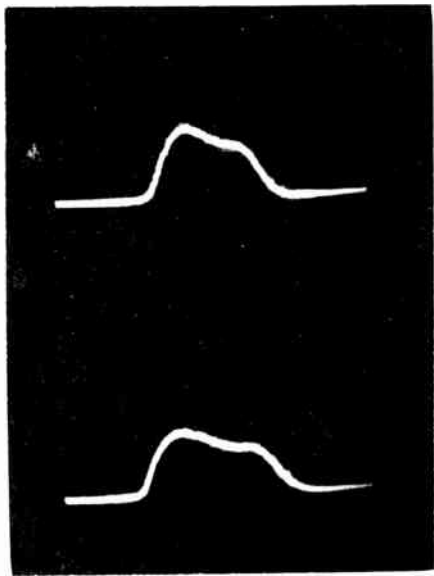


Fig. 12

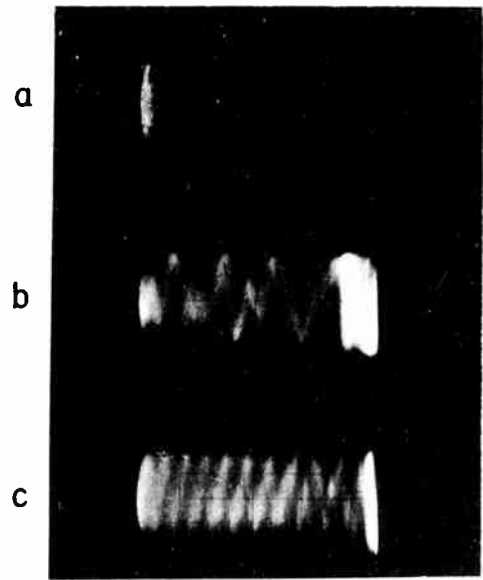


Fig. 13

CORRECTIONS TO THE THEORY OF THE GROUNDED-GRID TRIODE.

W. A. Harris
 Tube Department
 Radio Corporation of America
 Harrison, N. J.

The development of circuit equations for a triode used in a grounded-grid or cathode-drive circuit is usually based on theory and data applicable to grounded-cathode operation, with the addition of simplifying assumptions. Thus, it has been common practice to represent a triode in a grounded-grid circuit by an equivalent circuit including a shunt conductance which increases with the square of the frequency across the input terminals because it is known that the input conductance of a tube used in a grounded-cathode circuit increases in this manner. It has also been common practice to disregard the phase shift in the forward transfer admittance and to neglect the feedback susceptance in equivalent circuits for the grounded-grid tube.

This paper discusses an analysis of grounded-grid triodes, based on evaluation of the four-terminal short-circuit admittances. Hypothetical tubes are first subjected to mathematical treatment, and then data are given for tubes which have been measured at frequencies near 1000 megacycles per second.

Network Equations

The symbols and conventions used in the discussion of four-terminal admittances are illustrated in Fig. 1. The tube under test is represented by a four-terminal network having short-circuit admittances Y_{11} , Y_{12} , Y_{21} , and Y_{22} . The input termination is represented by the admittance Y_0 and the output termination by the admittance Y_3 . Y_1 is the admittance measurable at the input terminals when the output-termination admittance, Y_3 , is connected across the output terminals. The input admittance, Y_1 , is related to Y_3 by the equation

$$Y_1 = \frac{i_1}{e_1} = Y_{11} - \frac{Y_{12}Y_{21}}{Y_{22} + Y_3} \quad (1)$$

This equation can also be written as

$$\frac{Y_1}{g_{11}} = 1 + j \frac{B_{11}}{g_{11}} + \frac{R_0}{1 + \frac{g_3}{g_{22}}} e^{j\theta} (1 + e^{-j2\theta}) \quad (2)$$

if the following substitutions are made:

$$Y_{12}Y_{21} = |Y_{12}Y_{21}| e^{i\phi} \quad (3)$$

$$R_0 = \frac{1}{2} \frac{|Y_{12}Y_{21}|}{g_{11}g_{22}} \quad (4)$$

$$Y_{22} + Y_3 = \frac{g_{22} + g_3}{\cos^2 \theta_2} e^{j\theta_2} \quad (5)$$

The angle ϕ is the phase angle of the product of the short-circuit forward admittance, Y_{21} , and the short-circuit feedback admittance, Y_{12} . The angle θ_2 is the phase angle of the sum of the short-circuit output admittance, Y_{22} , and the output-termination admittance, Y_3 .

Then the output-termination conductance, g_3 , is constant and the output-termination susceptance, B_3 , is varied, the only quantity in equation (1) which varies is the angle θ_2 . The curve of B_1/g_{11} vs g_1/g_{11} obtained under these conditions is always a circle. When g_3 is zero, the radius of the circle is R_0 . In the curve shown in Fig. 2, the magnitude of R_0 is one-half and the phase angle ϕ is -30° .

If g_3 is constant, maximum power gain is realized when B_3 is adjusted so that the angle θ_2 is determined by the following equation:

$$\tan \theta_2 = \frac{R_0}{1 + \frac{g_3}{g_{22}}} \sin \theta \quad (6)$$

This power gain can be realized under test conditions by adjustment of the input-termination admittance, Y_0 , to a conjugate match with the circuit input admittance, Y_1 . The magnitude of the power gain, G , is

$$G = \frac{|Y_{21}|^2}{g_{11}g_{22}} \frac{g_3/g_{22}}{\left(\frac{g_3}{g_{22}} + 1 - R_0 \cos \phi - R_0\right) \left(\frac{g_3}{g_{22}} + 1 - R_0 \cos \theta + R_0\right)} \quad (7)$$

The terms in equation (7) can be determined from the curve shown in Fig. 2, either by computation or by measurement. The terms $(1 - R_0 \cos \phi - R_0)$ and $(1 - R_0 \cos \theta + R_0)$ are the minimum and maximum values for the abscissae of the circle. Then the first of these quantities is positive, the gain is finite for all values of g_3 and the network is inherently stable. For this condition, a value of g_3 which provides maximum gain can be found. The required value for g_3 is given by

$$\frac{g_3}{g_{22}} = \sqrt{(1 - R_0 \cos \phi - R_0)(1 - R_0 \cos \theta + R_0)} \quad (8)$$

Then, the maximum gain, G , is

$$G_{\max} = \frac{1}{2} \frac{|Y_{21}|^2}{g_{11}g_{22}} \frac{1}{1 - R_0 \cos \phi + \sqrt{1 - R_0 \cos^2 \phi - R_0^2}} \quad (9)$$

When R_0 is zero (the condition for zero feedback), maximum gain is obtained with g_3 equal to g_{22} . The gain for this condition is

$$G_{\max} = \frac{1}{4} \frac{|Y_{21}|^2}{g_{11}g_{22}} \quad (10)$$

In the design of amplifier stages, the gain is often restricted by considerations of bandwidth. The bandwidth of the output circuit depends on the output admittance, Y_2 , obtained with the input termination connected across the input terminals. When the output-termination susceptance, B_3 , is adjusted for maximum gain, and the input-termination admittance, Y_0 , is matched to the input admittance, Y_1 , the total output conductance, $g_2 + g_3$, including the termination conductance is given by

$$g_2 + g_3 = g_{22} \frac{\left(\frac{g_3}{g_{22}} + 1 - R_0 \cos \phi\right)^2 - R_0^2}{\frac{g_3}{g_{22}} + 1 - R_0 \cos \phi} \quad (11)$$

The output susceptance, B_2 , is

$$B_2 = B_{22} - g_{22} R_0 \sin \phi \quad (12)$$

It is convenient to use a factor, x , given by

$$x = \frac{g_2 + g_3}{g_{22}} \quad (13)$$

The gain, G , expressed as a function of this factor is

$$G = \frac{|Y_{21}|^2}{g_{11}(g_2 + g_3)} \left(1 - \frac{1 - R_0 \cos \phi}{\frac{x}{2} + \sqrt{\frac{x^2}{4} + R_0^2}} \right) \quad (14)$$

Curves of gain vs total output conductance can be plotted by the use of equation (14). These curves have the same shapes as curves of gain vs output-circuit bandwidth. When the quantity $(1 - R_0 \cos \phi)$ is greater than R_0 , there is a value for x for which the gain becomes zero; consequently, a value providing maximum gain may also be found. When the quantity $(1 - R_0 \cos \phi)$ is less than R_0 , the gain approaches infinity as x approaches zero. Of course, this criterion for stability is the same as that applied to the previous equations.

The results obtained thus far apply to any linear four-terminal network. These results can be applied to a specific amplifier such as grounded-grid or cathode-drive triode circuit by determination of the four short-circuit admittances for the circuit considered.

Fig. 3 illustrates the determination of the required quantities for an ideal parallel-plane triode in which electrons are emitted at zero velocity. The short-circuit input admittance, Y_{11} , should be the same as that of a diode because the current measured at the cathode has the same value whether the electrons pass through apertures in the grid or are stopped at the grid plane. Although, strictly speaking, this argument applies only as the amplification factor approaches infinity, the modification for finite amplification factor has a relatively small effect on the form of the curves obtained.

The forward transfer admittance, Y_{21} , results from the electron current passing through the grid. This current is delayed in phase with respect to the voltage e_1 because of the finite time required for the transfer of electrons between the cathode and the grid and between the grid and the plate.

The theoretical value of the short-circuit input conductance decreases slowly with increasing transit angle; there is no transit-time loading term to be added. The phase angle is positive, and the susceptance corresponds to a capacitance which is less than the cold capacitance. The short-circuit transfer admittance is almost constant in magnitude, but it is delayed in phase with respect to the voltage. The theoretical value for this phase delay is the sum of $11/30$ of the cathode-grid transit angle and $2/3$ of the grid-plate transit angle.

In Fig. 3, the vector connecting the end points of the Y_{11} vector and the Y_{21} vector represents the input admittance which would be measured at the grid in a grounded-cathode circuit. It is evident that the major part of the conductance component of this admittance is caused by the phase shift in transfer admittance. This component is the transit-time loading observed in the grounded-cathode circuit. The increase in susceptance and, consequently, in capacitance as compared to values observed in a grounded-grid circuit is also evident.

The short-circuit feedback admittance is determined by the current at the cathode produced by the effective voltage at the grid. Consequently, the feedback admittance for the ideal situation considered is the quotient of the short-circuit input admittance divided by the amplification factor.

The short-circuit output admittance is determined by the current at the plate produced by the effective voltage at the grid, plus whatever currents result from the voltage between plate and grid. The first part is the short-circuit forward admittance divided by the amplification factor; this part consists of a real component proportional to the cosine of the phase angle of the forward admittance and an

imaginary component proportional to the sine of this angle. The second part is principally the susceptance of the plate-to-grid capacitance. This susceptance is generally much larger than the portion derived from the transfer admittance. The third part is a small component representing interaction of the plate-to-grid voltage on the electrons in the plate-to-grid space; this part will be neglected in the subsequent discussion. The total short-circuit output admittance is consequently a conductance that decreases with increasing frequency plus a susceptance which is principally due to the plate-to-grid capacitance. Approximate equations for the short-circuit admittances are as follows:

$$Y_{11} = g_{11} + j\omega C_{11} \quad (15)$$

$$Y_{12} = \frac{1}{\mu} (g_{11} + j\omega C_{11}) \quad (16)$$

$$Y_{21} = g_{11} e^{-j\omega\tau'} \quad (17)$$

$$Y_{22} = \frac{g_{11}}{\mu} \cos\omega\tau' + j\omega C_{22} \quad (18)$$

In terms of the electron transit time,

$$C_{11} = \frac{3}{10} \frac{\tau_1}{g_{11}} \quad (19)$$

$$\tau' = \frac{11}{30} \tau_1 + \frac{2}{3} \tau_2 \quad (20)$$

τ_1 and τ_2 are the transit times from cathode to grid and from grid to plate, respectively. When these values are used, the feedback admittance is approximately

$$Y_{12} = \frac{1}{\mu} \frac{g_{11}}{\cos\frac{3}{10}\omega\tau_1} e^{j\frac{3}{10}\omega\tau_1} \quad (21)$$

The quantities used previously in the equations for input admittance and gain may now be found.

When the output termination conductance, g_3 , is zero, the circle radius, R_0 , is given by

$$R_0 = \frac{1}{\cos\omega\left(\frac{2}{3}\tau_1 + \frac{2}{3}\tau_2\right) + \cos\omega\left(\frac{1}{15}\tau_1 + \frac{2}{3}\tau_2\right)} \quad (22)$$

The phase angle of the product of the forward and feedback admittances is

$$\phi = -\omega\left(\frac{1}{15}\tau_1 + \frac{2}{3}\tau_2\right) \quad (23)$$

The coefficient of the gain equations is

$$\frac{|Y_{21}|^2}{g_{11}g_{22}} = \frac{\mu}{\cos\omega\left(\frac{11}{30}\tau_1 + \frac{2}{3}\tau_2\right)} \quad (24)$$

The term from the gain equation which determines stability, $1 - R_0 \cos\phi - R_0$, is given by

$$1 - R_0 \cos\phi - R_0 = \frac{\cos\omega\left(\frac{2}{3}\tau_1 + \frac{2}{3}\tau_2\right) - 1}{\cos\omega\left(\frac{2}{3}\tau_1 + \frac{2}{3}\tau_2\right) + \cos\omega\left(\frac{1}{15}\tau_1 + \frac{2}{3}\tau_2\right)} \quad (25)$$

This term is always negative, approaching zero as the transit angles approach zero. Consequently, there is no finite maximum-gain value for a tube which is ideal in the sense discussed.

The first diagram in Fig. 4 shows the input-admittance circle for cathode-to-grid and grid-to-plate transit angles equal to 75° and 30° , respectively. The second diagram shows the input-admittance circle for transit angles equal to half these values. Curves of gain vs total output conductance are plotted for both these circles. The results show that the gain would increase with increasing frequency in an amplifier using an ideal tube, and that the gain would approach infinity as the termination conductance approached zero even at low frequencies. Moreover, a theoretical increase of gain with increasing frequency would be found even if the feedback were cancelled by neutralization. This increase results because the short-circuit input conductance and the magnitude of the short-circuit forward admittance vary only slowly with transit angle, while the short-circuit output conductance decreases in the manner of a cosine function.

Measurement of Short-Circuit Admittance and Gain

Data of the type discussed have been measured on several disc-seal triodes at frequencies in the vicinity of 1000 megacycles per second. A block diagram of the test equipment used is shown in Fig. 5. The test procedure is as follows:

- (1) Measurements are made of input susceptance vs input conductance, with output-termination susceptance varied, for several values of output-termination conductance, and curves are then plotted.
- (2) The power gain is measured for at least one stable operating condition, with output-termination susceptance adjusted for maximum gain.
- (3) The short-circuit output conductance is determined, either by direct measurement with the connections to the tube reversed or by a susceptance-variation method with the connections as shown in Fig. 5.

All of the short-circuit admittance magnitudes and the real and imaginary parts for the input and output admittances can be determined from these data. The phase angle for the product of the forward and feedback admittances can also be determined. Additional tests using different circuit connections would be necessary to obtain separate values for the phase angles of these two admittances.

Fig. 6 shows the short-circuit input admittance for an RCA developmental pencil tube as a function of biasing voltage for three different frequencies. In the space-charge limited region, the variation of conductance with frequency is too small to permit a conclusion as to whether the conductance increases or decreases. Very similar curves have been measured on close-spaced diodes. There is an increase of conductance with frequency in the retarding-field region; this region, however, is outside the scope of the theory considered previously.

Fig. 7 shows curves of short-circuit output conductance as a function of frequency for a similar developmental tube. The difference between hot and cold conductance can be fitted to a cosine curve having the extrapolated zero intercept at approximately 1200 megacycles per second.

The magnitudes of the short-circuit forward and feedback admittances are determined from measurements of the input admittance and the power gain on the basis of the theory developed previously. A curve of input conductance vs input susceptance, normalized by division by the short-circuit input conductance, is shown in Fig. 8. This curve was obtained for a developmental pencil tube at a frequency of 870 megacycles per second. The data obtained for this tube are as follows:

Developmental Pencil Tube

Heater Voltage	6.3 volts
Plate Voltage	125 volts
Plate Current	20 milliamperes
Cathode Voltage	0.8 volts
Cathode Resistor	40 ohms
Amplification Factor	55
Transconductance	18.5 millimhos
Plate Conductance	0.34 millimhos

Capacitances:

Grid to Cathode	= 5.1 μ f
Grid to Plate	= 1.9 μ f
Plate to Cathode	= 0.04 μ f

Short-Circuit Admittances:

Frequency, 870 megacycles per second.

Y_{11}	= 19.7 + j 25.6	millimhos
G_{11}	= 4.7	micromicrofarads
Y_{22}	= 0.15 + j 12.5	millimhos
G_{22}	= 2.	micromicrofarads
Y_{21}	= 18.5	millimhos
Y_{12}	= 0.25	millimhos
	= -26.5	degrees
R_0	= 0.67	
$L/R_0 \cos \phi - R_0$	= -0.275	

The values for g_{11} and Y_{21} are approximately equal to the low-frequency values of the tube transconductance. The value for g_{22} includes the dielectric loss in the glass and some series-resistance losses; even with these losses, however, it is lower than the low-frequency value. The feedback admittance, Y_{12} , is decidedly lower than expected. This result probably indicates that the series inductance of the grid is sufficient to cancel partially the effect of the electric field through the grid. The calculated value of inductance needed to obtain the observed result is of the order of a few tenths of a millimicrohenry.

Conclusions

1) The ideal parallel-plane triode, having zero initial electron velocities, shows no appreciable deterioration in performance in a grounded-grid circuit at frequencies up to those at which the transit angles amount to several radians.

2) Formulas giving maximum-gain values and operating conditions for this kind of tube are not possible because the inherent feedback properties predict oscillation as the limiting condition.

3) Dielectric losses and skin-effect losses in a tube often increase with increasing frequency at such a rate as to mask the decrease in electronic conductance. This effect probably explains the correlation obtained in many cases between observed gains and gains calculated by the use of incorrect formulas.

4) The phase shift in transfer admittance must be taken into account to explain the difference between hot capacitances measured at the cathode and at the grid at the lowest frequencies at which such measurements can be made.

5) Measurements at frequencies up to approximately 1000 megacycles per second show correspondence between the performance of actual tubes and the calculated behavior of ideal tubes. It is probably desirable to discuss actual tubes in terms of measurable phase angles instead of the transit angles, because the transit angles have a single value only in the hypothetical case of parallel-plane geometry and zero initial velocity.

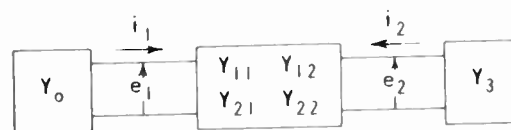


Fig. 1
Equivalent network for grounded-grid cathode showing symbols and conventions used in discussion of four-terminal admittances.

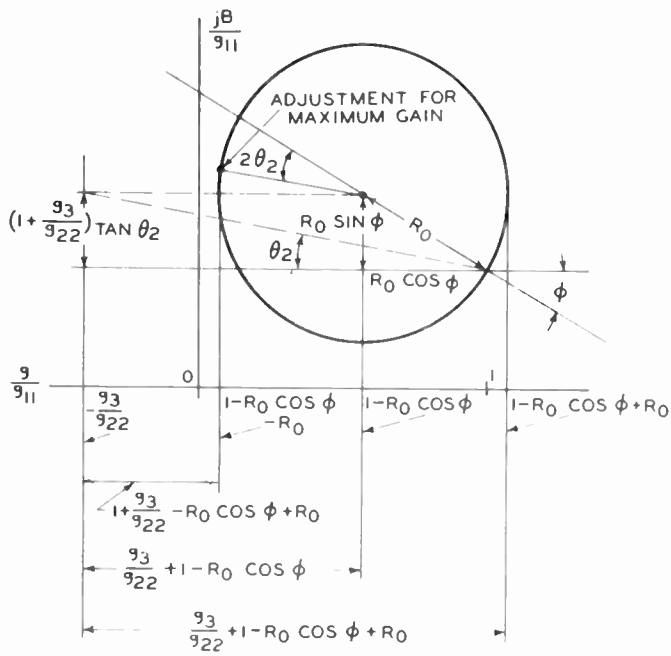


Fig. 2

Theoretical curve of input susceptance as a function of input conductance, normalized by division by the short-circuit input conductance.

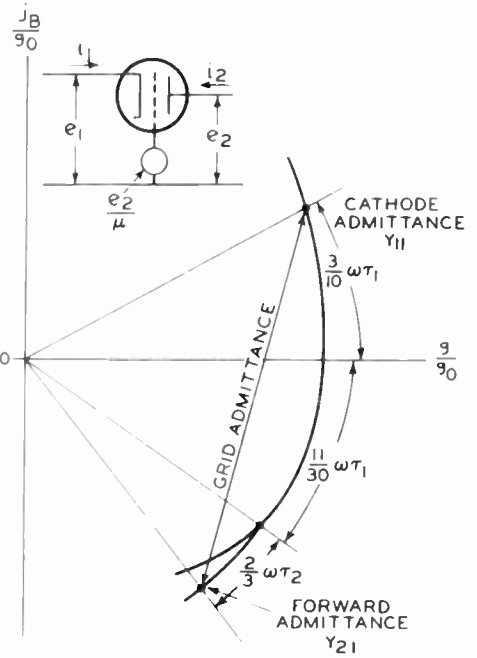


Fig. 3

Admittance curves for ideal parallel-plane triode having zero initial electron velocities.

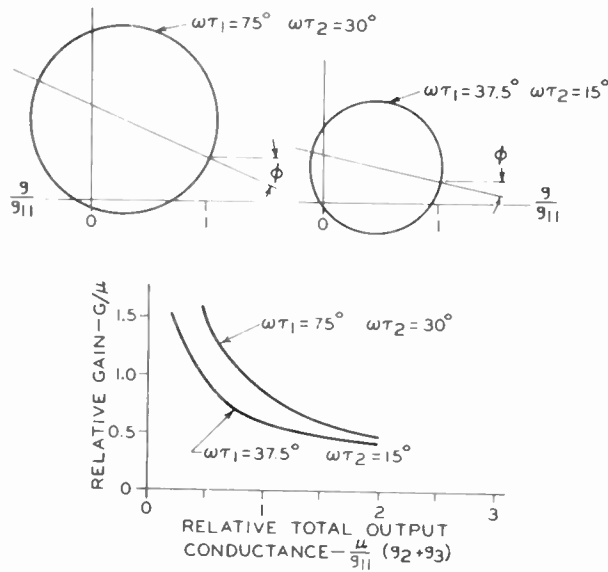


Fig. 4

Input-admittance data and curves of gain vs total output conductance for different transit angles.

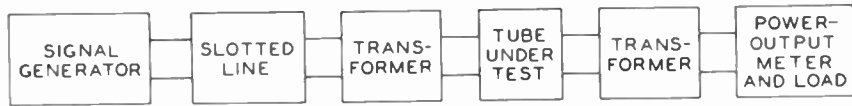


Fig. 5
Block diagram of test equipment.

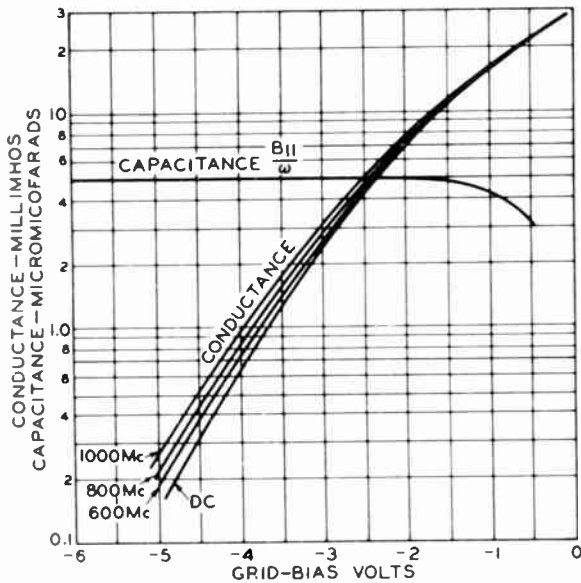


Fig. 6
Short-circuit admittance as a function of biasing voltage for an RCA developmental pencil triode at three different frequencies

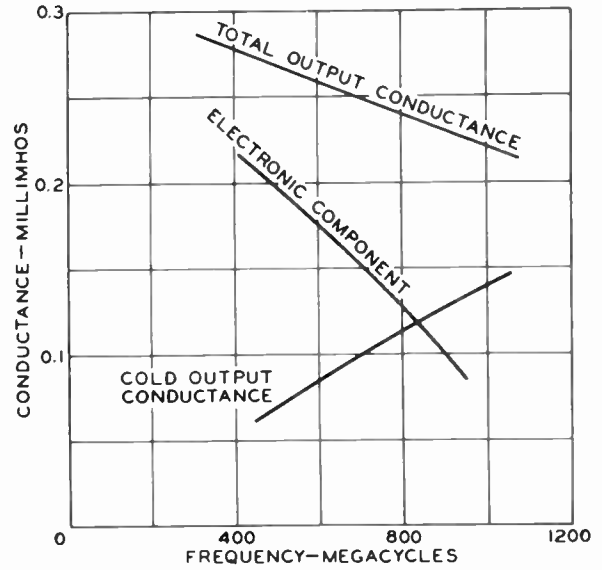
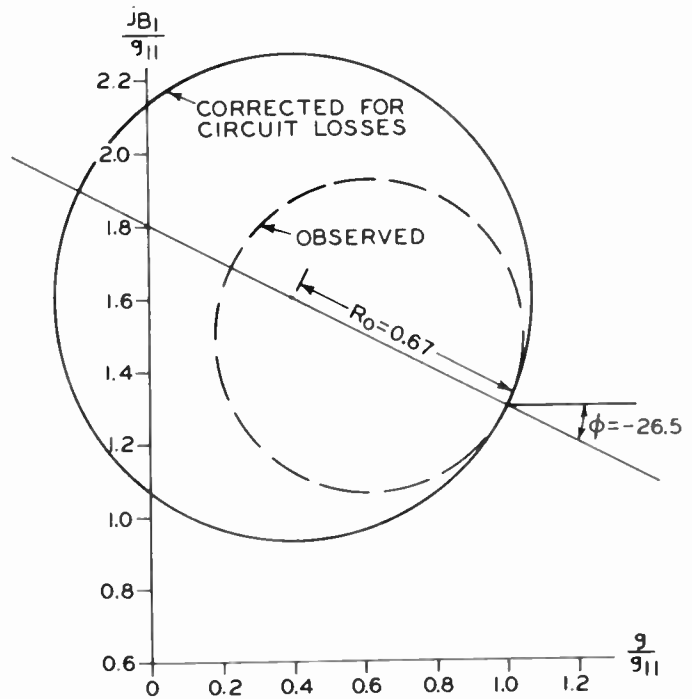


Fig. 7
Short-circuit output conductance as a function of frequency for developmental tube.

Fig. 8
Input conductance vs input susceptance, normalized by division by short-circuit input conductance, for developmental pencil tube at 870 Mc.



DEVELOPMENT OF A LARGE-DIAMETER DUMET LEAD FOR SEALING TO SOFT GLASS

D. L. Swartz and J. C. Turnbull
Radio Corp. of America
Lancaster, Pa.

ABSTRACT

Dumet leads having diameters greater than 0.030 inch have long been desired in the power-tube industry for increased rf-current-carrying capacity. This paper describes a 0.060-inch, high-conductivity dumet lead which was developed by careful matching of radial and axial thermal-expansion coefficient. In this lead, relative copper volume is about $\frac{1}{4}$ to $\frac{1}{3}$ that found in conventional

dumet leads. The core material is a nickel-iron alloy having an expansion coefficient of 90×10^{-7} in/in/ $^{\circ}\text{C}$. The use of this alloy provides a considerably better match to G0120 glass than that provided by conventional dumet leads. Relative merits of three possible techniques for producing the high-conductivity dumet leads are discussed.

NOVEL DESIGN APPROACH FOR MICROWAVE TUBES

J. E. McLinden and D. Lichtman

Airborne Instruments Laboratory, Inc.
Mineola, N. Y.

Summary

An approach to electron-tube construction is presented that is especially suited to tubes and components requiring establishment and maintenance of critical geometries in vacuum-sealed heated assemblies. In this method, spacings are established by optical measurements and maintained by coherence with the assembly envelope. This approach should not only improve the reliability of a component but also reduce its cost. The following discussion deals with the development of a planar microwave triode that has spacing tolerances of ± 0.0001 inch.

Introduction

This paper presents an approach to tube design that has thus far been directed toward the development of a planar microwave triode, but introduces a technique that has possible applications to other tubes and electron devices requiring close tolerances, critical dimensional stability, and high ambient and operating temperatures.

Despite many recent developments in velocity-modulated tubes, planar current-modulated tubes find many applications in amplifiers requiring high gain-band products. The possible applications of planar tubes would be greatly multiplied if their cost could be reduced significantly. For example, with the extension of commercial television into the UHF bands, a low-cost, low-noise planar tube would result in significant overall economies in television coverage.

One of the chief aims of the subject development was to evolve a design and assembly technique that could lead to substantial reduction in costs and improvement of quality in a tube whose grid-cathode spacing would be sufficiently small to enable the performance of the tube to closely approach the ultimate performance of microwave triodes.

A microwave tube cannot be thought of as an electron tube with an attached circuit: the tube and circuit must be thought of as a single electrical system. Thus, to optimize the performance and reduce the cost of such a system, the tube and circuit design must be thoroughly integrated.

The important parameters that must be considered in establishing such a microwave tube design include (1) dimensional requirements for electrical performance, (2) establishment and maintenance of critical internal dimensions, (3) minimization of r-f losses, and (4) dissipation of heat. Past tube developments undertook to resolve these problems in a number of ways. Many of these designs depended upon the establishment of critical internal dimensions by means of structural features of the tube itself, such as the use of shims. This approach dictates an

expensive design, because all parts of the tube must be made to closer tolerances than the spacings required in the final assembly. Other designs depended upon precise and elaborate jigs to support the tube elements during sealing-in. Such jigs are not only expensive initially but must include tolerance requirements that are difficult to maintain.

In our approach to this problem, we introduced a technique whereby spacings are established during assembly through the use of optical measuring equipment. This permits relatively loose tolerances on the tube parts and yet makes spacing tolerances of ± 0.0001 inch practical; it also optimizes the electrical performance by contributing to quality control in manufacturing and tube reliability in application.

In order to maintain these dimensions, the elements are bonded by a refractory cement that can be applied conveniently and exhibits satisfactory vacuum properties and dimensional stability. The cement, which forms portions of the tube envelope, is not vacuum tight. It is therefore glazed during the sealing-in. The application of the glaze to the assembly required the development of special techniques, and a number of practical methods were established.

Tube Structure

The structure of the tube thus evolved is here presented (Figure 1). It consists essentially of three coaxial cylinders, terminating in the cathode, grid, and anode, respectively. Each of these cylinders is assembled separately to reasonably close tolerances, but the tolerance requirements on these subassemblies are far less than those required by the final geometry.

The cathode cup is machined and polished from nickel stock rather than punched or drawn, because it was found that only by this technique could the required planarity of the cathode surface be obtained. The cathode cup is then mounted on a $1/2$ mil Inconel X cylinder that not only provides the necessary structural rigidity and thermal isolation of the cathode from the rest of the tube structure, but also has satisfactory r-f conduction properties.

The cathode is heated by a conventional coiled heater mounted on a ceramic stem, which also supports the ribbon getter on a third lead. In this tube, the heater-cathode connections are separate.

The molybdenum anode serves as the termination of an assembled cylinder comprising the anode, a glass-sealing alloy cylinder with exhaust holes, and an OFHC copper exhaust tubulation.

The grid consists of a gold-plated 0.0003-inch-diameter tungsten wire wound at a pitch of 1900 turns per inch and brazed to a molybdenum washer. The wound grid is welded to the end of a

supporting cylinder.

Assembly

The principal envelope materials are Allegheny-Ludlum 4750 alloy and Alsimag 243 Forsterite. Forsterite was chosen as the envelope ceramic because of its low-loss factor of 0.002. The strength of Forsterite is relatively low, but it was found to be adequate for the requirements of this development both in fabrication and operation. Allegheny-Ludlum type 4750 glass-sealing alloy was chosen because its expansion coefficient closely matches that of the Forsterite. The cement and solder glass frit complete the envelope and provide the necessary structural and electric properties.

The refractory cement used in this application has an expansion coefficient approximating that of soft glass,--that is, approximately 90×10^{-7} centimeter per centimeter per degree C. It has the important feature that it satisfactorily wets most ceramics, metals, and glasses, and thus can be used as a bonding agent in electronic tubes having components whose expansion coefficients approximate that of the cement. The vacuum properties of the cement have been tested, and tubes containing this cement have performed for well over 5000 hours with no apparent deterioration of vacuum. The cement can be baked out at temperatures greater than 800 C without destroying the bond, and tubes assembled using this cement as a bonding agent have been operated at extremely high accelerations. Preliminary tests of r-f losses indicate that in the applications we have considered, the losses of the cement are negligible.

The Corning type 7570 solder glass has a softening temperature of less than 500 C and an expansion coefficient of 84×10^{-7} , which matches the other envelope materials reasonably well. It was furnished to us by Corning in the form of 325 mesh powdered frit. We have experimented with various techniques for applying the frit to the seal. In certain geometries, it can be applied as powder by simply placing it in the area where the seal is desired. The glass may be heated by means of a gas-air or gas-oxygen torch. In other applications where the frit is in intimate contact with r-f conducting elements, sealing-in can be accomplished by induction heating.

A third method of effecting seals is by placing the entire assembly, including the frit, in an oven that is elevated to the flow point of the frit.

We have found it convenient to draw the powdered frit into canes of about 1/16-inch diameter. By the use of this configuration, the glass can be applied in the same manner as metallic wire or strip solder--that is, it is held on the sealing point by hand, and heat is applied via a torch until the glass flows. It can then be shaped to the required fillet by means of a carbon rod. We have also explored the application of the frit in the form of molded preforms. The glass can either be molded with a volatile binder or the preforms can be molded and pre-melted to the required shape. This latter technique would of course be desirable in large production quantities.

In order to proceed with the completion of the envelope construction, the critical spacings between the planar elements must be established. The grid-anode spacing is established optically in a unit as shown in Figure 2. This unit consists essentially of a 300-power compound microscope in which the stage has been replaced by a structure on which can be mounted the grid and anode sub-assemblies. The anode assembly is held below and inside the grid-cylinder assembly. The latter is mounted on a platform supported above the anode in such a way that it can be moved laterally in two directions with respect to the anode holder. The anode can be moved vertically. By means of the microscope, observations are made through the grid laterals of the grid-anode spacing, which has a calibrated scale on its vertical movement. In this way, the grid-cathode spacing can be fixed by depth-of-focus measurements, and the anode can be located centrally with respect to the grid. When the final location has been established (approximately 0.003 inch), the cement is applied between the two cylinders while the assembly remains in the jig. When the cement has dried, this subassembly is placed in the grid-cathode spacing machine (Figures 3 and 4).

Basically, the grid-cathode spacing machine consists of two coaxial chucks mounted on a bed plate. The anode chuck can be translated axially to adjust the grid-cathode spacing. The cathode chuck can be tilted angularly to align the cathode parallel to the grid. Both chucks are rotated simultaneously to inspect the accuracy of the grid-cathode alignment. An optical system projects a shadow of the grid-cathode spacing for optical inspection. The optical system uses as an illumination source, a well-collimated beam produced from a zirconium arc point that is projected through the grid-cathode aperture. The image thus formed is magnified about 100 times and projected on a ground glass screen. This is sufficiently bright to permit comfortable operation by the operator. After the grid-anode assembly is inserted in the chuck, a retaining ring is tightened to cause the chuck to grip the anode tightly. The cathode subassembly is inserted in the cathode chuck, which is similar to the anode chuck.

The spacing between the grid and cathode is adjusted by a combination of coarse and fine adjustments for translating the feed tube.

When the cathode-grid spacing has been set, the spacing is inspected to determine the extent to which the cathode is tilted relative to the grid. This is done by means of the roll knob, which drives both the anode-chuck mandrel and the cathode-chuck mandrel in synchronism. These two mandrels ride in sets of aligned ball-bearing races. While the two subassemblies of the tube are rotated, the optical system projects a shadowgraph of the peripheral spacing between cathode and grid on a viewing screen. An angular scale on the left-hand end of the cathode-chuck mandrel enables the operator to read the angular position at which the space between the cathode and anode is the greatest. This angle is indicative of the plane in which the cathode is

tilted relative to the grid. After having determined this plane, the operator rotates the chuck mandrels back to their zero positions and tilts the cathode chuck as required.

In order that the cathode chuck may tilt in any direction, it is mounted in its mandrel by a brass surround whose external surface is a spherical zone. The center of the spherical zone is approximately at the center of the cathode face when the cathode is mounted in the cathode chuck. With some practice, the tube assembler can accomplish the alignment and spacing in about 5 minutes.

Following alignment and spacing, the Forsterite envelope is placed over the grid and cathode cylinders and cemented in place with the cement. The lining up of this is not extremely critical and is accomplished by means of a simple jig. After the assembly has dried sufficiently, it is ready for sealing-in. This is accomplished on a conventional sealing-in lathe with provision for flushing the assembly with forming gas during the sealing-in operation. The sealing-in operation is accomplished by means of the solder glass, which is presently applied in the form of cane and heated by means of a gas-oxygen hand torch as indicated in Figure 5.

Conclusions

The chief advantages of this type seal-in include the fact that it can be done directly in air. Furthermore, since the glass serves essentially as a vacuum seal and not as a structural member, this operation does not affect the internal tube geometry. In large-scale production, it

is anticipated that the frit will be applied in the form of glass preforms, and the sealing-in accomplished on an automatic seal-exhaust machine that will consist essentially of a series of ports in which the assemblies can be mounted with the glass preforms in place. This will be passed through ovens that will accomplish both bake-out and seal-in while the tubes are under vacuum. Activation and tip-off will follow in a conventional manner. In the laboratory, however, exhaust has been accomplished on a conventional trolley exhaust machine using water-cooled ports. Activation and pre-flashing of the getter are done while the tube is on the exhaust station, and tipping-off is accomplished by means of a conventional pinch-off tool. Following exhaust, the external conducting surfaces are gold-plated. A completed tube appears in Figure 6. The tubes are aged and dc-tested, and finally, rf-tested.

The sealing-in and processing techniques permitted by this design and assembly lead to a structure having excellent dimensional stability and reproducibility. It is rugged and can operate safely with seal temperatures as high as 250 C. The approach described introduces a method in which close tolerances are established by the use of precision assembly equipment coupled with relatively simple optical measurements, and these tolerances are maintained in operation by a coherent integrated construction.

Acknowledgment

This paper is based on a development program sponsored by the Navy Department, Bureau of Ships, under Contract NObsr-63230.

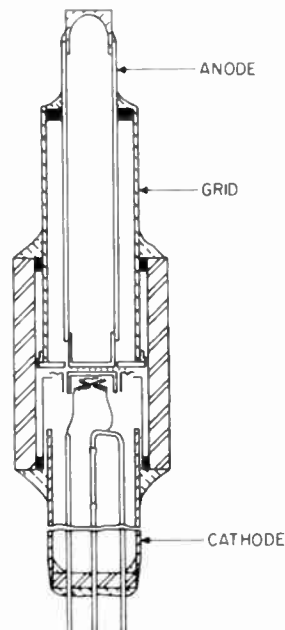


Fig. 1
Tube Structure.

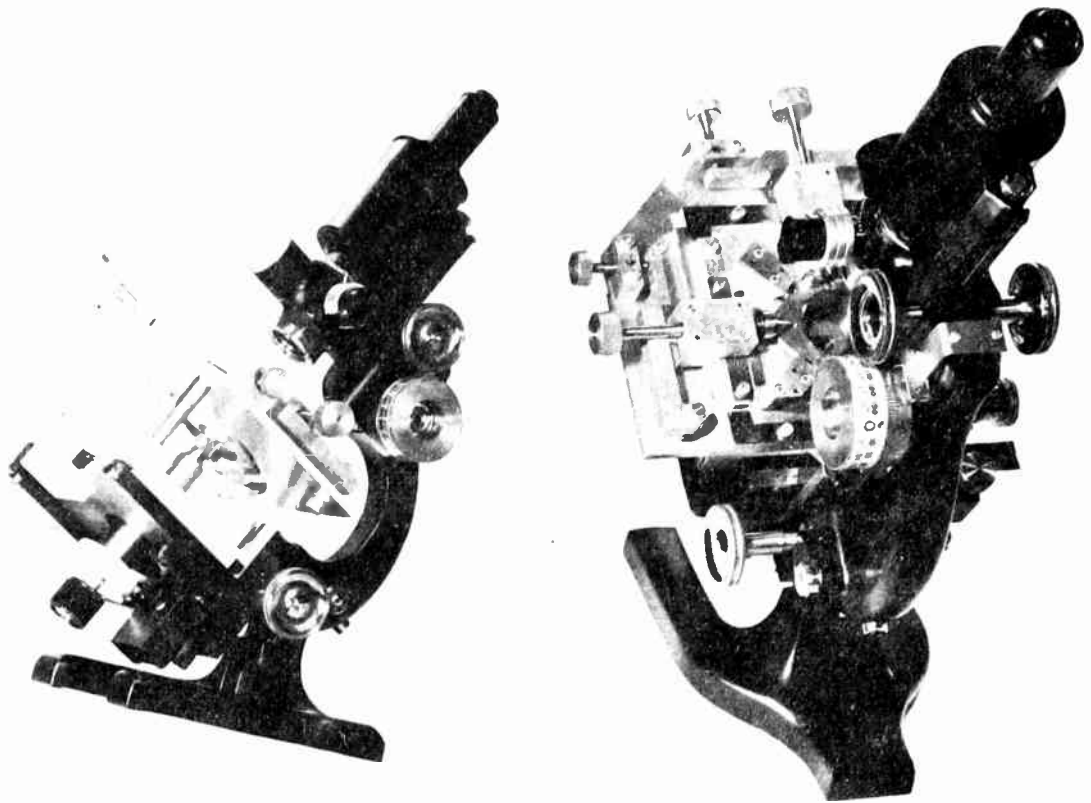


Fig. 2
Grid-Anode Spacing Fixture.

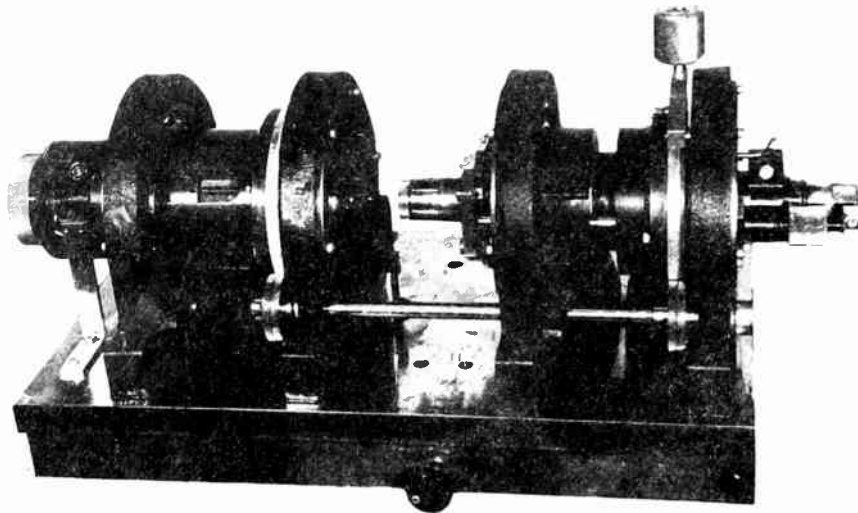


Fig. 3
Grid-Cathode Spacing Fixture.

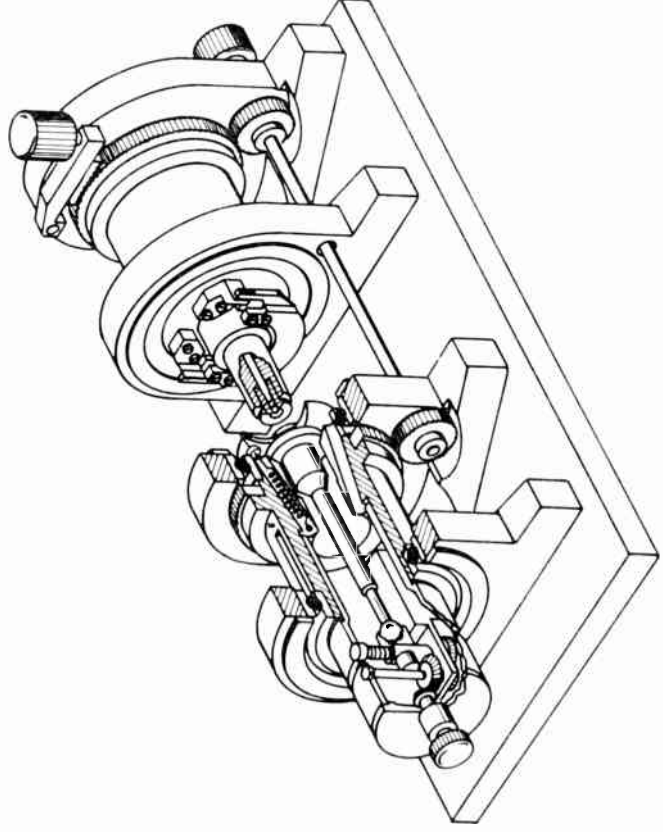


Fig. 4
Grid-Cathode Spacing Fixture,
Cutaway View.



Fig. 5
Sealing-in Operation.

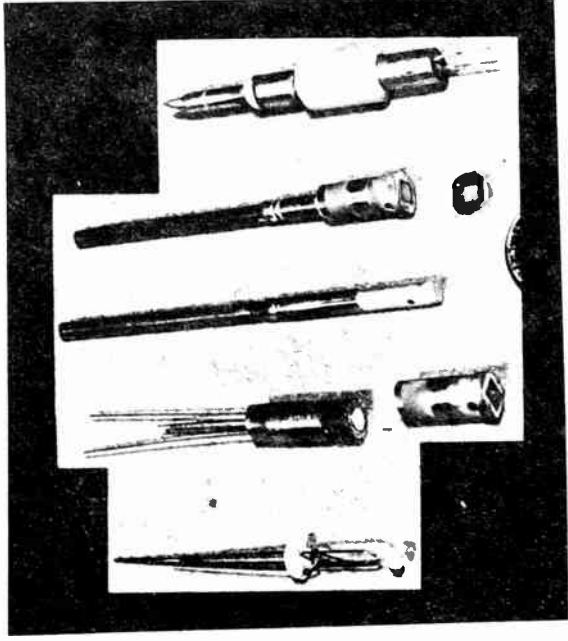


Fig. 6
Completed tube with subassemblies.

Markus Nowogrodzki
Amperax Electronic Corporation

INTRODUCTION

The part played by the cathode in a pulsed magnetron oscillator is more complex than simply that of a source of electrons. Owing to the presence of the so-called static electron cloud, whose diameter is dependent upon the magnitudes of both the electric and the crossed magnetic fields, the cathode diameter has a marked influence on the magnetron efficiency; the centering of the cathode in the interaction space, both radial and axial, is important not only because it affects the operating efficiency, but because of its effects on the shape of the rf spectrum as well; the geometry of the cathode and its end shields helps confine the electrons within the interaction space and also must be designed for proper heat transfer to the support structure under conditions of severe back bombardment, such as are encountered in magnetron operation; finally, the smoothness of the emitting surface is of great importance in pulsed-magnetron operation, since it will greatly affect the stability of the tube, i.e., the susceptibility of the magnetron to cathode sparking, cathode-anode arcing, and overheating.

The excellence of the magnetron cathode is put to an even more severe test when the tube is being triggered with very long pulses. Under long-pulse operation, demands on very considerable cathode emission for relatively long periods of time are made; and the tendency to spark at some point during the pulse interval is enhanced. It is for these reasons that life-test runs on pulsed magnetrons are usually performed at the longest pulse specified for the particular tube. Thus, in any cathode-evaluation program for a magnetron type, operation of the tube at very long pulses has a special significance as a measure of cathode quality.

This paper describes a still incompleting phenomenological study of a new type of emitter, viz., the Philips' impregnated cathode, in a magnetron operating at pulse widths hitherto not attained in operational tubes of this type. The RETMA designation of the tube, which has the outward appearance of, and is, electrically, an improved version of the 4J52 magnetron, is 6507.

THE CATHODE STRUCTURE

The Philips' impregnated cathode** is an improved version of a new cathode type developed in Holland and known as the "L" cathode (1) (2). While the original "L" cathode used a reservoir of barium carbonate contained by a layer of porous tungsten, the impregnated cathode employs an emissive layer of porous tungsten impregnated with barium aluminate. In either design the smoothness of the metallic emissive surface makes the cathode particularly suitable for magnetron applications,

but in the case of the "L" cathode, the required operating temperature is generally higher than that required for the impregnated cathode. Sketches of a typical "L" cathode design for a magnetron application and the 6507 cathode (impregnated) are shown in Figure 1.

In addition to the desirable emitting surface characteristics, the impregnated cathode has excellent thermionic emission qualities. Moreover, the susceptibility of the cathode to poisoning is small, so that the cathode structure can actually be exposed to air after operation in a tube and re-used in another mount. From a manufacturing point of view, this is a very desirable characteristic, as is the fact that there is no "breakdown" of the impregnated emitter comparable to that of the breakdown of the alkaline-earth carbonates in an oxide-coated type. The excellent life obtained with an impregnated cathode in magnetron applications (as discussed later in the paper) make this type of emitter even more desirable.

The applicability of porous-tungsten, dispenser-type cathodes (to which class both the "L" type and the impregnated type belong) to magnetrons has been predicted almost from the time these designs were developed. A study of the "L" cathode in a magnetron application (3) showed its advantages, even though this particular investigation was limited to operation of the tube (a 725A magnetron) within the scope of existing specifications. The present report, describing operation at extreme pulse-lengths, should, in the opinion of the author, help to establish the impregnated cathode as a superior design for magnetron applications.

DESCRIPTION OF TUBE; COMPARISON WITH 4J52

The 6507 magnetron is a 16-resonator, vane-type, packaged tube utilizing double-ended, double-ring strapping, and externally identical to the 4J52 tube. Its operating characteristics (at normal pulse-durations) are also identical with that of the 4J52 magnetron (including heater characteristics), so that the tube can be used as a direct replacement in all equipments using the 4J52. A performance chart of the 6507 is shown in Figure 2, and is seen to be essentially the same as similar charts for the 4J52 magnetron published in the literature. (4)

But the 6507 shows distinct improvement over the 4J52 even at operating conditions which are standard for the latter tube.

* The work described in this paper was carried out under United States Air Force Contract AF-33 (600) 23763.

** Developed at Philips Laboratories, Irvington, New York.

These improved qualities are in three general categories, viz., tube processing; stability; and life characteristics.

In addition to benefiting from the immunity to poisoning of the impregnated cathode and the simplified pumping procedure, both of which have been mentioned before, the processing of the 6507 differs from that of the standard 4J52 in another important aspect; the smoothness of the cathode surface greatly facilitates aging. Exact aging times cannot be given, since the normal aging schedules call for minimum aging times even for tubes not requiring the prescribed aging, particularly on systematized production runs; but a typical 6507 aging schedule is in the order of 10-20 minutes, while a 4J52 may require aging in excess of 1 1/2 hours.

The stability of the 6507 is likewise related to the quality of its cathode surface. The 6507 not only displays extremely stable operation at long-pulse conditions, where 4J52 magnetrons arc excessively (see below), but gives improved stability and life at standard 4J52 operating conditions as well.

LONG-PULSE OPERATION: TEST EQUIPMENT:

The 6507 was checked in a rather elaborate test equipment designed for a variety of test conditions in addition to the long-pulse operation of interest here. Even though the basic design principles of the test equipment are conventional, and the modulator follows the standard discharging-network type technique, the inclusion of extreme test conditions, particularly the long-pulse conditions, presented a number of design problems, some of which may merit a brief review.

With reference to the Test Set Functional Block Diagram, shown in Figure 3, the equipment uses a conventional d-c power supply, a control-and-metering section similar in design and construction to the standard Amperex Magnetron Test Station, a driver whose pulse-repetition frequency is derived from a commercial audio oscillator for ease of adjustment, interlock circuits incorporating a number of safety devices for the protection of both the test personnel and the tube under test, and a line-type modulator, shown in block-diagram form in Figure 4. High-voltage switching relays are used for rapid change-over between the various test conditions. Sand loads are used in the life test sets, while a water load is employed in the operational test set. The equipments can be operated under the following conditions:

- (a) High duty cycle (.001 - approx. .01) at 1/4, 1, and 5 microsecond pulse widths. Standard 4J52 operates at .001 duty cycle.
- (b) Long-pulse operation (5,6,7,5,9,10,12, 12.5 and 15 microseconds) at 0.001 duty cycle. Standard 4J52 has maximum pulse width of 6 microseconds.

- (c) Higher power input to magnetron (approximately 50% additional input above standard 4J52).

By designing for operation with linear, resonant, and subresonant charging, only two charging chokes are used in the modulator (cf. Figure 4). Two sets of pulse components are employed, for 0.25 - 5 usecond and 5-15 usecond operation, respectively. A design innovation is the use of a hydrogen thyatron clipper circuit, with the additional novel arrangement of a selenium rectifier triggering the thyatron. Otherwise, the circuit is conventional, as shown in the sketch.

Pulse-forming network: The problem in pulse-forming network design centered around the necessity to compromise between pulse rise time and acceptable pulse shape. (A fast rise time was desired because of the sensitivity of the 4J52 magnetron to voltage rate-of-rise, and with a fast rise time designed into the equipment, this parameter could be controlled by using an external variable high-vacuum capacitor.) The long-pulse network, in particular, posed a problem, since the long pulses, coupled with the fast rise times required, dictated networks comprised of unusually large numbers of sections (78 meshes as compared to 5 mesh networks normally employed), which, in turn, led to large values of dissipation the artificial line and deterioration of the pulse shape. The characteristics of the final network designs are as follows:

<u>Network</u>	<u>Rise Time</u> (microseconds)	<u>Droop</u> %	<u>Pulse Width</u> (microseconds)
78-mesh	0.125	11.6	14.2
25-mesh	0.244	7.7	13.5

The networks were tested by replacing the pulse transformer by a non-inductive resistive load and monitoring the pulse shapes by photographic methods.

Pulse Transformer: Different approaches were used by the various manufacturers in their designs of the 15-microsecond pulse transformers. The unit received from one supplier showed core saturation effects, manifesting themselves in a narrowing of the pulse at higher power levels. Thus, while full pulse length (approximately 15 useconds) was reproduced at power levels up to about 25% of the rated value, the trailing edge of the pulse deteriorated at high levels, the pulse width at rated power being approximately 9 microseconds. This unit was not acceptable. The second manufacturer used a low-current bifilar winding, the purpose being to minimize the wire size used in the windings and consequently the stray capacitance, leading to faster voltage rise times. This required the placing of the filament transformer at the magnetron (load) side of the pulse transformer. The third design was conventional, and proved even more satisfactory. The characteristics of the pulse transformers are summarized below:

<u>Pulse X-Former</u>	<u>Filament X-Former</u>	<u>Rise Time</u> (μ seconds)	<u>Drop</u> %
15 μ sec. Mfr. A saturation - not acceptable			
B high side		0.284	10
C ground side		0.266	6

The method used for testing the pulse transformer was as follows: For rise-time measurements, a 0.25 μ second pulse with a 0.08- μ second rise time was used, and the rise time was considered to be the total rise time (10-80% of the pulse) as measured at the output of the pulse transformer when the latter was loaded with a non-inductive matching resistor. The droop was determined using a network of the full pulse length having a known droop, the transformer droop being the difference in the droop at the output of the transformer and that of the network. The parameters involved were measured on photographs taken of the synchroscope traces.

LONG-PULSE OPERATION: TUBE PERFORMANCE

A. Test Conditions

(1) Pulse Characteristics - The characteristics of the line-type pulser used for testing the 6507 magnetrons for long-pulse operation are summarized below:

Rise time (10% - 80% of voltage pulse)	0.35 microsecond
Fall time (80% - 10% of voltage pulse)	3.64 microsecond
Pulse width (at 80% of voltage pulse)	13.5 microsecond
Droop (80% - 100% of voltage pulse)	13.7%

The data given above are for operation into a 1000-ohm noninductive resistive load. With a magnetron load, pulse conditions are as follows:

Pulse width (at 80% of voltage pulse)	13.8 microseconds
Pulse width (at 50% of current pulse)	13.4 microseconds

The magnetrons are operated at a duty cycle of 0.001 for these tests.

(2) Aging Procedure - The tubes assigned for long-pulse testing are first aged according to normal procedures for the 4J52 magnetron. The magnets are stabilized as for a 4J52, for tube operation at approximately 15 KV, 15 amperes. The tubes are subsequently aged for long-pulse operation at constant duty cycle (0.001) and pulse widths of 5, 8, 11, and 13.8 microseconds. The normal aging time up to maximum pulse width is 15-30 minutes.

(3) Cathode Temperature - The warm-up heater voltage is 12.6 volts. Warm-up time is 180 seconds minimum. At 15-ampere operation, the cathode temperature at $E_f = 8$ V is recorded. (Provisions have been made in the output waveguide transmission line for measuring the cathode temperature by means of an optical pyrometer without disturbing the rf

properties of the waveguide.) For electrical tests, the cathode temperature is set at 975°C. (brightness temperature).

B. Tube Evaluation

(1) MIL-E-1B Tests - All 6507 tubes are tested to 4J52 MIL-E-1B specifications, and pass these tests without difficulty. In addition, much better stability, easier aging, and, superior life characteristics result from the inclusion of an impregnated cathode. All electrical characteristics of the 6507 are identical with that of the 4J52 (power output, spectrum bandwidth, pulling factor, etcetera).

(2) Power Output - The power output at 14-microsecond operation shows no drastic inconsistencies as compared to that at JAN test conditions. It is to be noted that the duty-cycle factor in both cases is 0.001 and thus a drastic decrease in average power under long-pulse operation would be indicative of "cathode fatigue" (decrease of output during pulse). No evidence of cathode fatigue can be discerned in the measurements, nor was there any indication of output "droop" in the viewing of the detected rf envelope. Further proof of the equivalence of the tube's performance at long pulses is the 14 μ second performance chart shown in Figure 5, which is seen to be essentially the same as the 1- μ second chart of Figure 2.

(3) Cathode Temperature - The operating temperature of the impregnated cathode is obviously of great interest to the tube designer. Early reports indicating the necessity of higher cathode temperatures (as compared to an oxide-coated cathode) were not borne out by later experiments. 6507 magnetrons have operated quite successfully with impregnated cathode at brightness temperatures as low as 850°C. On this basis, a standard 4J52 heater is used in the 6507, with excellent results. Table I summarizes measured cathode temperatures on a number of 6507 magnetrons with the filament at 8 V and oscillating at 15 amperes plate current. Although the procedure has been to test the tubes at a constant cathode temperature (975°C.), it appears that adequate results would be obtained if the filament voltage were reduced to 8 V. after application of high voltage, making the procedure identical to that now specified for the 4J52 magnetron.

(4) Magnetron Stability - One of the most striking advantages of the impregnated cathode in magnetron applications appears to be the stability of the tubes incorporating this type of cathode in their design. This feature is particularly apparent in long-pulse operation, where sparking of a conventional cathode makes the tube useless for any practical application. Table II illustrates the stability of the 6507 under long-pulse conditions. It is to be noted that MIL-E-1B specification allows 60 arcs in a 5-minute interval for a 4J52 magnetron operated at 200 pps, or 0.1% arcs. The corresponding number of arcs for a 6507 operated at 75 pps would be 22 arcs/5 minutes. It is seen that all 6507 tubes are capable of meeting this requirement, while both the control tube (#135; a 6507 with an oxide-coated cathode) and a regular pro-

duction type 4J52 magnetron (#3031) show an arc count exceeding that number. Another important feature is the extreme care with which oxide-coated cathodes have to be aged for long-pulse operation. Thus, Tube #3031 was aged for 12 hours (prohibitive for production-type testing) as compared with 15-30 minutes of aging required for 6507 magnetrons.

LIFE-TEST PERFORMANCE

1. 5-Microsecond Life Test

The 6507, when operated at standard (5-microsecond) conditions on life test, is characterized by extreme stability of its electrical performance. No evidence of appreciable change in frequency, power output, rf spectrum bandwidth, and arc count can be detected after more than 1,000 hours of operation. A typical life-test record under these conditions is shown in Figure 6 for a tube which operated for 1,300 hours, after which the test was discontinued. It appears quite reasonable to specify for the 6507 tube a life of 1,000 hours under 4J52 test conditions.

2. Long-Pulse Life Test

The performance of the impregnated cathode is strikingly illustrated in Figure 7. Typical curves of magnetron stability are presented in these figures for tubes with an oxide-coated cathode and an impregnated cathode, respectively. The parameter monitored was the magnetron average plate current. It was found that the oxide-coated cathode arced considerably for the first 150 hours or so of life test. A marked improvement was noted during the later part of life (after 150-200 hours of operation). Tubes incorporating an impregnated cathode, on the other hand, started off with remarkable stability, later showing signs of slightly increased arcing, but after 750 hours of operation the number of arcs was still within 0.1% of the number of applied pulses. It appears quite feasible to specify for the 6507 a life of between 500-750 hours under long-pulse operating conditions.

CONCLUSIONS

It has been demonstrated that by utilizing a

Philips' impregnated cathode, a magnetron type was developed capable of meeting all test conditions specified for the 4J52 tube with four times the life expectancy of the latter; and of operating at pulse lengths hitherto not attempted with tubes of this type. The most striking features of the impregnated cathode in magnetron applications appear to stem from the smoothness of its emitting surface, leading, in addition to its capability of sustaining excellent emitting characteristics at very long pulses, to remarkable stability and excellent life characteristics.

ACKNOWLEDGEMENTS

The work described in this paper was carried out in the Amperex Magnetron Development Department, and the results could not have been achieved without the purposeful ingenuity and sustained efforts of its staff.

APPENDIX

TENTATIVE TEST SPECIFICATIONS, LONG-PULSE OPERATION

tp: 15-microseconds maximum
Du: 0.001
Average Anode Current: 15mA_{dc}
Stability: 0.1% missing pulses maximum
Pulling Factor: $\Delta f = 15$ MC maximum
Power Output: 65 watts minimum
Life Test: 500 hours minimum
Life Test End Point: 50 watts minimum
0.1% missing pulses max.

REFERENCES

- (1) G.A. Espersen, "The L-Cathode Structure" Proc. I.R.E., 40, 3; pp. 284-289; March, 1952.
- (2) H.J. Lemmens, M.J. Jansen, and R. Loosjes, "A New Thermionic Cathode for Heavy Loads," Philips Tech. Rev., Vol. 11, pp. 341-350; June, 1950.
- (3) G.A. Espersen, "Investigations Leading to the Development and Fabrication of Type 725A magnetrons," Final Technical Report NO. 58, Philips Laboratories, Inc.; 14 March 1952.
- (4) G.B. Collins, Microwave Magnetrons, McGraw Hill, 1948; p. 780.

TABLE I

TUBE NUMBER	CATHODE TEMPERATURE (1) DEGREES CENTIGRADE
130	916
138	932
140	975
143	1015
144	988

(1) BRIGHTNESS TEMPERATURE WITH $E_f = B \cdot V$, A-C;
TUBE OPERATING AT 14 μ SEC. PULSE, .001 DUTY
CYCLE, 15 MA PLATE CURRENT.

CATHODE TEMPERATURE-6507
LONG-PULSE OPERATION

TABLE II

TUBE NUMBER	ARCS/5 MIN. (1)	REMARKS
126	7; 14; 11 (2)	
130	14	
138	15	
140	5; 8; 4	
143	1	
144	9	
135	30; 45	=OXIDE COATED CON- TROL CATHODE
3031	76; 51	=PRODUCTION 4J52 TUBE AFTER 12 HRS. OF AGING

(1) 0.1% OF ARCS CORRESPONDS TO 22 ARCS/5 MINUTES.
(2) SUCCESSIVE NUMBERS INDICATE ARC COUNT IN SUC-
CESSIVE 5-MINUTE INTERVALS.

ARC COUNT-6507, LONG PULSE OPERATION
(14 μ SEC. PULSE, .001 DUTY CYCLE, 15 MA PLATE CURRENT)

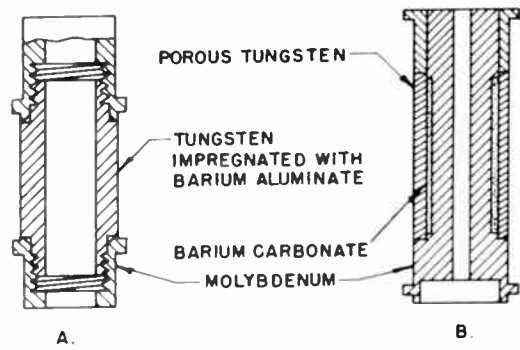
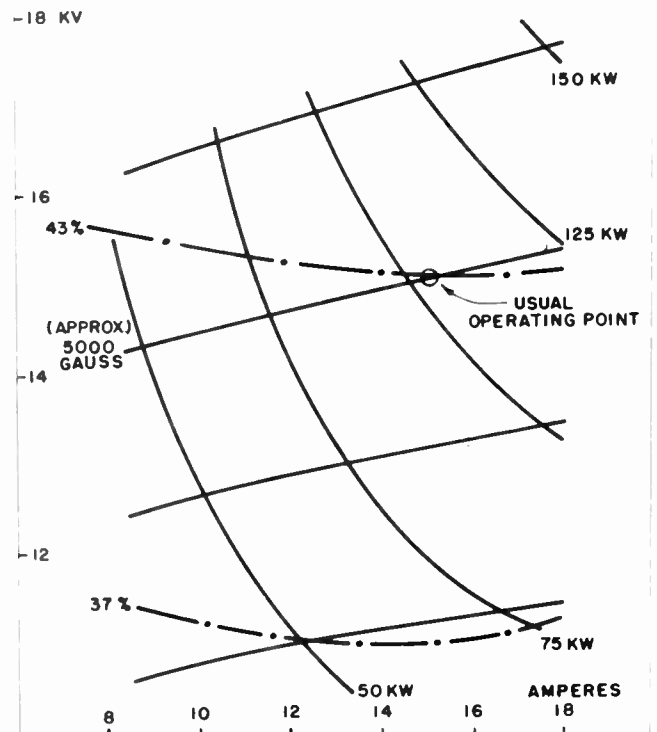


FIGURE 1: TYPICAL DISPENSER-TYPE
CATHODES FOR MAGNETRONS.

A. IMPREGNATED CATHODE (6507)
B. "L" CATHODE

FIGURE 2: TYPICAL PERFORMANCE CHART
6507 MAGNETRON
(1 MICROSECOND PULSE, 1000 P.P.S.)



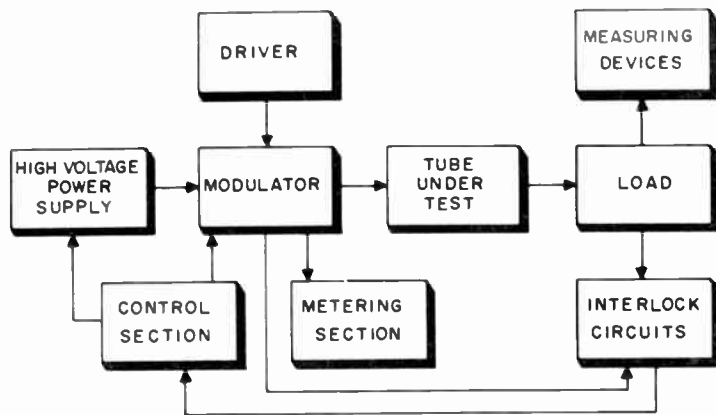


FIGURE 3: 6507 TEST SET-FUNCTIONAL BLOCK DIAGRAM.

27

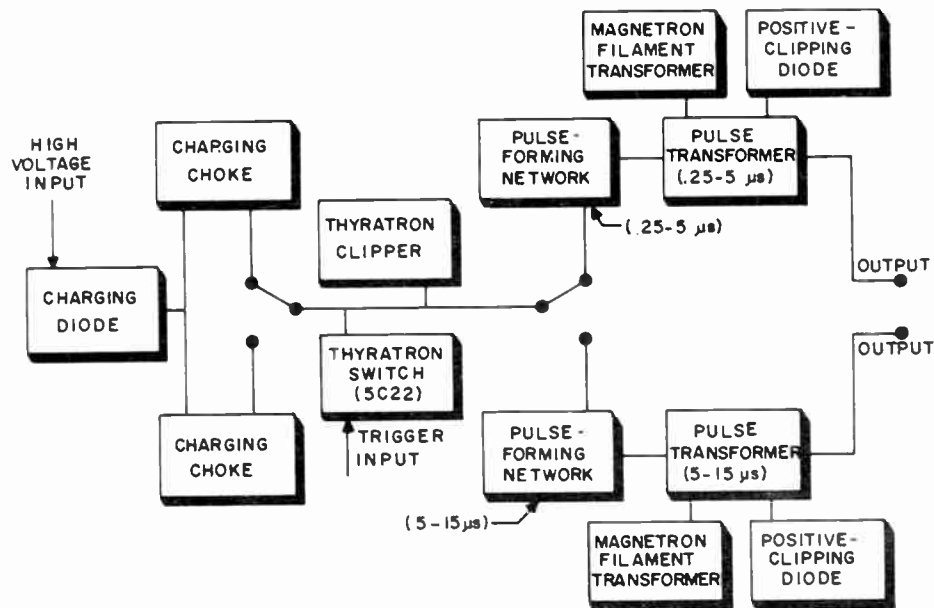
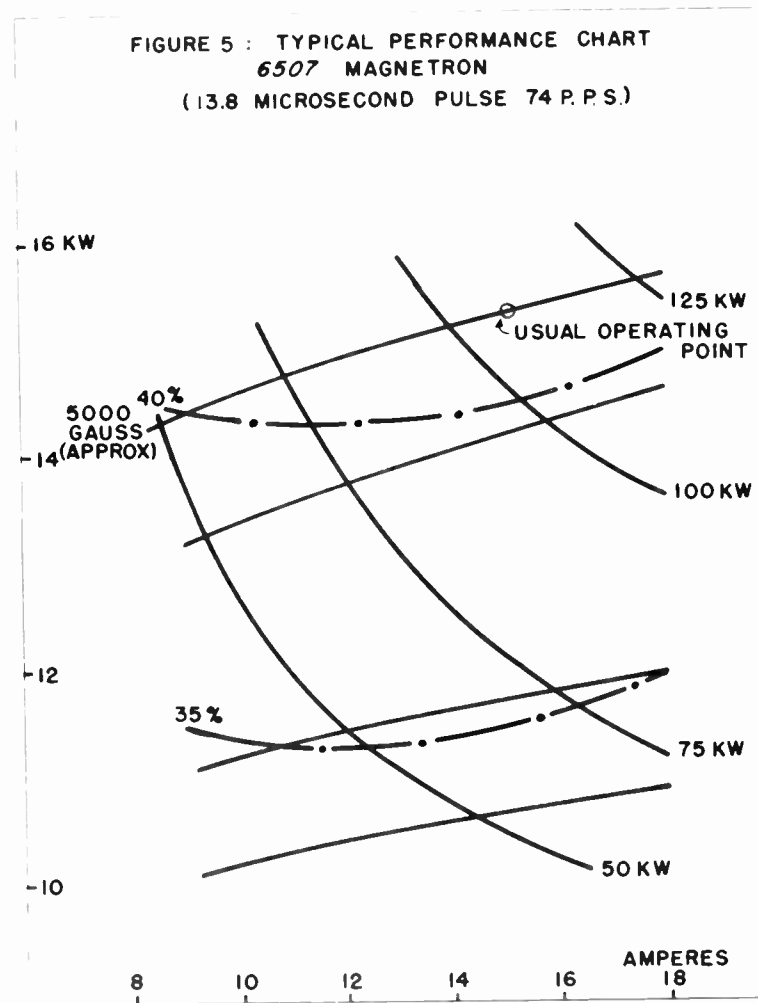


FIGURE 4: 6507 MODULATOR-FUNCTIONAL BLOCK DIAGRAM



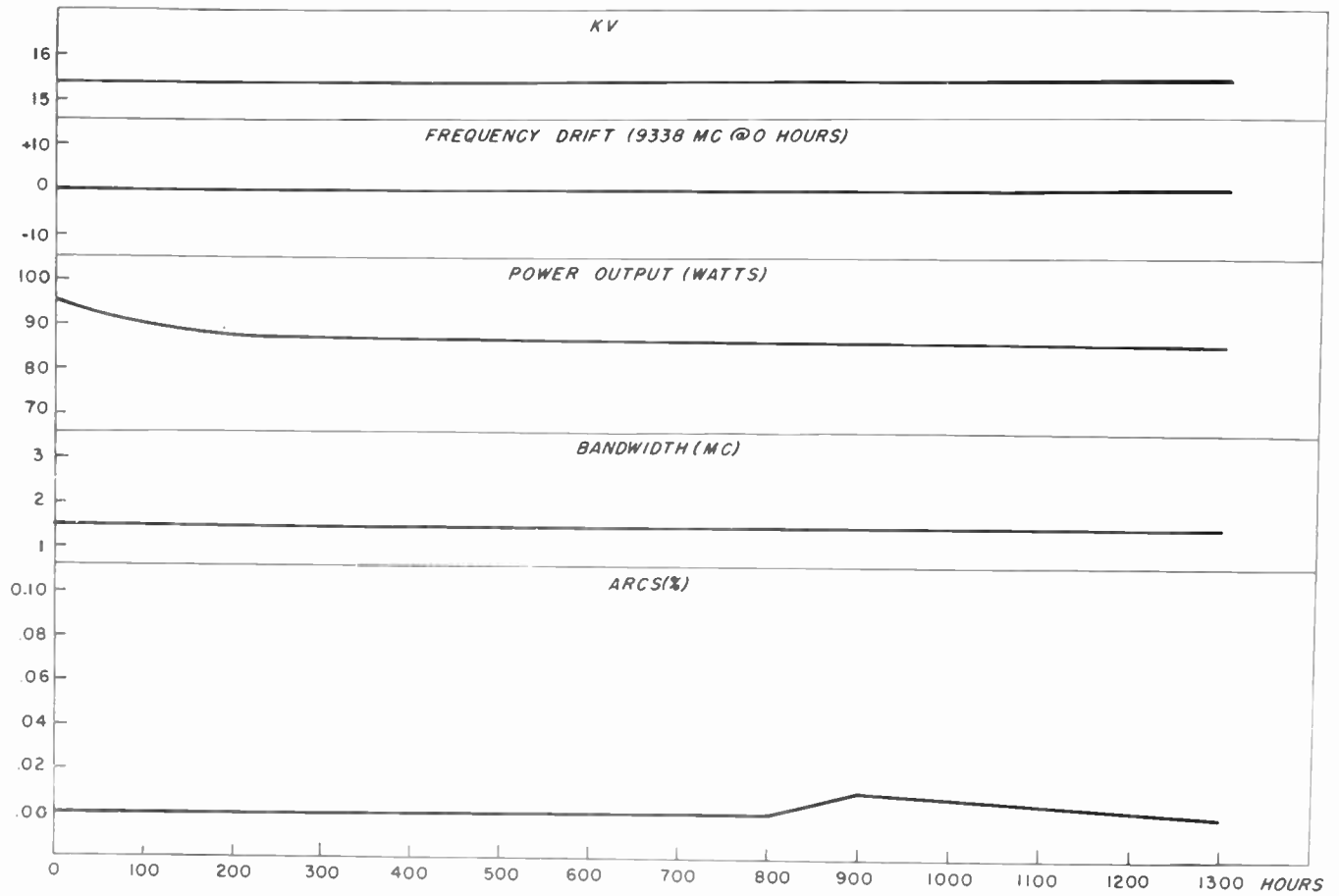
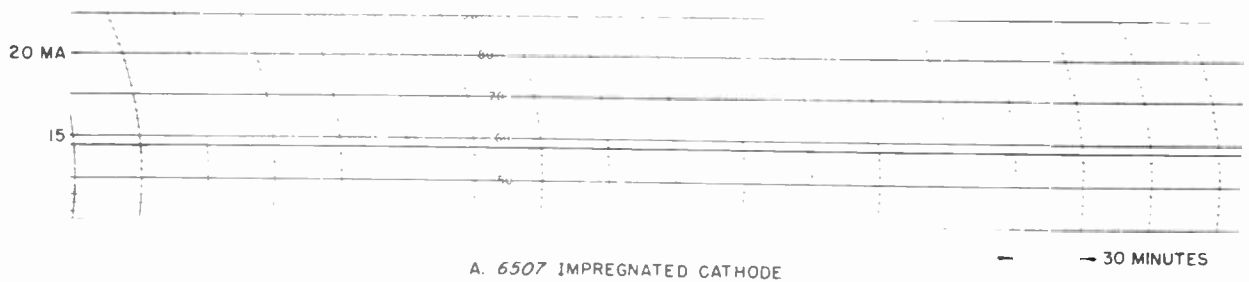
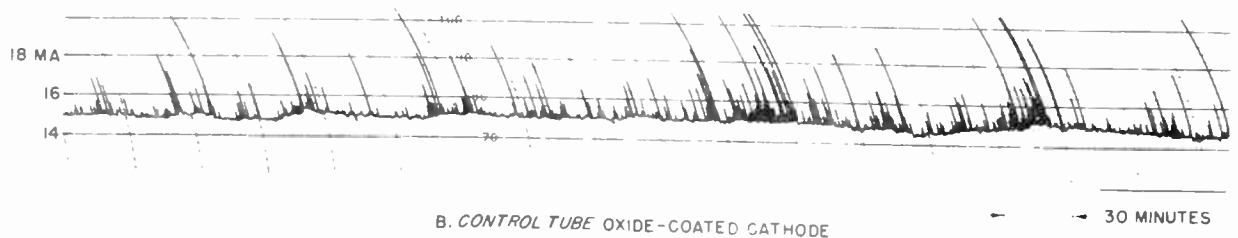


FIGURE 6 : 6507 MAGNETRON - LIFE TEST RECORD 5 μ SEC OPERATION



A. 6507 IMPREGNATED CATHODE



B. CONTROL TUBE OXIDE-COATED CATHODE

FIGURE 7 TYPICAL LIFE-TEST RECORD OF MAGNETRON PLATE CURRENT AFTER APPROXIMATELY 100 HOURS OF OPERATION (14 MICROSECOND PULSE, .001 DUTY CYCLE)

KLYSTRON POWER AMPLIFIERS FOR LONG-HOP MICROWAVE RELAY

Norman F. Hiestand
Manager - Power Tube Applications Engineering
Varian Associates
Palo Alto, California

INTRODUCTION

Recent experiments by Bell Telephone Laboratories, National Bureau of Standards and others have demonstrated the practicability of the transmission of microwave signals over the horizon. The implications of this development are beginning to become apparent through announcements such as that of the A. T. and T., Long Lines Department which stated that a Florida-to-Cuba (about 100 mile) single-hop microwave link is being prepared for service. Also, the Canadian Ministry of Defense has just revealed that a microwave communications system employing 150-mile hops is being placed in operation.

A discussion of these experiments and systems is not pertinent to this presentation except to point out that such long-distance propagation of microwave signals requires very high transmitter power. Reflex klystrons have long been the standby of the line-of-sight microwave relay links and one way to increase the transmission capabilities of such links is to add a stage of power amplification to step up their power output from milliwatts to watts or kilowatts. The klystron power amplifier offers a practical method of obtaining that power at any microwave frequency.

The purpose of this article is to bring the power amplifier klystron to the attention of the communications transmitter designer, to describe some of its basic characteristics, and to discuss its application as a high-power transmitting tube.

Such important considerations as power output, gain, bandwidth, modulation, distortion, noise, stability, tunability, power supply requirements, efficiency, size, cooling, life, and reliability will be discussed.

It is hoped that the material presented here will be of some value to the engineer not already completely familiar with microwave tubes, and that it will help stimulate further study and investigation of what can be a very useful and important communications tool.

In exactly the same way that the triode and tetrode can be used for a variety of different purposes in a communications transmitter,

such as oscillator, multiplier, buffer amplifier, and power amplifier, so too can the klystron. Tubes are available to perform any one or sometimes several of these functions. It is perfectly feasible to construct transmitters using only klystrons in the r-f stages, because of its increasing importance in the field of extended range communication, the klystron power amplifier is emphasized here.

It will be assumed that the basic microwave signal has been generated either by a reflex klystron oscillator, by a conventional crystal-controlled oscillator-multiplier arrangement, or by other means. The choice will depend principally upon the type of service. The balance of this paper is devoted to a discussion of the stage of power amplification necessary to raise the signal to the level required for 100- to 300-mile transmission. Actual power levels will be determined by frequency, distance, degree of reliability demanded, and many other factors. In general, power requirements will range from one to ten kilowatts.

LIMITATIONS OF CONVENTIONAL TUBES LEAD TO MICROWAVE TUBES

It is well known that tubes of conventional design, that is, triodes, tetrodes, etc. reach an upper limit of useful frequency range due to limitations imposed by the following factors: 1) lead inductance, 2) losses from lead and tube element radiation, 3) transit time, and 4) inadequate heat dissipation capabilities of the necessarily small structures. Substitution of the resonant cavity for lumped inductances and capacities, and careful attention to tube design have extended the range of the triode and tetrode well into the microwave region. However, there is a point as frequency goes up and power is increased where the limitations of transit time and heat dissipation make it advisable to turn to one of the so-called microwave tubes, such as the klystron. This tube combines the cavity resonator and the bunching principle to obtain the desired performance characteristics at microwave frequencies. It utilizes the finite transit time of electrons in the generation of power and, therefore, has no fundamental limitations on the amount of power that can be produced.

KLYSTRON AMPLIFIERS

The simplest form of klystron amplifier is the two-resonator single-stage type. This amplifier may be operated either as a small-signal, high-gain device or as a high-power generator, in which case gain is relatively unimportant. As we shall see, a "low-noise" klystron amplifier is generally used as a "voltage amplifier" to produce an output signal with a satisfactory noise figure. The second or "power amplifier" condition is the usual mode of operation. Another category of klystron is the "cascade amplifier" which has three or more resonators with each resonator after the first equivalent to a stage of amplification. These are referred to as multi-resonator klystrons and may have from three to six or more cavity resonators. High-gain low-noise klystron voltage amplifiers have been designed and successfully operated, but the cascade amplifier is operated principally as a power amplifier. It is the latter type of klystron, the cascade power amplifier, that is commonly used in high-power microwave relay link service.

The principal advantages of using a multi-resonator tube instead of several single-stage amplifiers (two resonators) are 1) single vacuum envelope - greater reliability; 2) one electron beam - less d-c power input; 3) only one additional resonator to tune per stage instead of two; 4) no coupled resonators present; 5) higher efficiency of multi-resonator tubes and 6) gain of an n-stage tube is 2^n times as high as an equivalent number of single-stage amplifiers.

FUNDAMENTALS OF KLYSTRON OPERATION

The three-resonator tube represented by Figure 1 illustrates how the klystron may be

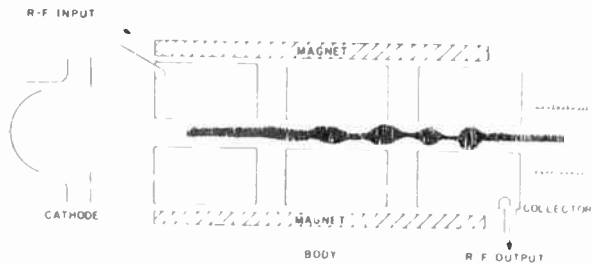


Figure 1

generated into three distinct regions for design purposes as well as operation. The first region is the beam formation or electron region; the second, the r-f interaction region or cavity; and the third, the beam deceleration or collector region.

Electrons emitted at the cathode are accelerated and focused by the electron gun. Traveling at a velocity corresponding to full beam voltage the electron stream enters the first gap. A-f energy introduced into the first resonator creates an r-f voltage across the first gap. As this voltage alternates, some of the electrons in the beam are accelerated and others, on the opposite swing, are slowed down. Thus, the electrons in the beam are modulated with velocities that are a function of the time they pass through the gap. Beam-pulse density in many klystron amplifiers produces the use of grids in the gaps. Coupling between the beam and the resonator is only slightly reduced in the non-uniform electric fields which exist across the grids gap.

The gap spacing is determined by the velocity of the beam as well as the frequency of operation. Beam voltage is chosen so that the gap distance is physically long but electrically short; then the time of electron transit is small compared to a cycle of the impressed r-f voltage.

Since the peak of the r-f voltage across the first gap is much less than the d-c accelerating voltage, the number of electrons leaving the gap per unit is essentially constant. That is, little density modulation of the beam takes place at this point. Also, since as many electrons are accelerated as are decelerated, little power is extracted from the drive source. In this way velocity modulation avoids the input circuit loss which occurs in conventional tubes at microwave frequencies.

The velocity-modulated beam is converted into a density-modulated beam by allowing it to travel through a gap where electric fields are not provided by the electrons themselves. Most high-power beams are focused during their passage through the drift space by an axial electrostatic field created externally by a long solenoid. Permanent magnets may also be used for this purpose and are often found on high-frequency (v-beam) tubes where time and cost are not excessive.

In the drift space the electrons that were decelerated during the r-f cycle travel faster

than those which were decelerated during the opposite half cycle. As a result the fast electrons overtake the slow and form regions of high and low density or bunches traveling at the velocity imparted by the beam voltage. Thus transit time is made to produce density modulation from velocity modulation.

Energy is removed from the beam as it passes through the last gap. The r-f component in the beam, now amplified by the drift action to considerable proportions, induces an r-f current impulse in the resonant cavity. Succeeding current bunches sustain oscillations. Power is then withdrawn from the resonator to the load by a coupling method such as a loop as shown.

In the triode or tetrode intended for use at microwave frequencies the plate must be small if the tube is to operate satisfactorily. On the other hand, it must be large if it is to dissipate an appreciable amount of power. In the klystron the beam collection region is removed from the region in which the r-f power is extracted from the beam. After passing through the last gap the electrons give up their remaining energy in the collector which may be as large as necessary to dissipate the required power without affecting the r-f characteristics of the tube.

In the cascade amplifier the second or middle resonator contributes to increased gain and efficiency by enhancing the velocity modulation of the beam. When the beam enters the second gap it has a small amount of intensity and velocity modulation, that is, it is essentially a d-c beam. The high ω of the second resonator makes it possible for even the small intensity modulation to induce a substantial r-f voltage across the gap. This high r-f voltage, in turn, further velocity-modulates the beam. The net result is a higher degree of density modulation in the output gap. It is approximately the result that would have been expected if the second resonator voltage existed across the first gap of a two-resonator amplifier. The multi-resonator tube does not produce greater power than could be obtained from a single-stage amplifier but it does produce the power with greater efficiency and higher gain.

There are, then, two basic innovations in the klystron amplifier which cause them to differ from the conventional electron tube and which make them useful at microwave frequencies. First is the process of velocity modulation and bunching which makes use of finite transit time to convert an input r-f voltage to conduction current with an r-f component, that is, to produce the desired transmittance. Second is the beam arrangement which makes possible the acceleration

of the electron beam to the full applied voltage before entering the r-f interaction region. It is this latter feature which greatly relaxes size limitations and makes possible operation of the klystron at high cw power without overtaxing the heat dissipation capabilities of its components.

POWER OUTPUT

The output power level chosen for a long-distance microwave relay link transmitter will be determined - apart from the demands of this mode of propagation - by the availability of transmitting tubes. Since this whole field is so new, the selection of standard off-the-shelf power amplifier klystrons is relatively limited compared with the array of conventional transmitting tubes now available. Therefore, it is important to know what sort of tubes are being developed for this service as well as what can be developed when a requirement arises.

As we have seen, there is no well-defined upper limit on the power that can be obtained from the klystron amplifier. Certain practical considerations tend to establish what might be called a "readily obtainable" limit. Further straightforward development can produce tubes up to a "relatively easy" level and intensive advanced development will result in tubes that can produce power above the "difficult" level. Figure 2 illustrates this as a function of frequency. Naturally the levels shown are somewhat

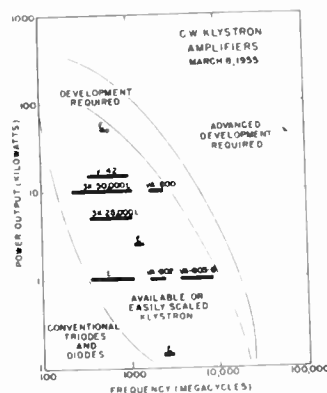


Figure 2

arbitrary and the regions between levels are not too well-defined, but these curves should provide a reasonably accurate concept of the state of the art. The dark bars represent units that are now either in active transmitter use or in the final stages of development.

Similar curves can be plotted for pulsed klystron amplifiers and these are shown in figure 3.

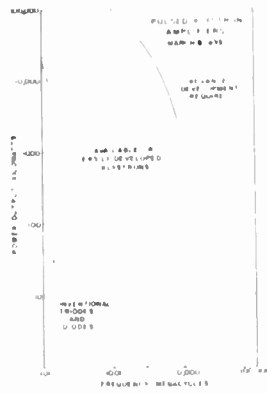


Figure 3

Klystron power amplifiers either are available, or can, within limits, be developed over a wide range of frequencies and power levels. Generally, limitations on power will be set by economic factors and the performance of other system components.

POWER GAIN

Gain in the klystron amplifier can be adjusted to just about any desired level by cascading resonant cavities. A rough rule of thumb which can be used to determine the gain of synchronously tuned klystron amplifiers is that a two-resonator tube has a gain of 10 db or slightly less and that each additional resonator will increase the gain by slightly more than 20 db. Thus, a three-resonator tube, such as the V-42, has a power gain of about 30 db; a four-resonator tube, such as the Varian VA-200 or the Limac X-655 has 60 db; and so on.

As stages are added, gain is rapidly increased and is limited only by feedback and regeneration and these problems are much less severe than in conventional circuits. Through careful design the creation of secondary electrons which cause feedback can be minimized with the result that the high-gain klystron is a very practical device. Tubes with power gains of 60 db are now common and 90-100 db gain has been provided.

In most high-power microwave transmitters gain is determined by the desired power output level and the drive power available. There is a growing tendency to use a high-gain final amplifier rather than several low-gain stages in cascade.

Gain of a klystron amplifier, like that of the vacuum tube amplifier, is a function of the relationship between the input signal voltage and the voltage at the load, a function of the level of operation of the final stage. This is illustrated in a typical gain curve for the Varian V-42 in figure 4. Beam voltage power is constant.

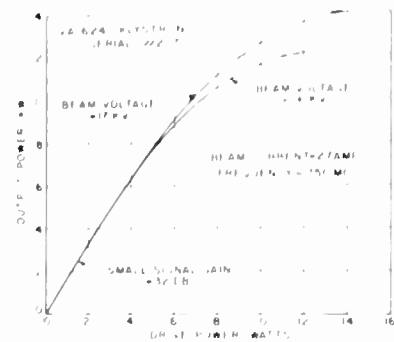


Figure 4

Maximum output power for klystron is said to be operating at saturation. This fundamental characteristic makes the klystron particularly suitable for amplification of rf signals since the limiting action in the region of saturation tends to eliminate undesired variations in signal amplitude.

BANDWIDTH

Bandpass characteristics of the klystron amplifier are similar to those of any amplifier with tuned input and output circuits and are often compared to those of the multistage i-f amplifier. Through judicious choice of input and output coupling, resonator Q's, and beam impedance, the bandwidth can be adjusted over a wide range.

Practically, gain and bandwidth cannot be considered independently since most communications systems require bandwidth greater than that of a synchronously tuned klystron. Bandwidth can be increased by stagger tuning at the sacrifice of gain. The three-resonator Varian V-42 is typical of this type of operation when used to transmit the video portion of a television signal. A bandwidth of about 4 mc is required and this is obtained by tuning the center resonator somewhat higher in frequency than the first and third. The gain is reduced from 35 or 40 db to between 26 and 30 db. A typical gain-bandwidth curve is shown in figure 5. The VA-200 series of 10-kilowatt cw, four-resonator 2000-mc tubes may be

operated either as high-gain, narrow-band amplifier or as medium-gain, broadband units. When

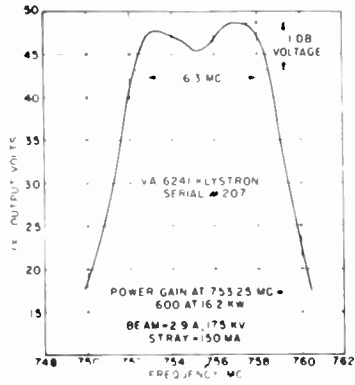


Figure 5

these tubes are synchronously tuned, the gain is about 40 db with a 3-db bandwidth of about 10 mc. By stagger-tuning to achieve a 20-mc bandwidth reduces the gain to just under 40 db. These examples are typical of the performance of existing tubes - higher gain and/or wider bandwidth can be produced in special units if required for particular applications. It is dangerous to postulate too many general rules, but another rule of thumb may be useful. Very approximately, the bandwidth of a synchronously tuned multi-resonator klystron amplifier of conventional design will be in the neighborhood of 1/2 of 1 per cent of the center frequency. The limits to which this band can be extended by stagger-tuning will be determined by the gain of the synchronously tuned tube, the Q's of its resonant cavities, and the input and output coupling circuits. Multi-resonator tubes have been produced which have power gains greater than 30 db over a bandwidth of several per cent.

For most applications, then, it is entirely impractical to choose a klystron power amplifier that has sufficient gain and bandwidth to permit the use of a single stage of power amplification. An example of such a system is shown in Figure 6. Here, the output of a conventional C-band (4500-mc) microwave relay system with a power output between 0.1 and 1.0 watts is amplified to the 1-kilowatt level through the use of a four-resonator klystron (Varion type VA-805). Bandwidth of 30 mc is inherent in the tube. Another "very approximate" rule is that the gain-bandwidth product of a klystron amplifier, like that of a conventional multi-stage i-f amplifier, is a constant.

EFFICIENCY

In most cw applications, the klystron

amplifier is operated with the full rated beam current flowing at all times. Under this condi-

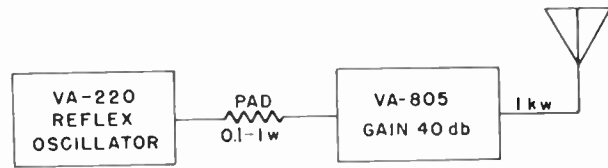


Figure 6

tion the maximum theoretical beam efficiency of a two-resonator klystron is 58 per cent, where efficiency is defined as $\frac{P_{out}}{P_{in}}$

is neglected. Practical considerations reduce this figure to close to 25 per cent. Cascading resonators increases the maximum theoretical efficiency. For a three-resonator tube, it is 74 per cent. This figure increases minutely as more resonators are added. In the UHF region (around 1000 mc), where circuit efficiency is very high, it is possible to achieve beam efficiency approaching 50 per cent in a three-resonator tube operated at saturation.

Highest efficiency, then, is obtained at saturation. This factor is another that makes the klystron particularly suitable for FM service. Pulsed efficiency of the klystron is also high. Operation of the klystron as a linear amplifier (similar to a triode class A amplifier) poses certain efficiency problems. Since with AM the average output power is limited to one-half (or less as we shall see) of the saturation power, efficiency is automatically one-half of the maximum obtainable. Limitations on linearity, which will be discussed shortly, reduce efficiency even further. This problem has led to the development of several systems for grid or anode modulation of the klystron amplifier to improve efficiency as well as to simplify modulation, but the transfer characteristics of these elements are not linear and considerable care must be taken in their application.

It can be shown that, by detuning the center cavity of a three-resonator klystron toward a high frequency and by supplying enough drive power to overdrive the tube, it is possible to enhance the fundamental component of the

fundamental component of the bunched electron beam and the power output by an appreciable factor. This improvement in efficiency is obtained at the expense of gain and is the usual mode of operation where bandwidth characteristics and availability of drive permit.

MODULATION

There are three principal types of modulation in use today in communications work, all of which may be applied to the klystron. These are: amplitude, frequency or phase, and pulse modulation.

Modulation signals can be applied to the klystron power amplifier either as part of the r-f drive or by varying the potential on one or more of the tube elements. Most often, amplitude modulation is applied to the signal to be amplified in a low-level stage. As we have seen, the relationship between power output and drive power is a beamlet function. Depending upon the degree of linearity required, the tube can be driven to from 50 to 90 per cent of cut ratio. While providing excellent linearity in the amplification of the amplitude-modulated signal, the efficiency is disappointing.

In a second mode of operation a constant cw r-f drive is connected to the first resonator of the tube and the modulating voltage is applied to a grid or modulating anode. The beam current and power output is varied as a function of modulation level. Unfortunately, the transfer characteristics of the grid and modulating anode are non-linear functions, which necessitates the use of negative feedback to achieve low distortion with high efficiency in the transmitter employing such modulation. Negative feedback in the klystron transmitter results in the same benefits that are observed in the conventional radio-telephone transmitter, that is, reduction of amplitude, frequency and phase distortion, and noise modulation. The reduction in distortion makes it possible to sacrifice linearity of modulation and amplification for efficiency. The reduction in noise modulation makes it possible to relax the tolerances on power supply ripple and still keep the hum modulation in the transmitter down to a desirable level.

The use of negative feedback results in improved operation at lower cut. However, it must be used with care since a result is required with conventional amplifiers.

While introducing certain complications in linear amplitude modulation, the grid and the modulating anode provide excellent means for applying pulse modulation to the klystron. With

the r-f drive adjusted for optimum performance at saturation output, the beam current is turned on and off by the modulating signal. Low-capacity non-intercepting structures have been designed which consume little power from the modulating source. In general, klystron bandwidth is sufficiently broad to permit transmission of very short pulses (11 μ sec or less) without distortion. Since the grids and anodes are, for all practical purposes, non-intercepting, there is no limit to the duty cycle which may be used, provided, of course, that the tube itself is designed for the required average power. Examples of this type of tube are the Varian X-605, the four-resonator L-band tube mentioned earlier, and the Varian 4A-24, a four-resonator X-band tube. The former employs a modulating anode and is a tube particularly suitable for pulsed radar or navigation systems. The 4A-24 is equipped with a non-intercepting grid designed for high duty cycle operation. This tube could be used in pulse modulation communication systems, for example.

The klystron without a control grid or modulating anode is also well-adapted to pulse modulation systems where the modulation is applied to the beam voltage. CW or pulsed drive is applied to the first resonator, and adjusted for optimum gain and efficiency.

Frequency or phase modulation has found more widespread application in the microwave communications transmitter than any other type of modulation. The klystron amplifier is particularly well adapted to this type of modulation. As we have seen, saturation level operation results in high efficiency, and amplitude limiting is obtained. Where the r-f signal is applied to the first resonator the phase relationship between input and output r-f voltages as a function of frequency is the same as that of any amplifier with tuned input and output circuits. Thus, the klystron does not introduce any greater phase distortion than a conventional amplifier.

A klystron amplifier can, however, readily be phase-modulated if desired. A given percentage of modulation of the beam voltage produces half this percentage of modulation of the d-c transit time. The longer the transit time the larger will be the phase modulation of the output signal. Since gain is relatively insensitive to small variations in beam voltage there will be no amplitude modulation accompanying the phase modulation. This modulation technique is often used in RTI radar transmitters and may well find use in communications systems.

DISTORTION

Modulation and distortion are really the same thing except that one is desired and the other undesired. The klystron amplifier is no different than any other amplifier in that its output may fail to reproduce the input as the result of frequency, amplitude, or phase distortion. Amplitude distortion occurs when different frequency components are not amplified equally. Amplitude distortion results, among other things, from the non-linear relationship between input and output power. And phase distortion occurs when the relative phases of the various components being amplified are not the same in the output as in the input.

Frequency distortion in the klystron will occur when the overall bandwidth of the amplifier, input and output circuits as well as the resonators, is inadequate because of either improper adjustment or design. Given the frequency characteristics of the excitation signal and the amount of frequency distortion permissible, it is usually possible to design a klystron amplifier which will exhibit exceedingly low frequency distortion.

In order to preserve the waveform of a signal in an amplifier, not only must the relative amplitude of the frequency components be preserved but their relative phase relationship must be held constant. If not, phase distortion results. The difference in phase between input and output is dependent upon the time of transmission of the particular frequency through the klystron amplifier. This transit time is directly proportional to frequency and length, and inversely proportional to velocity, which means that only variation in beam velocity can produce phase distortion in the klystron, since frequency and length are constant. Generally, trouble, when it arises, is due to excessive power supply ripple. However, it turns out that the most elementary of filters will reduce ripple to the point where it becomes negligible phase modulation. The filament current condition produces phase modulation; however, proper tube design can keep coupling between the magnetic field of the filament and the electron beam low enough to make this contribution insignificant.

With proper attention to power supply design and tube adjustment or tuning, frequency and phase distortion in the high-power klystron can be held to the same level that one would expect to find in any high-quality conventional r-f amplifier.

Amplitude distortion in the klystron may arise from a variety of causes, but, like frequency and phase distortion, can be controlled

through routine care in transmitter design. In a linear amplifier, any factor causing the amplitude of the output signal or voltage to have other than a linear relationship to the input voltage is said to produce amplitude distortion. As we have already seen, the usual relationship between input and output voltage or current in the klystron amplifier is the Bessel function of the first order. The function is linear to within about ± 4 per cent if the klystron is driven to 10 per cent of saturation; to within about ± 6 per cent to 90 per cent of saturation; and if driven to saturation the departure from perfect linearity does not exceed about 12 per cent. Thus, for most communications applications where amplitude modulation is applied to the r-f drive signal it is possible to operate the klystron at relatively high level without introducing excessive distortion. With 100 per cent sinusoidal modulation, efficiency is slightly less than one-half that obtainable at saturation. Typically, this might be 15 per cent at 2000 mc, which is considerably better than one could obtain in any other linear amplifier operating at a kilowatt or so at this frequency.

Other contributions to amplitude distortion may arise from power supply ripple, filament hum, and stray magnetic fields. The amplitude of the power output is relatively insensitive to beam voltage, so, again, only moderately well-filtered supplies are required. Since the filament of the power amplifier klystron is far removed from the r-f interaction region, it has little effect on hum. In unusually severe applications, filaments may be operated at dc, precisely as would be done in a conventional amplifier.

Ripple on the magnetic focusing current, as well as stray magnetic fields from poorly shielded components, can produce amplitude distortion in the klystron, but only reasonable care is required to keep these contributions below the undesirable point.

NOISE

Any amplifier has an inherent output noise power. Noise arises from several sources in the klystron amplifier. First, there is the thermal noise built up across the input gap. This is similar to the well-known "Johnson noise" produced across the terminals of a resistor and is, of course, the threshold noise level. Other noise sources in the klystron include shot effect or random fluctuations in beam current. These arise from the absence (or reduction) of space-charge smoothing at microwave frequencies and

thermal spread in electron velocity from the cathode. Effects of these noise sources can be materially reduced through special design techniques which are necessary in order to use the klystron as a low-level r-f amplifier. Low-noise klystrons show considerable promise as small-signal amplifiers, with noise figures less than 10 db. In general, the noise figure of the average klystron power amplifier may be expected to be between 20 and 30 db.

Recalling that noise figure is defined as the ratio of signal-to-noise at the input to signal-to-noise at the output, it follows that the noise power output in a one-megacycle band of a high-gain klystron amplifier operating in the kilowatt region is of the order of tenths of microwatts. Noise 90 to 100 db below the carrier level will not be troublesome in any but the most critical applications, and if necessary, careful attention to tube design can produce even lower noise levels.

In any long electron beam such as that employed in the klystron there is always the possibility - in fact, certainty - that ions will be present. If the beam design is not carefully executed it is possible for ions to become trapped at strategic places along the beam. The ions, which are positively charged, interfere with the desired velocity modulation through oscillation and space-charge neutralization. This can result in the production of ion noise at discrete frequencies and at appreciable power level. Fortunately, the art of beam design is such that, with care, the designer can avoid ion traps and drain the ions away from regions where they would be objectionable. Thus, ion noise is held within tolerable limits in a well-designed tube.

Klystrons are, of course, also subject to noises arising from faulty tube construction just as the more conventional triodes and tetrodes are. Hum, leakage currents, and microphonics can all be controlled by proper manufacturing procedures. In properly designed and built tubes, all of these noises are unimportant at the high-power levels considered here for microwave relay line service.

RELIABILITY

The klystron amplifier has no inherent instabilities. Power output, gain, and efficiency are relatively insensitive to variations in power supply voltages and currents as well as output load. Since the resonant frequencies of the various circuits are dependent upon dimensions which are affected by variations in temperature, some care must be taken in controlling ambient temperatures. In the case of the very powerful tubes which are water-cooled, the control

problem is greatly simplified since the whole tube body can be maintained at a constant temperature by controlling the water temperature. Air-cooled tubes require more careful attention. Trouble from frequency drift can be eliminated by temperature compensation or by providing extra bandwidth to accommodate drift of the center frequency of the final amplifier. For most commercial installations where equipment is operated inside heated buildings, temperature changes are small and occur slowly so that no special precautions need be taken to achieve satisfactory performance.

TUNABILITY

There are almost an infinite number of arrangements available to tune the klystron amplifier. These are all variations of two basic tuning methods, which are the equivalent of varying either the inductance or the capacity of the resonant circuit. Since the performance of the klystron depends upon transit time and that depends partly upon frequency, there are certain limitations to the range over which any klystron can be tuned without deteriorating performance. In general, we cannot expect to cover a frequency range as wide as the tube number range from 10 to 100 percent of the center frequency without seriously affecting power output, gain, and efficiency at the extremes of the range. Tubes have been built to cover greater ranges but these usually involve changing resonators or changing the varying reactance to hold performance constant.

At various frequencies, however, even 10 percent represents hundreds of megacycles and there is usually little point in extending the frequency range further.

POWER OUTPUT AND EFFICIENCY

Most power amplifier klystrons require a filament, a cathode heater supply, and a beam coil supply. The cathode heater supply may consist of a heater-cathode arrangement to provide for the heating of the cathode either by electron bombardment. Both methods are usually considered from a practical point of view in the literature, but the latter is preferred. All tubes operated at relatively high temperatures must be thermally protected by direct radiation. Shielding methods, which are not commonly used, are a- γ rays or their source of radiation and its limitations, which are useful at about the general level of the current ion development shown in the various stages will not only result in reliable high-current-qualitymitters suitable for high-power relay operation.

The cathode heating supply furnishes the usual filament voltage which may be either ac or dc, depending upon the degree to which hum must be controlled. The bombarder supply is generally rectified, unfiltered dc. Both of these supplies are at bear potential. In order to reduce the back heating effects of the cathode, it is usually recommended that a simple feedback circuit be provided to control the bombarder current by regulating filament voltage. Such a circuit permits the filament to run temperature-limited and will pay for itself in increased tube life.

Specifications on the beam voltage supply will be determined by incidental amplitude, frequency, and phase modulation requirements. A reasonably well-regulated line voltage and normal 1-3 filtered supply without electronic regulation will in most cases be adequate. For example, the 7A-30, the 10-kilowatt, 2-kmc amplifier, can be operated with a beam voltage ripple of slightly less than 0.1 per cent while all incidental modulation is kept well within FCC specifications for communications equipment.

Since the current drain from the power supply is independent of the r-f level, a regulated or low impedance power supply is not required to handle the modulation peaks when amplitude modulation is applied as part of the input drive signal.

LIFE AND RELIABILITY

In the communications field where service can be measured in terms of dollars and cents, long life and reliable operation are of utmost importance. Selection of tubes which will provide long, trouble-free, operation is a prime function of the system designer. Most of the criteria which are important in choosing a klystron power amplifier are the same as those usually considered in the choice of any transmitting tube. One should first determine whether or not the tube is conservatively rated. Any tube, klystron or otherwise, operated close to maximum ratings is apt to be unreliable. If the tube is not conservatively rated it should be operated at reduced ratings. It is important that the tube be designed to accommodate the prevailing environmental conditions. Variations in temperature and humidity beyond the manufacturer's limits can obviously cause trouble, particularly in high-voltage tubes. In the water-cooled tube, the manufacturer's design should be checked to be sure that no dissimilar metals are present in the water stream where galvanic action can produce serious trouble over a period of time.

Care must be used in arranging cooling so that insulator and probe temperatures are not excessive. Current-limiting resistors should be placed in series with cathode leads to mini-

mize damage in case of arcs in high-voltage circuits. Installation and operation instructions for the high-power klystron are similar to those of any high-power transmitting tube at any frequency, and because of their built-in tuned circuits and freedom from frequency-power limitations, klystrons are in many ways easier to handle than high-power triodes.

Unlike the triode and tetrode there is no limitation placed on the klystron in terms of life and reliability because of operation at microwave frequencies. As we have seen, the fundamental properties of the klystron provide for the complete separation of the three basic regions - cathode, body and collector. This means that each of the three regions may be designed essentially independently for optimum performance characteristics. Large size and freedom from close spacings in the power amplifier relieve dissipation problems. Sturdy, rugged construction eliminates damage from shock and vibration. All of this results in tubes having a useful life of many thousands of hours. Most klystron power amplifiers are designed with 20,000 to 30,000 hours' life as an objective. Experience has shown that this is a realistic goal. Many tubes now in service have been operating for well over 5,000 hours without signs of deterioration.

COST

Since it is not necessary to incorporate high-precision parts into the power amplifier klystron in order to maintain close spacings and tolerances, it is basically a low-cost tube. When produced in quantities comparable with that of conventional transmitting tubes with equivalent output power, cost definitely favors the klystron. When the fact that one high-gain klystron can perform the function of several conventional amplifiers is considered, cost becomes even more attractive.

Most high-power klystrons are designed to be repaired at end of life. Ultimate end of life in any tube results from evaporation and burn-out of the filament. When this occurs in most klystron amplifiers they can be returned to the factory and repaired at about one-third the original cost of the tube. A given tube body can undergo repairs several times. Thus, the total life of one tube can be extended for tens of thousands of hours. On the basis of cost per kilowatt hour of operation the klystron power amplifier compares very favorably with any other type of transmitting tube.

CONCLUSION

The advent of long-range microwave communications has opened a whole new field for the high-power klystron amplifier. Developed originally for television and radar applications, this tube is well-adapted to communications transmitter use. Activity of the major microwave tube manufacturers in this field assures that the spectrum will soon be adequately covered with a variety of tubes which will provide a wide selection of power, gain, and bandwidth.

Discovery of the forward scattering phenomenon and development of the power amplifier klystron have added new impetus to the ever-expanding microwave communication field.

In conclusion it might be interesting to note that the work of the National Bureau of Standards, Colorado Springs Tropospheric Propagation Laboratory helped demonstrate that over the horizon transmission of microwaves was feasible. One transmitter that played a key part in these experiments was powered by the first really high-power klystron amplifier - a 5-kilowatt cw, 39-db gain tube operating at 1046 mc. (The first tube operated continuously for 8,000 hours until accidentally damaged and its replacement has now been in service for several years.) This transmitter and tube were designed and built five years ago by Varian Associates. We are very proud of the part we have played in the development of extended range microwave communications.

BIBLIOGRAPHY

- Sullington, Kenneth - "Radio Transmission Beyond the Horizon in the 10 - 1000 mc band" Proc. IRE, Vol. 41, pp 132-135, January, 1953.
- Chambers, L.A., Herbstreit, J.H., and Norton, R. . "Preliminary Report on Propagation Measurements from 92-1046 mc at Cheyenne Mountain Colorado". National Bureau of Standards Report No. 126, July 23, 1952.
- Staff, S.I., M.I.T. - "Applied Electronics", Wiley, 1943.
- Fine, H., and Phillips, R.L. - "Long Distance Tropospheric Propagation in the GHz Frequency Band 20 - 700". FCC T.R.S. Report No. 2.1.10, October 13, 1950.
- McMillan, Donald L., Knipp, William K., Kuper, H.B., Horner - "Klystrons and Microwave Triodes", McGraw-Hill, 1948.
- Clater, John D., - "Microwave Electronics", Van Nostrand, 1950.
- Springenberg, Earl L., - "Vacuum Tubes", McGraw-Hill, 1944.
- Terman, P.L., - "Radio Engineers Handbook", McGraw-Hill, 1943.

WIDE-BAND, HIGH-POWER TRAVELING-WAVE TUBES AT S-BAND

by S. F. Kaisel and W. L. Rorden
Stanford University
Stanford, California

This paper will describe three experimental traveling-wave tube power amplifiers in the 100 w to 1-kw power range at S-band. The T-230 and the T-231 are pulsed traveling-wave tubes which will give the order of 1-kw output at 30 db gain from 2.5-3.5 kmc. The T-231 employs a control grid in the convergent flow electron gun, to allow beam-keying with low-voltage pulses. The T-351 is a cw power amplifier which will give greater than 100 w of cw output at 20 db gain from 2-4 kmc. The electrical design considerations for such tubes and the mechanical design details will be described.

Introduction

I would like to describe today several wide-band traveling-wave tubes that have been worked on at Stanford in the last few years. The T-230 and T-231 tubes give 1 kw pulsed output in the 3000 mc region. The T-351 tube has given a power output in excess of 100 w cw in the 3000 mc region. The paper title "High-Power Tubes" is somewhat of a misnomer in the case of the T-230 and T-231 in that pulsed powers at 3000 mc in excess of 100 kw have now been achieved. However, at the time that the work on the T-230 was begun several years ago the 1 kw level was considered high power for a helix tube. In the case of the T-351, the 100 w cw level represents high power as far as helix tubes at this frequency range are concerned.

In the course of the work on each of these tubes we ran into certain limiting factors on maximum helix voltage, on average helix dissipation, and on attenuator characteristics which pointed up the limitations on power level that one could hope to achieve in the 3000 mc region with tubes employing the single wound helix. By making these limitations quite apparent we hope to have stimulated the investigation of other structures which will allow the extension of the maximum power level in wide-band tubes.

I. The T-230

The T-230 was originally designed with an objective of greater than 1 kw pulsed power output at 30 db gain, over as wide a band as possible, centered at 3000 mc. The important design parameters are fairly restricted, as shown in Figure 1. In Equation 1 we see that the power output of a tube is equal to the product of the efficiency, the beam perveance, and the dc beam voltage to the 5/2 power. Experience has shown that a wide-band tube will typically show as much as a 3 db power variation over a 2:1 band. Therefore, let us choose the maximum power output as 2 kw in order to ensure a minimum power output of 1 kw at the edges of the band. Since the large signal theory of the traveling-wave tube is still not in a completely reliable state, we must make a guess at efficiency. Typically, efficiencies the order of 20 per cent can be expected in the center of the band. The state of the art in convergent flow Pierce guns is such that solid beams of perveance 2×10^{-6} represent the current practice.

With these assumptions one finds that the operating beam voltage of such a tube shall be 7600 v. If we consider the beam voltage rise due to large signal operation and the voltage rise due to space charge, a tube which operates at 7600 v under large signal conditions must have a cold velocity corresponding to the order of 5000 v. Let us see if this cold velocity is reasonable in terms of two other limitations. If we write the V_a of the helix and the k_a of the helix as shown in Equation 2 and take their ratio, we obtain an expression which only involves the voltage corresponding to the cold velocity of the helix. Now, for wide-band operation we typically choose a center frequency V_a of the order of 1.75. Tien has shown that if the k_a of a helix is much greater than 0.2, the impedance will be reduced due to the presence of space harmonic components in the fields. These space harmonic components may also lead to backward-wave oscillation difficulties. Therefore, if we choose $V_a = 1.75$ and k_a less than 0.2, we find a cold helix velocity less than 3350 v required. This voltage is a little low for the required power output. Therefore, one is faced with the choice of either choosing a higher k_a or a lower V_a . If one chooses a lower V_a , say $V_a = 1.0$ then a cold helix velocity less than 10,000 v will be satisfactory. This choice of a low V_a requires a sacrifice in bandwidth since the helix will be more dispersive over the operating band. One would be tempted then to choose a somewhat higher k_a than 0.2 and a V_a more like 1.4 in an attempt to preserve maximum bandwidth. However, in our early work we had tried a higher k_a design before the results of Tien's work were available and the performance was very disappointing. The gain and power output were considerably lower than expected. This experience led us to be very conservative on the choice of k_a and to take the resulting loss in bandwidth which went with the corresponding choice of V_a . Probably a somewhat higher k_a and V_a could be used in order to achieve 2:1 bandwidth.

After this choice of basic helix parameters, the further design of the tube resolves itself into solutions of the following major problems: (1) rf matching, (2) application of cold loss, (3) beam formation and focusing. Let us look at each of these.

A. Rf Matching

At the time this work began, the only satisfactory broad-band transducer from coaxial line to helix was the so-called "cavity match" shown in Figure 2. Coaxial input and output were chosen because of the desired bandwidth and because the use of coaxial input and output would allow a simpler mechanical package and simpler solenoid construction. Another reason for the choice of the cavity match was that we desired that the coax to helix transducer be external to the vacuum envelope and capable of adjustment to accommodate small variations in internal tube construction.

The VSWR-frequency characteristics of such cavity couplers is shown in Figure 2. Typically, on a

number of different tubes, this type of match allows a VSWR of less than 2:1 over an octave of frequency. By means of external adjustments the VSWR can be held below 1.2:1 over a 10 per cent band. The major disadvantage of the cavity coupler is that the diameter is generally large and requires a correspondingly large hole in the focusing solenoid. If one were to attempt to apply periodic permanent magnetic focusing to such a tube, the cavities would interfere with the magnetic structure.

B. Attenuator

In order to prevent oscillation in a traveling-wave tube amplifier it is necessary to provide attenuation between the input and the output of a magnitude somewhat greater than the maximum small-signal gain expected. The attenuator should provide sufficient magnitude of loss, should be short in physical length, and should be well-matched. In addition we chose to require that the attenuator be applied external to the vacuum envelope so that its magnitude and position could be adjusted after completion of the basic tube.

A lossy coupled helix was chosen for the attenuator because it met most of the above requirements. The attenuator is shown in Figure 3. It consists of a bifilar tungsten wire helix, 1" long, surrounded by a glass sleeve which is coated internally with Aquadag to give the loss. The helix pitch was chosen to give an attenuator phase velocity approximately equal to the tube helix velocity. The bifilar winding was chosen because experimentally it gave a flatter loss-frequency characteristic than a single winding. The bifilar winding gave higher loss at the high frequency end of the band. The loss characteristics of this coupled helix are shown in Figure 3. The match into the attenuator was less than 1.1:1 at the high frequency end of the band, but rose to 1.2:1 at the low frequency end of the band. In order to improve the attenuator match at the low end of the band, tapered Aquadag stripes were painted on the tube envelope at the output end of the attenuator. With these stripes, the VSWR looking into the attenuator was less than 1.02:1 over the band.

With such an attenuator, the tube is short-circuit stable and the fine structure variation of gain with frequency is the order of +1 db at the 35 db gain level. Several tubes have been operated with a klystron driver connected to the traveling-wave tube input and a klystron input cavity connected to the traveling-wave tube output with no evidence of instability.

C. Beam Production and Focusing

The electron gun used in this tube is a convergent flow Pierce gun of nominal perveance 2×10^{-6} . An oxide cathode is used which operates at a pulsed emission density of less than 2 amperes/cm². This gun is shown in cross section in Figure 4. As will be noted in the subsequent operating data, we normally operated the gun anode at a potential 1-2 kv above helix potential. This expedient was necessary in order to obtain sufficient beam power to achieve the desired power output and gain. A slightly higher perveance gun would be desirable for this tube.

For Brillouin flow focusing it is necessary to shield the cathode-anode region from magnetic flux, and to

position this shield at the proper axial position with respect to the beam minimum. Since it was desired to keep the construction of the tube as simple as possible, it was decided to place the shield outside of the vacuum envelope. By carefully forming the front face of the glass envelope it was possible to place the shield close enough to the beam minimum to obtain Brillouin focusing. This arrangement is shown in Figure 4. The mechanical setup by which the magnetic flux is fed from the solenoid end plate to the magnetic shield through a radial air gap is also shown in Figure 4. By slightly advancing the face of the shield into the solenoid beyond the solenoid end plate, the reluctance of the radial air gap can be compensated and a uniform axial field can be achieved at the face of the shield.

The tube requires a 1000 gauss magnetic field, 9" long for focusing. A typical air-cooled solenoid requires 450 watts of dc power and weighs 60 pounds. If one assumes that the beam is 0.090" diameter, which checks rf performance fairly well, then the calculated Brillouin focusing field is 880 gauss, 88 per cent of the field actually required. If we assume a beam diameter equal to the helix I. D., then the calculated Brillouin focusing field is 500 gauss, 50 per cent of the required field.

D. Tube Performance

Typical gain and power output characteristics are shown in Figure 5. This performance is typical of six tubes which were built. When the helix voltage is adjusted for maximum power output at 3.5 kmc, fairly flat power output results over the 2.5-3.5 kmc band. With this adjustment, however, the gain falls toward the high frequency end of the band. By optimizing for highest saturation gain at 3.5 kmc flatter gain characteristics can be obtained at a sacrifice in power output at 3.5 kmc. By optimizing helix voltage at the center of the band, better efficiency can be obtained. At 2.3 kmc, where dispersion allows a much higher helix voltage to be used, as much as 7 kw peak power has been obtained. Just to show what a "good" tube will do, Figure 6 shows the results obtained on one tube. We attribute this good performance to having been lucky in achieving a good attenuator which did not do the usual mysterious and deleterious things to performance that power tube attenuators usually do.

Figure 7 shows a picture of the glass envelope tube and the metal capsule in which the tube is mounted for use.

II. The T-231

At the conclusion of the work on the T-230 we were faced with the usual tube man's problem. Systems people found the rf performance of the tube useful, but---. The "but" was that some people wanted to key the tube with short rise-time pulses, but did not want to produce 7 kv pulses of the requisite rise-time. We, therefore, decided to install a low potential control grid in the gun of a T-230.

The approach was straightforward, and we were guided by some unpublished work of a similar nature done by Dr. J. K. Mann of Varian Associates, Palo Alto, California. It was arbitrarily decided to use a

positive grid potential of 1/25 the cathode-anode potential, on the basis that 300 volt pulses with short rise time were not too difficult to produce. The $V/25$ equipotential was traced in an electrolytic tank in the beam-free region as shown in Figure 8. It was found that this equipotential line came so close to the former cathode potential electrode, that this same electrode could be used as a positive electrode to which a grid could be mounted. The ledge on this electrode which maintained the proper potential at the edge of the cathode was replaced by a close-fitting cylinder surrounding the cathode. This construction is shown in Figure 8. The grid was made of 50 mesh, .002" tungsten wire, spaced 0.040" from the cathode, and was gold plated to reduce primary emission.

The first gun constructed did not provide sufficient cooling to the grid itself, and after about 100 hours of operation, evidences of grid emission were observed at cutoff. The gun was then redesigned mechanically as shown in Figure 8, so that there was sufficient radiating area on the grid support structure to keep its temperature low. With this construction, no signs of grid emission were observed after 400 hours of operation. The grid operates at a positive potential of 300 volts, when the anode potential is 7.2 kv, and cuts off at 50 volts negative with respect to the cathode.

The rf performance of the T-231 was similar to that of the T-230 with the exception that the power output is a little lower. The lower power output results from two causes. First, the grid intercepts 10 per cent of the cathode current, which reduces the current available for interaction. Second, a slightly larger beam diameter was found with the gridded gun. This larger beam reduced the space charge, which lowered the helix operating voltage to 5.6 kv and again reduced the beam power. Typical rf performance is shown in Figure 9.

III. The T-351

The work on the T-351 is not as far along as that on the T-230 and T-231, but we have obtained some preliminary performance data in several tubes which I would like to show. In the process of the work we have encountered and have had to solve some of the problems that seem to be inherent in cw amplifier tubes in this frequency range.

There are no particularly difficult problems in helix electrical design in a tube of this power level, so no discussion will be given of this point. The difficult problems have to do with helix cooling, backward-wave oscillation suppression, and attenuator dissipation. These topics will be discussed in some detail.

A. Helix Cooling

It has been shown analytically by H. Cole at Federal that a typical 3000 volt, S-band tungsten helix in vacuum, will be heated by its own rf losses to approximately 800° C when used as a transmission line at the 100 watt cw level. Our experiments have confirmed these predictions quantitatively. Then, even with perfect beam focusing, so that beam interception contributes no heating, one can expect to be operating with a hot helix. As a consequence of this heating, the helix losses are further increased and we have measured a drop in power in excess of 3 db from this cause in operating tubes.

To solve this problem we have attempted to conductively cool the helix through the vacuum envelope. The helix support is a quartz tube whose I. D. is held to a uniformity + .0001". The helix itself is wound with 0.020" x 0.050" tungsten tape, and the O. D. is centerless ground after winding to a diameter tolerance of + .0001". The nominal helix O. D. is 0.0004" smaller than the quartz I. D. at room temperature. This clearance allows the helix to be inserted in the quartz tube without distortion of the helix pitch. Then, when the helix temperature rises due to rf heating, good thermal contact results between the flat tape and the quartz, and an air blast on the outside of the quartz will effectively carry away the heat which is conducted through the quartz. With the tolerances described, we have been able to put 200 watts cw into a cold test helix at 3000 mc, and have observed no increase in helix loss due to rf heating. Helices with looser fits will show color due to temperature, while tighter fit helices will break the quartz. To date tests have not been run at higher power levels.

B. Backward-Wave Oscillation

In early tests on this tube, strong backward-wave oscillation at 7.5 kmc was observed. With a 0.120" diameter beam start-oscillation current was 12 milliamperes, while the desired operating current was 400 milliamperes. Reducing the beam diameter to 0.090" raised the starting current to 200 ma. In order to have a free choice of beam diameter, to satisfy focusing and rf considerations, it was felt desirable to include some method of backward-wave oscillation suppression.

The method of backward-wave oscillation suppression to be described was conceived by Howard Poulter, formerly of this laboratory. This scheme consists of applying a periodic dielectric discontinuity along the helix to give a stopband in the helix propagation characteristic in the frequency region where backward-wave oscillation occurs. The discontinuity consists of a helical groove on the inside of the quartz helix support tube as shown in Figure 10. The pitch of the groove is chosen to give the stopband at the proper frequency. For a free-space helix an axial discontinuity along one side of the helix would give a stopband at a $ka = 0.5$, the frequency at which backward-wave oscillation would occur. With dielectric loading due to a tight-fitting envelope, the discontinuities must occur at a position slightly less than a helix circumference apart. Hence, the helical groove must be opposite in sense to the main helix. The attenuation in the stopband is shown in Figure 10, for a 3" length of groove. In the tube the groove extends over the entire 8" of the helix. The groove has no effect on propagation in the 2-4 kmc useful range of the tube.

The helical groove in the quartz is obtained by a shrinking process. A 0.020" x 0.070" molybdenum tape is wound on a tungsten mandrel to the proper pitch. A straight quartz tube is slipped over this mandrel, evacuated on a forepump, and then the quartz is shrunk onto the mandrel by heating with a hand torch in the glass lathe. The mandrel can easily be removed after shrinking, and the helical tape unwound from the groove in the quartz. Finally, the quartz tube is centerless ground to remove the resulting ridge on the O. D.,

so that attenuators and matches can be slid onto the tube.

C. Attenuator

The attenuator on this tube must meet the usual requirements--sufficient magnitude of loss, good match, ability to be moved axially along the tube, and must be a component that can be applied external to the vacuum envelope. In addition, the attenuator should be capable of dissipating the full cw rf output of the tube in the event that a large reflection is connected to the output of the tube.

The solution to these problems finally resolved itself into the use of a lossy coupled helix attenuator. The attenuator consisted of a quadrifilar coupled helix in which the conductors were a thin platinum film, painted on the outside of a thin quartz sleeve which could be slipped over the main quartz helix support tube. The thin platinum film provided series loss and was capable of operating at a temperature of several hundred degrees centigrade in air. By passing a stream of air over this attenuator, over 100 watts cw could be dissipated satisfactorily. The quadrifilar configuration was chosen because it provided the flattest loss-frequency characteristic over the band of interest. This type of attenuator and its loss characteristics are shown in Figure 11. In order to improve the match into the attenuator, the end of the attenuator sleeve facing the output of the tube is flared radially away from the tube envelope and a lossy film of Aquadag or stannous chloride is applied to this tapered section. With the taper, the match into the attenuator has a VSWR of less than 1:02:1.

D. Matching and Beam Production

The matches used on this tube are the "cavity" type described before. The input and output VSWR are less

$$P_o = \eta I_o V_o \quad K = \frac{I_o}{V_o^{3/2}}$$

$$P_o = \eta K V_o^{3/2}$$

Choose $P = 2KW$; $\eta = 20\%$; $K = 2 \times 10^{-6}$

Then $V_o = 7600$ Volts

$$\gamma_a = \frac{\omega}{v} a = \frac{\pi d}{\lambda_o} \frac{506}{\sqrt{V}}$$

$$K_a = \frac{\omega}{c} a = \frac{\pi d}{\lambda_o} \quad \frac{\gamma_a}{K_a} = \frac{506}{\sqrt{V}}$$

Choose $\gamma_a = 1.75$; $K_a < 0.2$

$V_o < 3350$ Volts

Choose $\gamma_a = 1.0$; $K_a < 0.2$

$V_o < 10,000$ Volts

Fig. 1

than 2:1.

In all of the tests to date, a parallel flow electron gun, completely immersed in the magnetic field has been used. It is interesting that we normally run about 10 amperes/cm² cw emission density on the 0.090" D L-cathode used in this gun. However, the gun is only useful for preliminary experimental measurements, and work is under way on a convergent flow gun.

E. Performance

Figure 12 shows the sort of cw performance that has been obtained on an early tube, which did not incorporate good helix cooling, or the movable attenuator. In this case the attenuator was painted directly on the tube envelope. The power objective was achieved in this tube, but at poor efficiency. The low efficiency and the large gain compression at saturation make one suspect that the tube was saturating in the attenuator. Also, some of this loss in efficiency and saturation gain may have been due to helix rf heating. Figure 13 shows data on another tube, which apparently had a better attenuator, in that the efficiency is higher and compression less. Even in this case saturation in the attenuator is suspected. Unfortunately, the cathode did not like operating at 10 amperes/cm² cw, and it was necessary to operate at a 10:1 beam duty cycle in order to obtain data.

Figure 14 shows a picture of the tube.

The early work on the T-230 and the T-351 was done by Howard Poulter and the authors would like to acknowledge his help. Much of the testing of the T-351 has been done by William Newman. This work was supported by a Joint Service Contract administered by the Office of Naval Research and sponsored by the Signal Corps, the Air Force and the Navy.

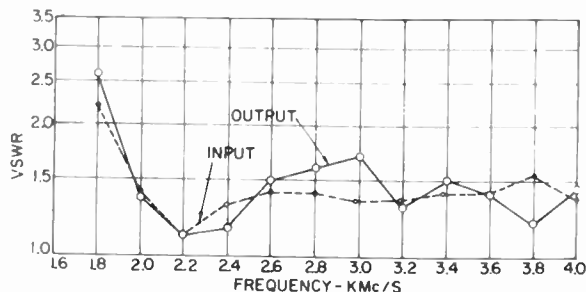
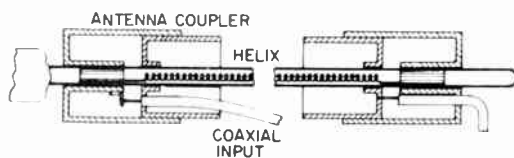
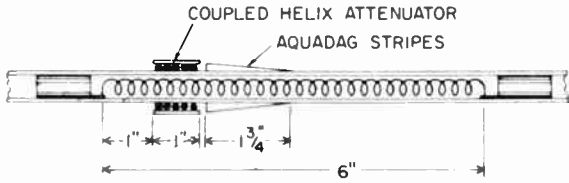


Fig. 2
R-f match configuration.



COUPLED HELIX: 7 TPI, BIFILAR, .020" D. WIRE, .300" I.D.
 MAIN HELIX: 13 TPI, UNIFILAR, .030" D. WIRE, .160" I.D.
 ENVELOPE: .220" I.D., .285" O.D., PYREX.

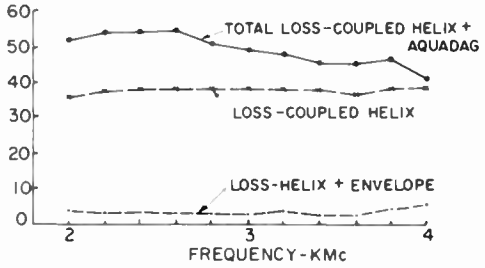


Fig. 3

Coupled helix attenuator for T-230 and T-231.

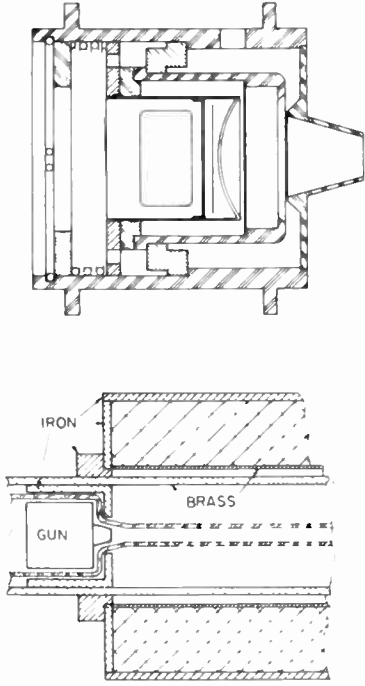


Fig. 4

Perveance 2×10^{-6} electron gun.

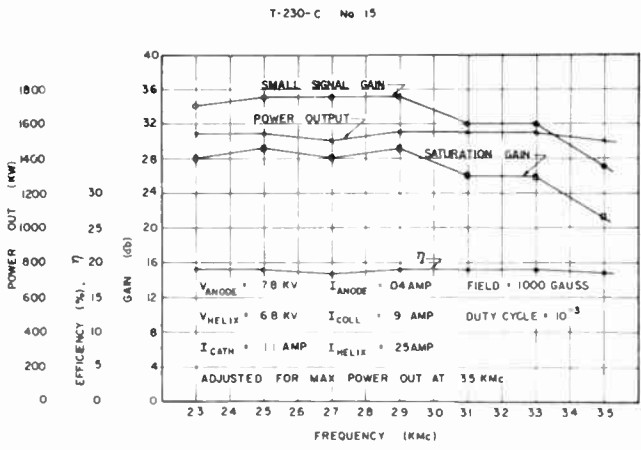
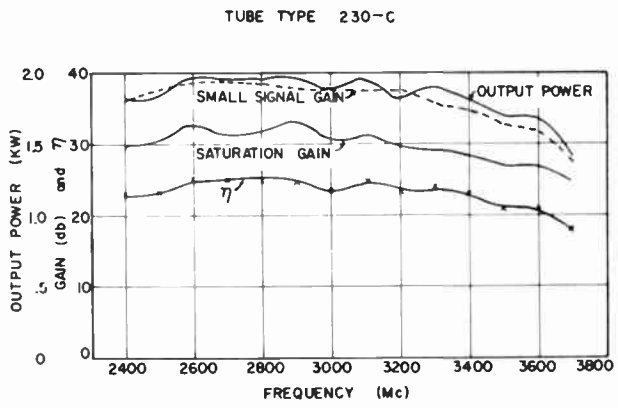


Fig. 5

Performance Characteristics of T-230



OPERATING CONDITIONS ANODE 9.0Kv. CATHODE 1.2 AMPS
 HELIX 7.2 Kv. COLLECTOR 1.1 AMPS
 (OPTIMIZED - 3700Mc) MAGNET 3.2 AMPS

Fig. 6

Performance characteristics T-230

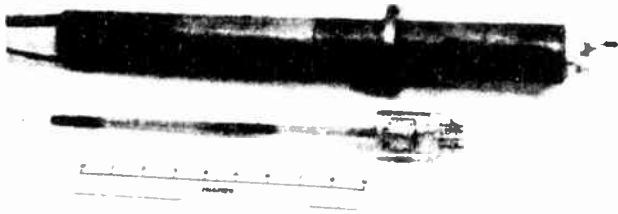


Fig. 7
T-230 and capsule.

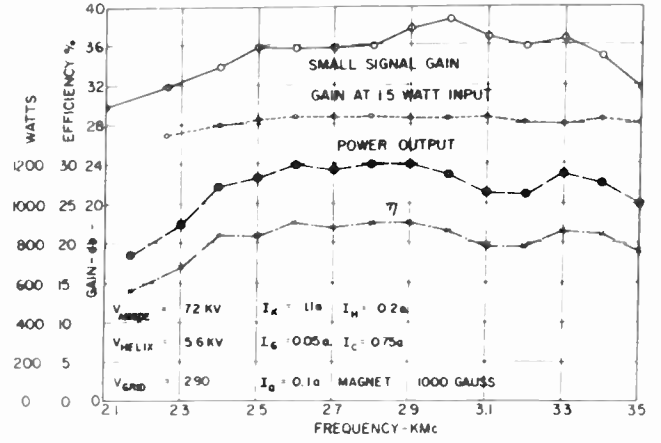


Fig. 9
T-231 performance characteristics.

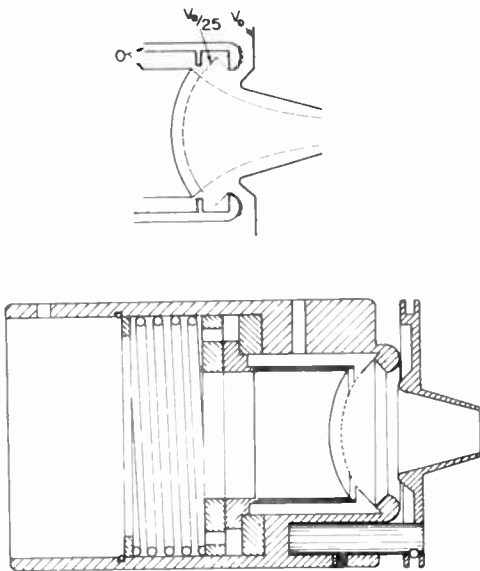


Fig. 8
Gridded perveance 2×10^{-6} electron gun.

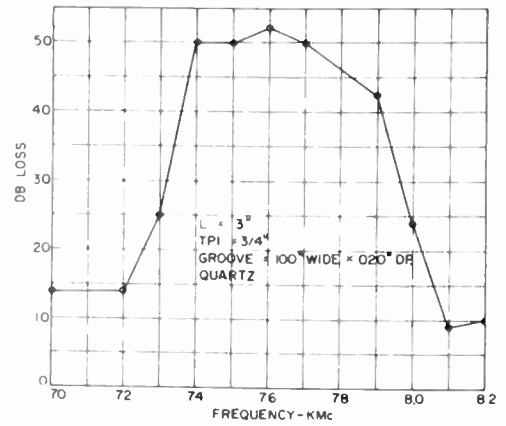
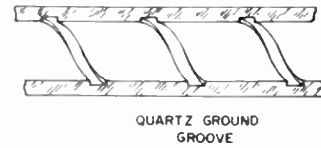
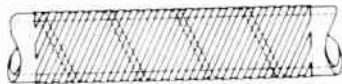


Fig. 10
Backward-wave oscillation suppressor.



PLATINUM PLATED COUPLED
HELIX ATTENUATOR FOR T-351

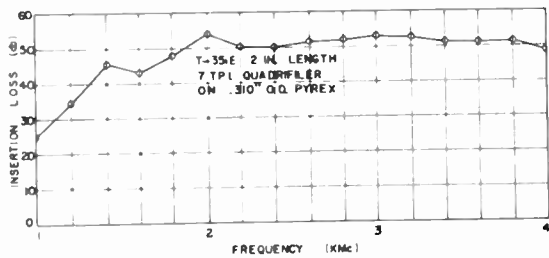


Fig. 11
T-351 platinum film attenuator.

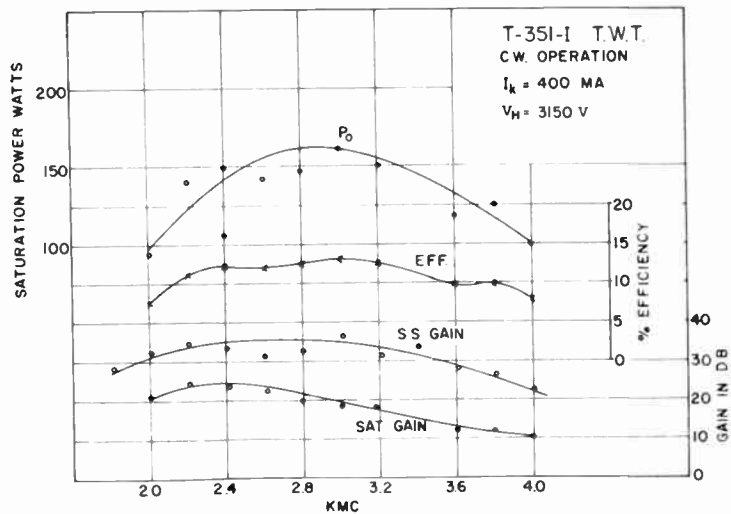


Fig. 12
T-351-I cw performance.

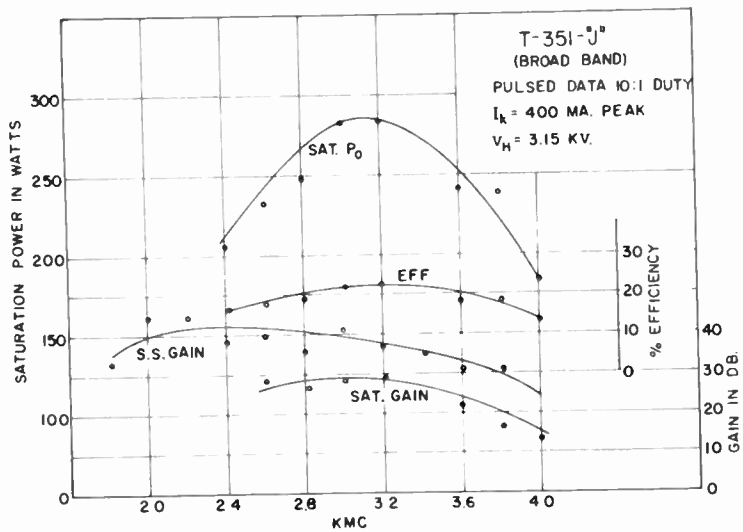


Fig. 13
T-351-J, 10:1 duty cycle performance.



Fig. 14
T-351 traveling-wave tube.

A-1 KW PULSED TRAVELING-WAVE TUBE AMPLIFIER AT X-BAND

J. E. Nevins, S. F. Kaisel, and M. Chodorow
Stanford University
Stanford, Calif.

ABSTRACT

This paper will describe the application of the contra-wound helix structure to a high-power, narrow-band pulsed traveling-wave tube amplifier for operation in the frequency range 8.5-9.6 kmc. Power output greater than 1 kw at 30 db gain has been obtained. The impedance of the contra-wound

helix as predicted by Chodorow and Chu has been verified by cold perturbation methods and by beam measurements. Some comparisons are made with performance and dimensions that would be predicted for the single-wound helix. A novel method for the cross-wound helix will be described.

NOISE ANALYSIS OF TRAVELING-WAVE-TUBE VIDEO DETECTOR*

Glen Wade
 Electronics Research Laboratory
 Stanford University
 Stanford, California

Summary

An analysis is made of the rectification characteristics and the noise characteristics of a traveling-wave tube modified for use as a video detector. The purpose of the analysis is to determine the sensitivity of such a device as limited solely by noise and to compare this sensitivity with that of a video-crystal detector and with that of a traveling-wave tube followed by a video-crystal detector.

The high-velocity electrons in the velocity-modulated beam at the output of a traveling-wave tube can be separated from the slower electrons by means of a velocity-sensitive deflecting field only biasing the collector near cathode potential. The current thus separated is a rectified version of the input signal.

With reasonable values for the tube parameters the calculated "minimum detectable signal" for such a device is approximately -77 dbm. This is a substantially lower value than the minimum detectable signal obtainable at present with video-crystal detectors. It is shown to be of the same order of magnitude as that obtainable with a high-gain traveling-wave tube followed by a video-crystal detector.

Introduction

The idea of velocity-sorting the electrons of a velocity-modulated beam to produce detection was proposed several years ago by Harn and Metcalf¹. Traveling-wave-tube video detectors based on this principle have since been constructed². The purpose of this paper is to present a noise analysis of such a device, and to calculate its sensitivity as limited by noise for comparison with the sensitivities of a video-crystal detector and of a traveling-wave-tube-crystal-detector combination.

Assuming an arbitrary law of detection, the following expressions are determined:

- (1) the rectified signal voltage in terms of the input power;

- (2) the output mean-square noise voltage; and
- (3) the minimum detectable signal.

In this treatment the minimum detectable signal is defined as that signal power for which the rectified signal voltage equals the rms noise voltage (with the signal power off). Experimentally a minimum detectable signal is defined as the input pulse power for the smallest-amplitude pulse immediately seen on an A-scope when its position along the trace is unknown. From experiments in connection with crystal rectifiers it appears that the latter definition is approximately equivalent to the former³.

A glossary of symbols to be used is given below. The mks system of units is employed in the calculations.

- G = Pierce's traveling-wave tube gain parameter⁴
- E_{si} = peak value of the rf electric field, due to the signal, at the helix input
- E_{so} = peak value of the rf electric field, due to the signal, at the helix output
- $\langle E_{ni}^2 \rangle_{av}$ = mean-square value of electric field fluctuation, due to noise, at the helix input
- $\langle E_{no}^2 \rangle_{av}$ = mean-square value of electric field fluctuation, due to noise, at the helix output
- e = the magnitude of the charge on an electron
- F = traveling-wave-tube noise figure
- G = power gain of traveling-wave tube
- I = collector current
- I_{act} = low-frequency current to the output filter (excluding dc) due to noise
- I_0 = dc traveling-wave-tube beam current
- I_r = rectified output current
- I_{tl} = total low-frequency current to the output filter (including dc) due to noise
- $I'(V_0), I''(V_0)$ = the first and second derivatives, respectively, of collector current with respect to helix voltage evaluated at $V = V_0$
- $i(v)$ = beam current distribution function

*The work reported in this paper was supported jointly by the U.S. Air Force, the U.S. Army, and the U.S. Navy, under Contract D-109 251(C7). The paper is based in part on a Ph.D. dissertation submitted to the Department of Electrical Engineering, Stanford University.

A-1 KW PULSED TRAVELING-WAVE TUBE AMPLIFIER AT X-BAND

J. E. Nevins, S. F. Kaisal, and M. Chodorow
Stanford University
Stanford, Calif.

ABSTRACT

This paper will describe the application of the contra-wound helix structure to a high-power, narrow-band pulsed traveling-wave tube amplifier for operation in the frequency range 8.5-9.6 kmc. Power output greater than 1 kw at 30 db gain has been obtained. The impedance of the contra-wound

helix as predicted by Chodorow and Chu has been verified by cold perturbation methods and by beam measurements. Some comparisons are made with performance and dimensions that would be predicted for the single-wound helix. A novel method for the cross-wound helix will be described.

NOISE ANALYSIS OF TRAVELING-WAVE-
TUBE VIDEO DETECTOR*

Glen Wade
Electronics Research Laboratory
Stanford University
Stanford, California

Summary

An analysis is made of the rectification characteristics and the noise characteristics of a traveling-wave tube modified for use as a video detector. The purpose of the analysis is to determine the sensitivity of such a device as limited solely by noise and to compare this sensitivity with that of a video-crystal detector and with that of a traveling-wave tube followed by a video-crystal detector.

The high-velocity electrons in the velocity-modulated beam at the output of a traveling-wave tube can be separated from the slower electrons by means of a velocity-sensitive deflecting field or by biasing the collector near cathode potential. The current thus separated is a rectified version of the input signal.

With reasonable values for the tube parameters the calculated "minimum detectable signal" for such a device is approximately -77 dbm. This is a substantially lower value than the minimum detectable signal obtainable at present with video-crystal detectors. It is shown to be of the same order of magnitude as that obtainable with a high-gain traveling-wave tube followed by a video-crystal detector.

Introduction

The idea of velocity-sorting the electrons of a velocity-modulated beam to produce detection was proposed several years ago by Barn and Litchfield¹. Traveling-wave-tube video detectors based on this principle have since been constructed². The purpose of this paper is to present a noise analysis of such a device, and to calculate its sensitivity as limited by noise for comparison with the sensitivities of a video-crystal detector and of a traveling-wave-tube-crystal-detector combination.

Assuming an arbitrary law of detection, the following expressions are determined:

- (1) the rectified signal voltage in terms of the input power;

- (2) the output mean-square noise voltage; and
(3) the minimum detectable signal.

In this treatment the minimum detectable signal is defined as that signal power for which the rectified signal voltage equals the rms noise voltage (with the signal power off). Experimentally a minimum detectable signal is defined as the input pulse power for the smallest-amplitude pulse immediately seen on an A-scope when its position along the trace is unknown. From experiments in connection with crystal rectifiers it appears that the latter definition is approximately equivalent to the former³.

A glossary of symbols to be used is given below. The cgs system of units is employed in the calculations.

- G = Pierce's traveling-wave tube gain parameter⁴
 E_{si} = peak value of the rf electric field, due to the signal, at the helix input
 E_{so} = peak value of the rf electric field, due to the signal, at the helix output
 $\langle E_{ni}^2 \rangle_{av}$ = mean-square value of electric field fluctuation, due to noise, at the helix input
 $\langle E_{no}^2 \rangle_{av}$ = mean-square value of electric field fluctuation, due to noise, at the helix output
 e = the magnitude of the charge on an electron
 F = traveling-wave-tube noise figure
 G = power gain of traveling-wave tube
 I = collector current
 I_{acf} = low-frequency current to the output filter (excluding dc) due to noise
 I_0 = dc traveling-wave-tube beam current
 I_r = rectified output current
 I_{tl} = total low-frequency current to the output filter (including dc) due to noise
 $I'(V_0), I''(V_0)$ = the first and second derivatives, respectively, of collector current with respect to helix voltage evaluated at $V = V_0$
 $i(v)$ = beam current distribution function

*The work reported in this paper was supported jointly by the U.S. Air Force, the U.S. Army, and the U.S. Navy, under Contract W-31(07). The paper is based in part on a Ph.D. dissertation submitted to the Department of Electrical Engineering, Stanford University.

K	= Boltzmann's constant
$P(R_n)$	= the probability density of R_n
P_{si}	= signal power to the helix input
P_{sim}	= minimum detectable input signal
R_n	= envelope of V_n
R	= output filter resistance
T	= room temperature in degrees kelvin (290°K)
T_c	= cathode temperature in degrees Kelvin
u_0	= dc electron velocity at helix output
V	= instantaneous helix voltage. (It is useful in determining the static characteristic of Fig. 3, and in the operation of the detector it may be thought of as the helix voltage equivalent to electron kinetic energy due to the dc helix voltage and rf fields on the helix.)
V_c	= helix voltage which corresponds to v_c , i.e., $V_c = mv_c^2/2e$
V_0	= dc value of helix voltage
V_m	= maximum value of equivalent ac helix voltage due to signal
V_n	= instantaneous value of equivalent ac helix voltage due to noise
$\langle V_{nt}^2 \rangle_{Av}$	= total mean-square voltage fluctuation across R due to noise
$\langle V_{n1}^2 \rangle_{Av}$, $\langle V_{n3}^2 \rangle_{Av}$, $\langle V_{n4}^2 \rangle_{Av}$	= the mean-square voltage fluctuations across R due to the first, third, and fourth noise sources described, respectively
V_s	= video signal voltage developed across R
v	= electron velocity at helix output
v_c	= critical beam electron velocity. (Electrons with velocities greater than this go to the collector; less than this, to the shield.)
v_{ac}	= ac component of electron velocity at helix output
$W(f)$	= power spectrum of the collector current
$W_c(f)$	= the continuous portion of $w(f)$
$w(f)$	= Power spectrum of V_n
α	= reduction factor in detector output noise due to bandwidth of output filter
β_e	= electronic wave number, π/u_0
Δf	= output filter noise bandwidth
Δf_t	= traveling-wave-tube noise bandwidth
δ_1	= Pierce's incremental propagation constant for the increasing wave
η	= charge-to-mass ratio of an electron
$\Psi(\tau)$	= correlation function for collector current
$\psi(\tau)$	= correlation function for V_n
$\omega/2\pi$	= mid-band frequency of traveling-wave tube

A signal on the slow-wave circuit of a traveling-wave tube produces velocity modulation on the electron beam. The high-velocity electrons can be separated from the slower electrons in either of two ways:

- (1) The beam is passed through a velocity-sensitive deflecting field, such as a transverse magnetostatic field, and then sorted by a properly positioned shield. The high-velocity electrons pass beyond the shield to a collector.
- (2) The collector is biased near cathode potential and only the high-velocity electrons reach it.

In either case, the collector current can be fed to a low-pass filter to be developed into a rectified signal.

The equations derived below are equally applicable to either method of sorting (although practical realization of the latter may involve difficulties). Let us use the first method to illustrate the analysis. Consider the traveling-wave-tube video detector shown diagrammatically in Fig. 1. An rf signal on the helix velocity-modulates the electron beam. The beam then passes through a dc magnetic deflecting field which deflects slow electrons more than fast ones. Beam spreading due to space charge is uninhibited in the direction parallel to the field, but the focusing action of the field tends to prevent such spreading in the perpendicular direction. Thus, just before the beam reaches the shield, its cross section (at any instant of time) somewhat resembles a fuzzy line whose long dimension is parallel to the magnetic field.

The velocity modulation causes a sinusoidal shifting in the beam's position at the rf rate. Thus, the fuzzy line has motion at right angles to the magnetic field and sweeps out an area proportional to the magnitude of the velocity modulation. The shield has a knife edge which is parallel to the magnetic field. The knife edge is placed in such a position that all electrons having a velocity less than a certain critical velocity (say, v_c) are intercepted by the shield. Electrons with greater velocities pass to the collector. The time-integrated cross section of the beam in relation to the shield position is shown in Fig. 2. A rectified current may be developed at either the collector or the shield.

If by some means all modulation (including noise modulation) could be removed from the beam, the beam's cross section would still be characterized by a finite width due to the half-Maxwellian velocity distribution of electrons and the imperfect focusing of magnetic field. If these factors also could be eliminated, the cross section would appear as an infinitesimally thin line having a

position parallel to and slightly to the left of the knife edge in Fig. 2.

All electrons would then be collected by the shield. In the presence of an rf signal, the beam moves from side to side at the rf rate. For the ideal case, the total beam current would abruptly shift from the shield to the collector, or vice versa, as the velocity passes through v_c .

However, because of the factors mentioned, the actual shift in current distribution between shield and collector is a more gradual one. A plot of collector current vs helix voltage would appear as shown in Fig. 3. The ideal case is indicated by the dotted line.

Derivation of Expression for Rectified Signal Voltage

The beam at the output of the helix contains both current modulation and velocity modulation due to the signal. For small signals let us assume that only the velocity modulation is important in producing a rectified current. An argument to justify this assumption is presented at the end of this section.

The effect of a signal on the helix in changing the kinetic energy of the beam electrons is equivalent to a change of helix voltage. Thus, a collector-current vs helix-voltage plot is useful in calculating the rectified signal current. In the following derivation let V_0 represent a dc value of helix voltage somewhat less than V_c . For values of V near V_0 , we may write

$$I(V) = I(V_0) + \frac{I'(V_0)}{1!} (V - V_0) + \frac{I''(V_0)}{2!} (V - V_0)^2 + \dots \quad (1)$$

where the primes indicate differentiation with respect to V_0 . Let V vary as $V_0 + V_m \sin \omega t$, where ω corresponds to the signal frequency. Then for any instant of time we have

$$I(V) = I(V_0) + I'(V_0)V_m \sin \omega t + \frac{I''(V_0)}{2} V_m^2 \sin^2 \omega t + \dots \quad (2)$$

If it is assumed that V_m changes at the video rate, the rectified video current is the time average of Eq. (2) less the dc term. For small V_m we obtain

$$I_r = \frac{\pi}{4} I''(V_0) V_m^2 \quad (3)$$

To put I_r in terms of the input signal, we need an expression for the ac field at the helix output which will have the same effect on elec-

tron velocity as does V_m . Let

$$v = u_0 + v_{ac}$$

for the case of $V_m \ll V_0$, we may write

$$v = [2\pi(V_0 + V_m \sin \omega t)]^{1/2} \approx [2V_0]^{1/2} \left[1 + \frac{V_m}{2V_0} \sin \omega t \right],$$

or

$$v_{ac} = [2\pi V_0]^{1/2} \frac{V_m}{2V_0} \quad (4)$$

From traveling-wave-tube theory (in which space charge is neglected) we have

$$v_{ac} = \frac{-E_{so}}{u_0 \beta_e \delta_1} \quad (5)$$

where E_{so} is the peak value of the ac signal field at the output of the helix. The other symbols are the familiar ones of the Pierce analysis⁴. (This assumes that the traveling-wave amplifier has reasonable gain so that only the increasing wave is of consequence.)

In Eq. (3) the phase angle associated with V_m is unimportant. Only the magnitude is needed. Thus from Eqs. (4) and (5) we obtain

$$V_m^2 = \frac{E_{so}^2}{|\beta_e \delta_1|^2} \quad (6)$$

To obtain E_{so} in terms of the signal power to the helix input we may use

$$E_{so}^2 = E_{si}^2 P_{si} \quad (7)$$

where E_{si} is the peak value of the field due to the signal at the helix input and P_{si} is the power gain of the traveling-wave tube.

Now the traveling-wave-tube gain parameter is given by⁴

$$G^3 = \frac{E_{si}^2}{\beta_e^2 P_{si}} \frac{I_0}{u_0} \quad (8)$$

where P_{si} is the signal power to the helix input. Combining Eqs. (3), (6), (7), and (8) gives

$$I_r = \frac{V_0}{I_0} \frac{2CG}{|\delta_1|^2} P_{si} I''(V_0) \quad (9)$$

The video signal voltage V_s is the product of this current and the resistance R of Fig. 1. Thus we

obtain

$$V_s = \frac{V_0}{I_0} \frac{2CG}{|\delta_1|^2} P_{si} I''(V_0) v. \quad (10)$$

As was previously stated, the preceding derivation takes into account the velocity modulation only. The beam also possesses a correlated current modulation. For small signals, the current variations as a result of this modulation are small compared to the total beam current. It follows, therefore, that the current variations can affect the instantaneous values of collector current by only a small percentage. The relative phase between the current variations and the velocity variations at the shield is a function of the distance between the helix and the shield. Assuming an in-phase relationship, the instantaneous collector current is slightly increased at the peaks and slightly decreased at the valleys due to the current variation. Since the rectified current depends upon the time-averaged collector current, the effect is necessarily small. This same conclusion (of small effect of the rectified current) holds for all other relative phase between current and velocity variations. The effect can be taken into account by multiplying the left side of Eq. (10) by a factor whose limit is unity as the signal strength approaches zero. Thus Eq. (10) is valid without alteration for small signals.

Derivation of Expression for Noise Voltage

The sensitivity of the detector is limited by the noise voltage across R . The important noise sources are the following:

- (1) Velocity fluctuations at rf frequencies in the electrons approaching the shield.
- (2) Current fluctuations at rf frequencies in the beam approaching the shield.
- (3) Additional current fluctuations at video frequencies resulting from partition current at the shield and spot fluctuations (at those frequencies) in the beam.
- (4) Thermal noise at video frequencies in the output resistance R .

Consider the first noise source. The equivalent helix voltage may be written

$$V = V_0 + V_n, \quad (11)$$

where V_n represents the equivalent voltage fluctuations due to this noise. For this analysis a convenient expression for V_n is²

$$V_n = R_n \cos(\omega_m t + \theta), \quad (12)$$

where R_n is the envelope of V_n and $\omega_m/2\pi$ is the mid-band frequency of the traveling-wave tube. R_n and θ are relatively slowly varying functions of time. Using Eqs. (11) and (12) in Eq. (1), and

neglecting third and higher order terms in R_n , we get for the total low-frequency (including dc) current

$$I(V)_{t\ell} = I(V_0) + \frac{I''(V_0)}{4} R_n^2, \quad (13)$$

where the subscript $t\ell$ stands for "total low" frequency. In Eq. (13) all high-frequency terms have been dropped because of the low-pass output filter. The dropped terms have frequencies in the vicinity of $\omega_n/2\pi$ and ω_m/π . We may write

$$I(V)_{t\ell} = I_{dc} + I_{ac\ell}$$

and

$$\langle I(V)_{t\ell}^2 \rangle_{Av} = \langle (I_{dc} + I_{ac\ell})^2 \rangle_{Av} = I_{dc}^2 + \langle I_{ac\ell}^2 \rangle_{Av} \quad (14)$$

where $I_{dc} = \langle I(V)_{t\ell} \rangle_{Av}$ and $\langle I_{ac\ell}^2 \rangle_{Av}$ is the total mean-square fluctuation current included in the low-frequency spectrum. (The ℓ in the subscript again stands for "low" frequency.) In the present application part of the low-frequency spectrum is removed by the filter. Therefore, only a fraction of $\langle I_{ac\ell}^2 \rangle_{Av}$ appears across the output. The value of the fraction is a function of the output power spectrum and the filter bandwidth. This function will be derived later. From Eq. (13) we obtain

$$I_{dc} = I(V_0) + \frac{I''(V_0)}{4} \langle R_n^2 \rangle_{Av} \quad (15)$$

and

$$\langle I(V)_{t\ell}^2 \rangle_{Av} = [I(V_0)]^2 + I(V_0) \frac{I''(V_0)}{2} \langle R_n^2 \rangle_{Av} + \left[\frac{I''(V_0)}{4} \right]^2 \langle R_n^4 \rangle_{Av}. \quad (16)$$

Combining Eqs. (14), (15), and (16) gives

$$\langle I_{ac\ell}^2 \rangle_{Av} = \left[\frac{I''(V_0)}{4} \right]^2 \times \left[\langle R_n^4 \rangle_{Av} - \langle R_n^2 \rangle_{Av}^2 \right]. \quad (17)$$

The probability density of the noise envelope R_n is required at this point³:

$$P(R_n) = \frac{R_n}{\langle V_n^2 \rangle_{Av}} \exp(-R_n^2/2 \langle V_n^2 \rangle_{Av}). \quad (18)$$

From Eq. (18) it follows that

$$\langle R_n^2 \rangle_{Av} = 2 \langle V_n^2 \rangle_{Av}. \quad (19)$$

From Eq. (1^c) we may write

$$\langle v_n^4 \rangle_{Av} = \int_0^\infty \frac{v_n^5}{\langle v_n^2 \rangle_{Av}} \exp$$

$$(-v_n^2/2 \langle v_n^2 \rangle_{Av}) dv_n = 3 (\langle v_n^2 \rangle_{Av})^2. \quad (20)$$

Combining Eqs. (17), (19) and (20) yields

$$\langle I_{accl}^2 \rangle_{Av} = \left[\frac{I''(V_0)}{2} \langle v_n^2 \rangle_{Av} \right]^2. \quad (21)$$

The traveling-wave-tube noise figure may be written in terms of the mean-square value of electric field fluctuations at the helix output and at the helix input:

$$F = \frac{\langle E_{no}^2 \rangle_{Av}}{G \langle E_{ni}^2 \rangle_{Av}}. \quad (22)$$

Eqs. (6) and (9) may be modified as follows:

$$\langle v_n^2 \rangle_{Av} = \frac{\langle E_{no}^2 \rangle_{Av}}{\beta_e^2 c^2 |\delta_1|^2} \quad (23)$$

$$G^3 = \frac{\langle E_{ni}^2 \rangle_{Av} I_0}{\beta_e^2 c^2 \Delta f_t 4V_0} \quad (24)$$

where Δf_t is the traveling-wave-tube bandwidth and $KT \Delta f_t$ is the noise power input. Using Eqs. (22), (23) and (24) in Eq. (21) gives

$$\langle I_{accl}^2 \rangle_{Av} = \left[\frac{V_0}{I_0} \frac{2CG}{|\delta_1|^2} FKT \Delta f_t I''(V_0) \right]^2. \quad (25)$$

As previously stated, the mean-square rectified noise current is only a fraction of $\langle I_{accl}^2 \rangle_{Av}$.

Let α represent the value of the fraction. It follows that the mean-square noise voltage across R due to this source is

$$\langle v_{n1}^2 \rangle_{Av} = \alpha \left[\frac{V_0}{I_0} \frac{2CG}{|\delta_1|^2} FKT \Delta f_t I''(V_0) \right]^2. \quad (26)$$

The subscript 1 identifies this noise with the first noise source previously listed. The derivation of an expression for α is reserved for Appendix A. The expression turns out to be

$$\alpha = \frac{\Delta f}{\Delta f_t} \left[2 - \frac{\Delta f}{\Delta f_t} \right], \quad (27)$$

where Δf is the output filter noise bandwidth.

The beam-current noise fluctuations at the helix output constitute the second noise source listed. The current fluctuations are correlated with the velocity fluctuations for noise as well as for signal. The arguments that were previously applied to justify neglecting the current modulation in the expression for the rectified signal voltage also are valid here. Current fluctuations affect noise and signal by precisely the same amount. Thus, just as Eq. (10) has validity in small-signal theory, so also has Eq. (26) and we leave it unaltered.

The third noise source is due to partition current at the shield and shot fluctuations in the beam. This noise may be taken into account by assuming full shot noise on the current to the collector. (This is, of course, a pessimistic assumption. However, it is unimportant even so because, as will be shown in the sample calculation, this source is small compared with the first source.) Since this noise is uncorrelated with the noise from the first source, the mean-square voltages corresponding to the two sources are directly additive in computing the total noise. Thus we have

$$\langle v_{n3}^2 \rangle_{Av} = 2eI \Delta f R^2, \quad (28)$$

where $\langle v_{n3}^2 \rangle_{Av}$ = mean-square noise voltage due to these fluctuations.

The thermal noise in the output resistance is the fourth and final source to consider. This noise is uncorrelated with the other noise and has a mean-square value of

$$\langle v_{n4}^2 \rangle_{Av} = 4KT \Delta f R. \quad (29)$$

Thus, the total mean-square voltage fluctuation across R due to noise is

$$\langle v_{nt}^2 \rangle_{Av} = \langle v_{n1}^2 \rangle_{Av} + \langle v_{n3}^2 \rangle_{Av} + \langle v_{n4}^2 \rangle_{Av}. \quad (30)$$

Minimum Detectable Signal

The minimum detectable signal as previously defined is found by equating V_s^2 and $\langle v_{nt}^2 \rangle_{Av}$ and solving for P_{si} . This gives

$$P_{sim}^2 = \alpha [FKT \Delta f_t]^2 + \left[\frac{I_0 |\delta_1|}{2V_0 CG I''(V_0)} \right]^2 \times$$

$$\left[2eI \Delta f + \frac{4KT \Delta f}{R} \right], \quad (31)$$

where P_{sim} = minimum detectable input signal.

Sample Calculation of Minimum Detectable
Signal for Traveling-Wave-Tube Detector

A rough estimate of the value of P_{sim} may be had by assuming that the half-Maxwellian velocity distribution is solely responsible for limiting the value of $I''(V_0)$. Assume that the current distribution function for $V < V_c$ is

$$i(v) = I_0 \frac{mv}{KT_c} s(v - v_c) \exp\left\{-\left[\frac{mv^2}{2} - eV\right]/KT_c\right\},$$

where

$$v = \text{electron velocity}$$

$$v_c = [2eV]^{1/2}$$

$$s(v - v_c) = \begin{cases} 1 & \text{for } v > v_c \\ 0 & \text{for } v < v_c \end{cases}$$

Then we may write

$$I = \int_{-\infty}^{\infty} \frac{I_0 \frac{mv}{KT_c} \exp\left\{-\left[\frac{mv^2}{2} - eV\right]/KT_c\right\} dv}{[2\eta V]^{1/2}}$$

$$= I_0 e^{-e(V_c - V)/KT_c}$$

$$\text{for } V < V_c$$

and

$$I = I_0 \text{ for } V > V_c.$$

From this we obtain

$$I''(V_0) = \left(\frac{e}{KT_c}\right)^2 I_0 \exp\left[-e(V_c - V_0)/KT_c\right]$$

$$= \left(\frac{e}{KT_c}\right)^2 I(V_0). \quad (32)$$

Now we are in a position to solve Eq. (31) for P_{sim} assuming reasonable values for the traveling-wave-tube and circuit parameters.

Let

$$F = 50 \text{ (17 db)}$$

$$\Delta f_t = 2000 \text{ Mc}$$

$$\Delta f = 2 \text{ Mc}$$

$$T = 290^\circ\text{K}$$

$$T_c = 1160^\circ\text{K}$$

$$I_0 = 3 \text{ ma}$$

$$|\delta_1|^2 = 1$$

$$V_0 = 450 \text{ v}$$

$$C = 0.03$$

$$G = 4000 \text{ (36 db)}$$

$$I(V_0) = 0.4 \text{ ma}$$

$$R = 10 \text{ kohms.}$$

(The traveling-wave-tube parameters are those of a commercially available tube.) Using these values in Eqs. (32), (27), and (31), we obtain

$$P_{sim} = \left[3.2 \times 10^{-22} + 0.99 \times 10^{-26} + 0.99 \times 10^{-30}\right]^{1/2} = 1.8 \times 10^{-11} \text{ w (-77 dbm).}$$

The three values in the radical correspond to the three terms in Eq. (31). The first term, which results from traveling-wave-tube noise, is by far the largest of the three for this set of parameters. If the gain only is changed, this term will continue to dominate until the gain is reduced to the order of unity.

Comparison with Other Video Detectors

The sensitivity of a video-crystal detector can be calculated from the following equation³.

$$P_{sim} = \frac{[4KT \Delta f]^{1/2}}{M}, \quad (33)$$

where M is a criterion of the excellence of the detector and is called its "figure of merit". A value of M of 100 is large but not uncommon. For this value of M and for a bandwidth of 2 Mc (as in the previous calculation) P_{sim} is 1.8×10^{-10} watt (-57 dbm). Thus the traveling-wave-tube detector is considerably more sensitive than is the video-crystal detector.

Consider a system in which a traveling-wave tube feeds a video-crystal detector. Appendix B gives the expression for the minimum detectable signal of such a system as

$$P_{sim} = \left[\alpha(FKT \Delta f_t)^2 + \frac{4i_0 T \Delta f}{G^2 R}\right]^{1/2}. \quad (34)$$

Assuming the parameters for the traveling-wave tube and the crystal to be the same as in the previous calculations we obtain

$$P_{sim} = \left[3.2 \times 10^{-22} + 2 \times 10^{-25}\right]^{1/2}$$

$$= 1.8 \times 10^{-11} \text{ w (-77 dbm).}$$

Note that the term corresponding to the traveling-wave-tube noise is still the dominant term in this case. If the other parameters are held constant, the traveling-wave-tube noise ceases to dominate when the gain falls below 100 (20 db).

Conclusions

For the parameters used, the calculated sensitivity of the traveling-wave-tube detector is the same as that of a traveling-wave tube followed by a video-crystal detector. It is only for low values of gain (in the example, gains less than 20 db) that the traveling-wave-tube detector shows promise of possessing the greater sensitivity. Both detectors are considerably more sensitive than the video-crystal detector.

The combination of traveling-wave tube and video-crystal has the great advantage of simplicity. On the other hand, this combination requires a wide band match between the tube and the crystal, a problem not present in the traveling-wave-tube detector.

Acknowledgment

The author is indebted to D. A. Watkins for his suggestions in the writing of this paper.

Appendix A: Derivation of Equation (27)

In deriving an expression for the factor α we must solve the following problem: Given a nonlinear device obeying the law expressed by Eq. (1) whose input consists of noise alone, find the output power spectrum. Several methods are available for solving this problem⁷. The one used here will be to determine the correlation function for the output current, and to use this function in solving for the output power spectrum. The correlation function is defined by

$$\begin{aligned} \Psi(\tau) &= \lim_{T \rightarrow \infty} \frac{1}{T} \int_0^T I(t)I(t+\tau) dt \\ &= \langle I(t)I(t+\tau) \rangle_{AV} \end{aligned} \quad (A.1)$$

The power spectrum $W(f)$ of the output current is related to $\Psi(\tau)$ as follows,

$$W(f) = 4 \int_0^{\infty} \Psi(\tau) \cos 2\pi f \tau d\tau \quad (A.2)$$

Using Eqs. (1), (11), and (A.1), and neglecting third and higher order terms, we have

$$\begin{aligned} \Psi(\tau) &= \left[\langle I(V_0) + I'(V_0)V_n(t) + \frac{I''(V_0)}{2}V_n^2(t) \rangle_{AV} \right. \\ &\quad \left[\langle I(V_0) + I'(V_0)V_n(t+\tau) \right. \\ &\quad \left. + \frac{I''(V_0)}{2}V_n^2(t+\tau) \rangle_{AV} \right] \end{aligned} \quad (A.3)$$

Eq. (A.3) may be evaluated by noting that

$$\langle V_n(t) \rangle_{AV} = \langle V_n(t+\tau) \rangle_{AV} = 0,$$

$$\langle V_n^2(t) \rangle_{AV} = \langle V_n^2(t+\tau) \rangle_{AV} = \langle V_n^2 \rangle_{AV}.$$

Let

$$\langle V_n(t)V_n(t+\tau) \rangle_{AV} = \psi(\tau).$$

From the theory of two-dimensional normal distribution it can be shown⁸ that

$$\langle V_n^2(t)V_n^2(t+\tau) \rangle_{AV} = \langle V_n^2 \rangle_{AV}^2 + 2\psi^2(\tau)$$

and⁹

$$\langle V_n^2(t)V_n(t+\tau) \rangle_{AV} = \langle V_n(t)V_n^2(t+\tau) \rangle_{AV} = 0.$$

Thus, (A.3) becomes

$$\begin{aligned} \Psi(\tau) &= I^2(V_0) + I(V_0) I''(V_0) \langle V_n^2 \rangle_{AV} \\ &\quad + \left[\frac{I''(V_0)}{2} \langle V_n^2 \rangle_{AV} \right]^2 + \psi(\tau) [I'(V_0)]^2 \\ &\quad + 2 \left[\frac{I''(V_0)}{2} \psi(\tau) \right]^2 \end{aligned} \quad (A.4)$$

Equation (A.4) contains three dc terms which correspond to the dc components of $I(t)$ ¹⁰. These terms are useful in calculating the dc output current (and give the same value as Eq. (15)) but are of no interest as far as the "continuous" power spectrum is concerned. Let $w_c(f)$ be the continuous portion of $W(f)$. Then

$$\begin{aligned} w_c(f) &= 4 \int_0^{\infty} \left\{ [I'(V_0)]^2 \psi(\tau) \right. \\ &\quad \left. + 2 \left[\frac{I''(V_0)}{2} \psi(\tau) \right]^2 \right\} \cos 2\pi f \tau d\tau \\ &= I'(V_0)^2 w(f) + \left[\frac{I''(V_0)}{2} \right]^2 \int_{-\infty}^{\infty} \\ &\quad w(x)w(f-x) dx, \end{aligned} \quad (A.5)$$

where $w(f)$ is the power spectrum of V_n and we define $w(f)$ for negative f by

$$w(-f) = w(f).$$

Assume that $w(f)$ has a constant value w_0 over a bandwidth Δf_c centered at f_m and is zero everywhere else. Then we have

$$\langle V_n^2 \rangle_{AV} = w_0 \Delta f_t.$$

Area of Eq. (A.5) under these conditions is given in Fig. 4. The area under the low-frequency portion of the spectrum must give

$$\langle I_{ac}^2 \rangle_{AV}:$$

$$\langle I_{ac}^2 \rangle_{AV} = \left[\frac{r^n(V_0)}{2} \langle V_n^2 \rangle_{AV} \right]^2. \quad (A.6)$$

Note that Eq. (A.6) is the same as Eq. (21).

The factor α as previously defined is the ratio of the cross-hatched area to the total low-frequency area. From geometrical considerations it is readily ascertained that

$$\alpha = \frac{\Delta f}{\Delta f_t} \left[2 - \frac{\Delta f}{\Delta f_t} \right]. \quad (A.7)$$

Appendix B: Derivation of Equation (34)

Eq. (34) can be derived by setting up the equivalent circuit for the video-crystal and following a procedure quite similar to that in deriving Eq. (31). However, for the sake of brevity, let us generalize from the results of the preceding work in a way which will allow us to arrive at the solution much more rapidly.

The signal voltage at the output of the video-crystal is given by³

$$V_s = \beta P_{ST} R, \quad (B.1)$$

where

- β = current sensitivity
- $P_{ST} = P_{si}$ (signal power out of the traveling-wave tube)
- R = barrier resistance of the crystal (in this appendix only).

Eq. (B.1) corresponds to Eq. (10) in the previous development.

There are two sources for the noise at the output of the video-crystal:

- (1) The noise due to the crystal.
- (2) The noise at the output of the traveling wave tube.

The mean-square of the noise voltage due to the crystal is³

$$\langle V_{NX}^2 \rangle_{AV} = 4KT \Delta f \frac{\beta^2 R^2}{M^2}. \quad (B.2)$$

The mean-square value of the noise voltage due to the second source can be arrived at by comparing Eq. (10) with Eq. (26). A generalization based on such a comparison indicates that the mean-square noise voltage at the output of the video-crystal due to the noise from the traveling-wave tube can be written

$$\langle V_{NT}^2 \rangle_{AV} = \alpha [\beta P_{NT}^2]^2 \quad (B.3)$$

where $P_{NT} = FK T \Delta f_t$ (the noise at the traveling-wave tube output). A step-by-step analysis confirms the correctness of (B.3) and shows that for square-law detection α has the same value as in Eq. (27).

By equating V_s^2 with the sum of $\langle V_{NX}^2 \rangle_{AV}$ and $\langle V_{NT}^2 \rangle_{AV}$ and solving for P_{si} , we obtain

$$P_{sim} = \left[\frac{4KT \Delta f}{\beta^2 R^2} + \alpha (FK T \Delta f_t)^2 \right]^{1/2}. \quad (B.4)$$

References

1. W. C. Harn and J. F. Metcalf, "Velocity-modulated tubes," *Proc. I.R.E.*, vol. 21, pp. 107-116; February, 1939.
2. F. W. L. Robinson, "Velocity-modulated detector," *Wireless Engineer*, vol. 29, pp. 200-202; August, 1952.
3. H. G. Torrey and C. A. Whitmer, "Crystal rectifiers," *R.I.T. Radiation Laboratory Series*, vol. 19, McGraw-Hill Book Company, Inc., New York, N.Y., pp. 345-347; 1946.
4. J. R. Pierce, "Traveling-Wave Tubes," D. Van Nostrand Company, Inc., New York, N.Y., 1950.
5. S. C. Rice, "Mathematical analysis of random noise," *Bell Sys. Tech. Jour.*, vol. 24, pp. 46-156, Eq. (3.10-2?); 1945.
6. *Ibid.*, Eq. (3.7-10).
7. *Ibid.*, esp. p. 124.
8. *Ibid.*, p. 132.
9. *Ibid.*, p. 49.
10. *Ibid.*, p. 137.

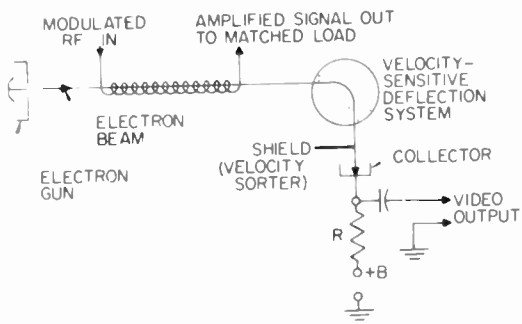


Fig. 1

Diagram of a traveling-wave-tube video detector which employs a velocity-sensitive deflecting field.

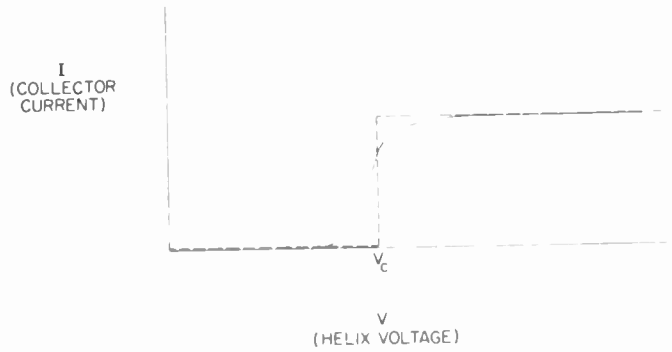


Fig. 3

Plot of collector current vs helix voltage. V_c is the helix voltage corresponding to the critical electron velocity, i.e., the velocity corresponding to the position of the knife edge of the shield.

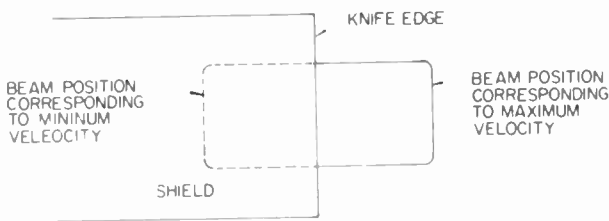


Fig. 2

Time-integrated cross section of beam at shield position.

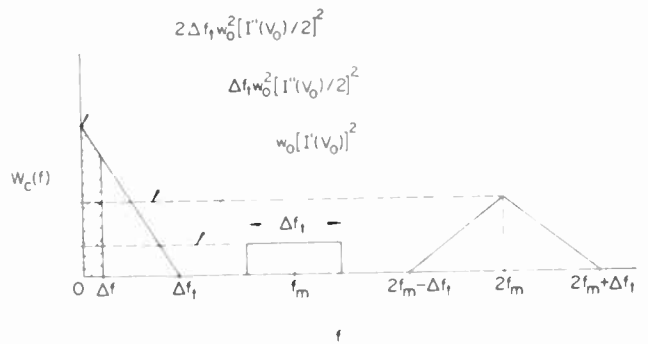


Fig. 4

Continuous-power spectrum of the output of the nonlinear device.

A TIME-SAMPLING AND AMPLITUDE-QUANTIZING TUBE

R. P. Stone, C. W. Mueller, and W. M. Webster

Radio Corporation of America
RCA Laboratories Division
Princeton, New Jersey

Summary

The possibility of a saving of bandwidth - or of transmitting additional information in a given bandwidth - by means of amplitude quantizing and time sampling is reviewed. The requirements on a tube to simultaneously time sample and quantize a video input, and to produce a residue output, are outlined.

Beam deflection type tubes were successfully built and tested which perform all of these functions. They will change a continuous signal into a quantized signal having six discrete amplitude levels. The signal may also be simultaneously sampled as often as ten million times per second. A residue signal is also generated. The tube response is sufficiently accurate to meet the requirements of the system outlined. The stability of operation is such that after initial set-up no critical operating conditions or adjustments are involved.

Two types of output structure have been used, both of which permit the external adjustment of the output amplitude levels. The tube operates with an anode voltage of 300 volts. While the useful beam current is only 55 microamperes, the signal-to-noise ratio of the tube is computed to be 80 db.

Introduction

The portion of the electromagnetic spectrum which can be used for communication is limited. It is therefore highly desirable to reduce the required bandwidth of each communication channel as much as possible. Until recently, it was believed that the bandwidth of a communications channel must be at least as great as the highest frequency component in the information to be transmitted. However, recent developments in communication theory indicate the possibility of exchanging transmitter power for bandwidth, providing one is willing to eliminate the transmission of superfluous information.¹⁻⁸

Information can be squeezed into a narrower channel than that conventionally required and thus save valuable bandwidth providing (1) the transmitter power is increased, (2) a coding system

is included in the transmitter and receiver, and (3) some loss in accuracy of signal level definition is tolerated. The third condition is not severe, since noise is always present and the individual at the receiver cannot detect inaccuracies providing they are sufficiently small.

In order to facilitate the discussion and description of the sampling and quantizing tube we will first describe a transmission system in which it might be used and which conforms to the conditions listed above. This system will be capable of transmitting two signals simultaneously over a channel which would normally only accommodate one.

Description of Transmission System

In order to separate two signals which are being transmitted over a single channel, we must do something to at least one of these signals which will enable the receiver to distinguish between them. In this case, we will permit one of them (Signal A) to exist only at certain discrete amplitude levels. This is called quantization in analogy with the energy states of atomic physics. If the receiver finds that the incoming signal has at any moment an amplitude different from one of the discrete levels of signal A, it concludes that the signal A amplitude is at the next lower allowed level of the discrete set, and that the difference between the received signal and this allowed value for signal A gives information as to the amplitude of signal B.

Obviously, to perform quantization on a signal, a device whose output vs. input characteristics looks like a staircase must be used. As the input signal varies continuously from zero to maximum value, the output signal must jump from one discrete level to the next in an abrupt fashion.

However, simply quantizing one of the signals and compressing and adding the other is not enough. Obviously, to transmit the combined signal would require a very broad bandwidth, since any rounding off of the quantum jump of signal A caused by circuits with insufficient high frequency response will

result in an appreciable error in signal B.

The problem is essentially that of eliminating the effect of transients produced by the quantum jumps of signal A on the apparent value of signal B. This can be done in several ways; one of the simplest is used in this system and is called "time sampling" or just "sampling".

Time sampling amounts to a periodic measurement of the amplitude of a signal, such as the combined quantized signal A and signal B. It has been shown that if the resultant pulses occur at the proper rate and are passed through appropriate filtering circuits, a continuous wave results which has no frequency components higher than the highest frequency component in either signal A or B. At the receiver, sampling this wave at the same rate as before gives pulses proportional to the desired signal ($A_q + B$).

Signals A_q and B are separated at the receiver by a device which is nearly identical to the quantizer used in the transmitter. The combined signal $A_q + B$ is requantized. As before, only certain amplitude levels are allowed and the output signal is again the quantized signal A_q . Subtracting this output signal from the input signal gives a residue signal, which is signal B.

Thus, for example, we may take two television picture signals, quantize one of them with some loss in accuracy of half tone reproduction, combine them and transmit them over a channel with a bandwidth no greater than that which would be required for one of them alone. Furthermore, we are able to separate the signals at the receiver with essentially the same device as we used to combine them at the transmitter, and display the two television pictures independently.

A tube has been described by Sears⁹ which performs the functions of quantizing and producing a coded signal. However, to accomplish all the above operations in both the transmitter and receiver, a special tube was designed and constructed. It may be used to sample and quantize the input signals in the transmitter, or to sample and separate the two signals in the receiver. It is to be noted that in both the transmitter and receiver a very wide bandwidth must be maintained between the operations of sampling and quantizing or separating in order that the system work properly. In order to eliminate very wide band circuits, the tube was designed to accomplish both operations almost simul-

taneously.

The Coding Tube

Fig. 1 shows the essential design of the sampling and quantizing tube, or coding tube, and its operation will be described with reference to this figure. A cathode and beam forming structure produces a thin, flat electron beam which passes down the length of the tube. A pair of deflection plates to which is applied a sampling signal sweeps this beam back and forth across a narrow slit. Only when the beam is centered on the slit will electrons pass through to the rest of the tube. Thus, short pulses of electrons are formed. The sampled beam passes between the signal deflection plates and is deflected up and down across the quantizing structure. As shown, this consists of a flat aperture plate in which a step-shaped opening has been punched. If the beam is of essentially constant current density across its width, the current which passes through the aperture increases in abrupt steps as the input signal moves the beam down the quantizing aperture assembly. The beam current which passes through the step-shaped hole is collected and constitutes the quantized output signal. A series of triangular apertures permit a current which is proportional to the difference between the input signal and the quantized signal to be collected on an electrode designated as the residue collector. This signal is used in the receiver.

In addition to deflecting the electron beam, as has been described, both sets of plates serve as lens structures for focusing the beam in the proper fashion. This is accomplished by externally adjusting the d-c biases on these plates. The beam is focused by the sampling deflection plates onto the slit and by the signal plates onto the target structure.

Parts from beam deflection tubes¹⁰ were used to form the beam and accomplish the sampling deflection. The beam thus formed has a thickness of a few thousandths of an inch. However, the width of the sampling aperture determines the effective beam width beyond that point, and this was four thousandths of an inch. Since the imaging action of the signal deflection plates constitutes a lens of a 1:1 magnification, the effective beam thickness upon incidence on the output structure was approximately four thousandths of an inch.

It was noted that a small deviation from the ideal quantizing characteristic will produce a large error in

signal B when it is separated at the receiver. Thus, it is important that the steps be "flat" and that the amplitude difference between steps be constant. Due to the finite thickness of the beam, a certain amount of rounding is to be expected at the step edges. The amount of rounding which can be tolerated determines the ratio of beam thickness to step dimensions. The practical difficulty of forming an electron beam which has uniform (or even predictable) current density across its width is such as to require some mechanism to adjust the current collected by each quantum step independently and externally.

Two methods were employed to correct for non-uniformity in beam current density. The first of these permits one to correct the current gathered by each quantum step in either an additive or subtractive direction, by means of secondary emission between the collector and a set of correcting wires.

The secondary emission ratios of the quantized collector and the correcting wire were not always constant along the length of the structure. As a result, if one applied a saw-tooth wave to the input structure, the output wave could be adjusted for equal step heights, but it did not necessarily have perfectly flat steps.

A typical input-output characteristic, such as recorded from a tube of the sort just described, is shown in Fig. 2. The roundness of the steps, which is due to the finite width of the beam, is not excessive from the standpoint of the system accuracy. However, it will be noted that the steps are by no means flat.

The residue signal, i.e., the current which passes through the triangular shaped holes, is collected by a small wire which runs through a U-shaped suppressor electrode behind the quantizing aperture plate. The current which passes through the triangular hole is proportional to the width of the triangular hole at the point where the beam passes.

In order to obtain flatter steps, the correcting structure illustrated in Fig. 3 was designed. In this case, the correcting wires serve only to deflect the beam toward or away from the aperture fins which are attached to an aperture plate similar to the one previously described. Suppressor wires are included to minimize the effect of secondary electrons which are generated on the aperture plate and correcting wires and

thereby prevent them from reaching the quantized output electrode. If the potential of a given correcting wire is the same as the potential of the aperture plate, the beam which passes through that section remains relatively undisturbed and arrives at the quantized output electrode. If, however, the potential of the correcting wire is negative with respect to the fins on the aperture plate, a large proportion of the current passing through the aperture plate is deflected and strikes the fins, thus diminishing the current which reaches the output electrode. In this way it is possible to decrease continuously the current through each slot. Notice that the slots are of varying width. This was done in an effort to pre-adjust for non-uniformities in the beam current density since the beam current density would be the greatest at the center and the least at the edges.

Fig. 4 shows the output of the revised quantizing structure, and it will be noted that the steps are of essentially equal height and are extremely flat. The rounded portion of the step is less than 10% of the step width. Since the beam thickness was four thousandths of an inch and the step of the aperture plate was forty thousandths of an inch, this rounding was to be expected.

Some features of the tube can be seen in the Fig. 5. In order to shield the output from the input, all the leads from the electron gun structure and both sets of deflection plates were brought out through one end of the tube and the output leads and the individual leads to the correcting wires brought out the other end. The region of the electron beam is surrounded by a cylindrical shield, and a mesh shield surrounds the output leads, in order to further shield the input from the output.

Performance Data

In the preceding section describing the operation of the coding tube, many of the features of its mechanical design were discussed. In this section typical operating conditions will be described.

The tube operates under the following conditions:

Heater	6.3 volts	.3 amp.
Cathode		0 volts
Beam Forming Structure		300 volts
Sampling Deflection Plates		165 volts
Sampling Slit		300 volts
Signal Deflection Plates		75 volts
Aperture Plate		300 volts

Under these conditions of operation the total current drawn from the cathode is of the order of 10 milliamps., of which about 7 milliamps. goes directly to the beam forming structure in the process of collimating the beam. The actual current in the flat electron beam is of the order of 100 microamps. At the point of focus, this beam is about .004 inch thick and .300 inch wide.

When the beam is not modulated and is adjusted to fall on the largest step opening in the aperture plate, a current of about 55 microamps. reaches the quantized collector output. This indicates a current of 11 microamps. per unit step of the quantized output. The current through the widest part of a residue triangle is 10 microamps.

This largest step opening in the aperture plate has a dimension of .190 inch parallel to the width of the beam. The residue openings are right isosoles triangles .040 inch on a side. The height of each step opening, in the direction of the thickness of the electron beam, is also .040 inch. For the six levels involved in this tube, the total deflection required of the electron beam is thus .240 inch.

The deflection sensitivity is such that a voltage of about 35 volts rms applied to the signal deflection plates will swing the electron beam over the whole step pattern on the aperture plate. The sampling voltage required on the first deflection plates is of the order of 6 volts rms to produce pulses with a duty cycle of about 10%. These signal voltages are applied push-pull to the deflection plates and are super-imposed on the DC focusing voltages applied to these plates.

The correcting wires were operated so that they were individually adjustable over a range of 45 volts. They were each adjusted in a manner to best equalize the step amplitude in the output.

The tubes were operated successfully with a 5 megacycle sampling voltage and a television video signal on the signal deflection plates.

Signal-to-Noise Ratio

If the predominate source of noise in the tube is presumed to be due to shot effect in the electron beam, and noise sources following the tube are neglected, the approximate peak signal to noise ratio may be readily computed. For typical operating conditions, with a maximum collector current of 55 microamperes and a bandwidth of 4 megacycles, the signal-to-noise ratio is about 80 db.

This signal-to-noise ratio should not cause appreciable degradation of the signal.

Conclusions

Beam deflection type tubes have been successfully built and tested which simultaneously perform the functions of time sampling and amplitude quantizing of a video input, and producing a residue signal.

The tubes were operated successfully with a 5 megacycle sampling voltage and a television video signal on the signal deflection plates.

The work which has been described was done at the RCA Laboratories in Princeton, N. J. The project was carried out on a research basis. The tubes were hand made in our Laboratory Tube Shop, and are not commercially available, at present.

References

1. F. Okolicsanyi - British Patent 505,673, May 11, 1939.
2. D. Gabor - "Theory of Communications", Journal of Institute of Electrical Engineers (British), Vol. 93, p. 429, Sept. 1946.
3. N. Wiener - "The Extrapolation, Interpolation and Smoothing of Stationary Time Series", Cambridge Technology Press, 1949.
4. C. E. Shannon - "Communication in the Presence of Noise", PIRE, Vol. 32, p. 10, January 1949.
5. W. G. Tuller - "Theoretical Limitations on the Rate of Transmission of Information", PIRE, Vol. 37, p. 468, May 1949.
6. G. C. Sziklai and A. V. Bedford, U. S. Patent 2,664,463.
7. G. C. Sziklai, U. S. Patent 2,643,289.
8. G. C. Sziklai, U. S. Patent 2,617,879.
9. R. W. Sears, "Electron Beam Deflection Tube for Pulse Code Modulation", Bell System Technical Journal, Vol. 27, p. 44, January 1948.
10. E. W. Herold and C. W. Mueller - "Beam Deflection Mixer Tubes for UHF", Electronics, May 1949.

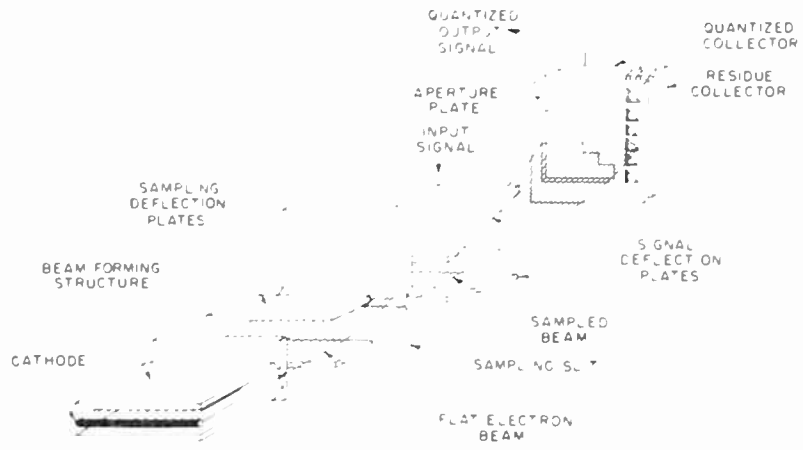


Fig. 1
Arrangement of the Elements in the
Sampling and Quantizing Tube.



Fig. 2
Output of Quantizing Tube as
Observed on Scope.

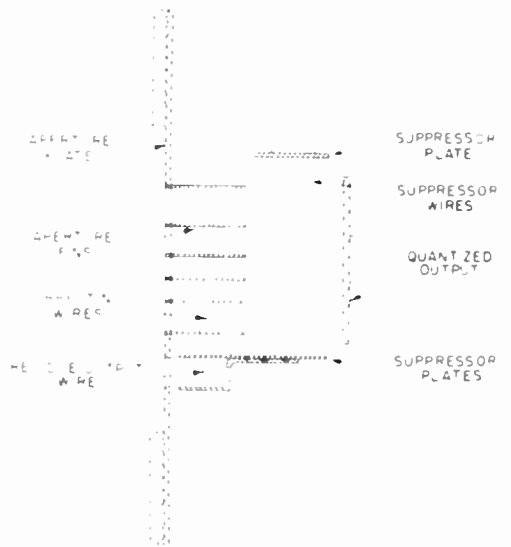


Fig. 3
Revised Target Assembly.

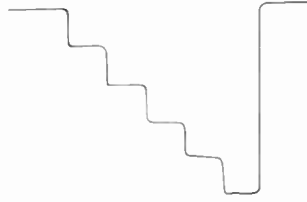


Fig. 4
Quantized Output as Observed on Scope
With Optimum Adjustment of Correcting
Wires.

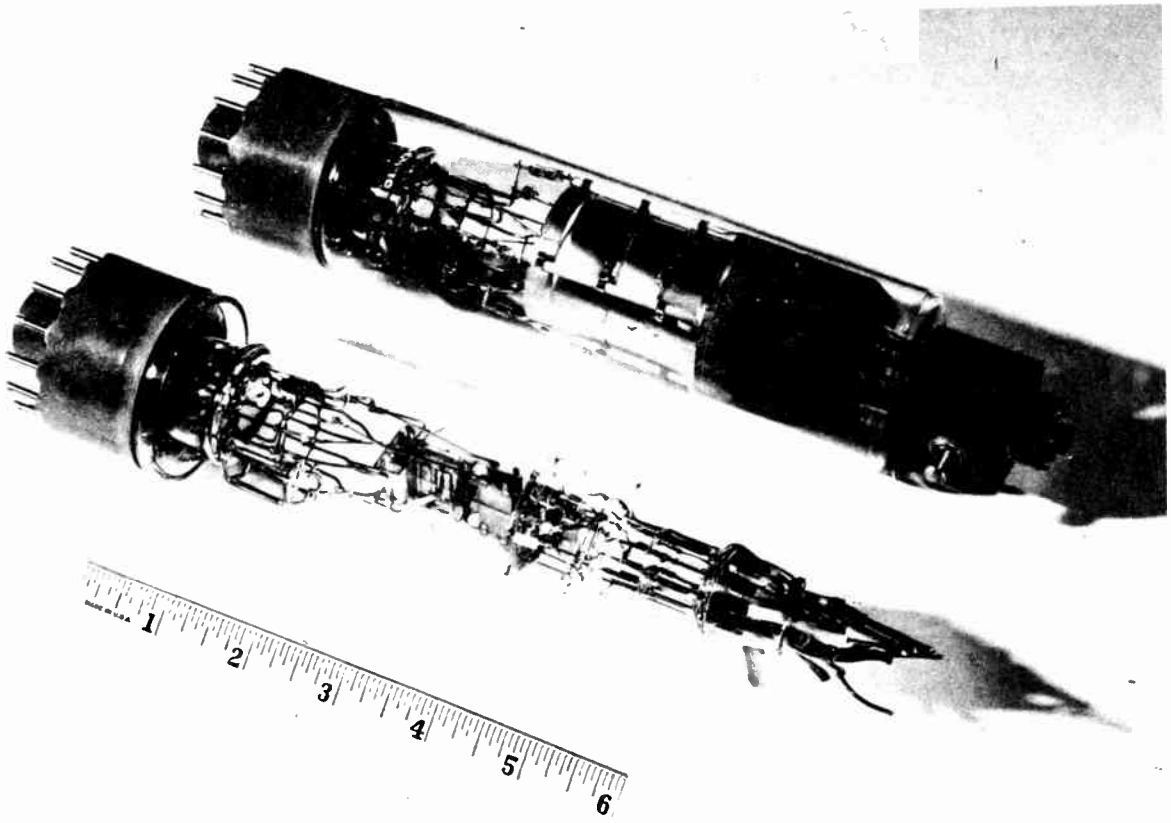


Fig. 5
Photograph of Time Sampling and
Amplitude Quantizing Tube.

CATHODE-RAY TUBE WITH SINGLE STEP INTENSIFIER

Jenny E. Rosenthal
A. B. Du Mont Laboratories, Inc.
Passaic, N. J.

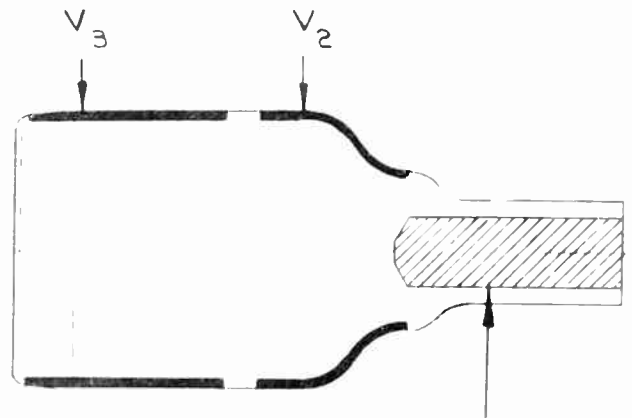
Summary

This report describes the techniques used in the design of cathode-ray tubes with single step intensifier. The fields corresponding to different electrode shapes are shown in terms of field plots. In the experimental tubes built on the basis of these plots part of the third anode is constituted by a truncated cone. Data are given on the tubes and it is shown how pincushion or barrel distortion of the raster may be eliminated by suitable design and positioning of the truncated cone with respect to the other components of the tube.

This investigation concerns the following problem in electrostatic CR tubes:

To form a bright picture on the screen of a CR tube at moderate beam currents, the electrons impinging on the screen must have a high velocity, preferably over 10 KV. If a voltage in excess of 10 KV is put on the second anode, the electrons enter the deflection system at a high velocity and thus require a much higher deflection voltage than is usually practical. For example, to scan a 12" face plate 16" away from the front deflection plates requires about 1.5 KV deflection voltage at 5 KV anode voltage and twice that at 10 KV. To keep the deflection voltage low, the beam must be accelerated after going through the deflection system, which is accomplished by putting the high voltage on a third anode. The simplest arrangement of this type shown in Fig. 1 has a serious drawback: If V_2 and V_3 are the second and third anode voltages respectively (referred to the cathode as zero), then for $V_3/V_2 > 2$ the raster is no longer rectangular but shows either pincushion or barrel distortion caused by the electron lens formed by the two cylinders at different potentials. The difficulty has been avoided in tubes available at present by using a multiplicity of accelerating electrodes so that the voltage ratio between two successive ones can be kept low even though the voltage on the final electrode is at least 5 times that on the second anode. The rasters obtained in this fashion have been satisfactorily free of distortion. However, for certain applications the multiplicity of accelerating voltages is not acceptable from the circuit point of view. A differ-

ent type of electron lens is needed to eliminate the distortion.



gun and deflecting system

Fig. 1 Simplest type of single step intensifier.

The most direct way to attack the problem is to solve Laprange's equations of motion for an electron in an arbitrary axially symmetrical field, then find what conditions must be imposed on the field in order that a rectangular raster may be formed on the screen. Unfortunately mathematical techniques have not quite reached the point where this could be done, therefore I have been forced to improvise approximate design techniques based on the following analysis:

The potential field due to two coaxial cylinders of identical radius kept at different potentials is well known if the two cylinders are long and the spacing between them negligible as compared to the cross-section. Fig. 2 gives the different equipotential lines of this field in percent of the potential difference, one cylinder being at 0 and the other at 100%. The lines are not uniformly spaced, e.g. the maximum distance between the 80% and 70% lines is considerably larger than that between the 70% and 60% lines. Furthermore, the field is quite spread out, the distance along the axis between the 10% and 90% lines being larger than the diameter of the cylinders. This field is equivalent to a thick lens.

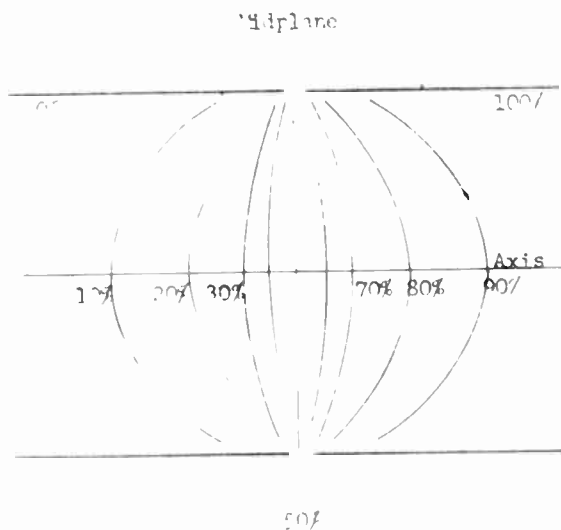


Fig. 2 Potential distribution in the symmetrical two-cylinder lens.

From analogy with the optical case we may conclude that in order to minimize the distortion of the electron path in the accelerating field, and hence to minimize the distortion of the raster shape, the lens should approximate a thin lens. The thin lens condition imposes the following distribution of equipotential lines at the junction of the potential regions formed by the second and third anodes respectively:

The lines corresponding to the range of 10% - 90% of the accelerating potential should cover as narrow a range of space as possible and should be as uniformly spaced as possible.

The basic problem therefore is to investigate the potential fields produced by electrodes of different shapes to find the field most closely approximating the one postulated. I hope shortly to complete a mathematical technique, which will permit to calculate potential distributions for axial symmetry problems to a satisfactory degree of approximation. In the meantime, since the straight-forward method of using an electrolytic tank is extremely laborious, we have resorted to 2-dimensional field plots. Of course, these field plots give the exact potential distribution only for problems where one electrode dimension is extremely large as compared with the others and where all the cross-sections perpendicular to this long dimension are identical. Thus strictly speaking all the drawings in Fig. 3 represent potential distributions where the electrodes are perpendicular to the plane of the drawing and infinitely

long in that direction. However, we proceeded on the assumption that the general potential distribution features would be the same if the plane of the drawing represented the cross-section (containing the axis) through a system with axial symmetry.

The electrode shapes investigated in these plots were chosen on the basis of the following considerations:

The rather extensive information available on electron lenses suggests that the desired type of field would be realized if at the junction of the potential regions formed by the second and third anodes, the diameter of the latter anode were smaller than that of the former. Probably the simplest design to embody this feature is one where the accelerating electrode terminates in a truncated cone. Fig. 3 shows characteristic field plots obtained using this type of accelerating electrode. The shape of the truncated cone and its position relative to the other electrode is varied from plot to plot. To make possible a more direct comparison with experiment, the low voltage electrode in every case follows the actual outline of the dagged portion of the tube neck. For the sake of comparison the limiting case is included where the two electrodes have the same diameter at the junction of the two potential regions.

The data shown in Fig. 3 confirm the premise that the use of a truncated cone will result in a thinner and stronger lens i.e. that the range corresponding to 10% - 90% of the accelerating potential will be shortened and that the lines corresponding to equal increments of potential will be spaced more uniformly.

It is interesting to note that the potential distribution in the region which would be traversed by the electron beam is practically unaffected by small changes in the relative position of the two electrodes i.e. whether the two terminate on the same transverse plane, or whether the truncated cone penetrates inside the low voltage electrode.

The results obtained by means of the field plots were considered sufficiently encouraging to warrant building experimental 5" tubes embodying the truncated cone shape for the third anode. The envelopes, gun structures, and deflecting systems were the same as used in the regular 5" intensifier "multiband" tubes. The factors that were varied in the construction were the dimensions of the truncated cones, their location in the tube, and the height of the dagging on the neck. The truncated cones were manufactured

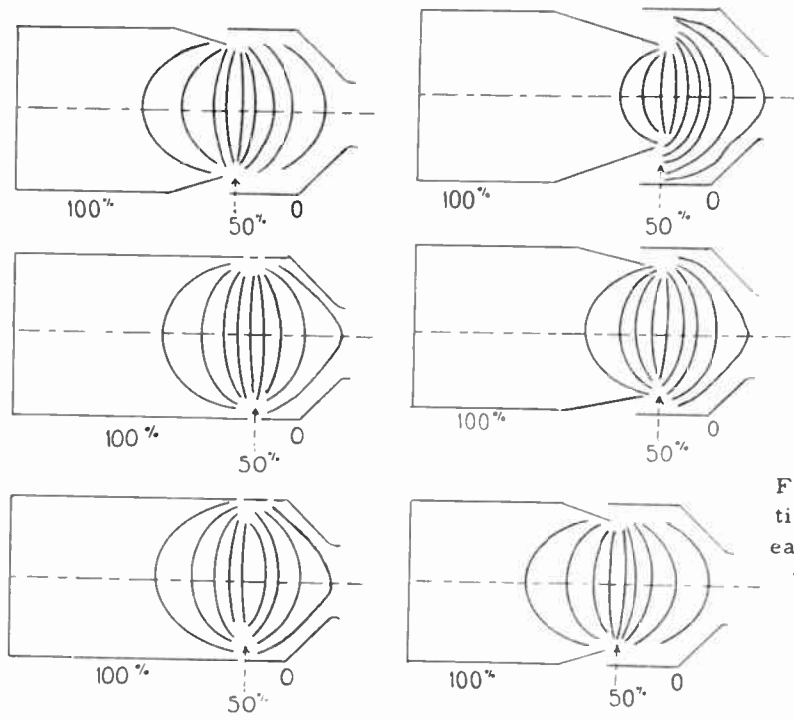


Fig. 3
Field plots for various electrode configurations. The equipotential lines are given for each 10% of the potential difference between the electrodes for the range 10% - 90%.

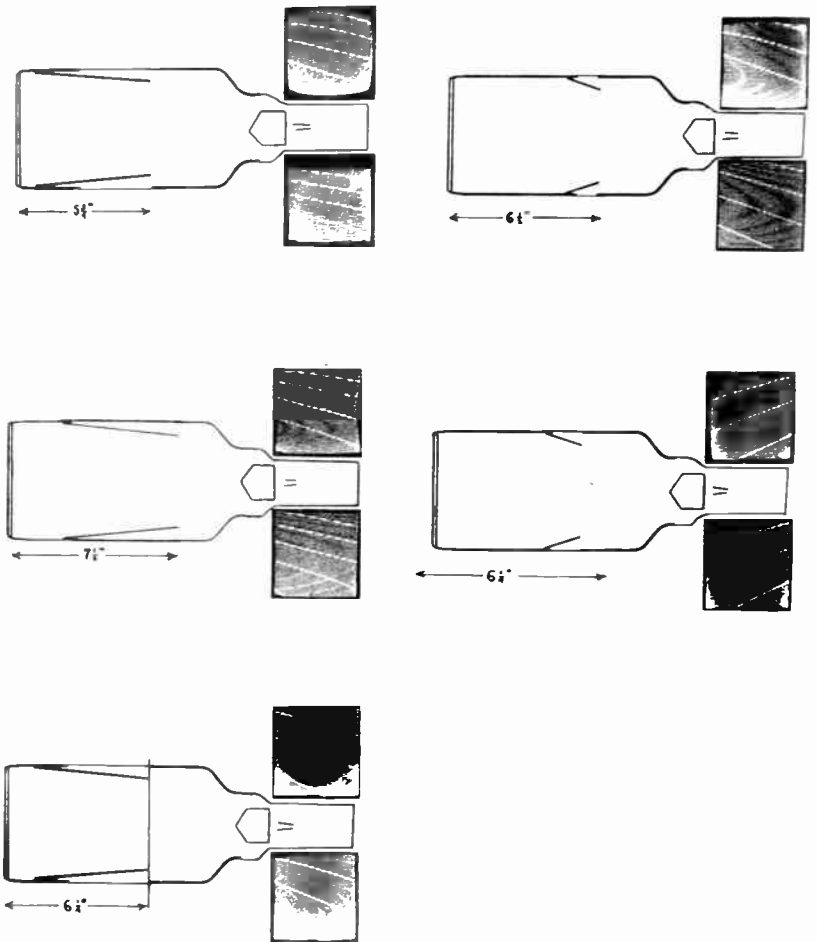


Fig. 4
Experimental tube structures and corresponding raster shapes.

with special care to avoid any sharp edges at the junction of the two potential regions.

Truncated cones with the following dimensions were used:

height	5"	3"	1.5"
top diameter	4"	3"	4"

The bottom diameter was 5" in each case to make contact to the dag coating. The schematic of various tubes built is shown in Fig. 4. The face plate of the tubes was aluminized to reproduce the closed cylinder condition investigated in the field plots.

Alongside each structure shown in Fig. 4 are photographs of two rasters, each 2" x 2", formed on the face plate of the corresponding tube for the voltage ratios $V_3/V_2 = 2$ and $V_3/V_2 = 5$ respectively. (V_2 and V_3 are the voltages on the second and third anode). Any distortion connected with scanning by the front plates will manifest itself in the departure of the sides of the raster from a straight line, while similarly the top and bottom of the raster will be affected by any distortion connected with scanning by the back plates. The photographs show that none of the structures exhibit any appreciable distortion for the lower value of the voltage ratio. The following facts have been definitely established as regards the shape of the raster at the higher ratio:

As far as the distortion connected with scanning by the front plates is concerned, the most important factor is the distance between the deflection plates and the third anode. Placing the truncated cone at different positions starting close to the face plate and progressing toward the deflecting system gradually changes the raster sides from barrel to pincushion. The optimum position when neither distortion affects the raster sides appears to be very critical. No tube has been built as yet where it is satisfied exactly, however, the structure in the lower left-

hand corner of Fig. 4 is a fair approximation. The shape of the truncated cone is not critical though every design has a different optimum position.

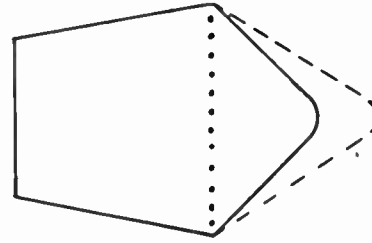


Fig. 5 Shape of front deflection plates

The shape of the deflection plates has no appreciable effect on the shape of the raster. The standard front deflection plates used are dome-shaped as shown in Fig. 5, which should allow for greater sensitivity at the center. However, when the truncated cone is in such a position as to give barrel-shaped sides, cutting off the domed portion of the plates along the dotted line in Fig. 5 does not diminish the extent of the barreling. On the other hand, when the position of the third anode is such as to give a pincushion effect, this is not corrected by accentuating the doming, e.g. by making the plate conform to the dashed line in Fig. 5.

As far as the distortion connected with scanning by the back plates is concerned, if it occurs, it is of the barrel type in all the tubes built. No pincushioning has been observed on the top and bottom of any raster. The factor that appears to have the greatest importance in controlling it and which is quite critical is the spacing between the end of the deflecting system and the height of the dag on the neck of the tube.

On the basis of the information obtained from these experimental tubes we believe that we know how to construct a single step intensifier so as to eliminate distortion. The problem is whether a tube requiring such close tolerance is economically practical in production.

A NEW HIGH EFFICIENCY PARALLAX MASK COLOR TUBE

M.E. Andursky, R.G. Pohl and C.S. Szegho
Research Department
The Rauland Corporation
Chicago 41, Illinois.

Summary

Electron transmission through parallax masks of present day tri-color tubes is no greater than 12%, with a consequent low picture brightness. This paper describes a new tube employing a parallax mask maintained at a potential much lower than that of the screen and a collector mesh maintained at anode potential intermediate to the screen and mask potentials; the brightness of the tube is increased 3-4 fold by virtue of enlarged mesh holes and the ensuing post-deflection focusing. In addition, secondary emission from the mask, which would dilute color, is minimized. In contrast to other post-accelerating tubes, the mask holes and fluorescent screen dots are uniformly spaced over the entire target area. 19" round and 24" rectangular tubes incorporating the new principle have been built.

Introduction

Color picture tubes have run through the gamut of size in a remarkably short time when compared with monochrome tubes¹, thus creating a brightness problem. Adequate light output on a 250 square inch screen can only be achieved, even with three guns, by raising the anode voltage well above the levels used in monochrome tubes. With one gun, the brightness leaves much to be desired. The reason for this, of course, is that the customary shadow-masks have only approximately 10% electron transmission, 90% of the electrons being intercepted by the mask. It has been suggested early in the development of color tubes² to employ post-deflection focusing which permits enlargement of the apertures in the shadow-mask and so increases brightness in the ratio of the increase in electron transmission. The usual practice in post-deflection focusing is to provide an accelerating field between the barrier electrode and the aluminum-backed tri-phosphor screen. The apertures in the barrier electrode followed by the field form an array of tiny electron lenses which focus an electron beam scanning this lens raster down to a fraction of the area of a phosphor element. Certain drawbacks of this customary scheme will now be explained and it will be shown how they can be overcome by a different configuration of the electric field.

Post-Acceleration Tube with a Single Field

In a tube with an accelerating field between the shadow-mask and the screen, the beam arriving from the center of deflection follows a parabolic path in that field and is bent toward the normal to the mask. As shown in Figure 1, the electron beam appears to come, after refraction, from a point O' displaced from the center of deflection O . In tubes without post-acceleration the screen elements are usually of equal size uniformly distributed over the screen area and are laid down by methods utilizing straight optical projection from a point which coincides with the center of deflection of the electrons. If the degree of refraction introduced by post-acceleration were constant, the screen for the tube with the accelerating field could still be made by optical projection using an optical center different from the center of deflection. In reality, with increasing deflection angles the beam appears to originate from different points (O' , O'' , etc.) because it is refracted by larger amounts; consequently, if the screen elements are of equal size, at large angles the beam no longer hits the proper phosphor elements. The situation is analogous to spherical aberration in optics and may conceivably be compensated by using an aspherical lens inserted in the optical path during the photographic part of the process of screen fabrication, to change the center-to-center distance of the phosphor elements. Another, but even more complicated method, is to utilize electron exposure of the emulsions which are used in screen fabrication. One would then have to provide the same accelerating field for the exposing beam as in the final tube. In practice, complete compensation by this method is difficult and at large deflection angles color purity is bound to suffer.

Another drawback of post-deflection focusing with a single accelerating field is that secondary electrons released by the bombardment of the mask are drawn to the screen. As shown in Figure 1, the secondaries which start out from the vicinity of an aperture in the mask do not follow the angle of deflection of the primary beam but are drawn to the screen orthogonally. In monochrome tubes, this secondary electron stream limits detail contrast³; in color tubes it also dilutes color.

The Principles of a Post-Acceleration Tube with Retarding and Accelerating Fields

By providing a retarding field on the cathode side of the mask, in addition to the accelerating field between the parallax mask and screen, the electron trajectories can be altered to make the beam go through the same point on the mask and land on the same phosphor element as it would in the straight parallax case for all deflection angles, since the center of deflection of the electron beam may be made identical with the center of parallax. Consequently, the screen can be fabricated by the customary straight-line optical projection methods with the mask apertures and screen elements uniformly spaced. The new structure then consists of an auxiliary mesh electrode at anode potential, V_a , followed by the parallax mask at a potential V_p lower than that of the anode and the screen, with the latter at a potential V_s much higher than the anode.

The electron paths in the tube with both retarding and accelerating fields are shown in Figure 2. The electron trajectory may be considered as having three parts. In region I, between the center of deflection and the mesh, the trajectory is straight; in region II, between the mesh and the parallax mask, it is a parabola convex with respect to the tube axis; and in region III, between the mask and the metal-backed screen it is a parabola concave toward the axis. The necessary operating relationships between electrode potentials and spacing for the proper position of the beam on the screen can be derived from geometrical, energy, and transit time considerations. Definitions of the symbols used in the derivations appear in the glossary.

Conventional magnetic deflection is used; consequently, in region I the electron speed is constant. Therefore, from the energy equation

$$v_{x,1}^2 + v_{y,1}^2 = \frac{2e}{m} V_a \quad (1)$$

$$v_{x,1} = \left(\frac{2e}{m}\right)^{\frac{1}{2}} V_a^{\frac{1}{2}} \cos \varphi \quad (2)$$

$$v_{y,1} = \left(\frac{2e}{m}\right)^{\frac{1}{2}} V_a^{\frac{1}{2}} \sin \varphi \quad (3)$$

As the two electric fields between the auxiliary mesh and the parallax mask, and between the mask and the screen have no components perpendicular to the axis, the vertical component of the electron velocity is constant in the three regions. Consequently

$$v_{x,2,p}^2 + v_{y,1}^2 = \frac{2e}{m} V_p \quad \text{and}$$

$$v_{x,2,p} = \frac{2e}{m} \left[V_p - V_a \sin^2 \varphi \right] \quad (4)$$

In a uniform field, in which acceleration is constant and is directed horizontally, the average horizontal component of velocity during any time interval equals one-half of the sum of the horizontal velocity at the beginning and at the end of the interval. Therefore,

$$\bar{v}_{x,2} = \frac{1}{2} (v_{x,1,a} + v_{x,2,p}) = \frac{1}{2} \left(\frac{2e}{m}\right)^{\frac{1}{2}} \left\{ V_a^{\frac{1}{2}} \cos \varphi + \left[V_p - V_a \sin^2 \varphi \right]^{\frac{1}{2}} \right\} \quad (5)$$

Since the transit time in region II is equal to $\frac{b}{\bar{v}_{x,2}}$, the difference of the ordinates

of the points where the scanning beam intersects the parallax mask and the auxiliary mesh is:

$$\frac{p-a}{p-a} = \frac{b}{\bar{v}_{x,2}} \frac{v_{y,1}}{v_{x,2}}$$

$$= \frac{b \left(\frac{2e}{m}\right)^{\frac{1}{2}} V_a^{\frac{1}{2}} \sin \varphi}{\frac{1}{2} \left(\frac{2e}{m}\right)^{\frac{1}{2}} \left\{ V_a^{\frac{1}{2}} \cos \varphi + \left[V_p - V_a \sin^2 \varphi \right]^{\frac{1}{2}} \right\}}$$

$$\frac{p-a}{p-a} = \frac{2b}{\cot \varphi + \left[\frac{V_p}{V_a} \csc^2 \varphi - 1 \right]^{\frac{1}{2}}} \quad (6)$$

We require that the beam go through the same point of the mask in the tube with the retarding and accelerating fields as in the straight parallax tube; consequently:

$$(r+b) \tan \theta = r \tan \varphi + \bar{p}-\bar{a}$$

$$= r \tan \varphi + \frac{2b}{\cot \varphi + \left[\frac{V_p}{V_a} \csc^2 \varphi - 1 \right]^{\frac{1}{2}}} \quad (7)$$

In region III, from similar reasoning

$$\frac{s-p}{s-p} = \frac{d}{\bar{v}_{x,3}} \frac{v_{y,1}}{v_{x,3}}$$

$$= \frac{d \left(\frac{2e}{m}\right)^{\frac{1}{2}} V_a^{\frac{1}{2}} \sin \varphi}{\frac{1}{2} \left(\frac{2e}{m}\right)^{\frac{1}{2}} \left\{ \left[V_p - V_a \sin^2 \varphi \right]^{\frac{1}{2}} + \left[V_s - V_a \sin^2 \varphi \right]^{\frac{1}{2}} \right\}}$$

and

$$\overline{s-p} = \frac{2d}{\left[\frac{V_p}{V_a} \csc^2 \varphi - 1 \right]^{\frac{1}{2}} + \left[\frac{V_s}{V_a} \csc^2 \varphi - 1 \right]^{\frac{1}{2}}} \quad (8)$$

The deviation, at the screen, of the point of landing of the beam from the point of intersection of a straight line through the center of deflection and the parallax mask aperture through which the beam passes, is:

$$\Delta = d \tan \theta - \overline{s-p} \quad (9)$$

If the expressions for $\tan \theta$ and the distance $\overline{s-p}$ are substituted from equations (7) and (8) we obtain the desired relation for the beam deviation as a function of deflection angle, tube geometry, and electrode potentials:

$$\Delta = \frac{rd}{r+b} \tan \varphi + \frac{2b}{r+b} \frac{d}{\cot \varphi + \left[\frac{V_p}{V_a} \csc^2 \varphi - 1 \right]^{\frac{1}{2}}} - \frac{2d}{\left[\frac{V_p}{V_a} \csc^2 \varphi - 1 \right]^{\frac{1}{2}} + \left[\frac{V_s}{V_a} \csc^2 \varphi - 1 \right]^{\frac{1}{2}}} \quad (10)$$

For small angles of deflection $\csc^2 \varphi$ is large so that the "ones" in the denominators can be neglected, and further $\csc \varphi \approx \cot \varphi$. With these approximations the electrode voltages can be so chosen that the deviation Δ in equation (10) becomes zero. By setting $\Delta = 0$ in (10) the resulting equation can be solved for the screen voltage, giving:

$$V_s^{\frac{1}{2}} \approx \frac{2(r+b)}{\frac{r}{V_a^{\frac{1}{2}}} + \frac{2b}{V_p^{\frac{1}{2}} + V_a^{\frac{1}{2}}}} - V_p^{\frac{1}{2}} \quad (11)$$

If it is assumed that the spacing between the auxiliary mesh and the parallax mask is much smaller than the distance of the deflection center to the auxiliary mesh, then it can be shown that by neglecting terms in "b" the paraxial equation (11) reduces to:

$$V_s^{\frac{1}{2}} \approx 2V_a^{\frac{1}{2}} - V_p^{\frac{1}{2}} \quad (12)$$

This relationship is valuable for determining approximate initial values for the various electrode potentials.

Calculation of the deviation Δ with the aid of equation (10) shows that, with the proper electrode spacings and potentials, the beam goes with negligible error through the same mask aperture and strikes the same phosphor dot as it would in the straight parallax tube with mask and screen at common anode potential. Deviation plots for various screen voltages and spacings between the auxiliary mesh and the parallax mask are shown in Figures 6, 7, 8 and 9. The mesh and mask

voltages were calculated from the paraxial equation (12). It can be seen that up to a scanning half angle of 30° , with certain of the parameters, the maximum deviation is .002". At small deflection angles the beam lands somewhat below and at larger angles somewhat above the parallax point but still well within the phosphor dot area.

Another important advantage realized with the new construction is the efficient collection of secondary electrons by the auxiliary mesh which otherwise contribute to poor contrast and color dilution. The voltages V_a and V_p for a given screen voltage V_s must not only satisfy equation (10) but must also be chosen so that the beam is focused down by the fields established by the auxiliary mesh, parallax mask, and metal-backed screen to a size smaller than a screen element. For paraxial rays the well known Davisson

and Calbick formula provides an expression for the focal length of the elementary lenses in terms of the voltage of the aperture electrode and the fields on both sides of it. For best focus, the focal length must equal the distance between parallax mask and screen; from the Davisson and Calbick formula, this distance may be expressed as:

$$d = \frac{4V_p}{\frac{V_s - V_p}{d} - \frac{V_p - V_a}{b}}$$

for $d = b$, this yields

$$V_s + V_a = 6V_p \quad (13)$$

The required auxiliary mesh voltage for a given screen voltage can now be estimated by solving the simultaneous equations (12) and (13). If "b" and "d" are equal, we obtain for the auxiliary mesh voltage $V_a = .57 V_s$ and for the potential difference $V_a - V_p = .32 V_s$. The auxiliary mesh, being at such a high positive potential with respect to the parallax mask, efficiently collects the secondary electrons originating there, which is an indispensable condition for successful operation of the tube.

Secondary emission would be completely absent if the parallax mask could be operated at zero or near cathode potential as in the direct-view storage tubes with electron-lens raster systems described by M. Knoll.⁴ In the absence of perpendicular incidence (for which Knoll makes provision) this mode of operation is not possible in the present case since with increasing scanning

angle the horizontal component of the electron velocity near the parallax mask soon becomes too low to enable the electron to reach the saddle point of the potential along the axis of the apertures, and they are reflected back to the cathode.

If one disregards the penetration of the accelerating field through the parallax mask apertures, the equation for the beam deviation, eq. (10) determines the maximum deflection angle at which the tube will operate for a given voltage ratio V_p/V_a , since if the square roots in the denominator become negative, the equation loses physical significance. Accordingly, the maximum deflection angle is:

$$\sin \varphi_{\max} = \left(\frac{V_p}{V_a} \right)^{\frac{1}{2}} \quad (14)$$

For the values of electrode voltages actually used

$$\varphi_{\max} = 42^\circ$$

which is a larger angle than necessary to scan the tube completely.

Tube Construction

The new principle has been incorporated into tubes utilizing 24" metal rectangular two-part envelopes as well as 19" glass round two-part bulbs. A 24" rectangular tube is shown schematically in Figure 3 and a photograph of it in Figure 4. The phosphor dot screen, parallax mask, and auxiliary mesh are all planar and assembled as an internal pack with a supporting framework and insulating spacers of uniform thickness. The pertinent dimensions and typical voltages applied to the electrodes are given in Table I.

The phosphor dot screen for these tubes was made by the silk-screening process. As the parallax mask which is normally used to produce the stencil has in this case apertures of double size, the resulting dots on the master positive must be reduced. This is achieved merely by the technique of successive exposures and dodging customary in photoengraving. In aluminizing the screen, a border is left as an insulating section between the frame and the phosphor area. Further insulation is provided between the mask and screen in the form of Mykroy insulator spacers.

The auxiliary mesh used was a woven cloth of .003" diameter stainless steel wire with 50 meshes per inch. This particular size was chosen from commercially available stock since it has a high transmission (80%) and is quite strong even though the wire diameter is sufficiently small that in the operation of the tube its out-of-focus image is invisible. The mesh was stretched and bolted between two rings supported by insulating bushings at a uniform distance (b) from the mask. The mesh

need not be precisely aligned with respect to either the parallax-mask or screen; however, in these tubes it was oriented at approximately 45° to the horizontal to eliminate moire between it and the scanning lines.

Connections to the screen and to the parallax mask were provided through additional buttons in the case of the glass bulb and through insulated connector bushings in the case of the metal envelope. The auxiliary mesh was directly connected to the metal flange and through the customary aquadag coating to the final anode of the gun.

As shown in the previous section, the auxiliary mesh voltage is .57 times the screen voltage. The anode voltage of these tubes is therefore twice that of post-deflection focused tubes having an accelerating field alone. Consequently, the conventional 3-gun assembly with mechanical convergence which employs an immersion type focusing electrode can be used. As a result of the higher anode voltage, the focusing electrode voltage is not inordinately low and current limiting in this electrode remains at a permissible value.

Performance

In the tubes described the parallax mask has a transmission of 50%; with the auxiliary mesh the overall electron transmission is 40%. Thus a brightness gain of 3 to 4 over that of the straight parallax-mask tube can be expected. Figure 5 shows the measured brightness-versus-cathode current characteristic of the new tube with 20 KV on the anode, and it can be seen that up to approximately 1 milliamperes total current a brightness gain of almost 3 1/2 is realized. At higher currents the characteristic flattens because the focusing electrode draws a portion of the current. The drives of each of the 3 guns were adjusted to give a total current to produce illuminant C white light output. In color pictures highlight brightnesses of 60 ft.lamberts have been measured.

To determine how efficiently the auxiliary mesh acts as a secondary emission collector, the ratio between the brightness produced by the primary beam and the secondaries still reaching the screen was measured. This was done on a white screen by first imaging a single line written by the primary beam and by subsequently imaging the line traced by secondary electrons onto a slit in front of a photocell, yielding ratios as high as 70 to 1. If the auxiliary mesh is kept at the same potential as the mask, this ratio drops to 10 to 1.

Secondary electrons not only detract from contrast but also desaturate color. For instance, in an area where only a saturated red is to be reproduced, the green and blue dots also become slightly luminous due to secondary electron bombardment. This condition is further aggravated by the fact that the red phosphor has the lowest luminous efficiency. An improvement in color saturation, over

what was achieved by the collection of secondary electrons, can be expected if the phosphor efficiencies are more closely matched.

In post-accelerated tubes there is another source of stray light, caused by primary electrons reflected at the screen and returned to it by the accelerating field. The intensity of this stray light was found, by the method of contrast measurement described, to be down by a factor of 200 when compared to that of the useful primary-beam light.

The markedly enhanced purity of the color fields is one of the major advantages of this type of tube. The accuracy of landing of the electron beam on the phosphor dots was mapped, with the aid of a microscope, over the entire screen area and was found to be in excellent agreement with the calculated deviation plots of Figures 7 and 9.

Moire due to the auxiliary mesh was not visible on a blank raster or on either black-and-white or color pictures.

Conclusions

It has been shown that post-deflection focusing with a retarding field preceding the accelerating field extends the brightness range of the parallax-mask type tri-color tubes considerably. Up to now this principle has only been applied to tubes with an internal screen pack. It appears certain that future commercial tri-color tubes will have the fluorescent screen deposited directly on the faceplate. This is desirable, if for no other reason than to avoid the rather disturbing sensation similar to "muscae volitantes" (fleeing flies), to borrow an expression from Physiological Optics, to which one is subjected by viewing a picture through a glass which is never quite free from striations. It is unlikely, therefore, that the tubes hitherto built and described above will be of practical importance. On the other hand, the new construction, because it employs a parallax mask is well suited for tubes with screens on the spherical faceplates requiring spherical parallax masks as masks can be formed into such shape, while wire barriers can not. Indeed, one of the principal motivations behind this project was just this: to find a principle which will permit post-deflection focusing in tri-color tubes having the screen on the faceplate. Work on such tubes is in progress.

Acknowledgments

The authors wish to thank T.S.Noskowitz for stimulating discussions and J.Wimpffen for taking measurements. The construction of experimental color tubes involves arduous and painstaking efforts and the authors are especially indebted for this to J.Fiore and various members of the Research Laboratory workshops.

References

1. R.H.Seelen, H.C.Moodey, D.D.Van Ormer and A.M.Morrell, "Development of RCA 21-in.Metal Envelope Color Kinescope", presented at Winter Meeting of A.I.E.E. February, 1955.
2. French Pat. #866,065 issued June 16, 1941.
3. L.S.Allard, "An Ideal Post-Deflection Accelerator C.R.T." *Electronic Engineer*, 22, 461, 1950.
4. M.Knoll, "Electron-Lens Raster Systems", *Electron Physics*, 329-337, National Bureau of Standards Circular 527, issued March 17, 1954.
5. R.Dressler, "The PDF Chromatron - A Single or Multi-Gun Tri-Color Cathode-Ray Tube", *Proc.I.R.E.*, 41, 851-858, July, 1953.
6. S.H.Kaplan, "Theory of Parallax Barriers", *Jour.S.M.P.T.E.*, 59, 18, July, 1952.

Glossary

- O - Center of magnetic deflection.
- r - Distance from center of deflection to auxiliary mesh.
- b - Spacing between auxiliary mesh and parallax mask.
- d - Spacing between parallax mask and screen.
- V_a - Auxiliary mesh voltage with respect to cathode.
- V_p - Parallax mask voltage.
- V_s - Metal-backed screen voltage.
- φ - Deflection angle.
- θ - Angle subtended by the phosphor dot and the tube axis at the center of deflection.
- a - Ordinate of the point where the beam trajectory intersects auxiliary mesh.
- p - Ordinate of the point where the beam trajectory intersects parallax mask.
- s - Ordinate of the point where the beam trajectory intersects the screen.
- v_x - Horizontal component of the electron velocity.
- v_y - Vertical component of electron velocity.
- \bar{v}_x - Average velocity in the horizontal direction
- Δ - Deviation at the screen between the point of landing with tripotential operation, and the corresponding point under unipotential parallax operation.

Subscripts 1, 2, 3 indicate the region in which the electron travels while the letter subscripts indicate the electrode nearest the position of the electron.

Table I

	19"	24"
Picture size	12" x 15 1/2"	13 1/2" x 18 1/4"
Deflection angle (Diagonal)	62°	62°
Parallax-Mask to Screen Spacing (d)	.400"	.416"
Parallax-Mask-Auxiliary Mesh Spacing (b)	.375"	.375"
Distance - Deflection Center to Auxiliary Mesh (r)	12.7"	14.8"
Parallax Mask Aperture diameter		.018"
Parallax Mask Aperture Spacing		.023"
Phosphor Dot diameter		.014"
Screen Voltage		20 kv
Parallax-Mask voltage		4.7 kv
Auxiliary Mesh voltage		10.5 kv

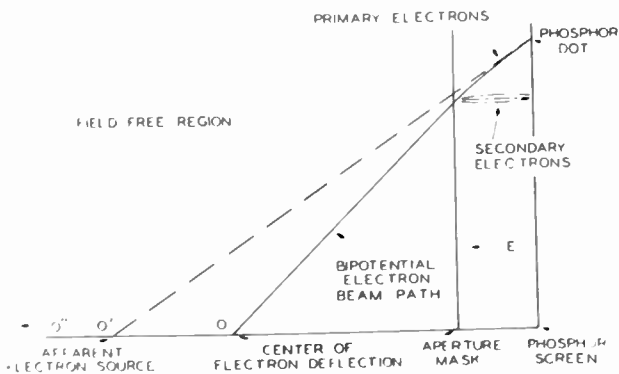


Fig. 1

Path of electron beam with bipotential operation.

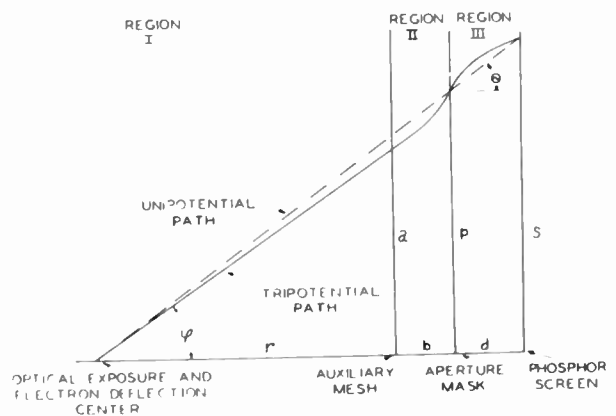


Fig. 2

Paths of electron beams with unipotential and tripotential operation.

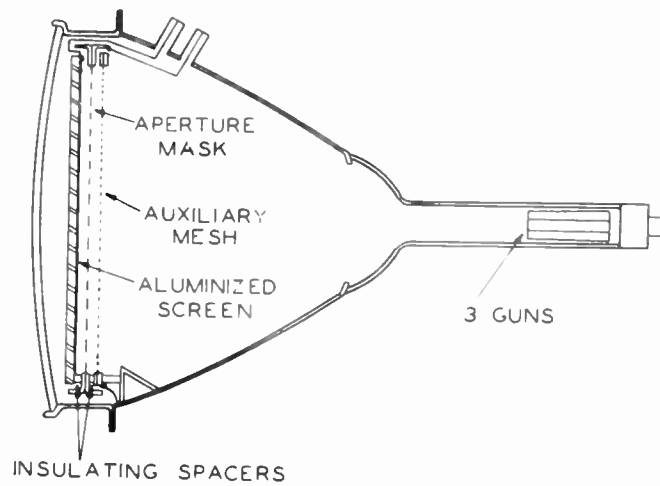


Fig. 3
Schematic cross-section of 24 inch tube.



Fig. 4
Photograph of completed 24 inch rectangular tube.

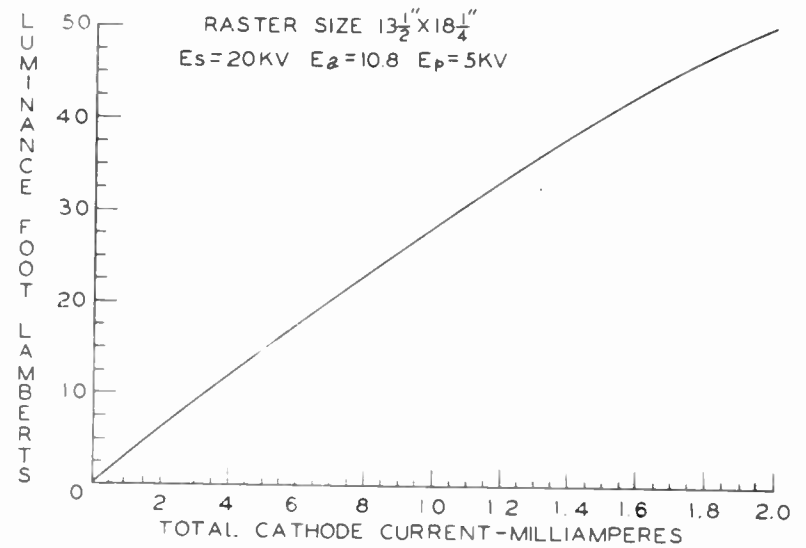


Fig. 5
Luminance - current characteristic.

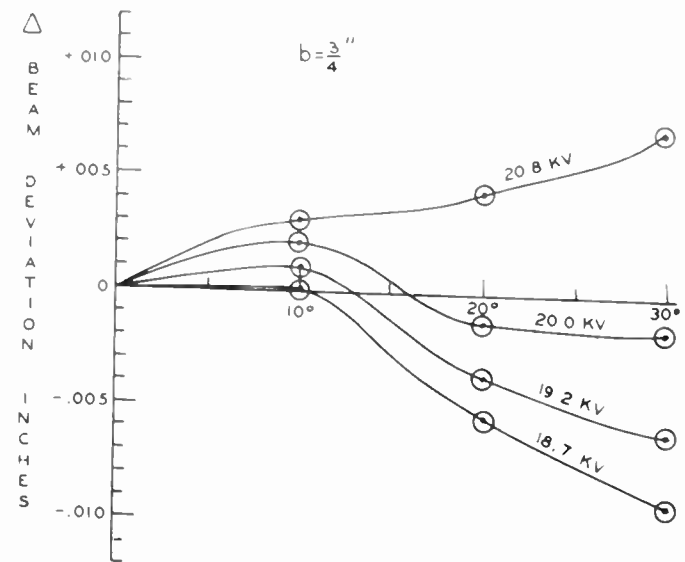


Fig. 6
Beam deviation vs. deflection angle as calculated from eq.(10) for $V_a = 9.80$ kv, $V_p = 3.60$ kv, $r = 12.7$ ", $b = 3/4$ ", and $d = .400$ ".

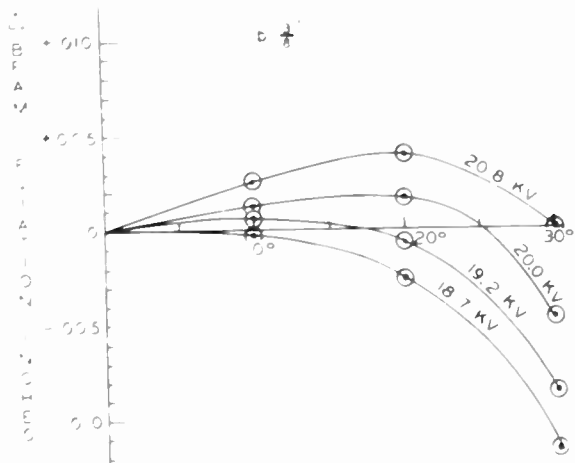


Fig. 7

Beam deviation vs. deflection angle as calculated from eq.(10) for $V_a = 9.80$ kv, $V_p = 3.60$ kv, $r = 12.7$ ", $b = 3/8$ ", and $d = .400$ ".

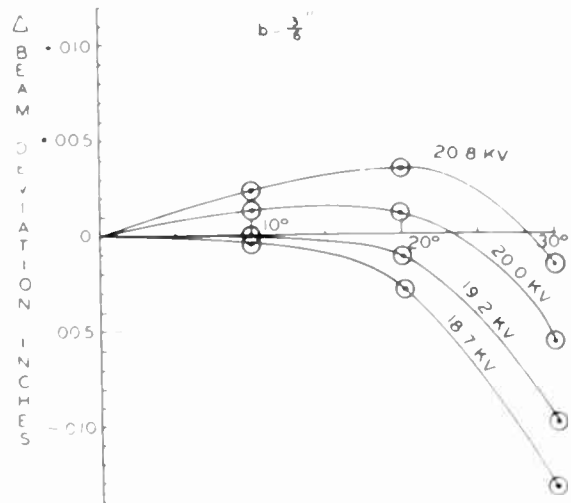


Fig. 8

Beam deviation vs. deflection angle as calculated from eq.(10) for $V_a = 9.80$ kv, $V_p = 3.60$ kv, $r = 12.7$ ", $b = 3/16$ ", and $d = .400$ ".

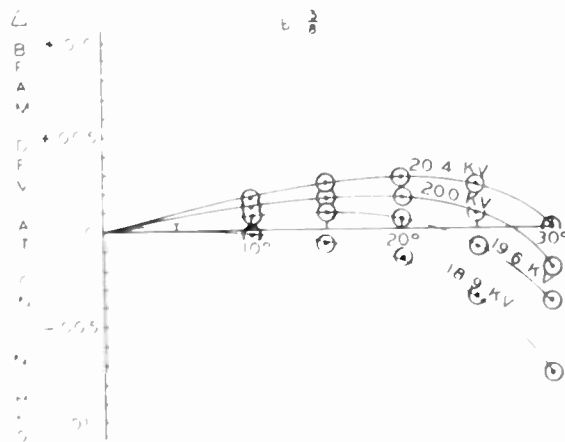


Fig. 9

Beam deviation vs. deflection angle as calculated from eq.(10) for $V_a = 10.80$ kv, $V_p = 4.80$ kv, $r = 14.8$ ", $b = 3/8$ ", and $d = .416$ ".

THE TRICOLOR VIDICON
AN EXPERIMENTAL CAMERA TUBE FOR
COLOR TELEVISION

P. K. Weimer, S. Gray, H. Borkan,
S. A. Ochs, and H. C. Thompson

RCA Laboratories
Princeton, N. J.

A television camera tube capable of generating three simultaneous color signals is now being developed. The experimental Tricolor Vidicon to be described is comparable in size to a standard monochrome Image Orthicon and has separate output terminals for each color channel. Color filter strips with associated conducting signal strips are built into a

photoconductive target. All signal strips corresponding to the same primary color are connected to a common output terminal. Special preamplifiers have been developed to obtain independent color signals in the presence of the high interstrip capacity of the target. Color fidelity independent of the scanning process is obtained with a single electron beam.

BLOCKING OSCILLATOR TRANSFORMER DESIGN

P. ROGER GILLETTE, KEITH W. HENDERSON,
AND KAZU OSHIMA

STANFORD RESEARCH INSTITUTE

Summary

Many types of electronic equipment, including radar systems, use low-power rectangular pulses for various purposes, and therefore must contain appropriate pulse-generating circuits. Most of these circuits are of a type commonly called a blocking oscillator, consisting essentially of a vacuum tube, a pulse transformer, a capacitor, and a resistor. The theory of operation of such circuits has heretofore not been sufficiently well developed to permit engineers to use other than trial-and-error procedures in designing the circuits and the transformers for them. This paper describes a recently-developed analytical method of calculating the transformer characteristics and circuit parameters necessary to produce pulses of specified amplitude, duration, and shape, and also outlines a straightforward procedure for designing transformers with the required characteristics. Complete details of the transformer design procedure are given in ref. 1, and the theoretical and experimental work which led to the development of the method of calculating parameters is described in ref. 2.

Introduction

As used in this paper, the term blocking oscillator denotes a single-tube circuit designed to produce rectangular voltage or current pulses. A common form of this type of circuit is shown in Fig. 1. More generally, a tetrode or pentode may be used instead of a triode, the transformer windings may be placed in the cathode and grid or cathode and plate circuits rather than in the grid and plate circuits, and the coupling capacitor may be placed in any of several other positions instead of the one shown. Further, there are other methods of shunt-feeding the load, i.e., by capacitive rather than direct coupling to the grid winding, by capacitive coupling to the plate winding, or by means of a third winding on the transformer. Or the load may be series-fed, by placing it in the cathode circuit, grid circuit

or plate circuit. Shunt-feeding is used for high-impedance loads and series feeding for low impedances or where there must be no backswing in the output pulse. The most common method of series feeding is by placing the load in the cathode circuit (or across a resistor in the cathode circuit, which is the same thing); perhaps the most useful method of shunt feeding is by means of a third winding.

It can be shown that the various circuit arrangements available for shunt-feeding a load can all be reduced to the same circuit, provided leakage and stray inductances and distributed and stray capacitances are ignored. These inductances and capacitances will affect only the leading edge and the first part of the trailing edge of the pulse, and it can be shown that their effect will be least for the arrangement shown in Fig. 1. This arrangement was therefore chosen for analysis. Series-feed circuits were not analyzed, but the procedure would be similar.

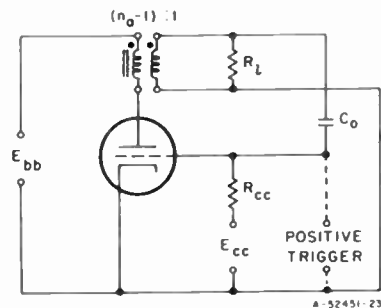


FIG. 1 Basic Blocking Oscillator Circuit

The type of analytical procedure required will be evident from a qualitative consideration of the manner in which the circuit operates. The operation is initiated when, by some means, the grid is raised above cutoff; in free-running circuits this occurs by discharge of C_0 through R_{cc} , and in triggered circuits through application of a positive trigger voltage to the point indicated in Fig. 1 (or of a negative voltage to the tube plate). Plate current then begins to flow in the tube, and a voltage drop appears across each transformer winding.

The voltage drop across the plate winding is equal to the drop that would appear across an impedance consisting of a parallel combination of the open-circuit impedance of the transformer, the grid-to-cathode impedance of the tube, and the load impedance (all impedances being referred to the impedance level of the plate winding) with a current equal to the plate current flowing through it. The voltage across the grid winding is equal to $V_g = V_p$ times the voltage across the plate winding, where N_g is the number of turns in the grid winding and N_p the number in the plate winding. Initially the open-circuit impedance of the transformer and the grid-to-cathode impedance of the tube are very high, so a small plate current will produce large voltages. The voltage across the grid winding drives the grid more positive, producing a further increase in plate current, and so on. As the action continues, the grid soon becomes positive with respect to the cathode, grid current begins to flow, and the grid-to-cathode impedance begins to drop. Eventually values of plate and grid voltage are reached for which the ratio $(l_g + l_l)/l_p$ obtained from the load impedance and the tube characteristics is equal to N_p/N_g . This condition is reached before the transformer magnetizing current can build up to an appreciable level, and before an appreciable charge builds up on the coupling capacitor. The plate and grid voltages then level off at these equilibrium values. If the capacitance of the coupling capacitor and the open-circuit inductance of the transformer were infinite, the plate and grid voltages would remain at these values indefinitely. However, the voltage across the capacitor gradually increases as grid current flows, and the transformer magnetizing current increases as long as the plate voltage is less than E_{bb} . As the magnetizing current increases, less current is available to the grid, and as the capacitor voltage increases, less voltage is available to the grid. The tube characteristics are such that these actions can continue for some time with the circuit remaining in a gradually shifting equilibrium condition. However, a point is eventually reached at which the plate current begins dropping too fast for the grid current to keep up, and the equilibrium is destroyed. A reverse regenerative action then begins, and the pulse voltage drops rapidly to a negative value.

The amplitude, duration, rise time, and shape of the pulse can be predicted mathematically with the aid of an equivalent circuit of the form shown in Fig. 2². It may be noted that tube interelectrode capacitances and other stray capacitances have

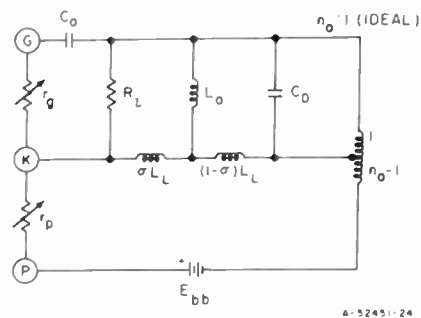


FIG. 2 Equivalent Circuit for Blocking Oscillator

been neglected in constructing this circuit. It should also be noted that the source is represented as a battery of constant voltage E_{bb} in series with a variable plate resistance r_p , rather than as a generator of voltage μV_g in series with a constant plate resistance, and that a variable grid resistance r_g is included in the circuit. The tube must be represented in this manner because both grid and plate voltages vary so widely during the pulse that the approximations commonly made in calculating the effect of a tube on small signals are not applicable.

The transformer, on the other hand, can be represented to a reasonable approximation by constant-valued elements; this can be done because (contrary to wide-spread opinion) the transformer core in a well-designed blocking oscillator is not driven to saturation. It will be noted that the transformer is represented in Fig. 2 by an ideal autotransformer, three inductances and a capacitance. An ideal reverso-transformer could be used instead of an ideal autotransformer, but it can be shown that if this is done two additional inductances must be included in the equivalent circuit to give a reasonably accurate representation of the transformer.

If the rise time and duration of the pulse used to trigger a triggered blocking oscillator are small compared with the rise time and duration of the pulse produced by the oscillator, and if the impedance of the trigger source is low during the trigger pulse and very high at all other times, the shape of the top and tail of the oscillator pulse will not depend upon the characteristics of the

trigger source. The shape of the oscillator pulse front will depend upon the trigger source characteristics, but the characteristics of commonly-used trigger circuits vary so widely that no simple description of this dependence can be given. Hence no attempt was made to represent a trigger source in the equivalent circuit of Fig. 2, and only free-running circuits were considered in the development of procedures for predicting pulse front shape.

Since the type of circuit under consideration is designed to produce a rectangular pulse whose rise time is short compared with its duration, the transformer open-circuit inductance L_0 and the grid coupling capacitance C_0 can be ignored in calculating the pulse front shape and rise time. Similarly, the transformer leakage inductance L_L and the transformer distributed capacitance C_D can be neglected in calculating pulse top shape and duration. Several simplifications can also be made in the calculation of pulse tail shape.

The first step in the analysis of the equivalent circuit is to determine the value of the load voltage at the end of the pulse rise. This calculation can be made most conveniently in reverse, by assuming various values for the load voltage e_L and then, with the aid of tube characteristic curves, calculating the value of load conductance G_L for which the load voltage will be equal to the assumed value. The values of e_L may be plotted against the corresponding values of G_L to give what may be called a pulse-initiation curve. For a normal free-running circuit the curve will be single-valued. For a triggered circuit, on the other hand, it will be found that the curve is of the form shown in Fig. 3. It can be shown that the upper branch of

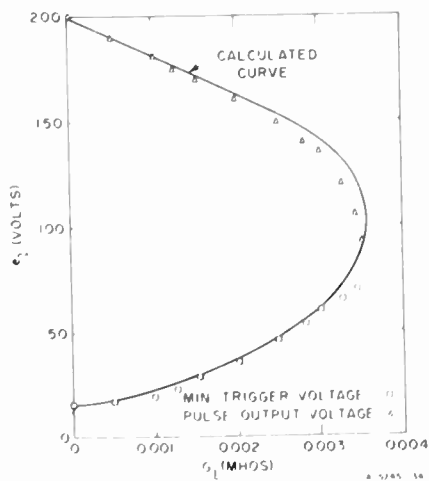


FIG. 3 Pulse Initiation Curve

the curve represents a condition of stable equilibrium, while the lower branch represents unstable equilibrium. For a given value of G_L , the voltage read from the lower branch is the minimum trigger voltage required to initiate the pulse, and the voltage from the upper branch is the amplitude of the pulse at the end of the initial rise. The validity of the mathematical procedure and of the interpretation of the resulting curve has been verified by calculations and measurements for a circuit using a 6SN7 tube. The curve and experimental data plotted in Fig. 3 represent the results thus obtained.

The detailed prediction of the pulse front, top, and tail shape can be carried out by deriving a differential equation from the loop and node equations for the simplified circuit applicable to each portion of the pulse and then plotting the solutions of the differential equations. Since the differential equations for the pulse front, the top, and that portion of the tail during which the tube is still conducting contain r_g and r_p , which are not constant, these equations cannot be solved analytically. However, straightforward step-by-step procedures involving the use of the tube characteristic curves have been developed and used successfully. The prediction of pulse front shape has been carried out for a free-running circuit using a 6SN7 tube, and the result is shown with the observed curve in Fig. 4. The discrepancy is ascribable to the fact

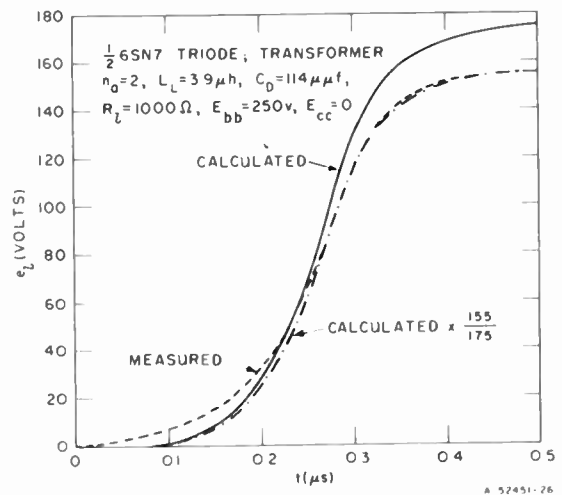


FIG. 4 Pulse Front, Free Running Blocking Oscillator

that both core loss and winding loss (which may be as important as core loss in blocking oscillators) were neglected in making the calculations. Calculated and measured top and tail shapes for a triggered circuit using a 6SN7 are shown in Fig. 5.

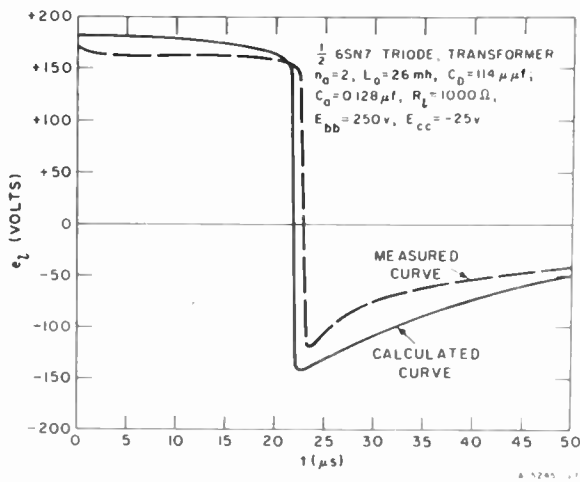


FIG. 5 Pulse Top and Tail, Triggered Blocking Oscillator

Again, the discrepancy is ascribable to losses which were neglected in the calculations.

DETERMINATION OF REQUIRED TRANSFORMER CHARACTERISTICS

The analytical procedures just described may be used to derive curves for determining the transformer characteristics required to deliver an output pulse of specified amplitude, duration, rise time, and droop, to a load of specified impedance. First a family of pulse-initiation curves is calculated for the tube with appropriate values of E_{bb} and E_{cc} and various values of n_a (where n_a is defined as the ratio of the total number of turns in grid and plate windings to the number of turns in the grid winding). This family of curves is plotted and their envelope is drawn as shown in Fig. 6. A set of constant-power curves can also be plotted in the same diagram, as shown in the figure.

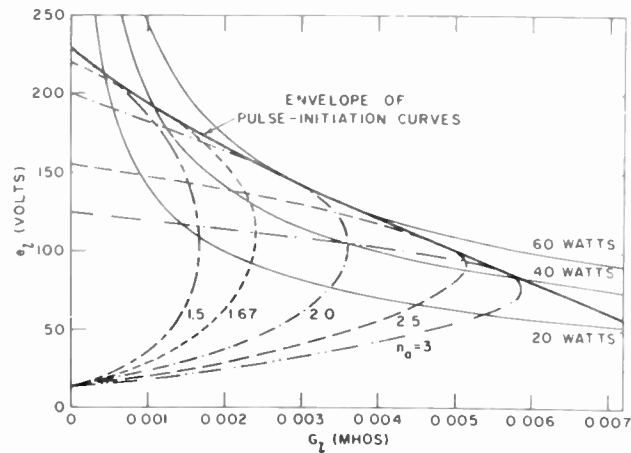


FIG. 6 Family of Pulse Initiation Curves

Curves of the type shown in Fig. 6 are used to determine an appropriate value for n_a . If a given amount of pulse power is to be produced, the value of n_a must be within the range for which the corresponding pulse-initiation curves are intersected by the appropriate constant-power curve. If the appropriate constant-power curve does not intersect the envelope of the pulse-initiation curves, the required power cannot be obtained from the tube chosen. Which value to use, of those within the range so determined, depends upon several factors. Space does not permit a complete discussion of these factors, but a careful consideration of them indicates that for most purposes the best value of n_a will be the one for which the maximum possible power output is the greatest. (Figure 6 indicates that for a 6SN7 tube with $E_{bb} = 250v$ and $E_{cc} = -25v$, n_a should be equal to 2.0; that is, the numbers of turns in the plate and grid windings should be equal.)

The values of i_L and \dot{u}_L specified by the customer will usually not correspond to the point at which the appropriate constant-power curve intersects the upper branch of the pulse-initiation curve. In such instances a third winding must be provided to step the voltage up (or down) to the specified value from the value given by this point of intersection. The transformer core and the plate and grid windings are designed on the assumption that the load conductance is equal to the value given by the point of intersection, and then the third winding is designed to give the required voltage ratio.

It can be shown from the form of the equation used in calculating pulse front shape that T_r , the time required for the load voltage to rise from 10% to 90% of the final pulse amplitude, will be given to a good approximation by

$$T_r = E_r \cdot \bar{T}_L \cdot C_D \quad (1)$$

where E_r is a function of the tube characteristics, E_{bb} , E_{cc} , n_a , \dot{u}_L and \bar{T}_L , C_D , but not of the actual values of i_L and C_D . Furthermore, if pulse front shapes are calculated for a given tube type and supply voltages, fixed values of n_a and \dot{u}_L , and various values of i_L and C_D , and if these curves are normalized to make T_r equal to unity, all curves for a given value of $\bar{T}_L \cdot C_D$ will be of identical shape. A family of such curves for a free-running circuit, using a 6SN7 tube and a transformer with $n_a = 2$, are shown in Fig. 7. The corresponding values of E_r are plotted against $\bar{T}_L \cdot C_D$ in Fig. 8.

Curves of the types shown in Figs. 7 and 8 can be used to determine appropriate values for I_L and C_D . A number of factors may be considered in choosing an appropriate value for $\sqrt{L_L/C_D}$. In most instances, however, minimum rise time will be of primary importance, and the value of $\sqrt{L_L/C_D}$ which will

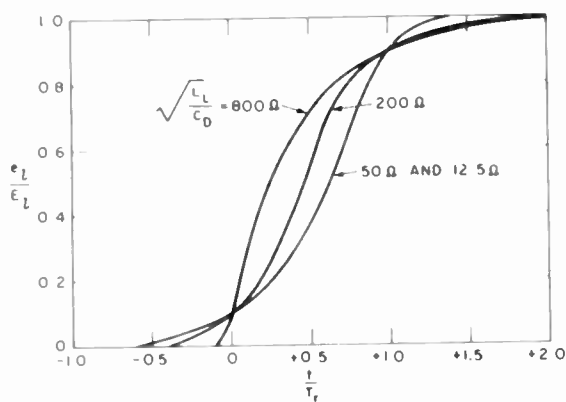


FIG. 7 Family of Pulse Front Curves

give a minimum value of K_r (and hence minimum rise time for a given value of $\sqrt{L_L/C_D}$) should be chosen. With this value of $\sqrt{L_L/C_D}$ and the corresponding value of K_r , the value of $\sqrt{L_L/C_D}$ required to give the specified rise time (or slightly less than the specified rise time, if a third winding is to be added later) can be calculated from Eq. (1).

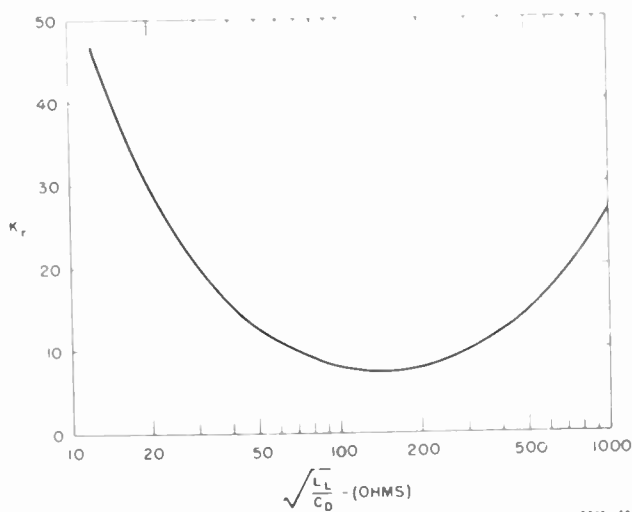


FIG. 8 Curve of K_r vs. $\sqrt{L_L/C_D}$

In similar fashion it can be shown that T_d , the pulse duration, will be given by

$$T_d = K_d \sqrt{L_o C_o} \quad (2)$$

where K_d is a function of the tube characteristics,

E_{bb} , E_{cc} , n_a , G_L , and $\sqrt{L_o/C_o}$; also all pulse top shapes for a given value of $\sqrt{L_o/C_o}$, normalized to make T_d unity, will be identical. A family of pulse top shapes for a triggered circuit presented in Fig. 9, and the corresponding K_d -vs.- $\sqrt{L_o/C_o}$ curve is plotted in Fig. 10.

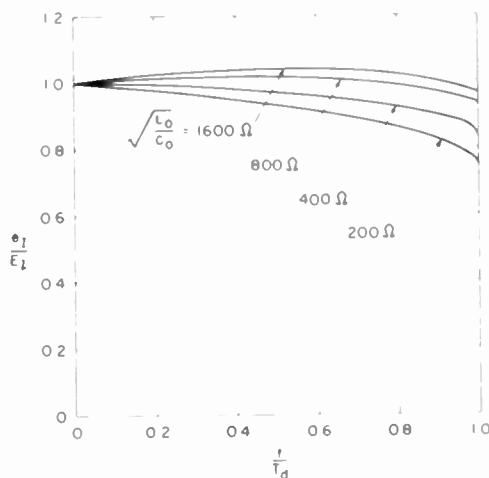


FIG. 9 Family of Pulse-Top Curves

The value of $\sqrt{L_o/C_o}$ that will give the specified amount of droop may be chosen directly from a set of curves of the type shown in Fig. 9. However, other considerations enter into the choice, including the sizes and costs of the transformer and capacitor and the ease with which the pulse duration can be held within specified limits. In most cases it will be found that the value of $\sqrt{L_o/C_o}$ for which K_d is a maximum will be a reasonably good compromise. With $\sqrt{L_o/C_o}$ and T_d known, the value of $\sqrt{L_o/C_o}$ required to give the specified pulse duration can be calculated from Eq. (2), and the required values of L_o and C_o can then be determined.

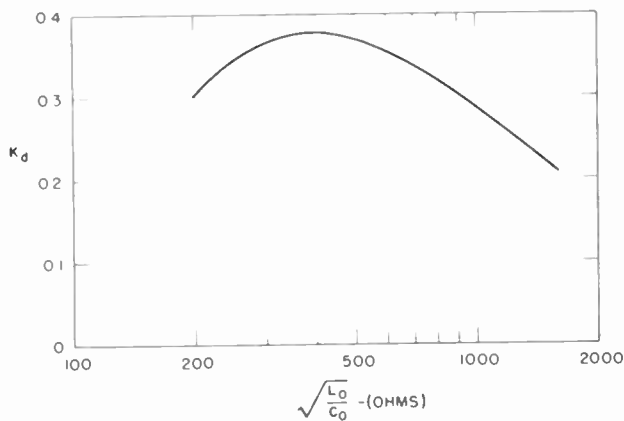


FIG. 10 Curve of K_d vs. $\sqrt{L_o/C_o}$

If a third winding is added, it is placed over the grid winding, the plate winding being placed next to the core. The insulation thickness between grid and output winding is chosen to make $\sqrt{L_L/C_D}$ for this space, referred to the impedance level of the output winding, equal to the specified load impedance.

Now that the required transformer parameters have been calculated, it is possible to proceed with the actual design of the transformer.

TRANSFORMER DESIGN PROCEDURE

Several methods have been suggested for designing pulse transformers with specified values of L_o , L_L , and C_D . One of the best of them is a method recently described by General Electric Company³. A new method has been developed at Stanford Research Institute¹ which is similar to the General Electric Company method but is believed to be superior to it in some respects.

The first two steps are the same in the GE and SRI methods. The first step is to choose the material and general shape for the core, the type of wire and insulating material, and the general winding arrangement. In the second step the margins required to withstand the voltage are determined, and insulation thicknesses and wire sizes are chosen that will withstand the voltage, carry the current, and give the proper value of $\sqrt{L_L/C_D}$. The third step in the SRI method is to express all core dimensions in terms of the core buildup or leg width, the number of turns in the high-voltage winding, and previously-established quantities, and the fourth step is to solve each of three pairs of simultaneous equations for values of these variables. The first pair of equations will give the values of core buildup and number of turns that will result in the proper value of the quantity $L_o \cdot \sqrt{L_L/C_D}$ and the maximum possible value of I_o ; the second pair will give the values of the variables that will result in the proper values of $I_o \cdot \sqrt{L_L/C_D}$ and I_o ; and the third pair will give the values that will result in the proper value of $I_o \cdot \sqrt{L_L/C_D}$ and the maximum permissible value of flux density. The solutions of these sets of equations are used as guides in choosing an available core size that will be satisfactory. The number of turns which will give the proper value of $L_o \cdot \sqrt{L_L/C_D}$ with that core size is then calculated, the resulting values of L_o , L_L , C_D , and B_{max} are calculated as a check, the transformer losses are calcu-

lated to determine whether or not the temperature rise is within the appropriate limit, and the core-and-coil design is complete.

EXAMPLE OF APPLICATION OF DESIGN PROCEDURE

The complete procedure outlined in this paper has been used in designing a transformer for use in a triggered circuit with a 6SN7 tube to deliver a +500v, 10 μ s pulse, with a 0.1 μ s rise time, to a 10k load. The core and first two winding layers were designed with the aid of the curves of Figs. 6-10. Allowance was made for core and coil losses in choosing n_a and G_L (from Fig. 6), and the values chosen were $n_a = 2.0$, $G_L = 0.001$ mho. Figure 8 was used in the calculation of L_L and C_D , even though it applies to a free-running circuit rather than a triggered circuit. The figure indicates that K_T will be a minimum for $\sqrt{L_L/C_D} = 140$ ohms. The value of $\sqrt{L_L/C_D}$ calculated from the minimum value of K_T and the specified rise time, with a reasonable allowance for the effect of the third winding, is 1.0×10^{-8} sec. Figure 10 indicates that K_d will be a maximum for $\sqrt{I_o/C_o} = 400$ ohms. This maximum value of K_d and the specified value of T_d give $\sqrt{I_o/C_o} = 2.7 \times 10^{-5}$. From these values of $\sqrt{I_o/C_o}$ and $\sqrt{L_o/C_o}$, $I_o = 11$ mh (referred to the grid winding) and $C_o = 0.07 \mu$ f. The wire size, insulation thickness, core size, and number of turns obtained by the transformer design procedure are as shown in the winding diagram of Fig. 11. Since the specified

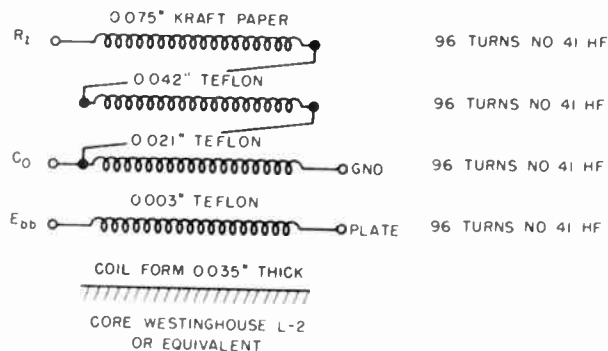


FIG. 11 Transformer Obtained by Design Procedure

load impedance is 10,000 ohms and the value of Z_L for which the plate and grid windings were designed is 1,000 ohms, a voltage step-up from grid winding to load winding of about 1:3 is required. This was obtained by adding two more winding layers and connecting them as shown in Fig. 11. The second and third insulation pad thicknesses have the correct

ratio to make $\sqrt{L_L C_D}$ a minimum and the correct sum to make $\sqrt{L_L/C_D}$ equal to the load impedance.

A transformer built to this design was tried in the circuit of Fig. 1. The value of C_o had to be increased to 0.085 μ f to give a pulse duration of 10 μ s, but the rise time was 0.1 μ s and the voltage on a 10k load was 500v, as specified. The pulse shape is shown in the photograph of Fig. 12.

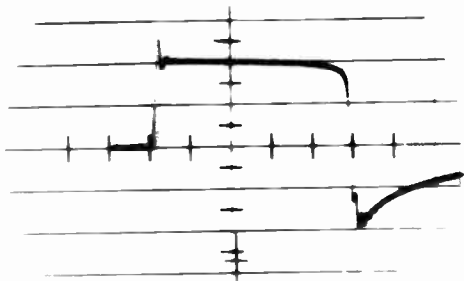


FIG. 12 Output Pulse Obtained with Transformer of Fig. 11

EXPERIMENTAL DETERMINATION OF BLOCKING OSCILLATOR DESIGN CURVES

Although the mathematical procedure used in obtaining the curves shown in Figs. 6-10 is feasible, it is quite laborious. Fortunately, such curves can be obtained experimentally for a given tube type in a simple manner. Pulse-initiation curves for a range of values of n_a can be determined with a set of transformers built with some arbitrary value of L_o , various values of n_a , and any convenient values of L_L and C_D . Pulse top shapes are then determined with a transformer built with this same value of L_o and the optimum value of n_a , and with capacitors and loads of various values. These pulse top curves are used to obtain K_d vs. $\sqrt{L_o/C_o}$ curves for the various values of load conductance. Finally, pulse front shapes are determined for various values of G_l and $\sqrt{L_L/C_D}$, using a set of transformers with the chosen value of n_a ,

arbitrary values of L_o , C_o , and $\sqrt{L_L C_D}$, and various values of $\sqrt{L_L/C_D}$. Curves of K_r vs. $\sqrt{L_L/C_D}$ for various values of G_l are obtained from these pulse front shapes. The design curves thus obtained will give more accurate results than curves calculated from tube characteristics, since fewer approximations are involved in making them.

Acknowledgment

The work on which this paper is based was carried out at Stanford Research Institute under Contract No. DA 36-039 SC-42645 with the Signal Corps Engineering Laboratories. We should like to thank the cognizant representatives of those laboratories for assistance and encouragement during the course of the work, and for permission to present some of the results in this paper.

Bibliography

1. P. R. Gillette, K. W. Henderson, K. Oshima, R. M. Rowe, Instruction Manual "Design Procedures for Pulse Transformers," Part II of Final Report, Contract No. DA 36-039 SC-42645; Stanford Research Institute.
2. P. R. Gillette, K. W. Henderson, K. Oshima, R. M. Rowe, Research Report, "Pulse Transformer Design and Test Methods," Part III of Final Report, Contract No. DA 36-039 SC-42645; Stanford Research Institute.
3. P. Fenoglio, C. W. Peck, T. B. Richardson, H. W. Lord, A. Boyajian, "High Power, High Voltage Pulse Transformer Design Criteria and Data," Part I of Final Report, Contract No. DA 36-039 SC-117; General Electric Company.

R. A. Mathias
Associate, I.R.E.

and

E. M. Williams
Fellow, I.R.E.

Carnegie Institute of Technology
Pittsburgh 13, Pennsylvania

Introduction

Sharply saturable reactors serve as power switches in applications where use may be made of the large relative change in impedance from unsaturated to saturated states. A pulse generator circuit using a series of stages of pulse switching reactors was developed some years ago in England by W. S. Melville.¹ A basic form of this circuit is shown in Figure 1. The saturable reactors (known as 'pulsactors' in this application) are designed with successively lower values of inductance, so that the energy is discharged from each successive capacitor more rapidly than in the preceding capacitor. This discharge takes place, for instance, from the second capacitor into the third capacitor when the second pulsactor reaches its saturated state. The energy flow is compressed timewise from stage to stage and the current level is correspondingly increased so that by the time energy reaches the load a narrow pulse is achieved.

Simplified Analysis of Ideal Pulsar

Analysis of the basic circuit in Figure 1 for the ideal case of no losses and ideal pulsactors is relatively simple, and yields information useful for the design of practical circuits. As shown in a previous paper on this subject,² the basic equation for proper circuit functioning equates the time to charge the kth capacitor to its peak voltage to the time required to drive the kth pulsactor flux through its operating swing to saturation. This equation may be expressed in a form which allows considerable insight into the circuit design. This expression gives the stage pulse compression ratio, P_k, in terms of the kth pulsactor core volume, M_k, and the energy per pulse, W_m. The kth stage pulse compression ratio is defined as the ratio of the time to charge the kth capacitor to the time to discharge the same capacitor. That is,

$$P_k \equiv \frac{t_{c-1}}{t_k} = \sqrt{\frac{M_k}{G W_m}} \quad (1)$$

*This paper describes work supported in part by the Rome Air Development Center under contract AF 30(602)-914. This paper contains part of a dissertation submitted by R. A. Mathias in partial fulfillment of the requirements for the Doctor of Philosophy degree in Electrical Engineering at Carnegie Institute of Technology.

where G is a constant for the pulsactor.

$$G = \frac{\pi^3 \mu_s 10^7}{(\Delta B)^2} \quad (2)$$

Equation (1) states that the volume of the kth pulsactor is directly proportional to the energy per pulse for a given stage compression ratio. For a complete pulsar, the over-all pulse compression ratio is then the product of the stage compression ratios. Thus, the total pulse compression ratio for an n stage pulsar is

$$P_T \equiv \prod_1^n P_k = \sqrt{\frac{\prod_1^n M_k}{W_m^n \prod_1^n G_k}} \quad (3)$$

So, for a specified over-all compression ratio and energy per pulse, the product of the core volumes is fixed. If the total core volume required for this n stage pulsar is then minimized, it is noted that the volumes of all n cores are equal. With all core volumes equal, the optimum number of stages, n_b, may be found for the least total core volume of the pulsar. This optimum number of stages is

$$n_b = F + \ln P_T^2 \quad (4)$$

in which F is a constant depending upon the type of input circuit and the definition of output pulse width. Since equation (4) proves to be useful for design purposes, ~~and~~ it is plotted for several types of input in figure (2).

Core Volumes for Less Than Optimum Number of Stages

The total core volume required does not vary much from optimum volume n_b for a number of stages, n, given by n = 0.5 n_b. In fact, for n = 0.5 n_b, the total core material required is only 1.36 times the optimum amount. This is shown in figure 3, where it may be noted that the required total volume is only doubled for n = 0.37 n_b. Thus, even high power pulsars would use n in the range of about 0.3-0.6 n_b. Any additional stages would usually prove uneconomical, and would not reduce iron losses to any noticeable extent. Actually, considerations such as high

voltage insulation of windings, low input frequency, etc., would require possibly even larger cores, and thus fewer stages.

Calculation of Iron Losses

The rapid changes of magnetic flux in the cores of the last stages of the pulser give rise to large eddy currents even for thin laminations. The distribution within each lamination is determined almost completely by eddy currents. The eddy current losses may be easily calculated for rectangular loop material by assuming that the total flux change occurs within a narrow boundary moving inward to the center of the lamination. Since the eddy current density between the moving boundary and the outside edge of the lamination is uniform, the calculation for the eddy current losses involves a simple integration once the applied winding voltage is known. Because all pulsactors (except the first one for some types of input sources) have similar waveforms applied, the eddy current loss may be found for the general kth stage. That is, the loss in watt-seconds per pulse is

$$W_{e_k} = 0.110 \times 10^{-8} \left(\frac{V_{mk}}{N_k} \right)^2 l_k T_k^2 \Delta B_k \sigma, \quad (5)$$

for $k > 1$

in which

- V_{mk} = peak voltage on kth capacitor,
- N_k = number of turns in kth main winding,
- l_k = effective magnetic path length of kth core in cm.,
- T_k = thickness of kth core laminations in cm.,
- ΔB_k = total flux swing in gauss for kth core,
- σ = conductivity of core material in mhos/cm.

In the case of a single pulse per cycle of the input supply, the eddy current loss for the flux return, if appreciable, would have to be added to equation 5 to get the total eddy current loss.

Equation 5 may be written in a form which is more familiar, as follows:

$$W_{e_k} = 0.440 \times 10^{-16} f_{k-1} M_k (\Delta B)^2 T_k^2 \sigma, \quad (6)$$

for $k > 1$

in which

- f_{k-1} = frequency of current discharge through the (k-1)th pulsactor, and
- M_k = volume of kth pulsactor core in cm.³

If the pulse repetition rate in pulses per second is f_r , then the total eddy current loss in watts is

$$P_{e_k} = 0.44 \times 10^{-16} f_r f_{k-1} M_k (\Delta B)^2 T_k^2 \sigma, \quad (7)$$

for $k > 1$

The total hysteresis loss in watts for the static loop is approximately

$$P_{h_k} = 1.59 \times 10^{-8} f_i M_k (\Delta B_k) H_c, \quad (8)$$

in which

- f_i = input supply frequency,
- H_c = static coercive force in oersteds.

Total iron losses calculated by means of equations (7) and (8) were checked with the results of some core loss tests made by Westinghouse Air Arm Division. These cores were tested in pulser-type circuits at a temperature of about 105°C. Some 2 mil tape cores were tested over an effective frequency range of 1 to 6 kc. and 1 mil tape cores over a range of 6 to 60 kc. The calculated values fell within about 15% of the experimentally determined values for the 2 mil material. However, at 50 kc., the calculated value was about 50% over the measured value. Though this is only a partial verification of this method calculating the iron losses, it should be pointed out that the method of measurement used was probably susceptible to error at the higher frequencies.

Example of Pulser Design

In order to illustrate the effect of losses, the method of design of a simple pulser circuit will be illustrated here. The specifications for this pulser are as follows: the output pulse is to have a peak of about 250 volts and width of about 50 micro-seconds for a load of about 5 ohms. The pulse is to have a repetition rate of 120 pulses per second and the power source is 115 volts, 60 cycles per second. This pulser, for example, might be used to pulse the ignitor for some types of ignitron control systems.

From the output specifications, the energy required per pulse is 0.625 watt seconds. Assuming over-all pulser efficiency to be about 70%, the estimated input power required is about 107 watts.

Detuned Input Stage

To find the size of the first capacitor, C_1 , information will be needed on the type of charging circuit at the input. For this example, it will be assumed that about maximum stable de-

detuning of $L_0 C_1$ from driving frequency will be employed. This gives additional pulse compression in this first stage. In fact, for this case, P_1 is 1.38 times its value for $\omega_0 = \omega_i$ since here

$$\omega_0 = 1.79 \omega_i \quad (9)$$

where

$$\omega_0 = \frac{1}{\sqrt{L_0 C_1}} \quad (10)$$

and the input supply voltage is

$$e = E_m \sin \omega_i t \quad (11)$$

Figure 4 shows the effect of this detuning upon first pulsactor volt-seconds, peak voltage on C_1 , and first stage compression ratio. For the detuning chosen, it is noted from the curves that the peak voltage on C_1 is

$$V_{m1} = 1.72 E_m \quad (12)$$

With an assumed 5% loss in the input stage (this includes iron losses of first pulsactor), $V_{m1} = 273$ volts.

This detuning of the input is also of value in cases in which there is required a specified phase angle of the output pulse with respect to the input voltage.

The value of C_1 is determined by

$$C_1 = \frac{2 W_{m1}}{V_{m1}^2} = \frac{2 \times 0.95 \times 0.893}{273^2} = 22.8 \mu f \quad (13)$$

where W_{m1} = peak energy on C_1 . To pick a standard capacitor size near this value, C_1 is chosen as 20

First Pulsactor Volume for Low Input Frequency

When input frequency is low, as it is for this example, the volume required for the first pulsactor is usually much larger than the optimum value based upon pulse energy alone. This volume requirement results from the problem of the winding losses of this pulsactor. The number of turns are fixed by the integrated volt-seconds absorbed. When too small a core volume is used, if an attempt is made to hold losses to an acceptable value by using large conductor cross section, the winding build-up will be excessive. This leads to a reduction in first

stage pulse compression ratio since the large build-up causes μ_{s1} to be large. μ_{s1} is the effective saturated permeability when the area, A_1 , and the mean magnetic path length, l_1 , in the following equation are the values for the core material alone. Thus, the saturated inductance of the first pulsactor is

$$L_{s1} = \frac{N_1^2 A_1 4\pi \mu_{s1} 10^{-9}}{l_1} \quad (14)$$

The expression for the required minimum volume of the first pulsactor, as determined by winding losses, was calculated under these assumptions:

1. Core cross section is approximately square, that is, the core tape width is no more than about twice the radial build-up.

2. Winding build-up is directly proportional to the square root of the core cross section.

3. The first stage efficiency is fixed. The efficiency can be specified this way since it is determined almost entirely by winding losses. (The iron losses are usually negligible in the first stage when the pulser is driven by frequencies low enough to require larger than optimum volume for the first pulsactor). If the winding resistance is R_{w1} and the winding energy loss per pulse is $W_{\lambda 1}$ then

$$\frac{W_{\lambda 1}}{W_{m1}} = \frac{\pi}{2\sqrt{2}} R_{w1} \sqrt{\frac{C_1}{L_{s1}}} \quad (15)$$

Thus, this condition specifies that k_{w1} should be directly proportional to the square root of L_{s1}/C_1 .

These three conditions lead to the following result.

$$M_1 \geq K \frac{W_{m1}}{f_i^2 A_1^2} \quad (16)$$

where K is a constant of proportionality. Toroidal cores with good proportions for this type service roughly obey this equation:

$$l_1 \cong 15 \sqrt{A_1} \quad (17)$$

This equation combined with the assumptions of about 90% efficiency for the first stage and a μ_{s1} of about 5, give a value for the first pulsactor core volume in cubic centimeters of

$$M_1 \geq 4 \times 10^3 \left[\frac{W_{m1}}{f_1^2} \right]^{\frac{3}{7}} \quad (18)$$

Inserting the values of pulse energy and input frequency into equation (18) for the example considered, it is found that M_1 should have a volume at least about 114 cm.³ A standard core size of 4 mil, 50-50 nickel-iron material very close to this value has a 90% core space factor (about 60% space factor for both core and protecting core box). This core has a 2.5" I.D., 4.0" O.D. and 1.0" tape width.

Calculation of Other Circuit Parameters

Now that the first core is chosen the number of turns for its winding may be determined. From figure 4, it is noted that for the amount of detuning previously chosen the volt-seconds to be absorbed by this winding are about $1.63 \times E_m / \omega_i$. Thus, the number of turns required is:

$$N_1 = \frac{1.63 E_m 10^8 \cdot 0.95}{\omega_i A_1 (\Delta B_1)} = 530 \text{ turns} \quad (19)$$

where the input stage efficiency assumed is about 0.95. Using No. 16 copper wire for this winding gives $R_{w1} \cong 1.1$ ohms and thus the assumed efficiency of about 90% for the first stage. The peak voltage on the second capacitor will be about 235 volts if a circuit of the type shown in figure 1 is utilized. However, the output voltage is specified to be about 250 volts. So a voltage step-up is needed since if the load resistance drops as low as 5 ohms, the peak voltage on the last capacitor should be about 1.3 times 250 volts (this is case of about critical damping of output stage). This required voltage step-up of about 1.4 may be achieved by the circuit shown in figure 5.

Since the first stage pulse compression ratio is about 15.5 the remainder of the pulse compression required is less than this amount. There is, therefore, no need to use a total of more than 2 stages and in fact the second core can be somewhat smaller. This core volume can be expressed as

$$M_2 = \rho_2^2 W_{m2} \frac{1.85^2 8\pi \mu_{s2} 10^7}{4 (\Delta B)^2} \quad (20)$$

Assuming $\mu_{s2} \cong 4$, $M_2 = 66 \text{ cm.}^3$

The nearest standard core size is one with 3.0" I.D., 4.0" O.D., and 1.0" tape width. Since 4 mil material has a better space factor and is less expensive than 2 mil material it would be advisable to check the iron losses using 4 mil material. Applying equations (7) and

(8) to determine the eddy and hysteresis losses, it is found that these are about 0.83 and 0.45, respectively. Thus, the total iron loss is about 1.28 watts, which should be dissipated through the core box with little temperature rise.

Change in Impedance Level

The two windings on the second core, as shown in figure 5, serve both to change impedance level and also to give electrical isolation, if necessary. In this type of configuration, the secondary winding should usually be the inner winding next to the core box, and well distributed so as to give as low a saturated inductance as possible. The first pulsactor could have had two windings (or auto-transformer connection) to give voltage step-up. However, in this case, space for conductors is at a premium on the first core, so the second core is used since build-up is not excessive, even with two windings.

The number of turns required on the second core primary winding is

$$N_{2P} = \frac{V_{m2} \pi \sqrt{L_{s1} C_1}}{2 \sqrt{2} A_2 (\Delta B_2) 10^{-8}} \quad (21)$$

$$N_{2P} = 75 \text{ turns.}$$

A standard size of capacitor for C_2 considering the voltage step-up requirements is 10 micro-farads. Hence, the number of turns on the secondary is about

$$N_{2S} = \sqrt{2} N_{2P} = 106 \quad (22)$$

and the peak voltage on C_2 is about 330 volts.

The current in the primary winding is the same as that in the winding on the first pulsactor, so this winding can be of No. 16 copper wire also, with little increase in first stage losses. The secondary winding, however, must carry the output pulse current. If No. 14 copper wire is used, the winding resistance is about 0.10 ohms. Since the resistance for critical damping at the output is about 4.8 ohms the copper losses in this stage are only about 2% of total energy.

At critical damping the peak voltage is about 245 volts and the peak current is about 50 amperes, with a pulse width of about 45 micro-seconds. If the load falls much below about 4 ohms in this case, a tendency for

unstable operation of the pulser results, since not all the energy on C_2 is discharged in each pulse.

There is a difference in the output current for the circuits of figures 1 and 5. The output stage in figure 1 has the magnetizing current of the last pulsactor flowing through the load in the same direction and immediately before the current pulse. However, the transformer stage of the circuit in figure 5 gives a somewhat different current just before the main pulse. In this case, the current flow is the charging current of the capacitor, C_2 , and is in opposite direction to the main pulse when L_2 saturates. This charging current is usually larger than the magnetizing current that flows through the load in figure 1. If the last stage pulse compression ratio is small, the capacitor charging current of the circuit in figure 5 may be large enough to be troublesome.

The over-all pulse compression ratio of the two stage pulser calculated for the example was about 186. From curve No. 1 in figure 2 it may be seen that the optimum number of stages for minimum total core material is about 10. Since only two stages are used, it may be seen from figure 3 that about 10 times the optimum total core material is used.

Effect of Peak Magnetizing Force

In the calculated example it was assumed for both pulsactors that the actual iron saturated to a permeability of 1.0. This is only true if the peak magnetizing force is above about 150 oersteds. Below this peak value, the average saturated inductance over the entire current pulse starts to increase. This seems to be due to a steady decrease in the actual incremental permeability of the material to a value of 1.0 at about 50 oersteds as the knee

of the saturation curve is rounded.

The peak magnetizing force for the first pulsactor is

$$H_{m1} = \sqrt{\frac{W_{m1} 4\pi 10^7}{M_1 \mu_{s1}}} \quad (23)$$

$\cong 440$ oersteds.

This is well above 150 oersteds, so the average saturated inductance of L_1 is probably close to the calculated value.

The general expression for the peak magnetizing force is

$$H_{mk} = \frac{2(\Delta B_k)}{P_k \pi \mu_{sk}} \quad \text{for } k > 1. \quad (24)$$

Since this peak value is inversely proportional to the stage pulse compression ratio, it is usually advisable to keep the stage pulse compression ratios each below about 20. If larger compression ratios are used, the average saturated inductances will increase, and result in wasteful amounts of core material and the pulses will have both sides rounding considerably into the zero level.

References

1. W. S. Melville, "The Use of Saturable Reactors as Discharge Devices for Pulse Generators", I.E.E. Proc., Vol. 98, Part 3, 1951, pp. 185-207.
2. R. A. Mathias and E. M. Williams, "Economic Design of Saturating Magnetic Pulsers", Trans. A.I.E.E., 1955.

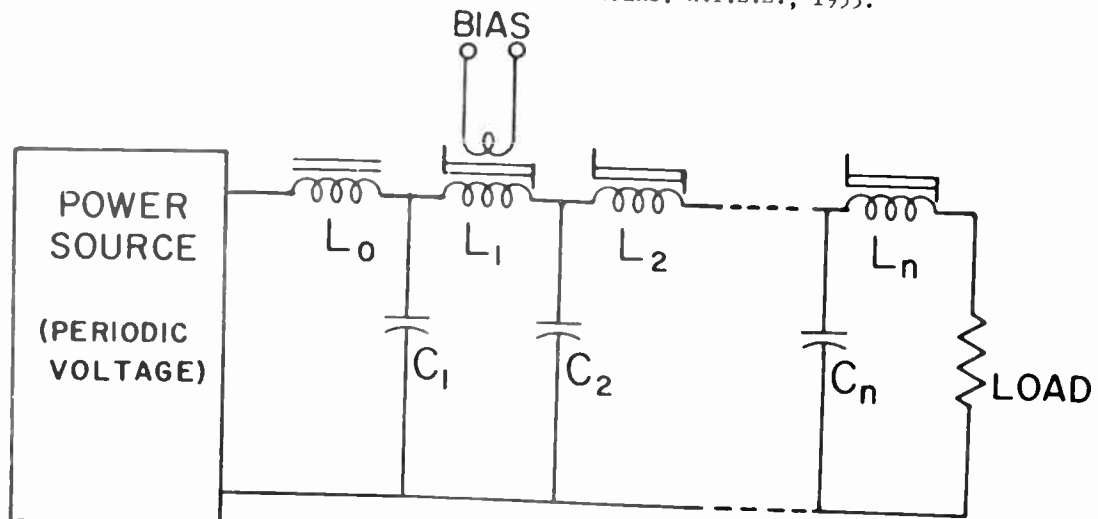


Fig. 1
Basic Magnetic Pulser Circuit.

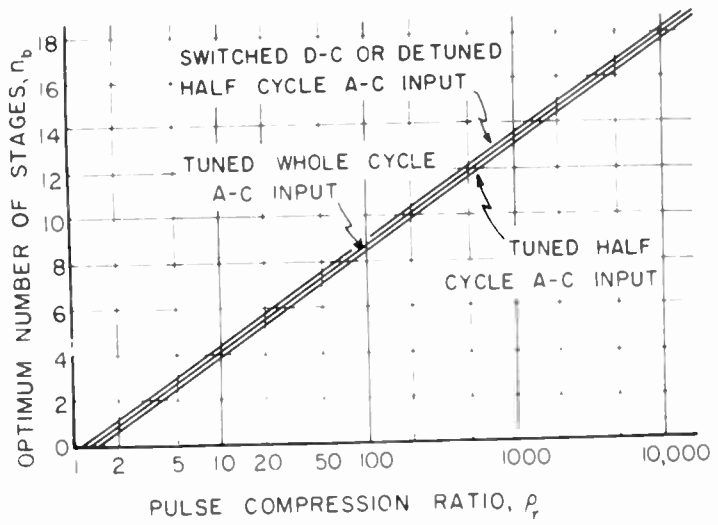


Fig. 2
Optimum No. of Stages for Minimum Total Core Volume.

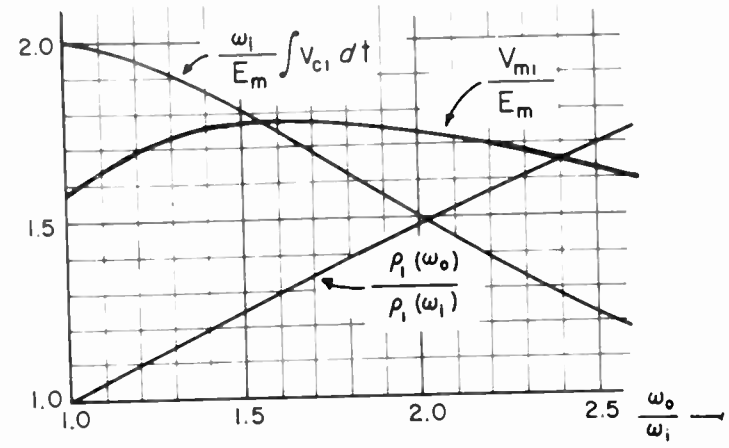


Fig. 4
Effect of Detuning L_0C_1 .

87

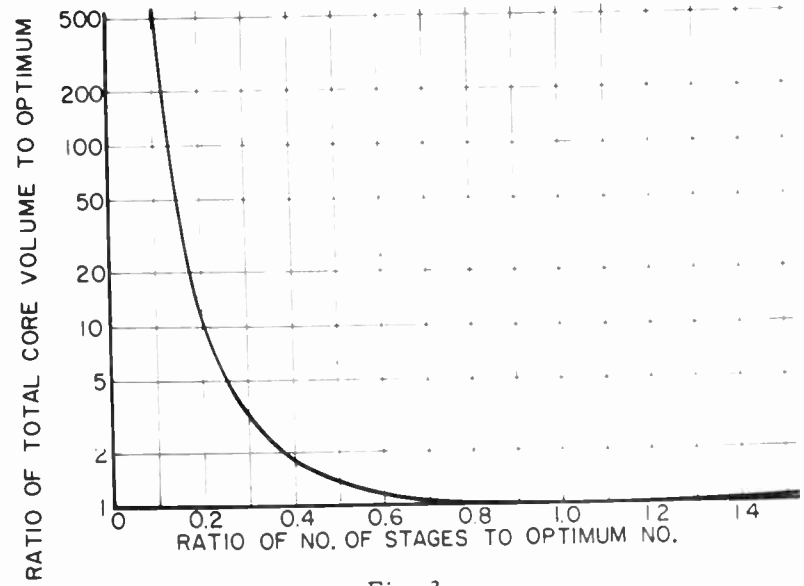


Fig. 3
Relative Total Core Volumes Needed for Pulsers.

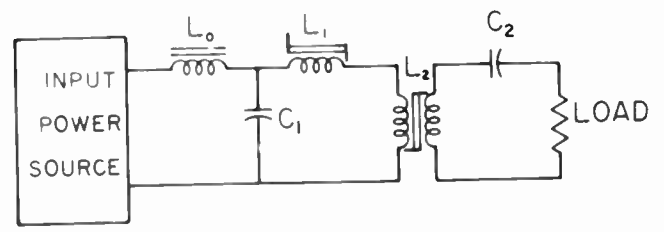


Fig. 5
Magnetic Pulsers with Transformer Connection.

MAGNETOSTRICTION RESONATORS AS CIRCUIT ELEMENTS

R. T. Adams
Federal Telecommunication Labs.
Nutley, N. J.

ABSTRACT

A compact magnetostriction rod resonator is described, applicable to a number of tone generator and filter circuits for carrier telephone and telemetering systems. The unit has properties of a single resonant circuit with independent input and output coupling. Frequency stability is ± 2 ppm per degree C, with typical Q's of 3,000 to 4,000 at 24 kc.

In addition to conventional applications as a "single-frequency" filter or as a frequency deter-

mining element, analagous to a quartz crystal, by suitable adjustment of magnetic bias, the resonator can be made to respond to sum and difference frequencies in the input and/or output circuit. A single rod can thus be used as a filter-modulator, as a modulator-filter, or as a complete heterodyne-tuned filter (modulator-filter-demodulator) tunable by means of an external local oscillator signal supplied to input and output. Efficient frequency doubling can also be performed by the element.

WIDE-BAND ELECTRICALLY TUNABLE OSCILLATORS

John L. Stewart
Kermit S. Watkins
University of Michigan
Ann Arbor, Michigan

Summary

This paper describes several recently explored low-level electronically tunable oscillators which illustrate techniques using conventional components and tubes for achieving rapid electrical tuning over relatively wide frequency ranges. The mechanism by which voltage (or current) control of frequency is achieved for each of the oscillators is described with particular attention being given to a most promising technique defined as parallel-network tuning. Typical circuitry as well as experimental curves relating output voltage and frequency as functions of the control voltage for the tunable oscillators are presented and practical limitations are discussed.

Introduction

Various techniques employing conventional tubes and components are available for achieving wide-range electrical tuning of low-level oscillators at frequencies below microwaves. It is the purpose of this paper to present experimental results on several oscillators which illustrate previously unexploited techniques in achieving rapid, wide-range electronic tunability.

Division of the various tuning techniques according to (1) reactance tuning, (2) resistance tuning, (3) pulse-circuit tuning, and (4) parallel-network tuning seems appropriate for this discussion. Resistance tuning and reactance tuning are achieved through the use of electrically variable elements, including the equivalent parameters of vacuum tubes. Pulse-circuit tuning can best be illustrated by the multivibrator whose repetition rate is varied as a function of a control voltage. A new technique, parallel-network tuning, is achieved by varying the relative gains of several parallel channels, each of which contributes to the over-all gain of the system.

Electrical control of reactance elements is perhaps the best known and most commonly employed tuning method. Reactance variations obtained through electrical control of ferro-electric and ferro-magnetic materials permit frequency control for many applications. The conventional reactance-tube modulator best exemplifies the use of the vacuum tube as an equivalent inductive or capacitive element. Oscillators utilizing a reactance tube have been built to operate at frequencies well above 100 mcs¹ and are suited to

applications which require tuning ranges twenty percent or less of the center frequency. Since reactance tuning and pulse-circuit tuning are quite common, specific examples of these techniques are omitted. Rather, emphasis will be placed on parallel-network tuning and simple, but relatively uncommon, resistance tuning.

Parallel-Network Oscillators

A parallel-network oscillator¹ is one having two or more variable-gain, parallel signal paths which have appropriately different transfer functions of frequency. The outputs of the two paths are added and returned to a common input with frequency tuning accomplished by varying the relative gains of the contributing channels. Theory invites consideration of systems involving any number of channels; however, the modulation of more than two channels simultaneously appears impractical. The typical two-channel, parallel-network oscillator is shown in Fig. 1. The particular choices for F_1 , F_2 , and F_3 control the oscillation frequency and amplitude characteristics depending primarily upon the functions F_1 and F_2 . It is usually desirable to make F_3 as independent of frequency as is conveniently possible. Both resonant and non-resonant (phase-shift) types of parallel-network oscillators have been explored experimentally. The phase-shift oscillator employs artificial transmission line high-pass or low-pass filter sections as illustrated by Fig. 2 and its approximate equivalent, Fig. 3. The frequency coverage ratio for this oscillator is roughly two-to-one. The resonant type oscillator represented by Fig. 4 employs parallel-resonant circuits operating off-resonance as leading and lagging networks. However, simple R-C lead and lag networks may also be employed in a similar fashion to achieve the proper phase relations.

Practical Design Requirements

The theory which has been developed for parallel-network oscillators permits reasonably accurate analytical design for the narrower tuning ranges. However, for frequency ratios larger than about 2-to-1, the design results obtained analytically represent only first-order approximations. The particular characteristics desired are more practically obtained experimentally. Several characteristics have been presumed desirable in all the oscillators presented here.

¹F. R. Dennis and E. P. Felch, "Reactance Tube Modulation of Phase Shift Oscillators" BSTJ, Vol. 23, No. 4, pp. 601-7, October, 1949.

¹The theory of parallel-network oscillators is the subject of a paper by J. L. Stewart entitled "Parallel-Network Oscillators", to be published, Proc. IRE.

First, and foremost, the frequency should be a near-linear (or logarithmic) function of control voltage. Second, amplitude variation with frequency (e.g., control voltage) should be a function that permits easy compensation if the application should require constant amplitude. Finally, reasonably good waveform should be maintained over the desired tuning range. Practically, the compromise of these various factors requires some experimental design.

Experimental Results

The experimental circuits and curves to be presented represent only a fraction of the possible useful circuit combinations. Particular requirements will invite a variety of modifications. In these examples, it should be noted that push-pull modulation has been employed to obtain tuning, although the number of tube sections modulated has been varied.

Figures 5 and 6 show the circuit and experimental behavior of a phase-shift type oscillator. Curves A and B of Fig. 6 were obtained with $L = 3.3$ and 5.5 microhenries, respectively, where C of Fig. 5 was adjusted in each case to give "compromise" behavior. The practical tuning range in each case is in excess of 30 percent. Figures 7, 8, 9, and 10 are variations of the oscillator of Fig. 4. The respective tuning characteristics are shown by Figs. 11, 12, 13, and 14. Note that in Fig. 7, 12AT7 twin-triodes are used with modulation applied to only two of the tube sections. In the circuit of Fig. 8, all four triode sections are modulated. Further, in the oscillator of Fig. 8, back-to-back diodes are employed to provide more symmetrical saturation characteristics. The resulting improvement in tuning behavior is marked. The circuits of Figs. 9 and 10 are similar, both employing R-C low-pass filters as one of the two signal paths. The circuit of Fig. 9 was designed and adjusted for a particular application requiring the linear frequency coverage shown in Fig. 13. The output, usually taken from the common grid, was padded with a capacitor for load simulation.

Except for the oscillator of Fig. 8, no monitor of wave shape was made while obtaining the experimental characteristics. It should be noted that for the higher frequency circuits, sufficient harmonic filtering is present to assure reasonably good wave shape. On the other hand, the oscillator of Fig. 8 (which tunes over an approximate ten-to-one range) exhibited considerable wave distortion below about two mc—between two and three mc the waveform was acceptable, and above three mc the waveform was excellent.

Whenever a parallel-network oscillator is made to have a tuning ratio appreciably greater than two-to-one, grid and plate saturation will have profound effects upon the waveform and cause considerable disagreement between linear theory and practice. In order to make theory and

experiment agree at all, it is necessary to limit the amplitude of oscillations to a small value.

The amplitude of oscillations is theoretically most constant with frequency at the output of the adding device. If the tuning range is small, a band-pass filter can be used at this point such that the harmonics are attenuated. Then, not only will the output have good waveform, but the feedback voltage will be a single-frequency signal in which case the agreement between experiment and theory will be good. However, if the tuning ratio is large, harmonics at the output cannot be entirely avoided. When such a distorted signal is fed back to the input, the agreement between theory and experiment may be quite poor—in the extreme case, discontinuities in the tuning characteristic may result. Further, a distorted signal, if too large, will not permit a reasonably linear addition of the signals from the two paths of the oscillator to be made.

If the tuning characteristic is satisfactory even though there may be considerable distortion, the waveform can be improved by passing the oscillator output through an electrically tuned tracking amplifier (which might also serve as a limiter). The tracking of this amplifier need not be critical nor will moderate hysteresis effects be important as, for example, when the tracked amplifier is tuned by means of ferromagnetic materials.

In order to minimize distortion, the amplitude of oscillations must be minimized. It is generally overly critical to minimize the open-loop gain in order to accomplish this; rather, some amplitude limiting device (other than the natural limiting characteristics of the amplifying tubes necessary to the oscillator) must be employed. For example, an automatic volume control circuit can be applied to a tube that carries the weighted sum signal. Another procedure that can be employed is to establish a symmetric saturation characteristic which effectively removes all even-order harmonics from the signal. A device commonly used to accomplish this is a thermistor. However, devices dependent on thermal behavior are not satisfactory when fast frequency modulation is desired. A less effective method, but one that can handle fast modulation, is to shunt some signal path to ground with crystal diodes connected in a back-to-back fashion such that large signals are amplified less than small signals.

Whatever the saturation characteristics may be, it can be expected that the tuning characteristics will be dependent upon them because the phase and magnitude characteristics of networks subject to saturation are generally dependent on the amount of damping furnished by grid loading and similar phenomena. If the saturation characteristics are determined largely by back-to-back crystal diodes, then the characteristics of the diodes will affect the tuning characteristics depending upon how important is the phase shift of the circuit in which they are located. Certainly, no general rules can be set down in this regard.

¹ Op. cit. pg. 2, footnote 1.

Electrical Resistance Tuning

A variety of common oscillator circuits utilize resistance as a primary frequency-controlling element. By the substitution of electrically variable resistances in such circuits, it is possible to obtain frequency variations in a manner somewhat analogous to reactance tuning. Resistance tuning appears to have been overlooked in the general search for tunable devices which is rather surprising considering the simplicity of the technique and its ready applicability to many existing oscillator circuits.

The basic three-mesh oscillator circuit of Fig. 15 adequately illustrates the technique. The frequency of oscillation for this device is given by

$$f_0 = \frac{\sqrt{6}}{2\pi RC}$$

In Fig. 16 the conventional resistances have been replaced with a series array of crystal diodes which, because of their roughly square-law behavior, permit the oscillator to exhibit a near-linear voltage-versus-frequency characteristic. If the diode resistance R_D varies as

$$R_D = k \frac{1}{E_A}$$

where E_A is the voltage applied to the crystal, then the frequency of oscillation may be expressed in terms of R_D as

$$\begin{aligned} f_0 &= \frac{\sqrt{6}}{2\pi C} \frac{1}{R_D} \\ &= \frac{\sqrt{6}}{2\pi C} k' E_A \end{aligned}$$

which shows f_0 to vary linearly with the control voltage E_A . Furthermore, the ratio of frequency tuning corresponds directly to the obtainable ratio of maximum to minimum resistance, which for crystal diodes in the forward direction may be five- or ten-to-one. If more complicated series and parallel crystal arrangements are employed, even greater frequency ratios may be obtainable.

The circuit of Fig. 17 illustrates the use of vacuum tubes as the variable resistances. In the arrangement shown, the output impedances of the cathode followers represent a resistive array which is controlled by the electrode voltages applied to the tubes. Since the output impedance of the cathode follower is approximately $1/g_m$, the oscillation frequency varies directly as g_m , which in turn is dependent on circuitry and control voltages.

Resistance Tuning Circuits and Experimental Results

The experimental oscillator of Fig. 18 was designed to operate at broadcast frequencies. It is basically the diode type oscillator with the crystal current being fed from the cathode follower. The cathode follower not only isolates the oscillator tube from the crystals but also has added virtue in that additional tuning is obtained

as a result of its changing output impedance. The filtering provided by the low-pass R-C sections (i.e., diodes and capacitors) preserves good waveform at the plate of the oscillator tube. Oscillations are maintained with as little as five volts control applied to the cathode follower plate. Figure 19 shows the tuning characteristics. The "A" curves show the initial experimental results. The "B" curves were obtained with a second oscillator with its rectified output providing a small amount of automatic gain control.

The experimental oscillator of Fig. 20 utilizes cathode follower sections. A pair of back-to-back diodes at the oscillator tube grid provides some amplitude control but slightly contracts the tuning range.

Both the diode and cathode follower oscillators are inherently suited to rapid modulation. The diode oscillator with unstabilized amplitude was modulated at a 6 kc rate with no evidence of instability. Higher rates were not attempted. While several milliamperes of current are required for modulation, modulation is single-ended and easily applied. The tuning capabilities of the cathode follower circuit could possibly be improved by controlling the tube bias while holding the plate-to-cathode voltage fairly constant. Screen-modulated pentodes operating as cathode followers may ease modulation requirements.

The cathode follower type circuits should be practical at fairly high frequencies—up to about one half the gain-bandwidth product of the tubes employed. It should be stated that little effort was directed towards optimizing the various circuits; consequently, the curves, except where back-to-back diodes are employed, should represent the characteristics predicted from analyses, although the analysis itself may in some cases prove quite burdensome.

References

- Fig. 1 Block Diagram of the General Parallel-Network Oscillator
- Fig. 2 A Parallel-Network Oscillator Employing Artificial Transmission Lines
- Fig. 3 Simplification of the Oscillator Employing Artificial Transmission Lines
- Fig. 4 A Parallel-Network Oscillator Employing Resonant Circuits
- Fig. 5 A Practical Oscillator Employing an Artificial Transmission Line
- Fig. 6 Tuning Characteristics of the Transmission Line Type Oscillator of Fig. 5
- Fig. 7 Resonant Type of Parallel-Network Oscillator
- Fig. 8 Experimental Parallel-Network Oscillator
- Fig. 9 An Oscillator Employing Lead and Lag Networks
- Fig. 10 An Oscillator Employing Lead and Lag Networks
- Fig. 11 Characteristics of the Resonant Parallel Network Oscillator of Fig. 7

- Fig. 12 Tuning Characteristics of the Oscillator of Fig. 8 Employing Lead and Lag Networks
- Fig. 13 Tuning Characteristics of the Oscillator of Fig. 9 Employing Lead and Lag Networks
- Fig. 14 Tuning Characteristics of the Oscillator of Fig. 10 Employing Lead and Lag Networks
- Fig. 15 Standard K-C Phase-Shift Oscillator

- Fig. 16 Electrically Tunable K-C Oscillator Employing Diodes
- Fig. 17 Basic Cathode-Follower Phase-Shift Oscillator
- Fig. 18 Experimental Control-Diode Oscillator: Experimental Tuning Characteristics of Diode-Diode Oscillator (Fig. 18)
- Fig. 19 Experimental Cathode-Follower Oscillator: Experimental Tuning Characteristics of Cathode-Follower Oscillator (Fig. 19)



Fig. 1
Block Diagram of the General Parallel-Network Oscillator

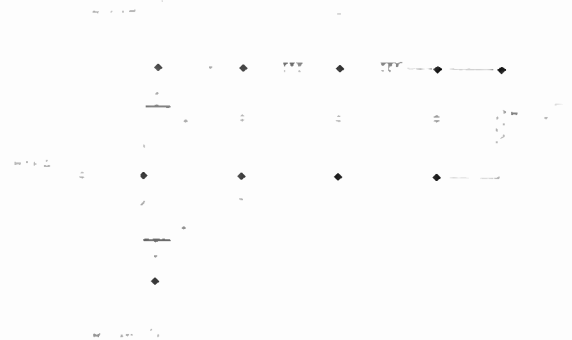


Fig. 3
Simplification of the Oscillator Employing Artificial Transmission Lines



Fig. 2
A Parallel-Network Oscillator Employing Artificial Transmission Lines

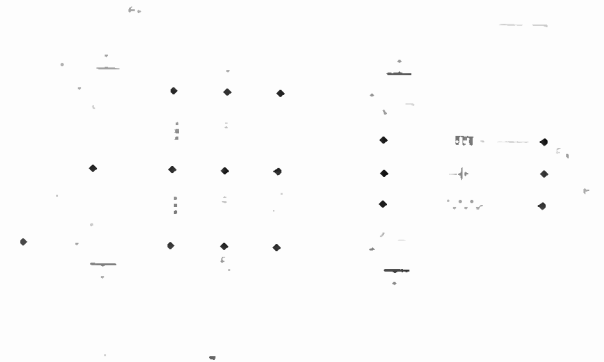


Fig. 4
A Parallel-Network Oscillator Employing Resonant Circuits

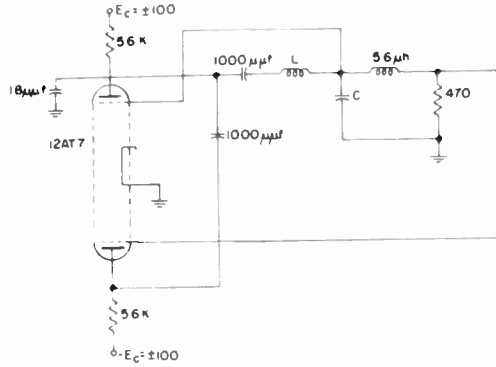


Fig. 5
A Practical Oscillator Employing an Artificial
Transmission Line

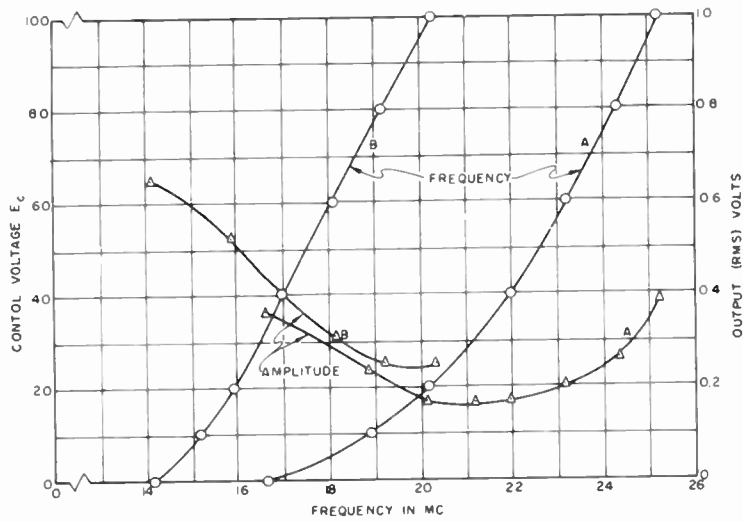


Fig. 6
Tuning Characteristics of the Transmission Line
Type Oscillator of Fig. 5

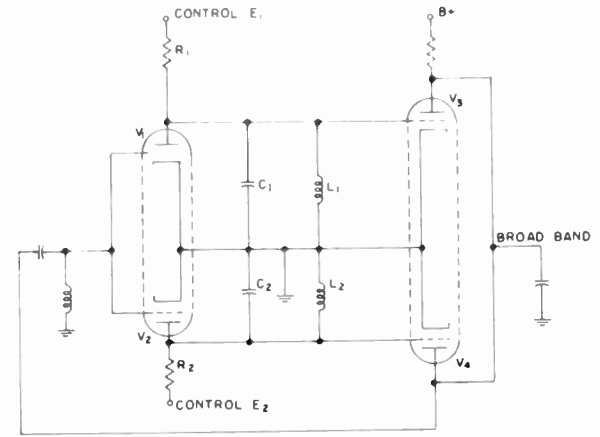


Fig. 7
Resonant Type of Parallel-Network Oscillator

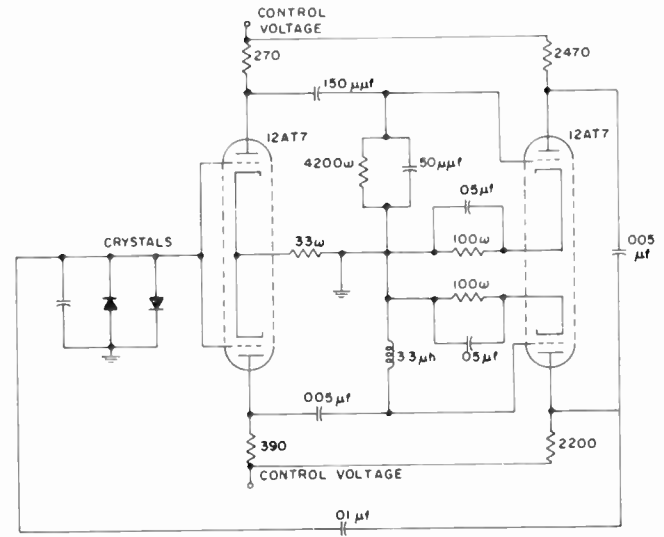


Fig. 8
Experimental Parallel-Network Oscillator

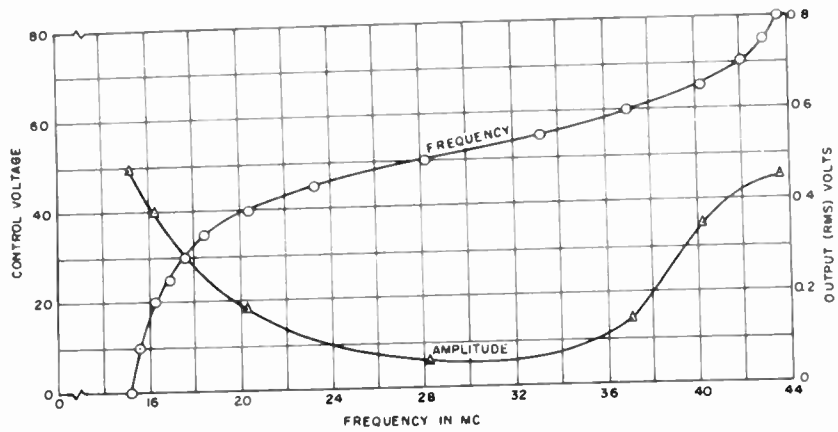


Fig. 13
Tuning Characteristics of the Oscillator of Fig. 9
Employing Lead and Lag Networks

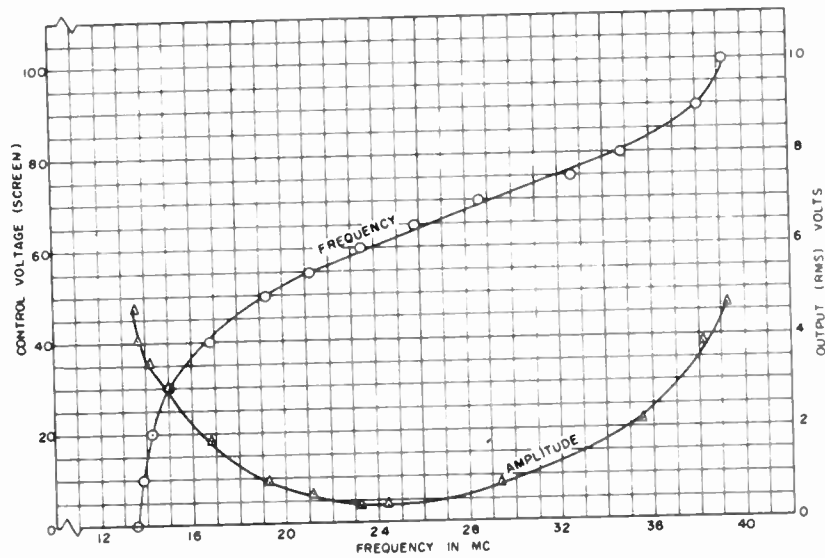


Fig. 14
Tuning Characteristics of the Oscillator of Fig. 10
Employing Lead and Lag Networks

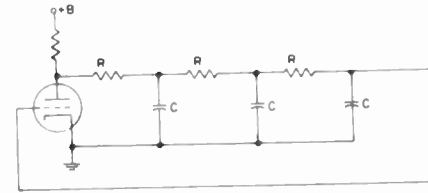


Fig. 15
Standard R-C Phase-Shift Oscillator

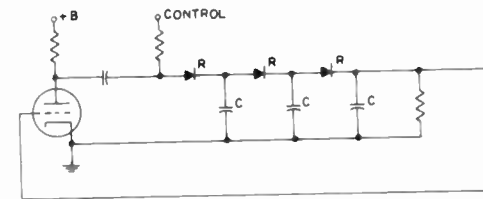


Fig. 16
Electrically Tunable R-C Oscillator Employing
Diodes

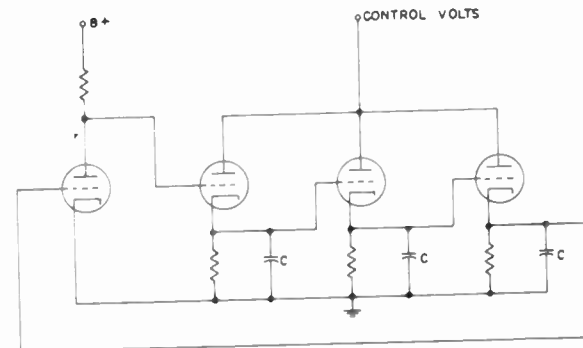


Fig. 17
Basic Cathode-Follower Phase-Shift Oscillator

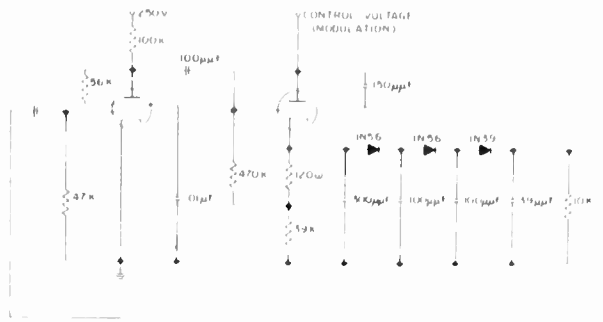


Fig. 18
Experimental Crystal-Diode Oscillator

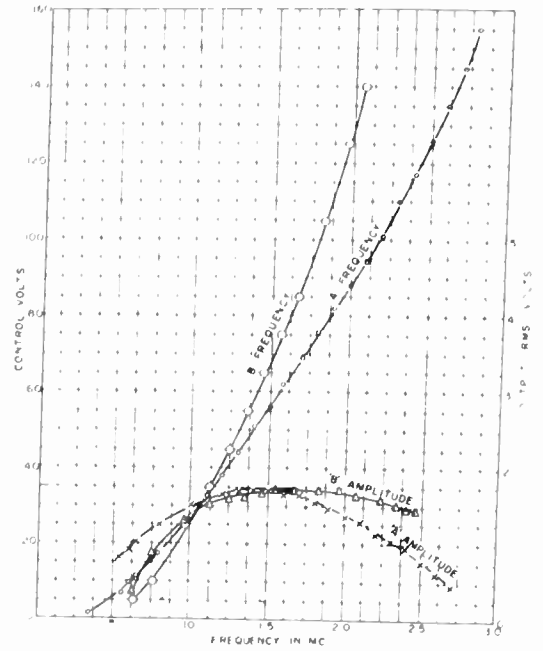


Fig. 19
Experimental Tuning Characteristics of
Crystal-Diode Oscillator (Fig. 18)

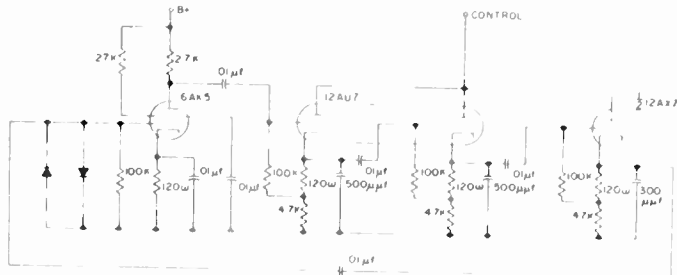


Fig. 20
Experimental Cathode-Follower Oscillator

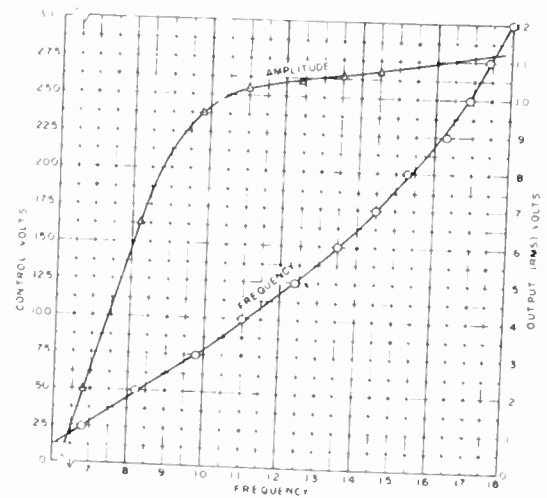


Fig. 21
Experimental Tuning Characteristics of
Cathode-Follower Oscillator (Fig. 20)

FLUORO-CHEMICAL LIQUIDS AND GASES
AS TRANSFORMER DESIGN PARAMETERS

L. F. Kilham, Jr. & R. R. Ursch
Raytheon Manufacturing Company
Waltham, Massachusetts.

Reduction of size and weight in electronic type transformers to keep pace with miniaturization in other phases of electronic component design has led directly to higher temperature operation. Temperatures in this region of 185°C require inorganic materials throughout, including where used, the dielectric coolant. In addition to materials that can operate at 185°C many other problems confront the transformer designer. Materials performance with respect to corona, heat dissipation, ability of liquid dielectrics to "self heal", toxicity, cost, thermal expansion, availability and other numerous characteristics are constantly under surveillance. Under BuShips Contract N0bsr/63239 entitled "Development of Transformers Utilizing recently developed Gases and Liquids, specifically Fluorochemicals", the Transformer Departments of the Raytheon Manufacturing Company have endeavored to develop design information and techniques resulting in reduction of weight and size and improvement of electrical characteristics of five specific Raytheon transformer designs. Although relatively expensive at the outset of this development, these new liquid and gaseous fluorochemicals have many characteristics of considerable interest to the transformer designer. A survey of fluorochemical suppliers ^{1, 2, 4, 5, 6, 7, 13} and a compilation of existing data ^{2, 8} indicates that these materials, in general, are stable, chemically inert and that they possess higher specific gravities and lower boiling points than liquids commonly used in transformers. Data indicates Liquid Fluorochemicals have low dielectric constants, power factors comparable to hydrocarbon transil oil, relatively high dielectric strength, self-healing abilities, non toxicity and most important, excellent high temperature characteristics.

Liquid and Gaseous Fluorochemicals have certain properties which would seem to make them good heat transfer agents ^{10, 11}. The more volatile liquid compounds with their low viscosity and high volume expansion offer interesting heat transfer possibilities by excellent convective cooling. It has been indicated that this convective cooling tendency could be related to various properties of the compounds and a characteristic assigned to the liquid which is known as the auto-convection modulus.⁹

Properties of Liquid & Gaseous Fluorochemicals.
Most Applicable to Magnetic Components.

To apply these characteristics to electronic type transformer designs it was necessary to develop, investigate and enlarge the scope of existing data. Specific points on which detailed investigation and tests were undertaken are as follows:

1. Compatibility of Liquid & Gaseous Fluorochemicals with Transformer Materials.
2. Further purification (where necessary) of fluorochemical liquids.³
3. Thermal stability of liquid & gaseous fluorochemicals.⁴
4. Dielectric properties of liquid and gaseous fluorochemicals.
5. Pressures anticipated in transformer designs using liquid and/or gaseous fluorochemicals.
6. Heat transfer data with simulated transformer design using liquid and/or gaseous fluorochemicals.

Compatibility of Liquid & Gaseous Fluorochemicals with Transformer Materials.

Compatibility of fluorochemical liquids with materials commonly used in the manufacture of high temperature transformers has been determined. Three cooperating vendors ran compatibility tests with common transformer construction materials sealed in ampules together with their specific liquid fluorochemicals. These samples were run for a considerable period of time at high temperatures. A most complete report was received from one of these suppliers. Table II shows a condensation of the Results of Compatibility Tests.

Initial testing of the volatile perfluoro liquids showed little or no effect on most transformer materials with the exception of silicone rubber. Interim reports on second round compatibility testing with the further purified liquids indicated that the compatibility problem was mitigated as a result of the extra purification.¹⁰

Further Purification of Liquid Fluorochemicals (where necessary).

A considerable number of commercially available liquid fluorochemicals have been checked for dielectric properties in the "as received" state. A simple means of further purification is as follows: Samples are mixed with a solution of caustic soda, separated and then run through a column of Fullers earth. Following treatments, the liquids show a marked improvement in their dielectric qualities. (Reference Table I.)

Thermal Stability of Liquid and Gaseous Fluorochemicals.

The method of testing was to purify all samples by the Fullers earth treatment and to measure insulation resistance. Samples were then kept at elevated temperatures for a period of one month and again readings were taken of insulation resistance. (Reference Table I.)

The insulation resistance tends to average slightly lower after the test. However, some of the liquids proved very stable and entirely suitable for transformer use.

Dielectric Properties of Liquid and Gaseous Fluorochemicals.

Test results of the dielectric properties of the tested fluorochemicals are shown (Reference Table I) and compared with transformer and silicone oils. Dielectric strength as shown by the table, is generally higher for the liquid fluorochemicals. The compounds are able to withstand repeated arcing without serious injury to their breakdown strength. The dielectric constant, power factor and loss factor were measured over a range of frequencies and are tabulated for 50 cycles and 100 kilocycles. As shown, insulation resistance is tabulated for the measurements before purification, after purification and after the thermal stability tests. In general the dielectric properties of liquid and gaseous fluorochemicals compare favorably with the conventional transformer materials.^{2,10}

Pressure Developed in an Enclosed System Using Liquid and/or Gaseous Fluorochemicals.

To obtain additional information for design use, tests have been run to determine pressures likely to develop in transformers filled with fluorochemical liquids and gases. The fluorinated liquids differ from conventional transformer oils in several important respects.

1. They have unusually high coefficients of thermal expansion, several times that of mineral oil or silicone oil.
2. They are volatile in varying degrees.
3. (In conjunction with gas.) The absorption by the fluorochemical liquid of a fluorochemical gas present in the expansion space may differ very materially from that experienced in a transformer filled with conventional transil oil.

Reference to Fig. I shows that pressures anticipated with fluorochemical liquids appear to be considerably greater than normally expected in a transformer filled with mineral or silicone oil. However it has been found that the pressure problem is mitigated by the solubility of the gas in the expansion space into the liquids. Proper selection of this combination may further help the design. A typical curve showing the re-

duction in pressure that may be obtained by using a more soluble gas is given (in Fig. 2) for a specific gas to liquid ratio (at room conditions). For a design purpose a curve similar to Fig. 3 which shows the pressures that may be developed when the gas-liquid ratio is varied, is useful.

The above-mentioned factors must be taken into consideration in the design of units utilizing fluorochemical liquids and gases as dielectric coolants.

Heat Transfer Data with Simulated Transformer Design Using Liquid and/or Gaseous Fluorochemicals.

Heat transfer characteristics of the fluorochemical coolants were compared to usual transformer fill liquids whose characteristics are known. Using a transformer enclosed in a test cell with the liquid dielectric coolants under investigation, the cooling efficiency of the various liquids was tabulated as shown in Fig. 4. It should be noted that this is a plot of coil temperature rise above case temperature versus watts input. Observation of the upper curve for silicone oil (100 cstks.), shows that the gradient between the highest measured coil temperature and the case temperature is about 85°C (at 60 watts loss) and that for fluorochemical B (lower curve) the comparative gradient is only 20°C.

Additional test information shows that the temperature gradient existing between various parts of the transformer is very small when using fluorochemical liquids as compared to conventional transformer-fill materials. (Fig. 5.)

Design Techniques

With the data developed as shown in the preceding portions of this paper, several methods of using the gases and liquids are apparent. With the realization of sufficient dielectric strength protection, low 'k' for higher frequency response, self healing properties, minimum corona problems, high temperature characteristics, etc., the attempted solution of the problem of reduction of size and weight of magnetic components is as follows:

Several design techniques using fluorochemicals have been developed in detail. The most promising techniques are listed, followed by detailed explanations.

1. Volatile Fluorochemical liquid fill.
2. Combination or "tailor-made" Fluorochemical liquid dielectric coolants.
3. Partial fill and use of wicking action of Liquid Fluorochemicals.
4. Liquid Fluorochemical fill with gas Fluorochemical at reduced pressure in expansion space.

5. Liquid and/or gas fluorochemical fill in conjunction with heat conducting tabs.

Volatile Liquid Fill

The liquid fluorochemical fill technique provides a means of transferring heat from the heat source to the case surface in a rapid manner. This method places the transformer in an enclosed system together with a suitable fluorochemical and expansion space. Cooling by this method is obtained from the high auto-convection of the fluorochemicals and from the heat transfer ability of the volatile liquid vapors as they come into contact with the container surface in the expansion space. The dissipation of heat through the expansion space, which in ordinary transformers is not too effective, is considerably increased.

The effectiveness of this method is demonstrated by Fig. 4. This figure shows that the more volatile liquids give more rapid cooling, however, they present greater internal pressure problems to which a transformer engineer must adjust his design.

Combination or "Tailor-made" Liquid Dielectric Coolants.

Since these fluorochemical liquids are inert and volatile in varying degrees, it is possible for the design engineer to calculate an optimum liquid mixture for a specific transformer at a specific operating condition. By reference to Fig. 1 the value of this approach can be observed. If the hot spot temperature is 200°C and a gradient of 40°C is assumed between case and hot spot the resulting case temperature will be 160°C. If the allowable internal pressure is arbitrarily set at a maximum of 45 psig, the characteristics of an "optimum liquid" is shown in Fig. 1. It can be seen by examination that this "optimum liquid" is a compromise between the volatility of the liquid desired for maximum cooling and mechanical considerations that limit the maximum internal pressure.

A method of calculating the "optimum liquid" is as follows: For a given transformer design and its operating ambients, the case surface temperature may be determined. For mechanical design an allowable safe value may be established for the internal pressure developed. The internal pressure due to the expansion of the optimum liquid (assuming two liquids have nearly the same coefficient of expansion) and the heating of the gas in the expansion void can be taken from a curve similar to Fig. 3. In addition to the pressure data taken from Fig. 3 the vapor pressure must be calculated. The allowable vapor pressure of the optimum liquid, P_o , is the maximum safe case pressure less the pressure determined for the expansion of liquid and the heating of the gas. The following equation may be solved for the ratio

$$\frac{W_B}{W_A}$$

$$\frac{W_B}{W_A} = \frac{(P_o - P_A)}{(P_B - P_o)} \frac{M_B}{M_A}$$

W_A - wt. of less volatile liquid.

W_B - wt. of more volatile liquid.

M_A - Molecular wt. of less volatile liquid.

M_B - Molecular wt. of more volatile liquid.

P_A - Vapor pressure of less volatile liquid, at the operating temperature.

P_B - Vapor pressure of more volatile liquid, at the operating temperature.

P_o - Maximum vapor pressures of the optimum liquid at the operating temperature.

A liquid mixture of this ratio should give maximum cooling possible consistent with pressure considerations for the given operating conditions.

Partial Fill and Use of Wicking Action of Liquid Fluorochemicals.

In some transformer designs where the dielectric strength is not too severe it is possible to fill partially the transformer container with a volatile fluorochemical liquid and utilize the exceptional wetting action of liquid fluorochemicals by the use of wicks to carry the liquid to the coil hot spots.

If the temperature of the hot spot is above the vaporization temperature of the liquid, the liquid will vaporize upon contact with the hot spot. The vapors complete the cycle by condensing upon contact with the cooler case surface. In this manner considerable heat is transferred to the container surface. A transformer of this type has been built.

Fluorochemical Liquid and Fluorochemical Gas Combination as Dielectric Coolants.

The use of a fluorochemical gas at lower than atmospheric pressure in the expansion space over the liquid (while being approximately equal to air at 1 atmosphere as a dielectric) offers advantages in relation to heat transfer. With a transformer container having a large surface area at the top to facilitate condensation of vapors, any air or gas present in the case at the time of sealing displaces a portion of the vapor during operation, thus reducing the effective cooling. By reducing the quantity of gas at the time the unit is sealed, the entire upper surface of the container provides condensing area for the vapor and the heat dissipation is increased. The use of this technique is also a practical means for the control of internal pressure within mechanical design limitations.

The use of fluorochemical gases in such a combination may give necessary dielectric protection when the liquid vapors are inadequate (i.e.) low temperature starting conditions, etc.

Liquids and/or Gas Fill in Conjunction with Conduction Techniques.

Presently, many dry type transformers are being produced with copper strips (Raytheon Pat. Application #1146) placed at strategic places in the coil and around the core to remove heat from a transformer. Considerable heat can be removed by this method, resulting in a reduction of size. The application of the "dry type conduction" appears limited to transformers of moderate voltages. In applications where high voltage and corona is a problem it is possible to enclose the unit, seal it under pressure with a fluorocarbon liquid and/or gas, and to utilize conduction tabs to transmit heat to the case which serves as a radiator. When a cold sink is provided this becomes more effective. This technique offers in many instances, a design of less weight and less cost. If fluorochanical gases are used under certain conditions in such an application instead of the liquid gas combination, greater savings in weight and cost may be realized.

Typical Applications

Although the application possibilities of the above techniques are numerous it is beyond the limits of this paper to detail more than the following representative designs.

Two Raytheon transformer designs have been chosen to demonstrate the use of the above design data in actual practice. Techniques using Fluorochemicals are applied to these existing designs to show reduction in size and weight.

A. Redesign of Filament Transformer Raytheon #292-1389G1

Transformer A, is a low-capacity, high test-voltage Magnetron Filament Transformer with specifications as follows:

Primary voltage - 115V. R.M.S. 400 cycles
Secondary voltage - 3.7V R.M.S. with primary tapped to give 4.3V.
Secondary current - 43 amps.
Capacity between secondary and primary tied to ground to be less than 20 MMF.
Primary test voltage - 1.7K.V. R.M.S.
Secondary test voltage - 43 K.V. Peak.

In addition to the usual high temperature electronic type transformer calculations other design considerations become significant. A transformer of this type has a certain capacitance to ground associated with the high voltage winding. For a given air spacing from winding to ground, there is also a maximum high voltage which cannot be exceeded without inserting additional dielectric insulating media in the spacing. If the dielectric material has a dielectric constant greater than the air which it replaces, the capacitance of the high voltage winding increases accordingly. With this type of transformer, the design problem calls for a dielectric material which has high dielectric strength and reasonably

low dielectric constant, if there is to be a reduction in size. A fluorochanical gas or liquid fulfills these requirements provided a non-metallic enclosure is used.

The use of fluorochanical gas at high pressure (30 to 45 psig) with a dielectric constant of practically one is a possibility. However a fluorochanical liquid with a dielectric constant of 1.8 could give satisfactory results as far as capacitance is concerned, and in addition, would "materially reduce the size" because of its greater heat dissipating properties.

To the previous electrical specifications a transformer has been developed using a fluorochanical liquid as a dielectric. A special ceramic enclosure of high density alumina serves both as a container and a high voltage terminal. The resulting size reduction is shown in Fig. 6.

Tests of this design indicate that the unit is capable of operating in ambients of 140°C with a hot spot temperature rise in the vicinity of 35°C. The high voltage capacitance measurement is less than 15 MMF. Electrical Performance is excellent including a considerable reduction of corona. The reduction in size is over 4 to 1 by volume.

B. Redesign of Ultrasonic Output Transformer Raytheon #292-2059G1

Transformer B is an ultrasonic output transformer to which the technique of a "tailor-made" liquid is applied. Its specifications are as follows:

Output Frequency - 19-29 KC.
Impedance - 4800 ohms CT to 1900/1100/890/450
Test Voltages - Pri. 25000 V. D.C.
Sec. 16,000V. D.C.
Response - Flat within $\pm 1\frac{1}{2}$ DB
Output - 2 KW continuous or 35 KW (35 milliseconds pulse) 7% duty cycle.

From the method previously outlined the optimum liquid was calculated for this specific design. These calculations indicated that under the conditions of 45 lb./sq. in. gage max., Ambient 125°C max., 200°C max. hot spot temperature that a mixture of two parts Fluorochemical A and one part Fluorochemical B is the requirement.

The resulting reduction of two to one in volume of the redesigned unit is shown in Fig. 7. In addition the "K" of 1.8 of fluorochanical liquid as compared to a higher "K" of the previous transformer oil resulted in considerably less distributed "C" and better high frequency response. Electrical performance including corona was improved.

Conclusions

Fluorochemical liquids and Gases have become established as transformer design parameters. Their ability to operate as stable and neutral

materials at temperatures in the vicinity of 200°C allows their use as high temperature transformer materials. Their electrical properties which parallel "Transil Oil" make them useful in transformer design. Their unique characteristics --self-healing under arc-over conditions, low dielectric constants, thermal stability, excellent heat transfer ability and minimum corona problems-- lead directly to the reduction in size and weight of various types of electronic transformers.

So efficient is their transfer of heat from the hot spots of the transformer to the case that it appears that the emphasis of further transformer miniaturization may well rest with the equipment designer. Optimum heat dissipation methods such as "heat sinks" or turbulent air bid for further reduction in size and weight of such magnetic components. Preliminary tests on this subject bear out this contention.

To speak only of the immediate present, it is now apparent that it is no longer practical for the equipment designer to be content with specifying an ambient temperature alone. Such improved heat transfer mechanisms as have been just described demand a statement of Ambient Temperature plus a statement of the Capacity (of the surrounding medium) To Transfer Heat. Such a modifying "Coefficient of Heat Transfer" would consider the radical difference between say still air 100°C ambient and a 100°C "cold plate". Further saving of size and weight in transformers is of great importance. Let us consider this approach.

References

1. "FLUOROCARBONS" - A Brochure published by Minnesota Mining and Manufacturing Company
2. "ELECTRICAL PROPERTIES - INERT LIQUIDS" - A Brochure published by Minnesota Mining and Manufacturing Company.
3. "SULFUR HEXAFLUORIDE" - A Brochure published by General Chemical Div. Allied Chemical and Dye Corporation.
4. "PROPERTIES OF KEL-F-OILS, GREASES AND WAXES" - Kel-F Technical Bulletin #51-52.
5. "FLUOROLUBES" - (Booklet #30) Hooker Electrochemical Company.
6. "PERFLUOROCARBONS" - A Brochure published by E. I. duPont de Nemours Company
7. "HALOCARBON OILS, WAXES & GREASES" - A Brochure published by Halocarbon Products Corporation.
8. "SOME FLUORINATED LIQUID DIELECTRICS" - N. M. Bashara A.I.E.E. Technical Paper 53-135 Winter General Meeting A.I.E.E. January, 1953.
9. "SOME FLUORO-CHEMICALS FOR ELECTRICAL APPLICATIONS" - N. M. Bashara Proceedings of Symposium on Progress in Quality Electronic Components. Washington, D.C. 1952.
10. "DIELECTRIC & COOLANT STUDIES OF INERT FLUORO-CHEMICAL LIQUIDS" M. Olyphant, Jr. and T. J. Brice, Minnesota Mining and Manufacturing Company, St. Paul Minnesota. Proceedings 1954 Electronic Components Symposium, Washington, D.C.
11. "PREPARED DISCUSSION" of above paper by L. F. Kilham, Jr. "Proceedings 1954 Electronic Components Symposium" Washington, D.C.
12. "GASEOUS INSULATION FOR HIGH VOLTAGE TRANSFORMERS" Camilli, Gordon & Plump -- A.I.E.E. Technical Paper 52-78 Winter General Meeting. January 1952.
13. "SULFUR HEXAFLUORIDE - PROPERTIES AND METHOD OF HANDLING" - A Brochure published by Pennsylvania Salt Manufacturing Company.

IDENTIFICATION LETTER	CHEMICAL FORMULA	DIELECTRIC CONSTANT 50 CYCLES TO 100 KC	POWER FACTOR %		LOSS FACTOR		RESISTIVITY OHMS/CM ³ 1.6 KV/CM			DIELECTRIC STRENGTH A.S.T.M D-877
			100 CYCLES	100 KC	50 CYCLES	100 KC	AS RECEIVED SAMPLES	AFTER ADDITIONAL PURIFICATION	AFTER THERMAL AGING	
PERFLUORO COMPOUNDS										
A	(C ₄ F ₉) ₃ N	1.89	0.0025	0.005	0.0025	0.0095	0.75 x 10 ¹⁴	6.3 x 10 ¹⁴	6.3 x 10 ¹⁴	> 40KV
B	C ₈ F ₁₆ O	1.84	0.016	0.029	0.118	0.053	2.5 "	6.3 "	0.63 "	> 40KV
C	C ₆ F ₁₂ O	1.80	0.0024	0.0048	0.0043	0.0086	0.21 "	6.3 "	----	> 40KV
D	C ₇ F ₁₄	1.7	0.0045	0.0005	--	--	0.93 "	12.5 "	----	≈ 35KV
E	C ₈ F ₁₆	1.75	0.0098	0.0010	--	--	0.08 "	6.3 "	1.5 x 10 ¹⁴	≈ 35KV
F	C ₁₂ F ₂₆	1.8	--	--	--	--	0.9 "	1.9 "	2.0 x 10 ¹⁴	--
CHLOROFLUORO COMPOUNDS										
G	(CF ₂ CFCl) ₂	2.51	0.022	0.005	0.023	0.012	0.03 "	0.6 "	0.09 "	> 40KV
H	(CF ₂ CFCl) _n	2.66	0.0017	0.0017	0.007	0.005	0.14 "	1.1 "	0.5 "	≈ 22KV
J	(CF ₂ CFCl) _n	2.75	0.0008	0.008	0.0043	0.022	0.62 "	2.5 "	0.75 "	--
K	(CF ₂ CFCl) _n	2.80	0.004	0.04	0.0046	0.115	0.08 "	1.4 "	2.5 "	--
L	(CF ₂ CFCl) _x	2.80	0.0002	0.0024	0.0022	0.0067	0.25 "	2.5 "	0.75 "	--
M	(CF ₂ CFCl) _x	2.80	--	--	--	--	0.17 "	0.8 "	0.5 "	--
CONVENTIONAL OILS										
O	TRANSIL	2.2	0.014	--	--	--	1.25 x 10 ¹⁴	6.3 x 10 ¹⁴	--	≈ 25KV
P	SILICONE	2.7	0.01	0.01	--	--	6.3 x 10 ¹⁴	--	--	≈ 30KV

Table 1
Electrical Properties of Selected
Fluorochemical Liquids.

TRANSFORMER MATERIALS TESTED FOR COMPATIBILITY	FLUOROCHEMICALS					
	LIQUID A		LIQUID H		LIQUID M	
	Δ WT %	APPEARANCE	Δ WT %	APPEARANCE	Δ WT %	APPEARANCE
TEFLON MAGNET WIRE	+0.6	SLIGHT DARKENING	+10	SLIGHT DARKENING	-	GRAY COLORING
COPPER FOIL	-	DULLING OF COLOR	-	WHITE COATING	-	GRAY COATING
SILICONE RUBBER	-2	LITTLE EFFECT	+50	BAD SWELLING	+30	SPLITTING & SWELLING
SILICONE GLASS	-3	SLIGHT DARKENING	+20	DARKENING	-0.2	DARKENING
TEFLON SHEET	+5	NO CHANGE. (PLASTISIZER ACTION)	+5	NO CHANGE. (PLASTISIZER ACTION)	+6	NO CHANGE. (PLASTISIZER ACTION)
SILICON STEEL	+0.3	SLIGHT DARKENING	+7	GRAY TARNISH	-	NO CHANGE

LIQUID "A" AND OTHER LIQUIDS OF THIS TYPE APPEAR TO BE THE MOST SUITABLE LIQUIDS FROM THE STANDPOINT OF COMPATIBILITY WITH TRANSFORMER MATERIALS

Table 2
Results of Compatibility Testing of
Fluorochemical Liquids.

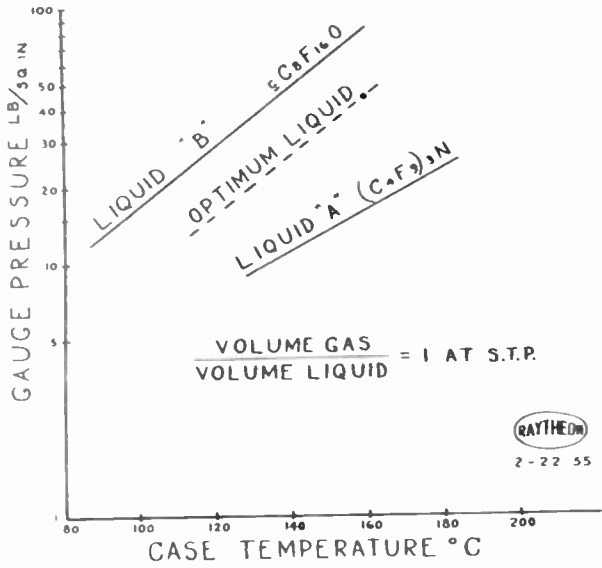


Fig. 1
Typical Pressure Curves of Fluorochemical Liquids in a sealed container.

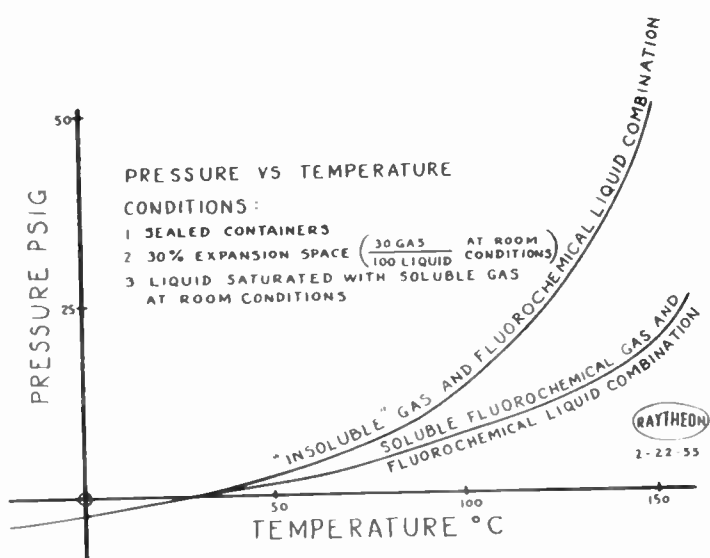


Fig. 2
Typical Curve of Pressure - Temperature Relationship of Fluorochemical Liquids Showing Effects of Gas Solubility.

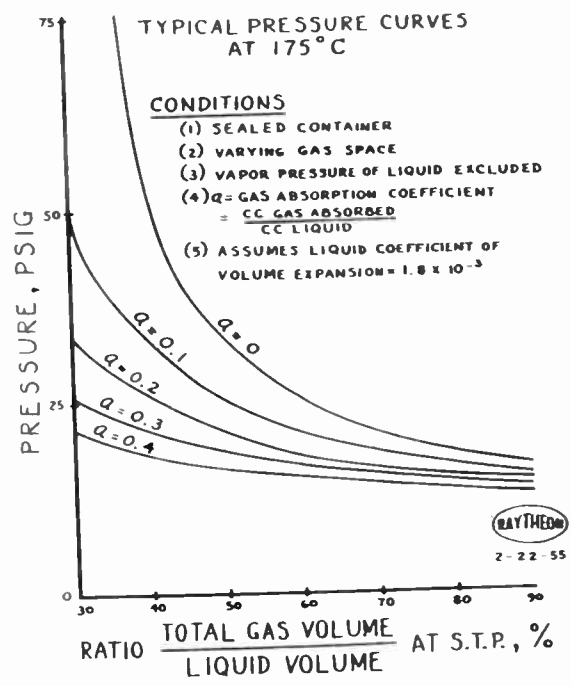


Fig. 3
Typical Pressure Curves for Fluorochemical Liquid - Gas Combination with Various Gas Absorption.

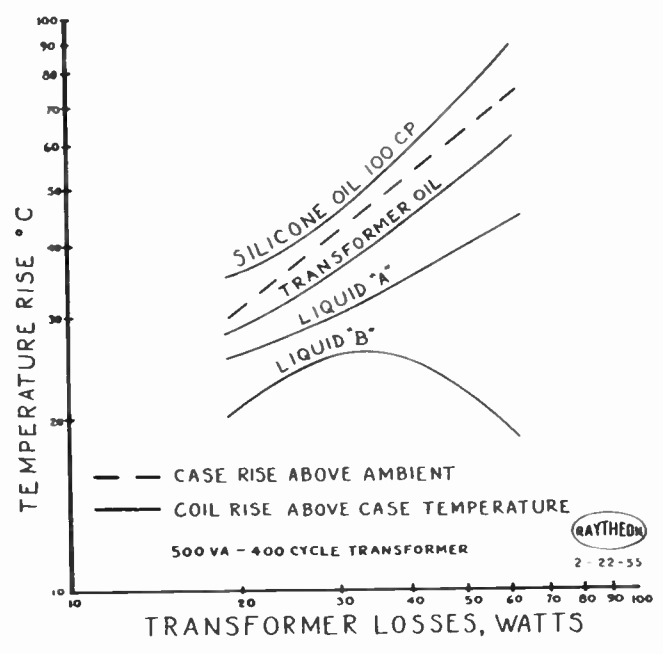


Fig. 4
Comparison of Coil Temperature Rises with Various Fluorochemical Liquid Coolants.

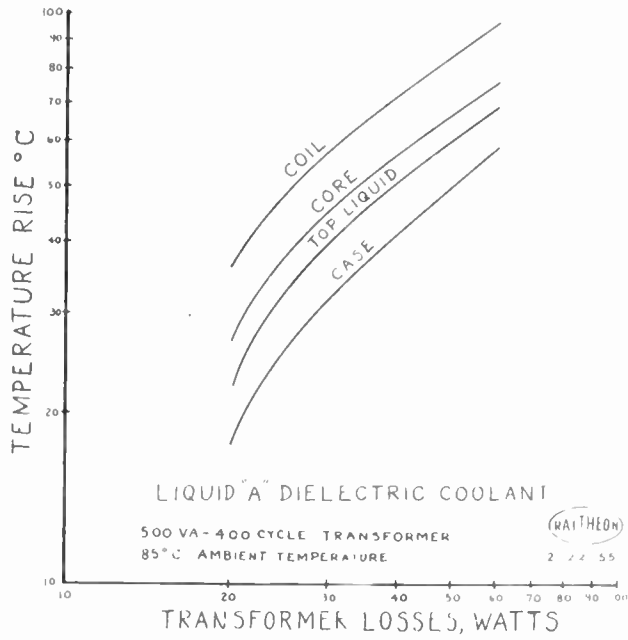


Fig. 5
Temperature Rise of Various Transformer
Parts Above Ambient Temperature.

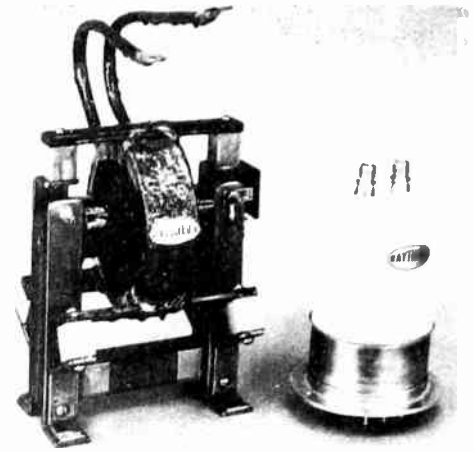


Fig. 6
Size Reduction of a Fluorochemical Liquid
Fill Magnetron Filament Transformer
(4 to 1 by Volume).

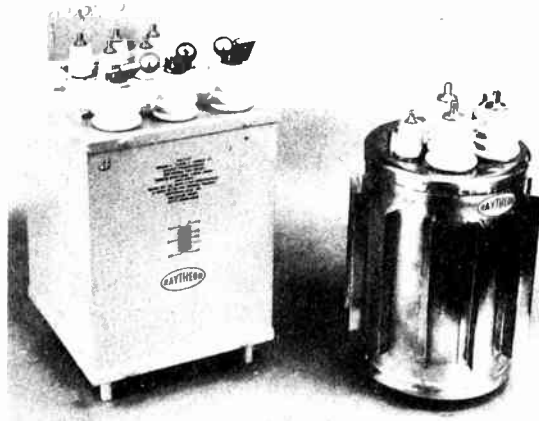


Fig. 7
Size Reduction of a Fluorochemical Liquid
Filled Ultrasonic Output Transformer
(2 to 1 by Volume).

THERMAL PROPERTIES OF SEMICONDUCTOR DIODES

J. N. Carman and W. R. Sittner
Pacific Semiconductors, Inc.
Culver City, California

Summary

Methods for determining steady state and transient thermal properties of semiconductor diodes are presented. Comparisons of power dissipation constants and thermal time constants of various diode package designs are given.

Curves of measured junction temperature rise as a function of power dissipation are shown together with effects of dissipated power on electrical characteristics.

Operation of diodes at elevated temperatures and power derating considerations are discussed. The relationship between the package dissipation constant, the mount dissipation constant, and the combined dissipation constant is outlined.

Introduction

The power handling capability of a semiconductor diode is dependent on the design effectiveness of both the device development engineer and of the application engineer who uses it. The user has often been limited unnecessarily by a package design with inherently poor thermal transfer capabilities.

The power handling limitation set by the diode package design can best be evaluated by considering the package alone; that is by placing the package in a heat sink so that its external pin or lead is held at a constant temperature. The other part of the problem, the dissipation properties of the mounting arrangement, can be analyzed separately.

Diodes produced by 11 manufacturers were analyzed and found to fall roughly into three classes. Figure 1 is a schematic representation of the three classes showing the elements essential to a heat flow analysis. The three diagrams are to the same scale; however some averaging was necessary for both A and C types since there were minor variations between designs within each of these classes. Type B is a diode of new design.

Analytical Treatment

Theoretical analysis of the heat flow problem is very difficult unless one makes some simplifying assumptions. Figure 2 shows a schematic of the model used where the simplifying assumptions are:

1. All the electrothermal energy conversion takes place at the diode junction (radius r_0).
2. The metal-to-solder junction is an

isothermal plane.

3. The thermal conductivity of the solder and the semiconductor are equal. The thickness of the solder layer may be increased by the ratio of thermal conductivities if more accuracy in the results is desired.

4. Heat losses by convection and radiation may be neglected.

The flow within the metallic pin and whisker was analyzed in cylindrical coordinates whereas the flow problem inside the crystal was solved by the method of images. Solutions for the power transferred through the crystal pin and through the whisker are shown in Figure 2. The power removed through the whisker is negligible except when considering the transient situation in a short time interval. With diodes of Type A, the term

$\left(\frac{4}{\pi d} \frac{l}{K} \frac{3}{3}\right)$ is of predominant importance and with

Type C about half the thermal drop is due to it. However with diodes of Type B, its contribution is less than 10%. In this case the $\frac{l}{r_0}$ becomes

a critical factor. Clearly r_0 varies considerably between point contact, gold bonded and alloy junction diodes.

Metallographic sections were made of several gold bonded diodes so that the dimensions could be accurately measured. The dissipation constants were then calculated and compared to previously determined experimental values. Thermal conductivities of materials shown in Figure 1 which were used for calculation are:

Pins	(Copper	.94	cal/sec/cm/°C
	(Brass	.2 - .3	
	(Dumet average about	.4 - .5	
Mounts	(Solders	.07 - .15	
	(Conducting plastic	.1 - .3	
Semicon- ductor	(Germanium	.14	
	(Silicon	.20	
Whiskers	(Gold	.71	
	(Tungsten	.48	
	(Moly.	.35	

Figure 3 shows a comparison between calculated and measured dissipation constants for several diodes.

The agreement is good; however all of the deviations are in one direction. This can be

accounted for by noting that the junction is not really a complete hemisphere but a segment of one and that since W is not extremely large with respect to r_0 , the solder interface is not exactly an isothermal plane. This is particularly significant where the pin is of high conductivity material such as copper. Diode No. 10 was of that type -- others with thinner crystals might show still further disagreement. Diodes no. 78 and no. 79 were of Type B construction using brass-type pin material. Diode no. 26 was gold bonded and its r was assumed to be the same as numbers 78 and 79. Diode no. 75 was a point contact type and so r was estimated, giving the range of values 6 to 13 milliwatts/ $^{\circ}\text{C}$.

Experimental Method

The method¹ used to experimentally evaluate the dissipation constants was extremely simple, although it did involve considerable care and technique. A diagram of the circuit employed is shown in Figure 4. The constant voltage generator was used for forward power and the constant current generator for back power. While this relay is normally make-before-break, by very light excitation, the relay will break before make with an effective transit time of from 10 to 50 microseconds.

Figure 5 shows an example of the back current as a function of time as it was observed on the oscilloscope. This Type B' diode (a Type B diode with a brass type pin) was dissipating 1.12 watts before being switched to the 12v back bias. The scale of the upper trace is 100 microseconds per cm. In descending order, the remainder are 1, 10, and 100 milliseconds per centimeter and the bottom line is the quiescent current at -12v. The two frames in the photograph were taken under identical conditions to demonstrate the reproducibility of the method.

In order to relate back current to temperature, each diode had to be calibrated by measuring its back current at -12v in an oven. Such a calibration is shown in Figure 6. The principal precaution that must be taken in this calibration is to be certain that there is no diode drift. Therefore, measurements were taken going up and down in temperature so that a diode which did not retrace could be eliminated. A second scale, power in watts, has been added to the horizontal coordinate in Figure 6; in this case the particular diode dissipated 44 milliwatts per $^{\circ}\text{C}$ indicated rise.

Figure 7 shows diodes of the A, B, C, types as they were actually mounted in the heat sink for measurement. The temperature of this sink was measured by measuring the back current of the calibrated diode on a $1/4\%$ micrometer. This was used as the quiescent, or starting temperature for each measurement.

Figure 8 shows plots of the equivalent junction temperature rise as a function of dissipated power for the different types of diodes

noted. The indicated dissipation constants for the various diodes in milliwatts per $^{\circ}\text{C}$ are as follows: Type A point contact, 4.5; Type A gold bonded, 6.5; Type C point contact, 16; Type B' gold bonded, 25; Type B gold bonded, 46. Type B' is identical to Type B in every respect except that the pin was of a brass-type material whose thermal conductivity was about one-fourth that of copper. A greater range of values was found for Type B and B' diodes because other factors were low enough so that small variations in r_0 and crystal thickness became significant.

If the heat is generated by reverse current rather than forward current, one finds a dissipation constant to be somewhat lower. Figure 9 shows the power vs. temperature rise curves for a typical diode when dissipating either forward or reverse power. The second derivative of the forward curve is seen to be negative and that of the back curve positive. This was generally true for most of the diodes examined as was the fact that the "forward K " was generally larger than the "back K ," particularly at higher power levels. This difference is attributed to a change in effective r for, when forward current flows, carrier injection modulates resistivity near the junction so that electrothermal conversion takes place well into the bulk material.

Non Ideal Heat Sink

Let us now consider the non-ideal heat sink situations. Two thermal conductances in series, K_1 and K_2 , add to give a combined thermal conductance K_t such that:

$$(1) \quad \left\{ K_t = \frac{K_1 K_2}{K_1 + K_2} \right\}$$

If K_1 is the diode constant and K_2 the mount or sink constant, it is clear that for K_1 , much larger than K_2 , K_t is essentially K_2 , or if K_2 is much larger, as in the case of a good heat sink, K_t is essentially K_1 . For typical circuit installations the value for K_2 will normally be found in the range from 4-12 milliwatts per $^{\circ}\text{C}$, depending on lead size, clip dimensions, and effectiveness of thermal contact. If cooling fins are actually used, they normally radiate from 6-8 milliwatts per square inch per $^{\circ}\text{C}$. Discussions of power dissipation characteristics of various fin arrangements or radiating areas have been presented by several authors, particularly Paul Richards of Transistor Products, Leroy A. Griffith and Howard T. Mooers of Minneapolis-Honeywell.

This oscillogram of back current decay shown in Figure 10 was taken on a Type B diode held by an ordinary pair of clips. The top trace was 1 millisecond per centimeter and the lower one 1 second per centimeter. The bottom line represents the quiescent current at -12v. Here the effects of K_1 and K_2 are clearly separable. First the junction temperature dropped from its power dissipating level of $+33^{\circ}\text{C}$ above ambient to the temperature of the diode pin. The temperature decay from

that point on is dependent on the dissipation constant of the pin and mount in air. This K_2 is clearly much smaller, about 12 milliwatts per °C.

Figure 11 is a plot which combines the effects of K_1 and K_2 . The first curve, asymptotic to .210 watts, is for a K_1 of 7, typical of the Type A class of diodes. The next curve, asymptotic to .460 watts, is for a K_1 of 16, representative of the Type C diodes. The third curve, which would eventually be asymptotic to 1.35 watts, is for a Type B diode having a K_1 of 45. These curves are for a temperature rise of 30°C.

Here it is evident that for a given temperature rise, small values of K_1 limit the power dissipation to a very low figure. Unless values of K_1 are large, the addition of fins or other special mounting techniques would contribute very little to the dissipation of large amounts of power.

The temperature rise of 30°C, though not an absolute limit, is a reasonable figure to expect of germanium. However, for silicon diodes, 100°C is probably acceptable. If K_1 is equal to 50, and a temperature rise of 100°C were allowable, such a diode could dissipate 3.3 watts with a K_2 of 100 milliwatts per °C rise.

Transient Considerations

Up to this point we have considered only static power dissipation. However, it is evident that the problem of the transient situation can be of considerable importance.

Figure 12 is a plot of the decay characteristics of reverse current as a function of time. The Type B diode drops 10% of its current increase in .2 milliseconds, 33% in .6 milliseconds, and 63% in 5 milliseconds. Figure 13 summarized the same information. It shows the thermal relaxation times in milliseconds after removal of heating power for diodes of various types imbedded in the heat sink. A rather wide range of values is evident, particularly in the 33% and 63% values. The data for Figures 12 and 13 were taken from photographs similar to those of Figure 5. Figure 14 shows a relaxation curve of indicated temperature vs. time for a Type B diode. This curve is arrived at by use of a temperature calibration curve similar to the one shown in Figure 6 and a typical current relaxation curve.

Power Rating and Derating

It does not appear unreasonable that a forward power rating on the diode, or the diode and a particular mount, can be reached directly from an allowable effective temperature rise and a K value for the mount and diode. For example, the new

Type B copper pin diode in an ideal heat sink would have a combined K of about 50 milliwatts per °C. With an effective junction rise of 30°C above a 25°C ambient, the indicated junction temperature would be 55°C. Under these conditions, 1.5 watts of power could be dissipated. For a typical circuit installation, the combined K of a Type B diode and mount would be nearer to 10 milliwatts per °C and a permissible power of about 300 milliwatts would be indicated.

The permissible indicated junction temperature is of course dependent upon the allowable deterioration in the reverse characteristic as well as a yet undetermined relationship between indicated junction temperature and diode life. Arriving at a power rating in this manner for a specific ambient temperature of course suggests power derating for higher ambient temperatures using the same approach.

Reverse current produced power will present similar considerations in regard to change in electrical characteristics but will undoubtedly require a somewhat more detailed approach when life is considered. This is expected due to the fact that the junction is much less likely to arrive at a uniform temperature when heated by reverse current. This assumption is borne out by experimental results wherein diodes underwent a permanent change in electrical characteristics at moderately high reverse power levels but at an indicated junction temperature which would normally be considered safe.

Conclusions

Methods for determining the dissipation constant of a semiconductor diode have been discussed and comparisons between various typical diode packages have been made. The manner in which the diode dissipation constant and the constant of the mounting means can be combined to determine the effective operating temperature of the diode junction has been outlined.

Comparisons of the relaxation time of various diodes have been presented showing that diodes which have a high thermal conductance are potentially able to recover from elevated junction operating temperatures much faster than those whose thermal conductance is lower.

An approach to the power rating and derating problem has been discussed together with factors of concern in such an approach.

Reference

1. J. Tellerman, "Measuring Transistor Temperature Rise," Electronics, April 1954.

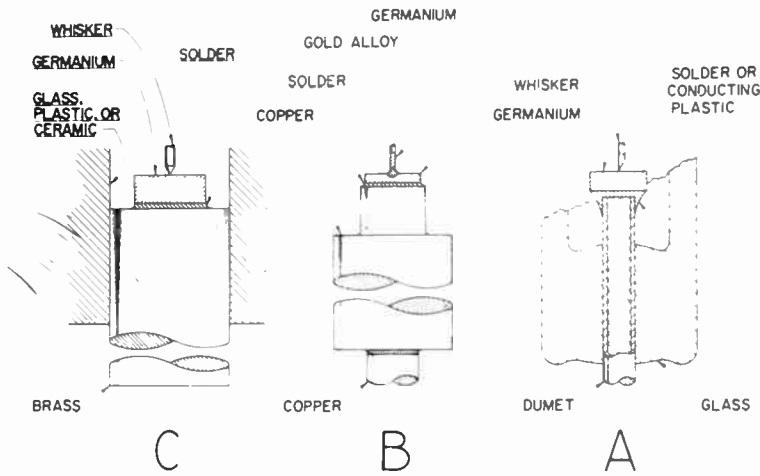


Fig. 1
Schematic Representation of Diode
Package Types.

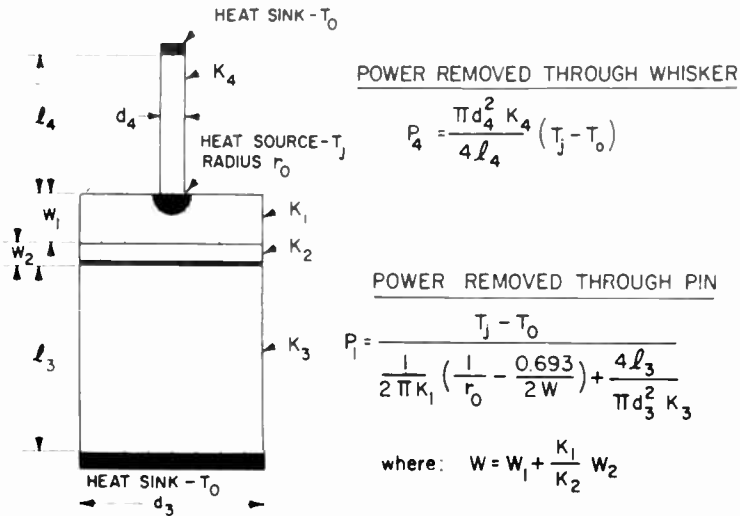


Fig. 2
Idealized Diode Package Drawing.

DIODE NUMBER	DIODE TYPE	CALCULATED K IN mw/°C	MEASURED REVERSE K IN mw/°C
10	B	20	35
78	B	168	22
79	B	16.8	24
26	A-G.B	6.2	7
75	C	6 TO 13	16

Fig. 3
Comparison of Calculated and Measured
Dissipation Constants.



Fig. 4
Test Circuit for Observing Diode Reverse
Current as a Function of Previously
Applied Power.

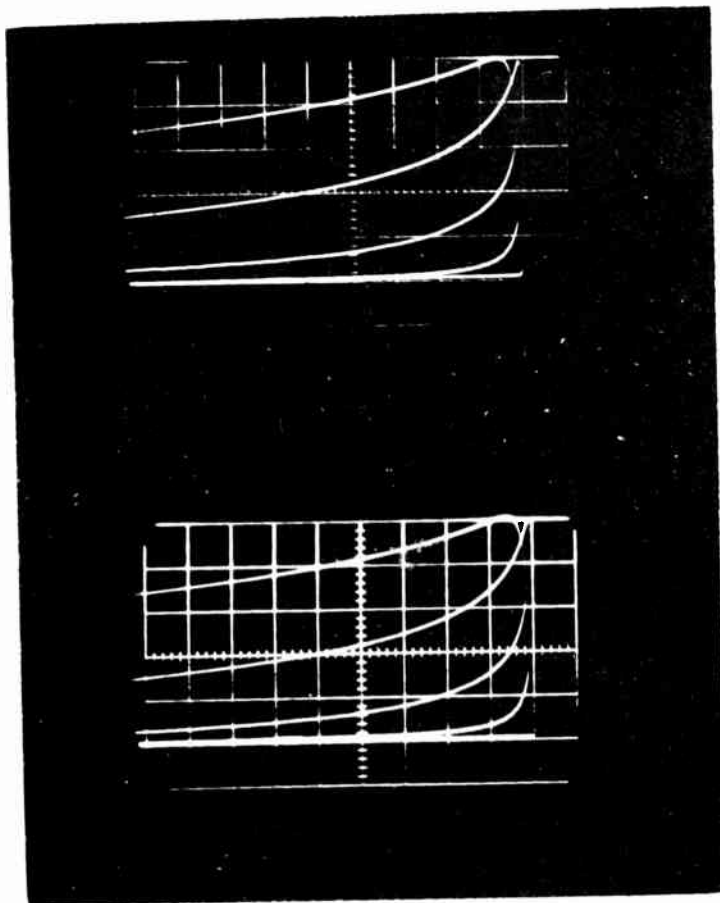


Fig. 5
Current Relaxation Oscillogram After
Removal of Forward Power.

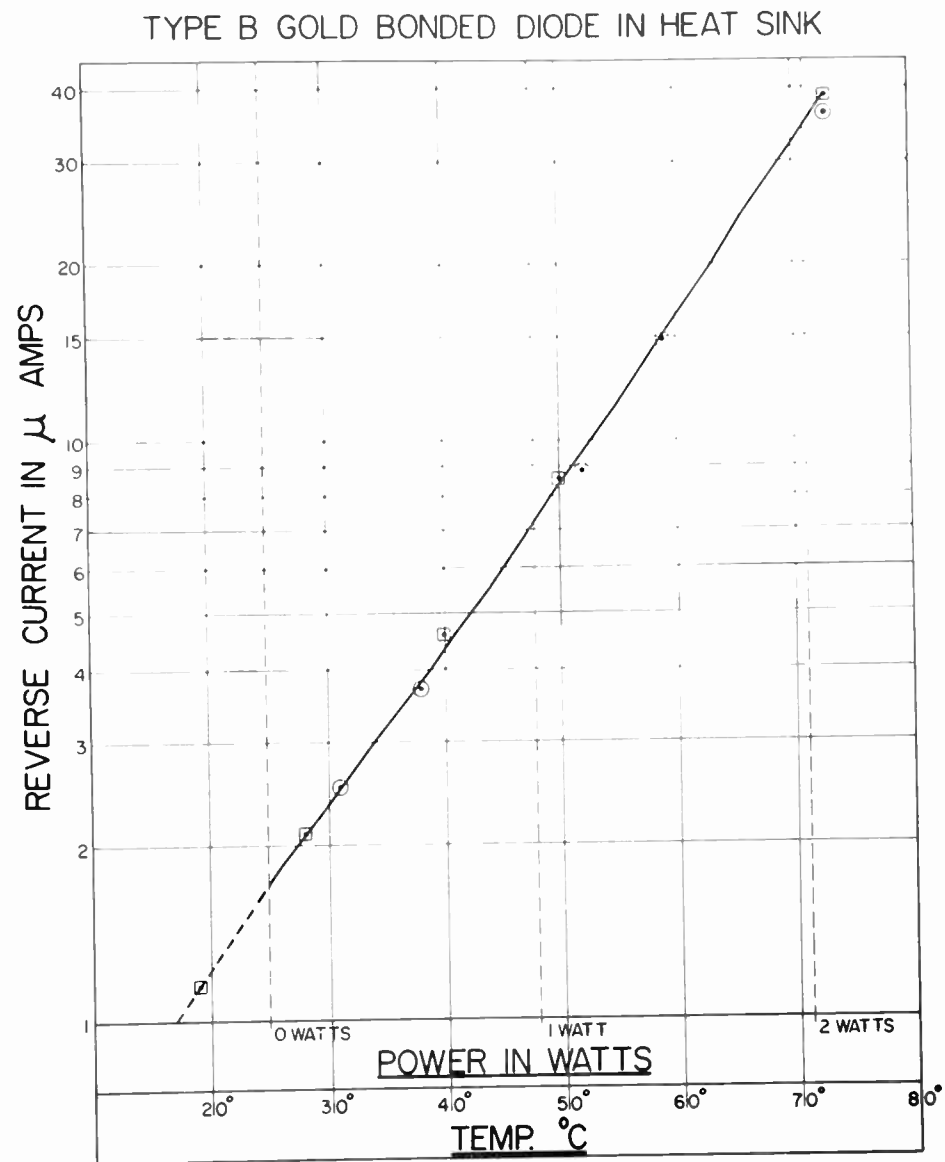


Fig. 6
Reverse Current at 12 volts vs. Temperature
and Forward Power.

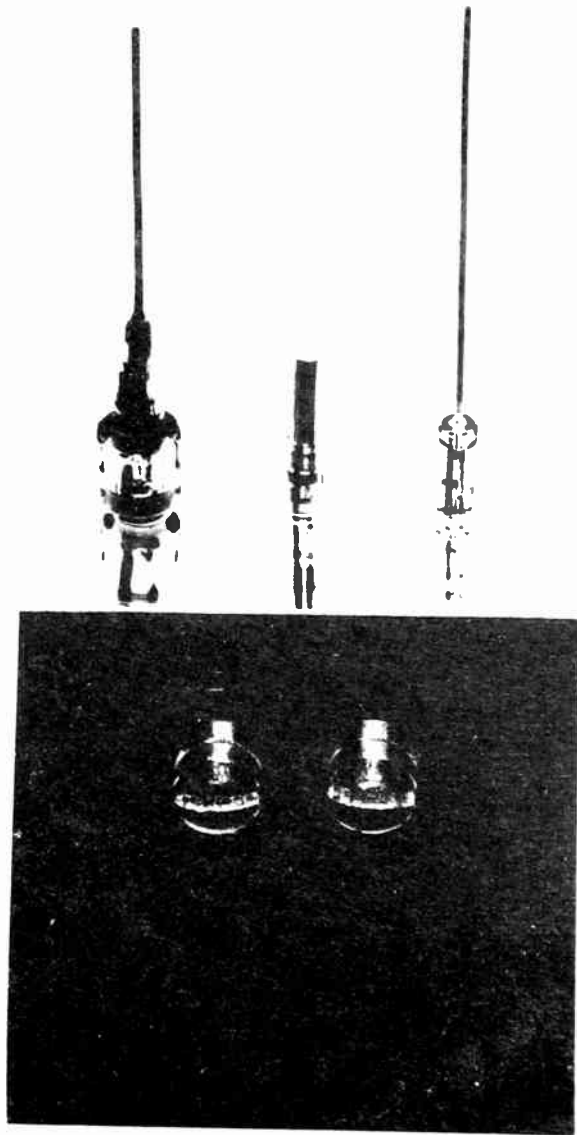


Fig. 7
Diodes in Heat Sink.

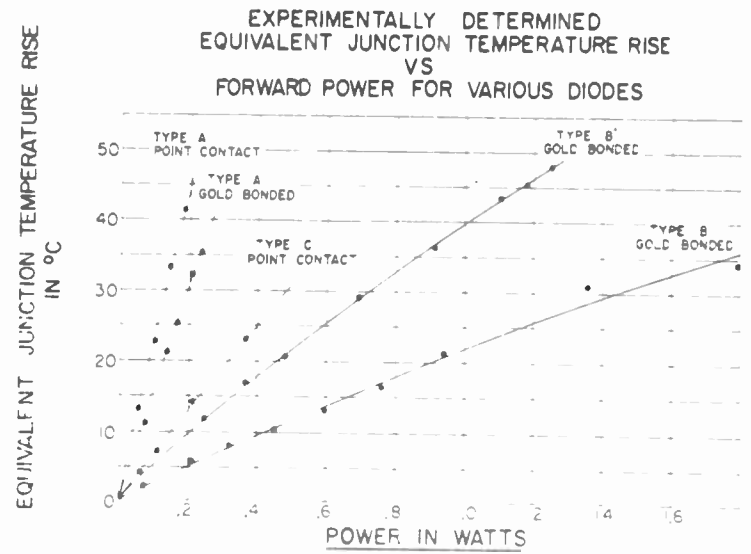


Fig. 8

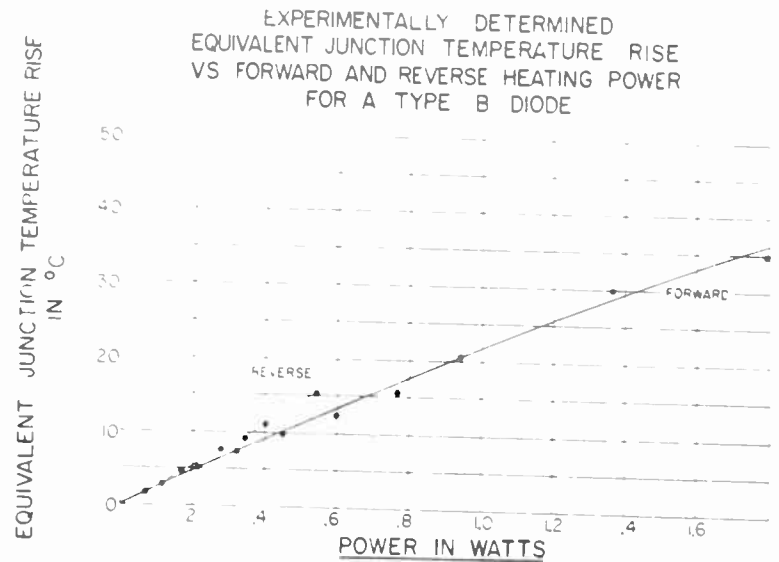


Fig. 9

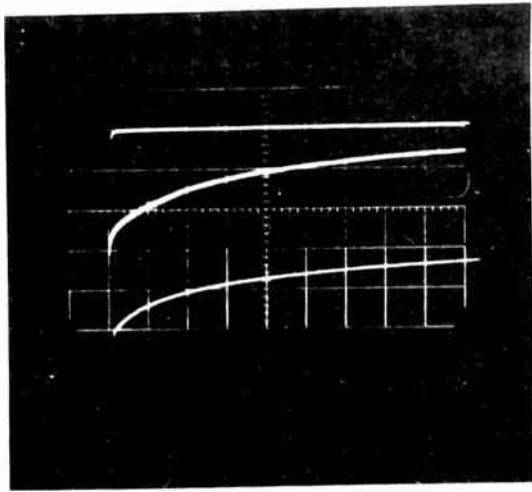


Fig. 10
Current Relaxation of a Type B Diode
in a Non-Ideal Heat Sink.

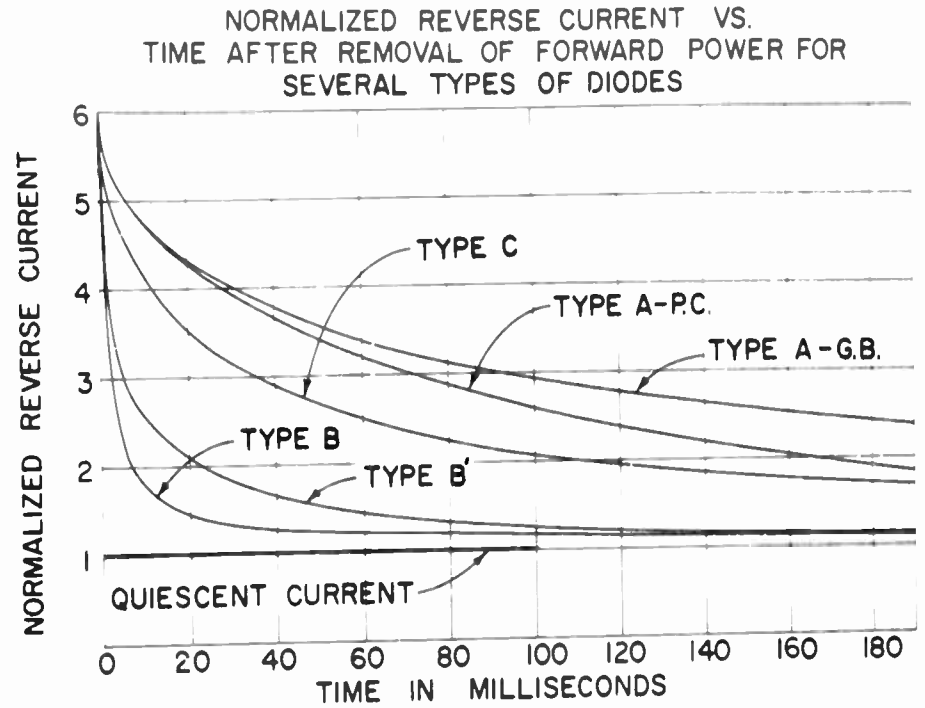


Fig. 12

111

POWER VS DISSIPATION CONSTANT OF MOUNT
(TEMP. RISE OF 30°C)

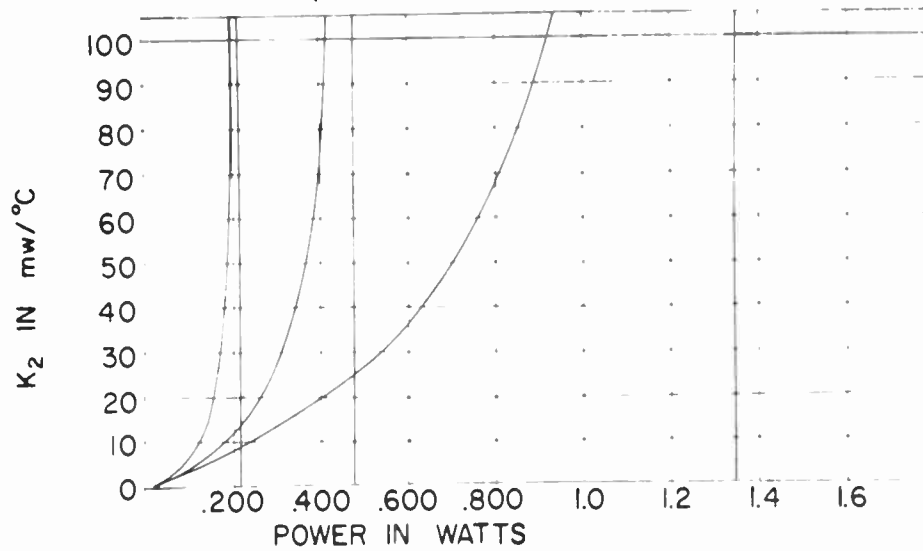


Fig. 11

TYPICAL RELAXATION TIMES*
OF REVERSE CURRENT
AFTER REMOVAL OF HEATING POWER

- DIODE CRYSTAL PIN IMBEDDED IN HEAT SINK -

	10%	33%	63%	90%
TYPE A GOLD BONDED	1	16	150	1000
TYPE A POINT CONTACT	12	16	100	400
TYPE B GOLD BONDED	2	6	5	50
TYPE B GOLD BONDED	3	1	9	60
TYPE C POINT CONTACT	7	8	60	400

* TIME EXPRESSED IN MILLISECONDS

Fig. 13

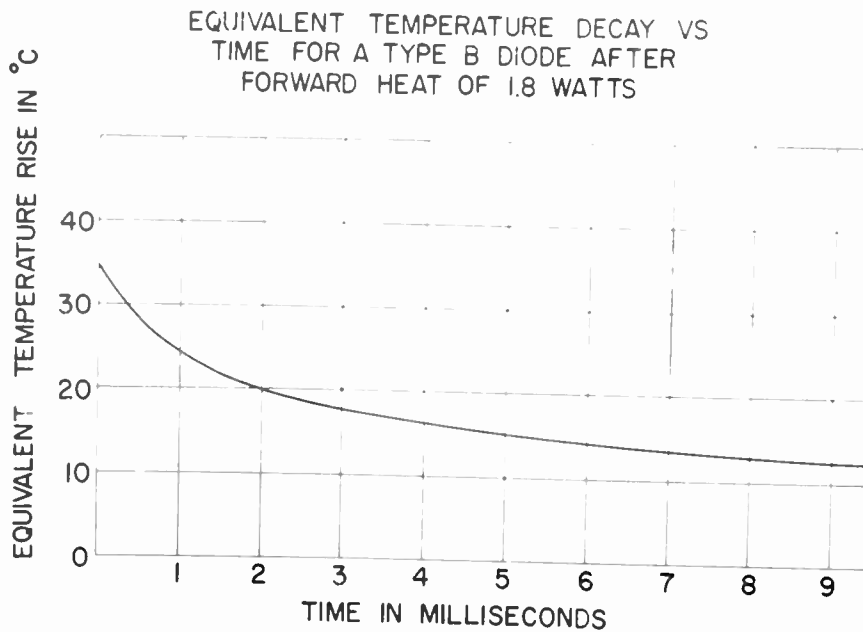


Fig. 14

GRAIN BOUNDARIES AND TRANSISTOR ACTION

by

H. F. MATARE

Sr. Member I.R.E.

Signal Corps Engineering Laboratories, Fort Monmouth, N. J.

Summary:

Dislocation models in the form of grown grain boundaries between two crystals of a specific mutual angle of misfit may be considered as zones of special electronic behavior. The mechanical stress field in a grain boundary zone is the origin of a field-dependent trap-mechanism. The P-type behavior of this zone may be used in structures similar to N-P-N-devices. The main difference lies in the fact that the height of the blocking layer is strongly dependent on the cross-polarization since the number of extra-electron-states increases with field strength. Furthermore the thickness of such zones may be limited to some microns for the case of disturbed twins. When carrier-injection into the p.b.-field is used to modulate the cross-current through the p.b.-double carrier layer, saturation of the cross current occurs and current multiplication factors as high as 50 and more may be measured.¹⁾ Grain boundaries may be used therefore in filamentary type of transistor structures, as well as in other arrangements to be described.

INTRODUCTION

As a result of the work of Pearson²⁾ and Fan and his co-workers³⁾ it is known that a grain-boundary zone has special electrical properties such as: p-type-behavior in an otherwise perfect n-type crystal-structure and a blocking double layer which permits a build-up, at the p.b.-interface, of abrupt jumps of the potential, often corresponding to 95% of the total potential difference applied to the sample.

It is known, furthermore, that these properties are, in most cases, not due to impurity segregation in the p.b.-zone since the effect disappears when the boundary zone is changed to p-type, either by nuclear irradiation⁴⁾ or by heating and subsequent quenching.²⁾ The high-blocking characteristic reappears when the specimen is reverted to n-type by annealing.

From these facts, and other indications, the conclusion may be drawn that the principal reasons for the presence of the acceptor-type characteristic of the material and the high-blocking layer are: 1) elastic deformation of the lattice in the p.b. region and 2) the number of locked lattice points in the p.b. line. A simplified demonstration of a cubic lattice appears in Fig. 1. In other words, we may correlate the p.b.-stress field or the mechanical energy localized in the p.b.-zone to the blocking layer across such a barrier-zone.

The electronic behavior of p.b.'s may be varied with the relative orientation of the two

grains. The grain-boundary, as a center of high energy, has been investigated by several authors. C.G. Dunn⁵⁾ measured p.b.-energies as a function of difference in orientation θ . The dependence of the energy on the orientation of the grain-boundary, with regard to the x-direction in the plane perpendicular to the p.b.-plane, is neglected. In fact, ϕ has little influence on the p.b.-energy. In general, the stress field of a p.b. between crystal grains will be a function of the relative orientation of the two grains (three degrees of freedom) and the orientation of the boundary surface itself with respect to the two grains (two degrees of freedom), but Read and Shockley⁶⁾⁷⁾ have shown that a good approximation, in the case of small orientation differences, is reached when we consider the two grains joined with a suitable array of dislocations which lies in the p.b.-plane.

A further analysis leads to the assumption of two main parts of energy. One part is due to the elastic deformation of the lattice in the neighborhood of the p.b. (Fig. 1). This part extends over a certain area. The other part is due to the energy of the locked lattice points in the p.b.-line.

The total energy per unit area is:

$$E = E_0 \theta (A - \ln \theta) \quad (1)$$

$E_0 \theta A$ represents a constant energy per dislocation and $E_0 \theta \ln \frac{1}{\theta}$ represents the elastic energy. In the simplified case of an array of dislocations in the p.b. plane or, small angle of misfit between the two grains, there is a weak dependence on the p.b. orientation. E_0 is a function of orientation and elastic constants:

$$E_0 = G \cdot a (\cos \phi + \sin \phi) / 4\pi (1 - \sigma) \quad (2)$$

where:

G = rigidity modulus
a = lattice constant
 σ = Poisson's ratio
 ϕ = orientation

For small angles: $E_0 = G \cdot a / 4\pi (1 - \sigma)$
The constant A may be put 0.3. For more detail see footnote⁶⁾. Dislocations in the form of small angle boundaries may have the electrical properties of rows of closely spaced acceptor centers with energies slightly above the middle of the gap.⁸⁾

An occupied acceptor may act as a hole trap and an empty acceptor as an electron trap. Measurements made by Pearson et. al.⁹⁾ on deformed samples show that deformation strongly influences mobility and carrier concentration in the case of

n-type, but has little influence on p-type Ge. This is one reason for the assumption that the boundary states act in the sense of increased electron density, which will be discussed analytically. Furthermore, the p.b.-states, or acceptor-type lattice disturbances, may act like discrete energy levels with localized wave functions near the middle of the gap.

It is known that in this way p.b.'s act as zones of increased trapping, and thus a deformation of the energy levels in the band scheme results¹⁰⁾

"Boundary surface states" have been supposed to exist in the forbidden band and were introduced in a theory explaining the measured non-ohmic behavior at the surface of such boundaries.³⁾

The increased trapping probability, however, must be a bulk material effect also where a grain boundary crosses the otherwise perfect crystal structure. In the following analysis, first the surface mechanism will be discussed.

Measurements of the "locking" voltage of such grain-boundaries at the surface have given high values. The boundary resistance may be about 200 k ohms at 100 volts potential difference and more. This means that specific resistivities jump to unusually high values. Probe measurements reveal this effect.

Fig. 2a) shows a double-seed arrangement used for the growth of oriented bicrystals. There are three angles θ of misfit. Fig. 2b) shows the relative grain boundary energy as a function of the angle of misfit θ_1 . Fig. 3 shows the case of cross polarization and the corresponding resistivity values. The boundary is located at 0. These results were found on a bicrystal (100) with $\theta_1 = 50^\circ$, $\theta_2 = 0^\circ$, $\theta_3 = 0^\circ$. (Ge, n-type, 12 ohm cm). There is a very high resistance jump due to a cross polarization when the potential is measured across the g.b. line.

The height of such jumps should be dependent upon the boundary energy as discussed previously. In this way, it is possible to define the electrical behavior of p.b.'s in terms of θ and ϕ .¹⁾ First conclusions which may be drawn from this work so far are:

1. Twinning in the proper sense gives low energy boundaries.
2. Boundaries with angles of misfit $\theta = 20^\circ$, 30° give a high probability of high stress fields and large trapping rates.
3. Disturbed twins with Frank or Shockley partials⁷⁾ might also give high p.b.-energies and disturbed zones in very thin layers.

The resistivity vs. x (crystal dimension)-diagram reveals in general the character of a p. b. Two probe resistivity measurements across the surface of a crystal show typical jumps when the

boundary zone is included in the current path. A characteristic of a p.b. (silicon, 5 ohms cm. n-type) is shown in Figure 4. It is symmetrical in the negative current range. Rectifying properties are apparent. As Taylor et. al.³⁾ pointed out, the boundary states act as acceptor levels located in the gap between the valence and conduction bands, slightly below the Fermi-level. In equilibrium these states are occupied by electrons and cause the curving up of the bands. Under applied voltage a stronger deformation of the band scheme takes place and accumulation of electrons is increased. This enhancement of the trapping-rate by potential change in the p.b.-layer will be discussed further and transistor action based on the injection into the p.b.-zone will be the ultimate scope.

GRAIN BOUNDARY BARRIERS

The electric behavior of grain-boundaries as investigated by Fan and co-workers, Pearson, and the author, indicates that the potential drop across the barrier is comparable to the behavior of the backward characteristic of high voltage Ge diodes. (Fig. 4) We may understand this behavior by the assumption that electron concentration at the boundary increases whereas the hole concentration decreases when external voltage is applied. Under the assumption that the number of extra electron states in the boundary zone is constant, application of the Gauss-Theorem applied to electric field-strength E and potential V across the p.b. gives a value of the critical potential (break-down) of the p.b. as $V_c = 4\phi$. ϕ = work function 1 e Volt. This could give barrier voltage of only a few volts.

Since the actual voltage drop is far greater, the inherent assumption of constant electron concentration at the boundary surface cannot be true. Taylor and co-workers³⁾ applied Schottky's barrier layer theory¹²⁾ to the p.b. field and found indications that the number of bound electrons at the p.b.-interface increases with applied voltage while the number of holes decreases. The Schottky type current equation for the p.b.-barrier layer is:

$$i = e\mu E \left[n_B - n_A \exp\left(\frac{eV_{AB}}{kT}\right) \right] \left[1 - \exp\left(\frac{eV_{AB}}{kT}\right) \right] \quad (3)$$

Subscript A refers to the bottom and B to the top of the barrier. The minus sign refers to electron, the plus sign to hole current. Since the concentration of electrons at the bottom (A) is equal n_{e0} and for barriers in an n-type semiconductor $eV_{AB} \gg kT$, we get

$$i = e\mu_e E \left[n_{e0} - n_{e0} \exp\left(-\frac{eV_{AB}}{kT}\right) \right] \quad (4)$$

a current equation similar to that in the case of a current through a P-N-junction. Introducing the fields on either side of the barrier E_1 and

E_2 and the relation $V_a = V_1 - V_2$, (see Fig. 5) one obtains for electron and hole currents by elimination of n_{eB} :

$$i_e = -\mu_e e \frac{E_1 E_2}{E_1 - E_2} n_{e0} \exp(-eV_2/kT) [1 - \exp(-eV_a/kT)] \quad (5)$$

$$i_h = e \mu_h \frac{E_1 E_2}{E_1 \exp(-eV_1/kT) - E_2 \exp(-eV_2/kT)} n_{h1} \exp(-eV_1/kT) \quad (6)$$

With the Notations:

- E_1, E_2 = electrical field strength on either p.b. barrier side
 - n_{e0} = neutral-carrier density
 - μ_e = electron, μ_h = hole mobility.
 - e = electron charge
 - k = Boltzman constant
 - T = abs. temperature
 - V_a = external voltage applied across the p.b.
 - V_1, V_2 = voltage drop on either side of the p.b. barrier. ($V_a = V_1 - V_2$)
 - n_{h1}, n_{h2} = hole densities on either side.
- The electron current-voltage relationship (5) is such that with increasing external voltage V_a applied the electron current is dependent only on V_2 . With V_2 increasing this current should diminish since the barrier height would increase. It is, however, important to note that the potential on one side of the barrier is practically not only dependent on q , the number of electrons in the p.b.-states. While q depends on eV_a , there is a dependence of both, eV_1 , and eV_2 , on eV_a . In principle $V_a = V_1(V_a) - V_2(V_a)$, for the signs, chosen in Fig. 5.

The hole current (6) could tend toward the value:

$$i_h \approx \frac{E_1 E_2}{E_2} e \mu_h n_{h1} \quad (7)$$

for V_1 more rapidly increasing with V_a than V_2 . The dependence of q (electrons bound to the g.b. interface, q_0 being the original equilibrium number) is apparent.

The next step is the evaluation of the electron concentration at the top of the boundary: n_{eB} . Equaling a current-voltage relationship according to (4) for both sides of the barrier yields:³⁾

$$n_{eB} = -n_{e0} \frac{E_2}{E_1 - E_2} \exp(-eV_2/kT) \quad (8)$$

for applied voltage $V_a \gg kT/e$. The hole concentration becomes:

$$n_{hB} = 2 n_{h0} \exp(eV_2/kT) \quad (9)$$

$E_1 - E_2 = -q$ is the number of electrons on the boundary states. When we put $q = q_0$ constant the differentiation of n_{eB} and n_{hB} with V_a gives:

$$\frac{\partial n_{eB}}{\partial V_a} \approx V_2^{1/2} \frac{n_{e0} e}{q} \frac{1}{kT} \left(\frac{kT}{2eV_2} - 1 \right) \exp(-eV_2/kT) \frac{\partial V_2}{\partial V_a} \quad (10)$$

$$\frac{\partial n_{hB}}{\partial V_a} \approx 2 n_{h0} \frac{e}{kT} \exp(eV_2/kT) \frac{\partial V_2}{\partial V_a} \quad (11)$$

for $V_2 \gg kT/e$ (10) is positive while (11) becomes negative, indicating an increase of n_{eB} and a decrease of n_{hB} with V_a . As pointed out before, and what is apparent by the conclusions, q is not constant but a function of V_a and thus V_2 also is a function of V_a . In principle, the increasing number of electrons trapped in p.b.-states with increasing applied external voltage enhance the building of a steep interface-barrier until there occurs a Zener-break through the inversion layer which limits the blocking-voltage. In absolute values V_1 and V_2 increase with V_a for $q \neq q_0$.

In a first order approximation q may be put constant to evaluate n_{eB} as $f(V_a)$ and since V_2 increases with V_a

$$\begin{aligned} n_{eB} &= \frac{n_{e0} e}{q} \frac{1}{kT} \int |V_a|^{1/2} \exp(e|V_a|/kT) d|V_a| \\ &= \frac{n_{e0} e}{q} \alpha e^{\alpha |V_a|} \left[\frac{1}{\alpha} |V_a|^{1/2} - \frac{1}{2\alpha^2} |V_a|^{-1/2} - \frac{1}{4\alpha^3} |V_a|^{-3/2} - \dots \right] \end{aligned} \quad (12)$$

$$\alpha = e/kT$$

$$\text{For } V_a \gg 1/\alpha : \quad (13)$$

$$n_{eB} \approx \frac{n_{e0} e}{q} |V_a|^{1/2} e^{\alpha |V_a|}$$

This equation shows that the limit for strongly increasing n_{eB} is given by the fact that $q = f(V_a)$ and by the Zener effect i.e. quantum mechanical tunneling of electrons through the barrier layer. The transition processes between the different energy levels will thus tend to increase the number of electrons on the boundary states.

Therefore, the behavior of the σ .b. is similar to that of a P-N-junction. It might be said that: The hole current is carried by material of higher hole conductivity outside the boundary than inside. Thus the gradient is much greater in the boundary region. Here, as in the case of a P-N-junction the cross resistance is much greater than the integrated resistivity of the material comprising the σ .b. Thus polarized grain boundaries have rectifying properties.

It is however, important to note that according to equation (13) the number of electrons in boundary states increases whereas the number of holes decreases. This means an increase in V_2 with V_a as pointed out. In this respect the σ .b. double layer behaves different than a p-n-junction double layer. Polarization across the line of dangling bonds is thus influencing the number of extra electron levels built up in the σ .b. line. This may cause a strong increase in trapping rate or high current multiplication.

INFLUENCE ON GRAIN BOUNDARY BARRIERS BY CARRIER INJECTION AND LIGHT

The aforementioned assumptions lead to the conclusion that there must be a strong influence on the σ .b.-resistance or the σ .b.-cross current by carrier injection into the σ .b.-region itself. Several different forms are possible.

a. Filamentary type surface modulation by injection through a polarized electrode on the boundary zone. Figure 5 gives a descriptive view of the σ .b. surface modulation and the schematic equivalent in the band scheme. Quite independently from the external voltage, applied to the σ .b., injected minority carriers, (holes), may recombine with electrons, present in σ .b.-states, thus causing a barrier lowering and strong changes in current across the σ .b.-region. As an additional effect there should be a saturation region in which the cross current becomes strictly independent from the cross voltage. Both cases have been observed as the diagrams show.

b. Modulation by light injection. The same effect can of course, result from light quanta. Light injection in the proper frequency range increases the number of excitons in the boundary zone. Under the applied field, electrons drift to the collector side and the holes increase the minority carrier density in the σ .b. region. The injection of light into a σ .b.-layer has a higher efficiency with respect to carrier release and influence on the cross current than injection into a normal crystal structure (photo-transistor). The σ .b.-stress field has a high capture-cross section for carriers and, with external field applied, the influence on the cross-current may be extraordinarily strong. This is apparent also by the extremely high current multiplication factors which are found by injection into σ .b.-zones. For a definite number of injected carriers, the fluctuation of the Quasi-Fermi level is strongest when the carriers are injected into the σ .b. zone itself.

c. Modulation of a current across a bulk-crystal in which a σ .b. is interposed.

The structure of the σ .b. may easily have a line-shaped form at the surface (see Fig. 2) and may be arranged in such a way that the σ .b.-plane crosses the otherwise perfect crystal structure in a definite orientation, perpendicular to the cutting-plane. We have seen that the boundary zone is characterized by an energy state higher than the one of the surrounding lattice. In normal cases, and especially in the cases of high resistance-jumps, which are characteristic for high boundary energies, there is a high number of carriers (electrons) present inside the σ .b.-region. This plane-shaped region is therefore surrounded on both sides by high resistivity inversion layers and may be put on a specific potential with respect to the rest of the crystal.

Recent investigations of other authors on grown σ .b.'s using (100) seeds bound symmetrically on either side of a molybdenum wedge confirm these assumptions¹³⁾.

The wedge angle was 5° to 15° and lay in a (110) plane common to the two seeds. Contacts were made on wafers cut from the bicrystals. In the case where these contacts were on the σ .b.-zone, the measured resistances were $2 \cdot 10^5$ to 10^6 ohms. If the contacts were made on the normal crystal material, resistances lay at 10^6 ohms. This behavior and especially the potential-dependent carrier-density in the σ .b. zone make possible a bulk modulation equal to that by a P-type layer between two N-type parts of a crystal.

The energy level diagram for a σ .b. across the bulk crystal structure must be defined by the array of dislocations, with the stress field and its subsequent higher carrier density. The band scheme is given, as was discussed, for the surface σ .b. (Fig. 5). Fig. 6 gives a schematic construction. Since the current I_1 is supported mainly by electrons (majority carriers) and I_2 modulates the barrier height by an injection of holes which do not necessarily appear as a hole current through the specimen, frequency response should be better than in any N-P-junction device. Moreover, the σ .b.-stress-field may be concentrated at a very thin layer. Disturbed twin boundaries may be as thin as a few microns.

INTERNAL MODULATION AND POSSIBLE APPLICATIONS

Two and three probe measurements and experiments with grain boundaries in bulk material have been carried on which confirm the above developed theory. It is fairly possible to make electric contact to the σ .b.-zone itself since the thickness of this zone is under polarization in general, larger than the diameter of electrolytically pointed Tungsten-probes. When the probes are placed outside the σ .b.-region a weak transistor-action can be measured because of the normal minority carrier injection. Care was taken that no contact formation occurred during measurement.

which would have falsified the results. When the specimen was moved so that the medium whisker was placed on the p.b. a very different electric behavior could be measured. Fig. 7 gives an example of such measurements for a germanium bicrystal. It is apparent that there is carrier injection also outside of the p.b. zone but the higher α -values (current multiplications: $\Delta I_1 / \Delta I_2$) and the saturation of the cross current I_1 show a pronounced n.b.-action. Fig. 8 gives another typical result for Germanium. $\rho = 5 \text{ ohm cm}$.

Special consideration was given to silicon. Initially, samples were studied which had been cut from polycrystalline material so that only one boundary crossed the otherwise perfect crystal structure. These bicrystals had very different properties conforming to the relative orientation of the crystals on either side of the boundary.

Two probes are put on either side of the p.b. The characteristic is symmetric and extends in the same manner to the third quadrant. A three probe measurement with negative polarization of the p.b. region of silicon with 5 ohm-cm resistivity is shown in Figure 9. High current amplification was found in samples of the kind represented in Fig. 10.

As we have seen before, the efficient current multiplication at a proper p.b. interface may be explained on the basis of the high trapping rate and consequent carrier density in the p.b.-zone. While the hole density decreases strongly with applied field across the p.b., the electron density increases.

At the other hand, hole injection into the p.b.-layer changes the p.b.-potential barrier and causes a shift of the Quasi-Fermi level as a consequence of the barrier lowering.

Thus the electron current:

$$i_e = e \mu_e E \left[n_{eB} - n_{e0} \exp(-eV_{AB}/kT) \right] \quad (21)$$

changes strongly, since n_{eB} and V_{AB} undergo variations by carrier injection into the p.b.-field. An evaluation of the change in conduction of the barrier region by V_2 -variation can be made as follows:

$$n_{eB} = -n_{e0} \frac{E_2}{E_1 - E_2} \exp(-eV_2/kT) \quad (22)$$

with the notations already used.

Since $E_1 - E_2 = -q$ and $E_2 \approx V_2^{1/2}$

$$n_{eB} \approx n_{e0} \frac{V_2^{1/2}}{q} \exp(-eV_2/kT) \quad (23)$$

$$\text{with } \alpha = \frac{e}{kT}$$

$$\frac{\partial n_{eB}}{\partial V_2} = \frac{n_{e0}}{q} \alpha V_2^{1/2} \left[\frac{1}{2\alpha V_2} - 1 \right] \exp(-\alpha V_2) \quad (24)$$

Since $V_2 \gg \alpha$,

$$\frac{\partial n_{eB}}{\partial V_2} = -\frac{n_{e0}}{q} \alpha V_2^{1/2} \exp(-\alpha V_2) \quad (25)$$

corresponding to:

$$\frac{\partial n_{hB}}{\partial V_2} = 2\alpha n_{h0} \exp(\alpha V_2) \quad (26)$$

We may now introduce these carrier-density variations with V_2 into the equation for the conductivity-change due to trapping:

$$\Delta \sigma = e \mu_e (\Delta n_e + \Delta n_{et}) + e \mu_h (\Delta n_h + \Delta n_{ht})$$

Since we may consider the injection into the p.b. as a variation of V_2 independently of V_1 and in this way change the actual number of trapped holes (Δn_{ht}) and electrons (Δn_{et}) in the p.b.-zone. The result is:

$$\Delta \sigma = e \mu_e \left[\Delta n_e - \frac{n_{e0}}{q} \alpha V_2^{1/2} \exp(-\alpha V_2) \right] + e \mu_h \left[\Delta n_h + 2 n_{h0} \alpha \exp(\alpha V_2) \right] \quad (27)$$

Thus the conductivity in the p.b.-zone increases by a change of Δn_{et} with V_2 and increases exponentially with V_2 as far as hole trapping is enhanced.

The normal case is, that under the applied barrier voltage the actual number of electrons in the p.b.-zone is so much higher than the number of holes that only the first part of equation (27) has to be considered. This decrease in ρ (resistivity) is equivalent to a higher cross conductance or higher current-density as is found by the injection experiment.

The explanation of high current multiplication-values may be based at first hand on the situation known from the case of the Filamentary Transistor and formed point contact transistors.¹⁴⁾

Here the explanation can be given on the basis of the induced charge of the extra-electron layer. (See Figure 11). The current will be supported mainly by electrons. Holes from electrode 1 are kept at the p.b. and thus the electron current flowing from 2 to 1 is much larger than the hole current flowing across the p.b. to the collector electrode 2. Here we have realized the

ideal conditions for high α -values which have been defined by W. Shockley.¹⁵⁾

"If a concentration of centers which had the property of binding holes tightly could be produced directly in front of the collector, then the holes could tend to accumulate there with a resultant increase in space charge". In other words, if $\Delta I_n = b \Delta I_p$

$$b = \mu_n / \mu_p$$

I_n = electron current

I_p = hole current

mobility ratio, the current multiplication could

$$\text{be } \alpha_i = 1 + b$$

In the case of a p.b. this is easily possible since:

1. The ratio of mobilities (b) is affected by the high fields near the collector point at the p.b.

2. Holes and electrons do not flow along the same current paths.

3. Holes accumulate easily at the g.b. where higher electron density is produced under applied field across the p.b.-junction or growth-junction. The increased trapping in the p.b. region causes a hole to spend a fraction x of its time in a trap. It moves (1-x) of its time with normal mobility. The net effect is that its mobility is reduced by a factor (1-x) and b is raised to

$$b_{eff} = b / (1 - x)$$

If (1-x) is small this leads to large b_{eff} values and hence to high α_i -values. The theory for the p.b.-transistor has yet to be worked out in detail. Experiments are being made, at present, in the direction of useful application of the p.b. field. Equivalent forms may be worked out, using P-N-junctions as well. For instance a P-N-p.b.-N-structure may prove effective. (Fig. 12) High current multiplication in a base to ground connection may give new possibilities to combine high frequency response with higher current multiplication.

ACKNOWLEDGEMENT

The author is indebted to Dr. P. H. Keck and Dr. H. Kedesdy for help in the preparation and x-ray measurement of bicrystals; to Mr. McDonald and Mr. R. Sidensticker for much skillful work in the pulling-technique and electrical measurements of grain boundary structures and to Mr. Solid for outstanding work in the construction of a special micro-manipulator set.

References

- 1) H.F. Mataré, Z. f Naturforschung Bd 9a H. 718 (1954)
- 2) G. Pearson, Phys. Rev. 76 459 (1949)
- 3) W.E. Taylor, M.H. Odell, N.Y. Fan, Phys. Rev. 88, 867-875, (1952)
- 4) W. Taylor and K. Lark-Horovitz, Purdue Semiconductor Res. Progress Rpt (Oct 1948)
- 5) C.G. Dunn and F. Lionetti, Trans. A.I.M.E. 185-125 (1949)
- 6) W.T. Read and W. Shockley: Phys Rev 78, 275 (1950)
- 7) W.T. Read, Dislocations in Crystals, McGraw-Hill (1953)
- 8) F. L. Vofel, W.T. Read, and L. C. Lovell, Phys Rev 94, 1791 (1954)
- 9) G.L. Pearson, W.T. Read, and F. J. Morin, Phys Rev 93, 666 (1954)
- 10) W. Shockley Electrons and Holes in Semiconductors, VanNostrand, 68 and 343-346 (1950)
- 11) Publication: H. Kedesdy and H.F. Mataré, under preparation
- 12) W. Schottky: Z.Phys (German) Vol 118, 546 (1941/2)
- 13) A. G. Tweet: Bull Am Phys Soc 29, June 28, p 17 (1954)
- 14) H. Jacobs, F. Brand, H. Matthei, A. Ramsa, J. Appl Phys 25, 1406-1412 (1954) (Report Values as high as 10 with an extreme value of 25.)
- 15) W. Shockley: Electrons and Holes in Semiconductors, Van Nostrand Co. N.Y. (1950) p 113

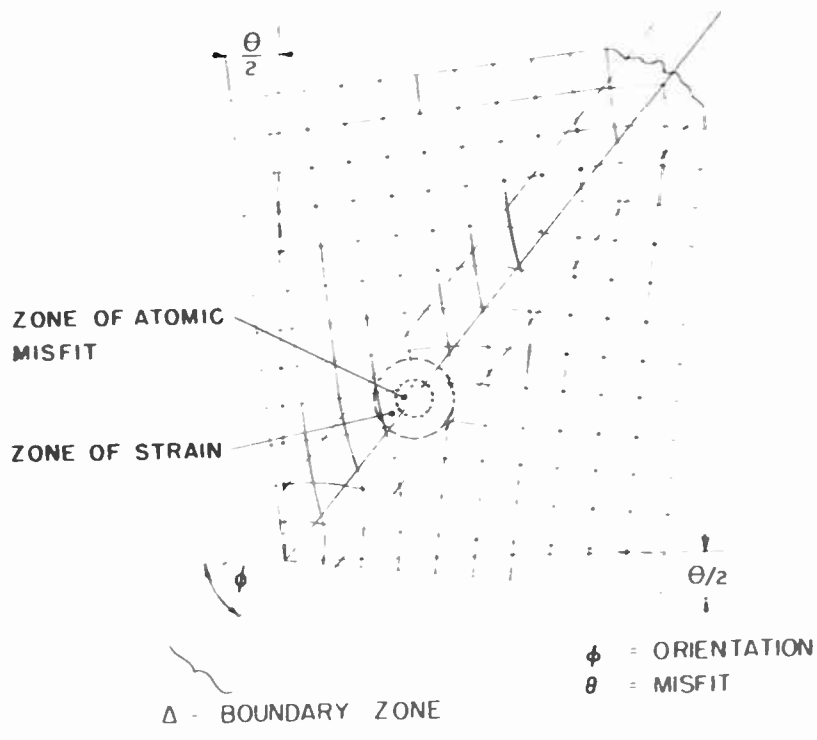


Fig. 1
 Dislocation model of a g.b. (grain-boundary)
 for a cubic crystal.

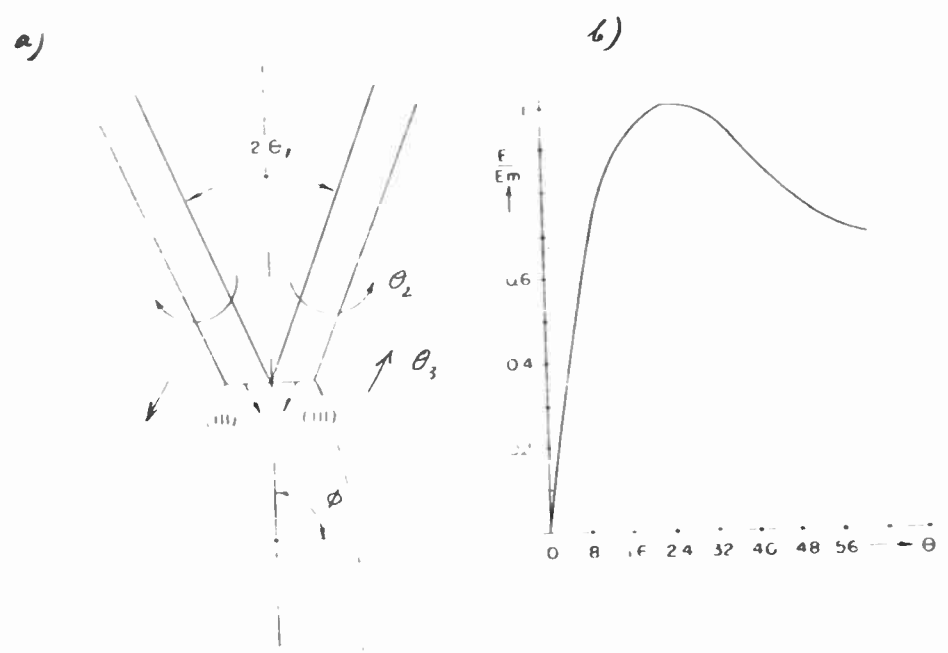


Fig. 2
 a. Schematic representation of a double seed
 crystal pulling arrangement. b. Gain
 boundary energy (relative) as a function
 of angle of misfit θ .

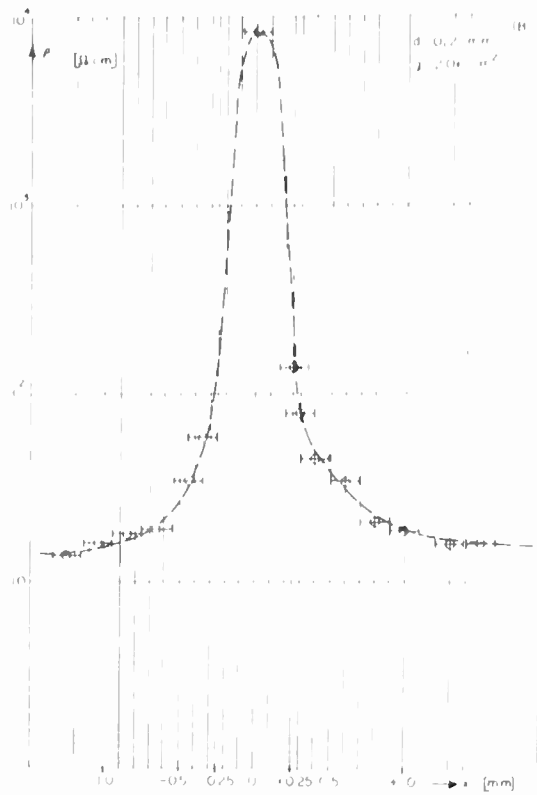


Fig. 3
Diagram for the dependence of resistivity ρ on x (boundary location at 0.)

CHARACTERISTIC OF A GRAIN-BOUNDARY SILICON, $5 \Omega \text{ CM}$

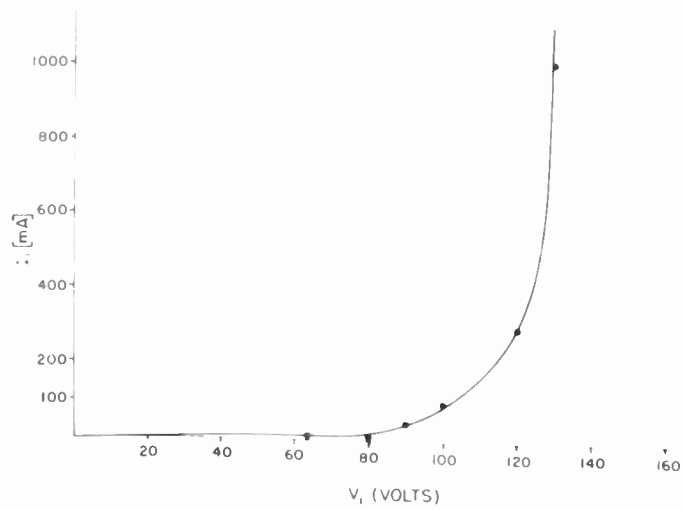


Fig. 4
Characteristic of a silicon g.b. (symmetrical for negative voltage and current).



Fig. 5
Surface measurement device for a g.b. and modulation of quasi-Fermi levels by carrier injection.

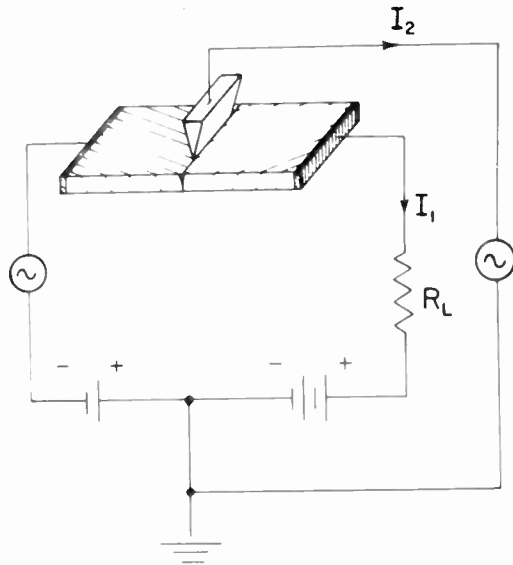


Fig. 6
Bulk-effect measurement of a g.b.-field with injection of carriers into the g.b. field.

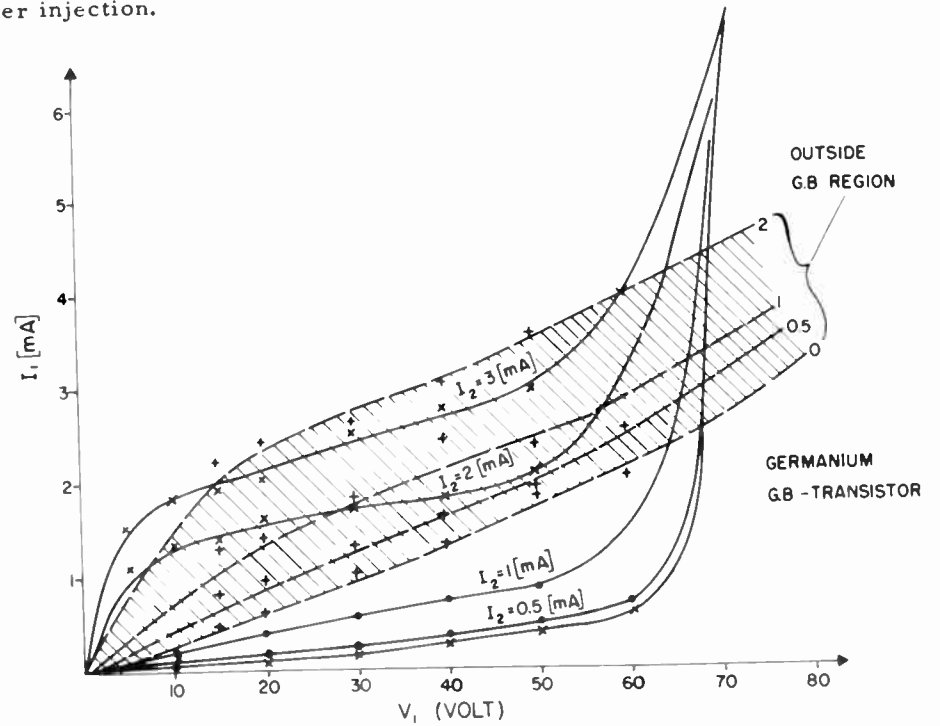


Fig. 7
Three-electrode characteristics of a g.b. on Germanium $\rho \approx 1$ ohm cm. n-type. Striped region outside g.b. zone.

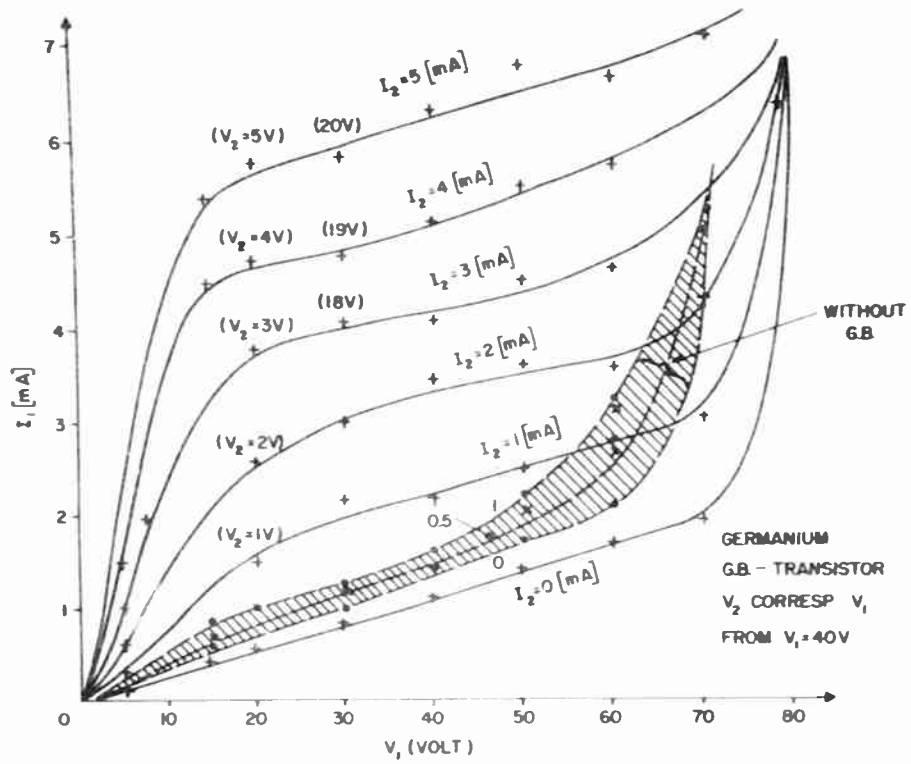


Fig. 8
 Germanium g.b. transistor action. Striped region outside g.b. zone. $\zeta \approx 5$ ohm cm. n-type.

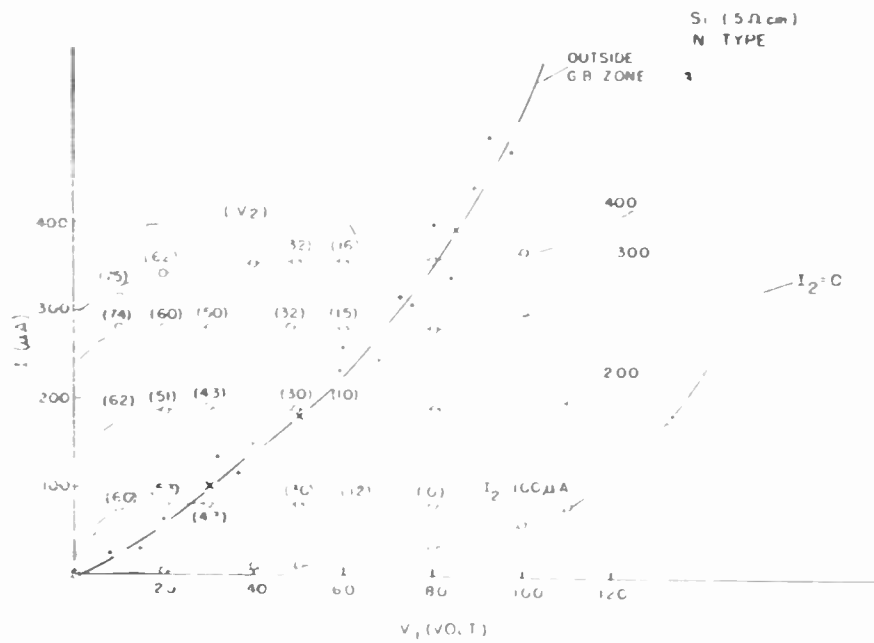


Fig. 9
 Silicon g.b. transistor. Injected current: I_2 , voltage drop to reference electrode: V_2 . Saturation region between 20 and 100 volts cross polarization.

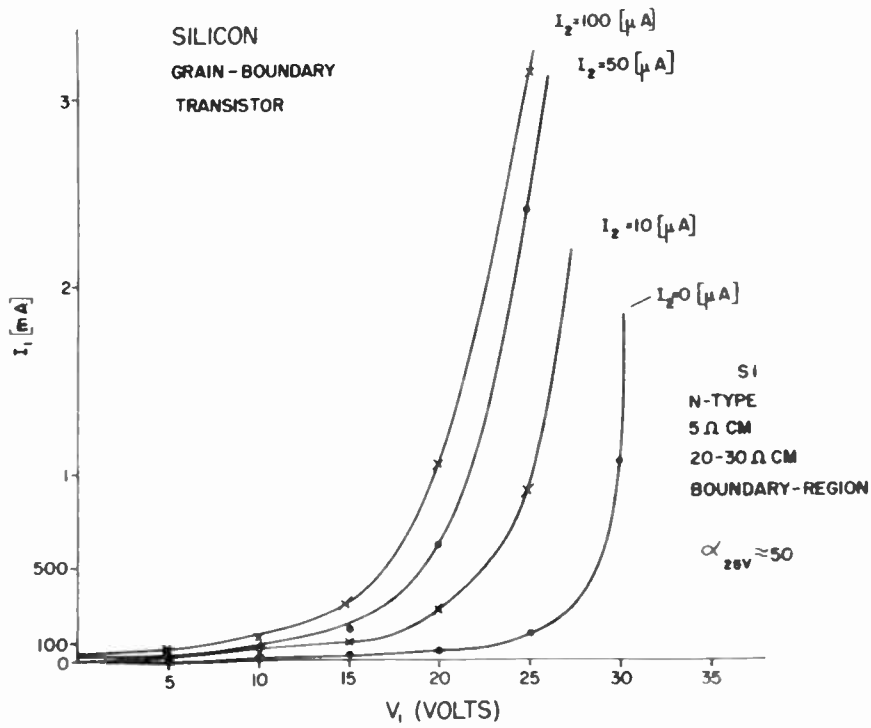


Fig. 10
Characteristic of a Silicon g.b.-transistor.
(5 ohm cm, n-type) Minority carrier
injection into g.b. zone. Relative
polarization positive to reference
electrode.

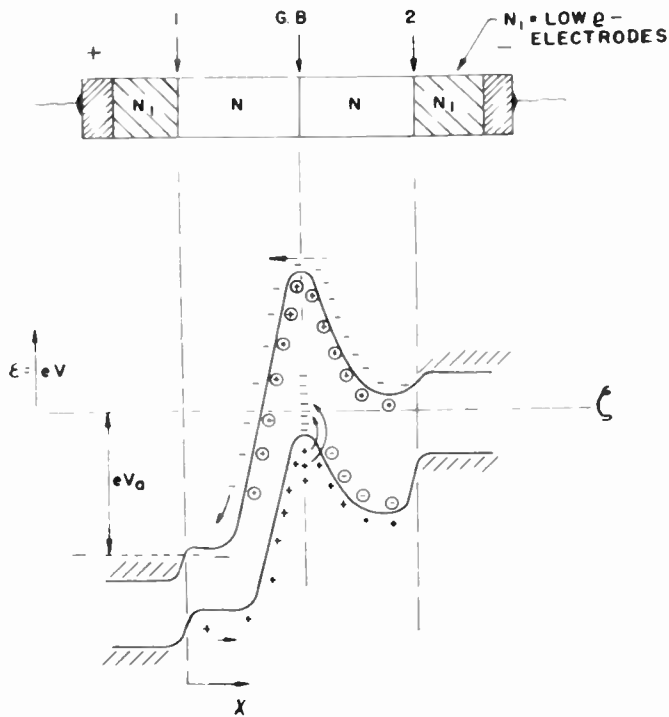


Fig. 11
Energy level diagram for a g.b. under applied
voltage V_a with electrodes showing Hook-action.

SCHEMATIC ENERGY LEVEL DIAGRAM
FOR N-P-N-G. B.-STRUCTURE

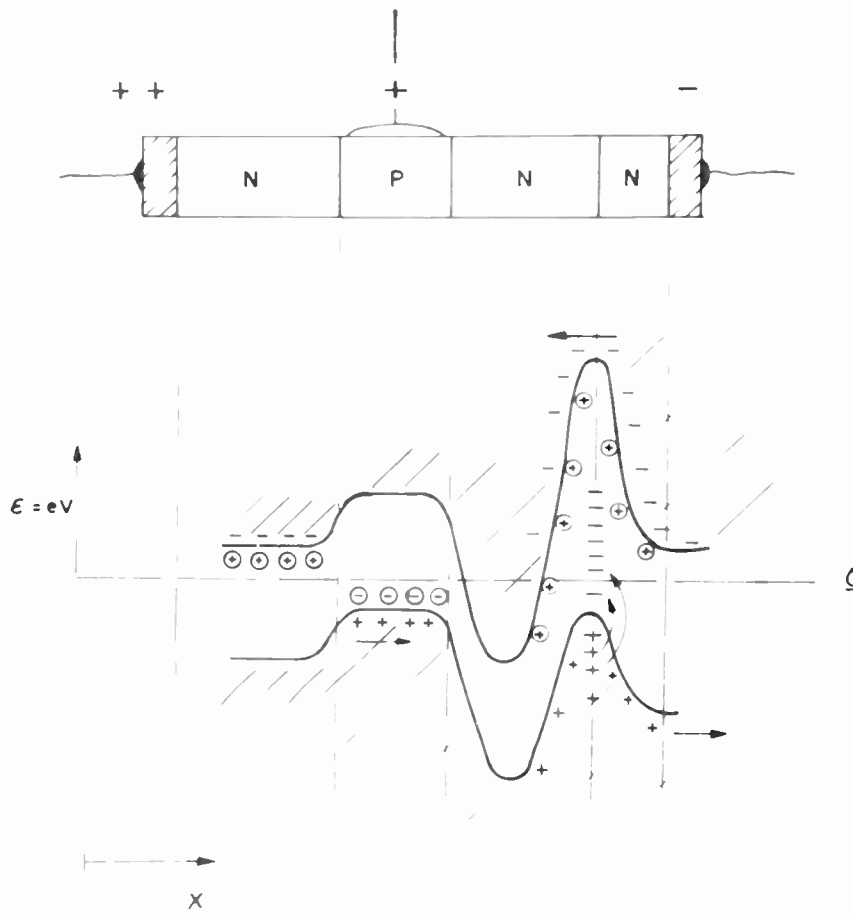


Fig. 12
Energy level diagram for a N-P-N-g.b.
structure.

DEVELOPMENTS IN SILICON JUNCTION DIODES AND POWER RECTIFIERS

H. Gunther Rudenberg
Transitron Electronic Corporation
Melrose, Massachusetts

New silicon junction rectifiers are presented. Different alloying techniques provide p-n junctions of smaller as well as much larger areas than formerly available. Types now developed handle kilowatts of alternating current, others milliwatts of high-frequency signals. They have low forward voltage drops, excellent rectification efficiencies at rated power, inverse currents of microamperes or fractions thereof, and inverse voltages from 10 to 1,000 volts even at high ambient temperatures.

SILICON DEVICES

Very considerable improvements in silicon technology have recently led to a realization of many practical devices which had been predicted only from theoretical analyses. Perfection of single crystal silicon and metallurgical control of alloying and junction formation have led to the development both of large area power rectifiers and of small area high frequency junction diodes. Each of these have inherent advantages which make them suitable for certain specific applications.

It seems pertinent to review the basic characteristics which can be obtained from single crystal silicon rectifiers of various resistivities, in order to compare these with other power rectifiers like selenium cells. Figure 1 shows the cell voltages plotted against current densities expressed in amperes or microamperes per square inch. Thus a single cell silicon rectifier may have a voltage drop of hundreds to thousands of volts. Here the comparison with dry disc rectifiers is visible. These have only 36 volts rms or 100 volt DC peak inverse voltage per cell. Thus on a unit cell basis, the inverse characteristics of silicon show a much sharper current and voltage saturation, as well as currents one-tenth as large and cell voltages ten to a hundred times higher. At the same time, the extremely good forward characteristics of a silicon rectifier are apparent, since silicon junctions are capable of current densities of the order of one thousand times higher than selenium cells of equal area.

Power dissipation may set an upper limit to the currents and voltages at which each cell may operate. Nevertheless, a tremendous improvement in recti-

fier performance may be realized by using silicon diodes or rectifiers instead of dry disc units. Another considerable advantage of silicon is the fact that it can be operated at junction temperatures of 150°C and higher without any aging effects. 250°C operation may be obtained through further development, and the devices described here are based on 150°C operation of the junction in 125°C ambients.

Five types of silicon junction diodes and rectifiers are described. These are a high current developmental rectifier, a medium current power rectifier which is in quantity production, a developmental high voltage silicon rectifier, a junction diode having very low inverse currents, and a small area high frequency bonded junction diode. The last two types are also in production. All units are hermetically sealed with ceramic or glass-to-metal seals. Figure 2 shows the diodes of small size. These are manufactured either in a ceramic cartridge with axial leads, in a developmental subminiature glass package, or in a welded miniature metal can. Figure 3 shows the higher power rectifiers which require cooling by conduction to a chassis in order to permit the highest power ratings. Thus these rectifiers are manufactured on a copper base with a stud which can be screwed tightly against a chassis to insure intimate thermal contact.

SILICON POWER RECTIFIERS

Both the medium power rectifiers and the developmental high current units have forward and inverse characteristics as shown in Figure 4, curves B and A respectively. The high current unit type PS-1 is rated at 15 to 30 amperes current with a peak inverse voltage of 125 volts, and is suitable for the rectification of kilowatts of power. The medium power rectifiers such as the 1N341 or 1N332 will handle tens of watts, a bridge circuit capable of supplying 200 watts of rectified power at an ambient temperature of 125°C occupying a volume of only one cubic inch. The temperature characteristics of these units are excellent, as even at 125°C the medium power rectifier will draw inverse currents ranging from 10 microamperes to 1 milliamperes. This extremely low inverse current at high temperatures contributes to their high

efficiency, and provides for higher voltage output than could be obtained from conventional dry disc units.

Two factors control the power conversion efficiency of a rectifier. At low current levels, the inverse leakage current produces an appreciable power loss compared to the load current. At high currents this is small, but the forward voltage drop reduces the voltage and power available to the load. Both these factors are very small in these silicon power rectifiers, leading to the high efficiency shown in Figure 5. This shows the power conversion efficiency of a typical silicon rectifier 1N341, which is 96% at its rated output current of 400 milliamperes. The dotted line at the bottom of the figure refers to the efficiency of a representative selenium rectifier of similar ratings in single phase service. This 30% greater efficiency of silicon has a very important practical aspect, because transformers and generators designed for use with silicon power rectifiers need be only 70% as large as those designed for selenium rectifiers, and only 50% as large as those designed for copper oxide or magnesium sulfide units in single phase service. For polyphase rectifiers the reduction in size of transformers are also appreciable.

A number of rectifier types have been developed from the generic type discussed. The specifications of the types designed for power supply applications are shown in Table I. Current ratings refer to resistive or inductive loads, those for capacitive filters being somewhat less.

TABLE I
Silicon Power Rectifiers
Power Supply Types

SPECIFICATIONS AND RATINGS AT 125°C

	P.I.V. Volts	I_{dc} mA	E_f Avg. Volts	I_r Avg. mA
1N341	400	400	3.0	.5
1N342		200		
1N343	300	400	3.0	.5
1N344		200		
1N345	200	400	2.5	.5
1N346		200		
1N347	100	1000	2.5	.5
1N348		400		
1N349		200		

Typical of the advanced characteristics of these silicon rectifiers is the 1N341. This has 400 volts DC peak inverse voltage, thus allowing direct operation of a single cell rectifier from a 135 volt AC power line to a capacitive filter with proper surge limiting resistance. Lower voltage units are manufactured from silicon crystals of lower resistivity. These have a higher forward current rating such as the 1000 milliamper type 1N347.

MAGNETIC AMPLIFIER TYPES

By means of special processing techniques, the inverse leakage currents of some types of silicon power rectifiers may be held to extremely low limits even at elevated temperatures. Figure 6 shows the maximum averaged inverse leakage current of such units as a function of temperature. At voltages below the "Zener" breakdown voltage, this current ranges from fractions of a microampere at room temperature to tens of microamperes at 125°C, and is almost independent of voltage. This inverse leakage current is so small, that in magnetic amplifier applications it is too small to saturate the iron cores. This extremely low leakage current, corresponding to megohms of inverse resistance, makes these types of rectifiers especially suited for use in magnetic amplifier circuits.

Magnetic amplifier designs are frequently limited by the characteristics of conventional rectifiers, since the gain of a self-saturated magnetic amplifier is limited by the ratio of forward rectifier current to inverse rectifier leakage current averaged over a cycle. It is evident that rectifiers with forward currents of amperes and inverse currents of microamperes allow very large stable gains to be obtained from such magnetic amplifiers. Here also the increased efficiency and higher maximum temperatures allow very compact design of cooling structures.

The relatively small change of forward voltage drop with temperature illustrated in Figure 7 is another feature of the silicon power rectifiers which makes their use attractive in precision electronic equipment. This curve shows the average forward voltage drop as a function of temperature for some of the magnetic amplifier types whose specifications are shown in Table II.

TABLE II

Silicon Power Rectifiers
Magnetic Amplifier Types

SPECIFICATIONS AND RATINGS AT 125°C

	P.I.V. Volts	I _{dc} mA	E _f Avg. Volts	I _r Avg. mA
1N332	400	400	1.5	.100
1N333		200	3.0	
1N334	300	400	1.5	.100
1N335		200	3.0	
1N336	200	400	1.3	.050
1N337		200	2.5	
1N338	100	1000	1.0	.100
1N339		400	1.3	.050
1N340		200	2.5	.050

This table illustrates the forward and inverse characteristics obtainable with various rectifier designs. These medium area rectifiers range from types allowing one ampere average current with one volt average forward drop to units having 400 volts peak inverse voltage.

MCOUNTING AND COOLING

Even with their high power conversion efficiency, rectifiers providing 50 watts DC output per cell have losses of a few watts in the silicon wafer. This heat is generated in the inherent electrical resistance of the semiconductor, and is conducted away from the junction by the copper base. The silicon power rectifiers are designed for conduction cooling, as this affords a major saving in rectifier size and weight for any given power requirement. Sufficient surface area can generally be provided by proper utilization of the chassis to aid in dissipating the rectifier power losses.

Figure 8 illustrates the mechanical arrangement and the thermal circuit of these power rectifiers. The silicon wafer is mounted on a copper base, which in turn conducts the heat through an insulating washer to the metal chassis. The thermal resistance of the rectifier from the junction to the copper base is of the order of 5° to 10°C per watt. Mounting on a chassis or heat sink with a total thermal resistance of 7.5°C per watt to the

ambient environment will allow operation at 1.5 to 2 watts of dissipated power even at 125°C. In cases where the copper base can be operated at chassis potential, and when using a large chassis, units may be operated at still larger power dissipation.

Actual ratings are derived for average chassis sizes, about 5" x 5" x 1/8" with a mica washer insulator. A few drops of silicone oil will insure better contact by preventing entrapment of air. Forced cooling can naturally reduce cooling fin areas by a large factor in cases where forced air is available.

On the basis of the current ratings described, Figure 9 gives the heat sink thermal resistance which, at the various ambient temperatures shown, will not exceed the 150°C junction temperature permissible with these power rectifiers.

The use of conduction cooling to a chassis or large plate, which in turn is convection or forced air cooled to the ambient surroundings, allows a full realization of the excellent characteristics of these silicon power rectifiers. It is through careful mounting that continuous service at 125°C with high power handling ability and negligible leakage currents can be obtained. Also the utilization of a conductive cooling connection permits the use of a hermetically sealed rectifier cell to provide complete environmental protection in a miniature package of less than .2 cubic inches in volume.

HIGH VOLTAGE RECTIFIERS

Development is proceeding on high voltage rectifiers, exceeding the 400 volt types described already. Voltages of 600 to 800 volts have been obtained from production type power rectifiers, and developmental high voltage units have been assembled with breakdown voltages in excess of 1000 volts as shown in Curve "C" of Figure 4. In all of these cases the increase of breakdown voltage with higher temperature is of considerable advantage, since it permits full voltage rating at elevated temperatures, which is not generally possible with other types of rectifiers.

Units may also be placed in series to obtain higher voltages. It is recommended that a parallel equalizing resistance be placed across each rectifier in the series string such that each 600 volt rectifier would be paralleled by a 1 megohm 1/2 watt resistor. This provides somewhat better balancing of the series rectifiers than is generally obtained

from the inverse characteristic alone. Units having higher back currents should naturally have somewhat lower values of stabilizing resistance connected across the rectifier. In this manner high voltage operation can be obtained from standard units with forward and inverse characteristics as good as those from the single cell high voltage rectifier.

SILICON JUNCTION DIODES

Silicon junction diodes have been developed for some time¹, and each new development in technology², produces some further improvements in their specific characteristics and ratings. The extremely high inverse resistance of these silicon junction diodes, even at 150°C, makes them ideal for exacting high temperature applications such as low level magnetic amplifiers. New techniques have allowed the development of units having a somewhat higher conductance than previously available. The curves marked "D" in Figure 4 illustrate the range of characteristics obtained from one particular group of such diodes. These diodes are tested at 125°C to provide satisfactory performance at high temperatures. Since these units as well as the power rectifiers have exceedingly sharp voltage saturation curves with a sharp Zener break, they are well applicable for voltage regulators. The Zener voltage changes only of the order of 10-15% between 25°C and 125°C so that their stability is as good as that of gas filled regulator tubes. Minimum currents are very small, simplifying low level regulators.

HIGH FREQUENCY BONDED JUNCTION DIODES

Techniques for obtaining very small area junctions in silicon have been developed to provide units with excellent high frequency characteristics. These small silicon diodes have about 0.1 micro-micro-farad junction capacitance, to which must be added the capacitance of the ceramic or glass case of about 0.5 to 1 micro-micro-farad in most practical circuits. Figure 10 shows the 100 megacycle rectifications efficiency of such units, but these diodes will rectify efficiently up to 500 megacycles. Some of these diodes have pulse recovery characteristics below 0.1 microseconds to a 50,000 ohm impedance with driving pulses of 20 volts. As always, exact comparisons with other types of diodes depend upon the measuring circuit, but these bonded silicon junction diodes perform extremely well compared to conventional high frequency whisker diodes or specially processed units³.

The high frequency diodes have forward currents ranging from 1 milliampere to 4 milliamperes at 1 volt. Figure 11 shows the forward current characteristics of various grades of these high frequency silicon diodes. In viewing this curve, it must seem somewhat of a paradox that units with such low forward current can give excellent high frequency response. However, both are due to the extremely small area of the rectifying junction. Figure 12 shows the inverse characteristics of the same grades of high frequency junction diodes. Although their inverse currents are not as minute as those of the somewhat larger junction diodes already described, it should be realized that these units were specifically developed to obtain good high frequency performance. At 100°C these diodes still have extremely low inverse currents, below 10 microamperes for the S5 and S7 types.

One objection to all silicon devices as high frequency rectifiers can be readily avoided. This is their high impedance at low signal levels. A small forward bias current applied through a high resistance, even as small as 1 or 10 microamperes, is sufficient to bias any silicon junction diode to a point where optimum sensitivity can be developed for the impedance level desired. Under these conditions more output power can be obtained for a given input power with silicon junction diodes than with germanium diodes or microwave point contact silicon crystals up to 500 or 1000 megacycles.

SUMMARY

Five types of silicon junction diodes and power rectifiers have been described which have been developed to various stages of production. These units are capable of operating at ambient temperatures of 100 to 125°C at full ratings and will withstand 150°C in lower power applications. All units are hermetically sealed to provide excellent stability under all environmental conditions.

High power rectifiers with areas exceeding 1 square centimeter of silicon have been operated at currents above 100 amperes. Such units can handle kilowatts of rectified power at elevated temperatures. Even with the low forward voltage drop of a few volts, such units must be extremely well cooled to prevent their exceeding a junction temperature of 150°C. The high current and peak inverse voltage ratings of such production and developmental units, as well as their extremely minute inverse leakage currents even at

elevated temperatures, make these rectifiers attractive for a large number of critical applications which must function reliably at high temperatures. Furthermore, the high rectification efficiency of 90 to 98% obtainable from silicon power rectifiers provides power and weight savings in electronic equipment, as well as permitting extremely compact rectifier design. Significant is the complete absence of any aging effects even after long time operation.

Medium power units scaled down in area from these high power types range from 100 to 400 volts peak inverse voltage and forward current ratings from 1 ampere to 200 milliamperes. The design of the mounting structure required to obtain full rated rectifier power at 125°C, or to allow increased ratings at lower temperatures have been described. Such units have been in daily operation for over a year, illustrating their excellent life⁴.

The lowest power diodes are characterized by minute junctions of extremely small area. These diodes have back currents of small fractions of microamperes in room temperatures and a few microamperes at 100 to 125°C. Various types allow operation at very high frequency or at very high impedance levels, with voltage breakdowns from 10 to 300 volts. Several types are useful as voltage regulators in the breakdown region of their characteristic.

Other types with somewhat differing characteristics may be interpolated be-

tween the units shown, in order to take full advantage of the amazing characteristics of the silicon junctions. Since rectifier characteristics can be so readily designed, the electrical engineer has a further dimension at his finger tips which allows adjustment of rectifier performance beyond those permitted by permutations of cell area and number. In all cases these units illustrate the really phenomenally low inverse currents and high forward current densities which are achieved through careful processing of single crystal silicon.

ACKNOWLEDGMENT

The development and production of such a diverse range of diodes and rectifiers was possible only through the cooperation of a number of staff members at Transitron Electronic Corporation. Certain types of these rectifiers with characteristics particularly suited to military specifications have been developed in cooperation with the Signal Corps Supply Agency and the Signal Corps Engineering Laboratories.

BIBLIOGRAPHY

- ¹G. L. Pearson & B. Sawyer - Proc. IRE
40 1348 (1952)
- ²G. L. Pearson & P. W. Foy - Phys. Rev.
37 190 (1952)
- ³C. G. Thornton & L. D. Hanley, Proc. IRE
43 136 (1955)
- ⁴H. G. Rudenberg, Electronics
26 April (1955)

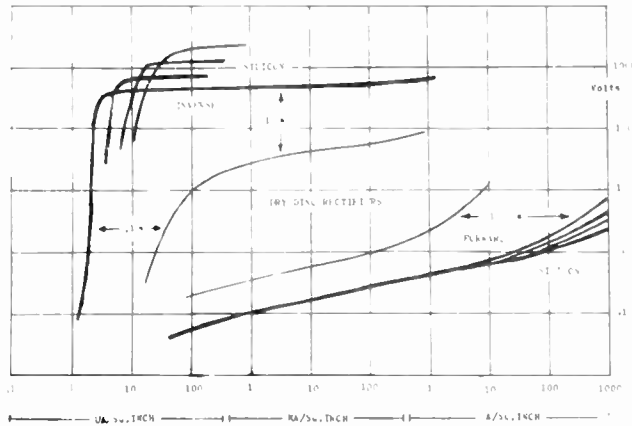


Fig. 1
Current Densities of Silicon Rectifiers.



Fig. 3
Silicon Power Rectifiers.

130



Fig. 2
Silicon Junction Diodes.

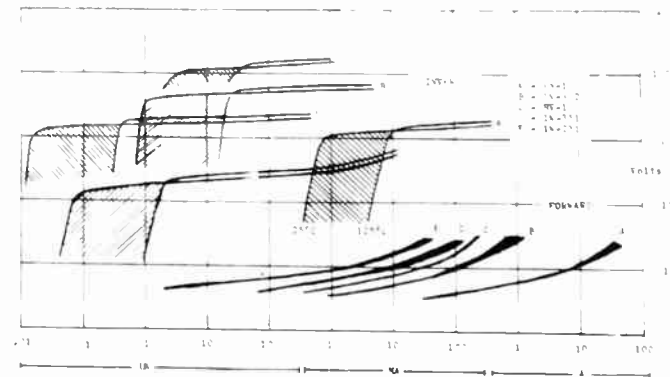


Fig. 4
Characteristics of Silicon Diodes
and Rectifiers.

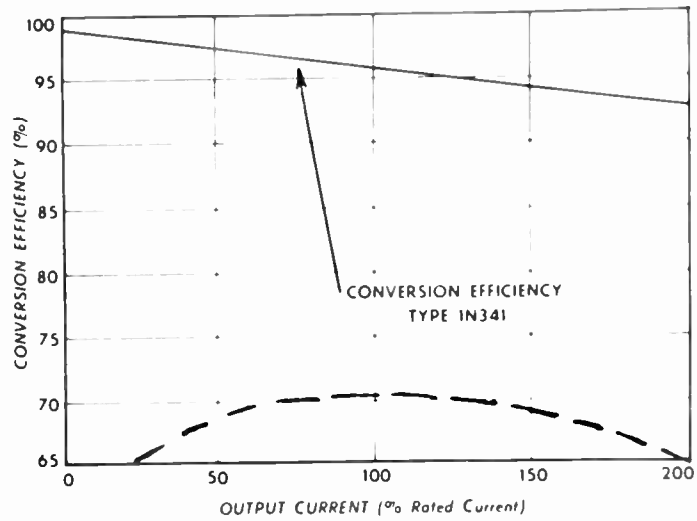


Fig. 5
Power Conversion Efficiency.

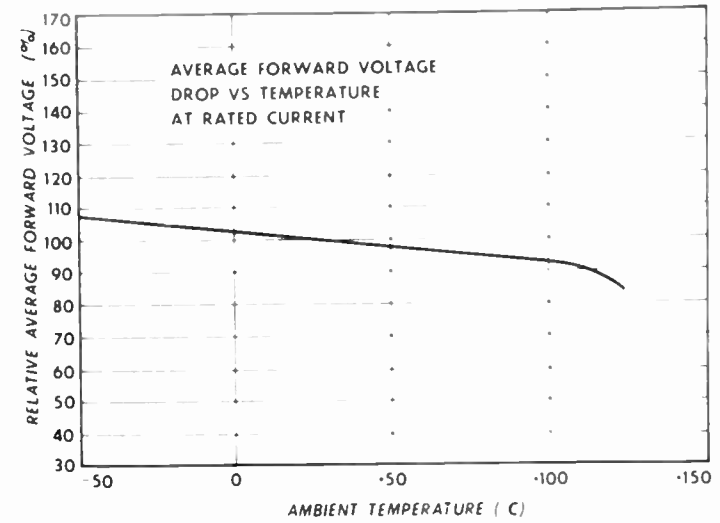


Fig. 7
Average Forward Voltage Drop vs. Temperature.

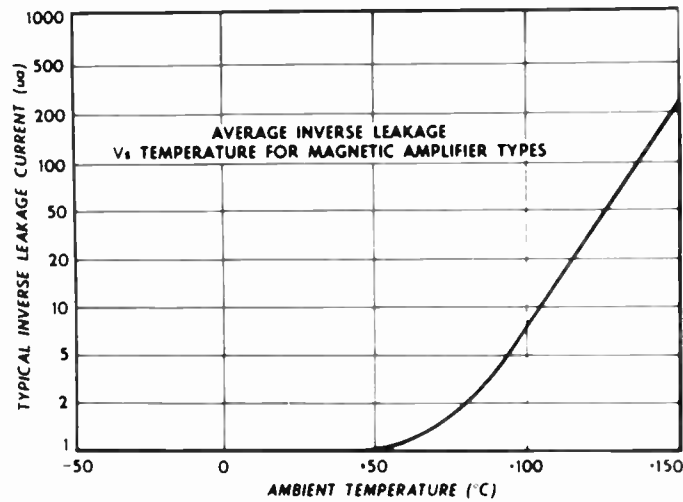


Fig. 6
Average Inverse Leakage Current vs. Temperature.

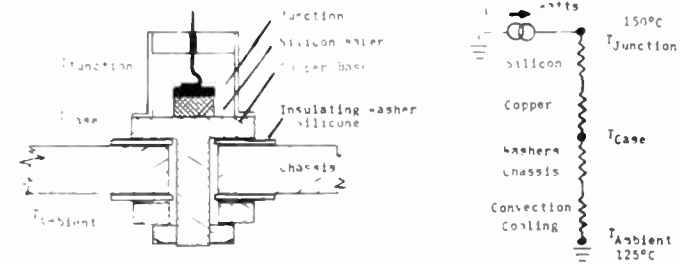


Fig. 8
Mounting and Cooling of Rectifier.

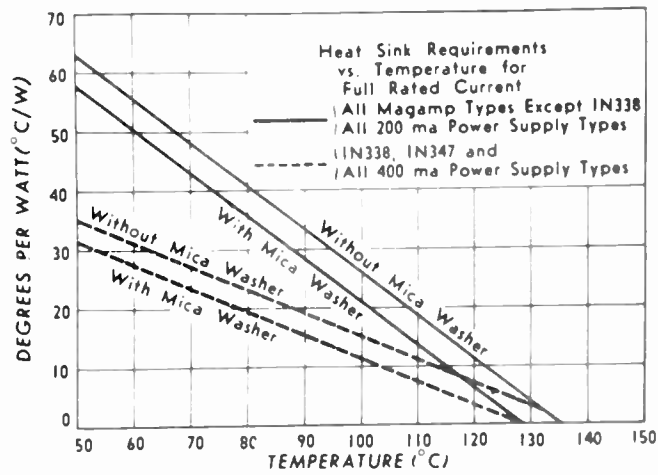


Fig. 9
Heat Sink Requirements of Rectifier.

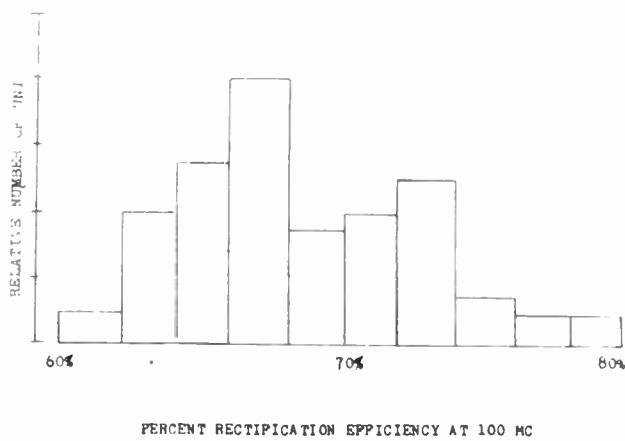


Fig. 10
100 Mc Rectification Efficiency.

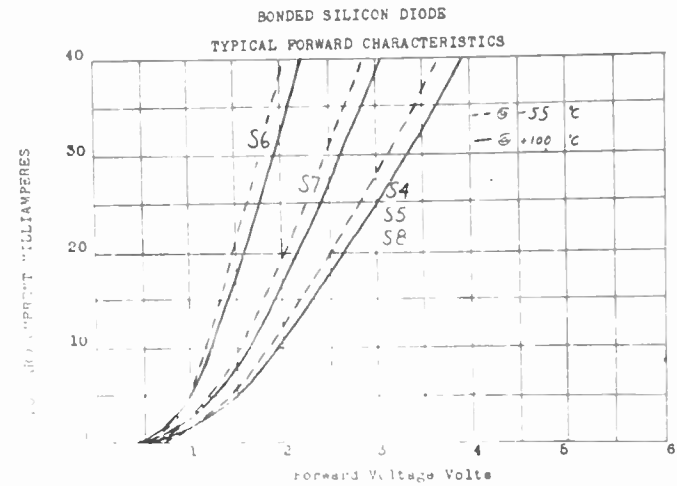


Fig. 11
Forward Characteristics of h.f. Diodes.

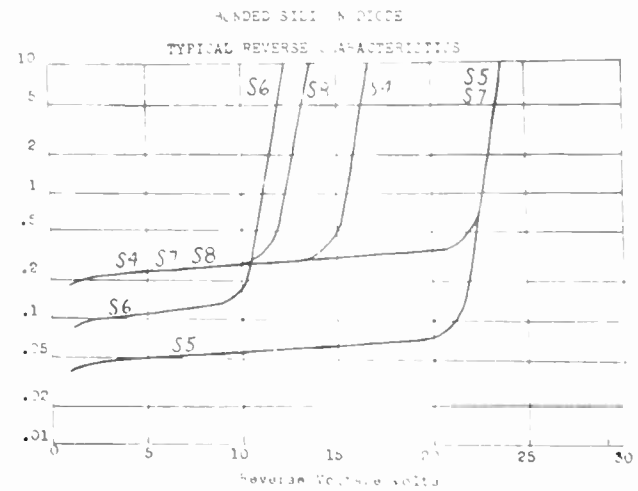


Fig. 12
Inverse Characteristics of h.f. Diodes.

COMPARATIVE HIGH-FREQUENCY OPERATION OF JUNCTION TRANSISTORS

MADE OF DIFFERENT SEMICONDUCTOR MATERIALS*

L. J. Giacoletto
RCA Laboratories
Radio Corporation of America
Princeton, N. J.

Summary

The high-frequency performance of junction transistors is determined in part by the time required for the injected minority carriers to traverse the base region. Large minority carrier mobility contributes to reducing this transit time. However, the high-frequency performance is also affected by factors such as base-lead resistance and collector-to-base junction capacitance, and it is shown that large majority carrier mobility will reduce the detrimental effects of these factors.

An important result of the analysis of high-frequency operation is the discovery that both minority and majority carrier mobilities are of about equal importance. It follows that the high-frequency performance of an n-p-n transistor should be about the same as that of a geometrically identical p-n-p transistor. Furthermore, for evaluation of new semiconductors, a knowledge of the values of both mobilities is required, and a figure of merit is proposed which is formed by the product of the two drift mobilities divided by the square root of the dielectric constant.

Introduction

Charge carriers in semiconductors are of two types - minority carriers and majority carriers. In an n-type semiconductor, the electrons are the majority carriers and are normally present; the holes are the minority carriers, often injected from one of the boundaries. The reverse is true for p-type semiconductors.

Because, in the conventional junction transistor, it is the minority carriers which flow out of the emitter, through the base, and into the collector, the role of the majority carriers is often neglected. This leads to an incorrect concept of the factors which enter into high-frequency behavior. It is true that the high-frequency performance of a junction transistor is affected by the time required for the minority carriers to traverse the base region, and that large minority carrier mobility contributes

to the reduction of this transit time, but this is only part of the story. Since charge neutrality must exist, minority carriers flowing into, and out of, the base region are accompanied by flow of majority carriers also into, and out of, the base region. This produces a high-frequency voltage drop in the base-lead resistance which is determined in part by the majority carrier mobility. In addition, majority carrier mobility affects the very important collector-to-base junction capacitance.

An important result of this analysis of high-frequency operation is the discovery of the fact that the majority and minority carrier mobilities are of nearly equal importance. It follows that, in general, p-n-p type transistors should not be very different from n-p-n type transistors in high-frequency performance. Furthermore, for evaluation of new semiconductors, a knowledge of the values of both majority and minority carrier mobilities is required. A figure of merit for semiconductors is proposed which is formed by the product of the two drift mobilities, divided by the square root of the dielectric constant. With the aid of this figure of merit, semiconductor materials that have been considered good because of their large electron Hall mobility are shown to be poor for use in transistor devices.

In this article, after a discussion of the general equation for high-frequency performance, a comparison is drawn, first between transistors of different polarity (n-p-n and p-n-p) but made with the same semiconductor material, and second between transistors of the same polarity but made with different semiconductor materials. This report covers only the analysis, but the conclusions drawn are in accord with extensive small-signal experimental data on germanium and silicon junction transistors.

High-Frequency Operation

The hybrid- π common-emitter equivalent circuit as shown in Figure 1a will be employed as the basis for the study of high-frequency operation.¹

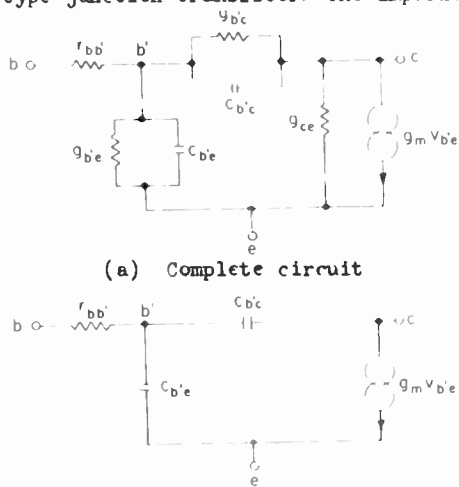
At higher operating frequencies the conductances shown in Figure 1a are negligible in comparison with the capacitive susceptances, and the equivalent circuit which is applicable

*First published in RCA Review, vol. 16, pp. 34-42; March, 1956.

is that shown in Figure 1b. An approximate analysis of this circuit indicates that the maximum power amplification is given by

$$P.A. \approx \frac{g_m}{4\omega^2 r_{bb'} C_{b'e} C_{b'c}} \quad (1)$$

With the aid of equations for the transistor parameters and some approximations, this equation can be written in terms of the semiconductor constants and the operating point. Expressions will be written of general validity, but, for clarity, the subscript notation will be that for an n-p-n transistor. In order to obtain the expressions for a p-n-p transistor it is only necessary to interchange n and p subscripts and d and a (donor and acceptor) subscripts wherever they occur. The development throughout this article is for abrupt impurity transitions as found in alloy-type junction transistors. In grown-type junction transistors the impurity



(b) Circuit applicable at high frequencies.

Fig. 1 - Hybrid- π common-emitter equivalent circuit.

transition is generally gradual. Although the detailed results differ, the basic conclusions are the same for both alloy- and grown-type junction transistors.

For a reasonably good transistor, emitter and collector currents are approximately equal, so that $g_m \approx \Lambda I_E$ where Λ is 39 volts⁻¹ at room temperature and I_E is the emitter current. The base-lead resistance, $r_{bb'}$, is a function of transistor geometry. From measurements, $r_{bb'}$ is

For other temperatures, $\Lambda = \frac{e}{kT}$ where e is the electronic charge and k is Boltzmann's constant. Hence $\Lambda = 11600/T$ where T is in degrees K.

known to be inversely proportional to the conductivity of the base-region semiconductor, σ_b , so that $r_{bb'} = 1/(G \sigma_b)$ where G is the constant of proportionality involving the transistor geometry. The expression for the diffusion capacitance, $C_{b'e}$, is

$$C_{b'e} = \Lambda^2 I_E \frac{W_b^2}{2\mu_n}$$

where μ_n is the electron mobility in the p-type base semiconductor and W_b is the base thickness between points of zero electrostatic voltage gradient. Throughout this report, W_b will be considered constant. The collector-to-base capacitance, $C_{b'c}$, generally consists of two factors - a barrier capacitance and a transit time capacitance. In high-frequency transistors where W_b is small and σ_b is large, the collector junction barrier capacitance will predominate, so that

$$C_{b'c} \approx A_c \left[\frac{K_e \epsilon_0 \sigma_b}{2\mu_p V_{CE}} \right]^{1/2}$$

where A_c is the collector area, K_e is the dielectric constant of the base semiconductor, ϵ_0 is the permittivity of free space, μ_p is the hole mobility in the p-type base semiconductor, and V_{CE} is the collector voltage. With the expression $\sigma_b \approx eN_a \mu_n$ (where e is the electron charge and N_a is the acceptor density of the base impurity atoms), Equation (1) can be written

$$P.A. \approx \frac{G \mu_p \mu_n}{\omega^2 A_c \Lambda \left[\frac{2K_e \epsilon_0}{eN_a V_{CE}} \right]^{1/2} W_b^2} \quad (2)$$

As mentioned above, this expression is applicable to alloy-type junction transistors where the collector junction barrier occurs in the base semiconductor.

Examination of Equation (2), at first glance, makes it seem advisable to choose a high collector bias, V_{CE} , and a high base impurity density, N_a . However, the "breakdown" phenomenon of the collector, considered in the next section, is such that, when N_a rises, the maximum V_{CE} falls. Furthermore, when N_a rises sufficiently, the mobilities μ_n and μ_p begin to decrease noticeably. The next two sections discuss these interrelationships.

Effect of Collector Voltage

In so far as the operating point is concerned, Equation (2) indicates that the high-frequency power amplification is independent of emitter current but directly proportional to the square root of the collector voltage. For improved high-frequency performance V_{CE} should be made as large as possible. There are two possible limits to the magnitude of V_{CE} . First, the collector voltage may be so large that the collector junction barrier thickness is comparable to W_b . This is not likely to occur in high-frequency transistors where σ_b is relatively large. As mentioned before, W_b the variation of W_b with V_{CE} must be considered in this region of operation; other factors which are considered in the last section may also be significant. Second, the collector voltage may be so large that collector breakdown occurs. This is more likely limitation on the magnitude of V_{CE} . The practical maximum collector voltage will generally be less than the collector breakdown voltage. Two mechanisms, Zener breakdown³ and avalanche breakdown⁴, have generally been used to account for collector breakdown. Zener breakdown is due to internal field emission and should in theory occur when the collector-to-emitter voltage is

$$V_Z = \frac{K_e \epsilon_0}{2eN_a} E_Z^2. \quad (3)$$

The critical Zener field, E_Z , is proportional to the "band gap" and the lattice spacing of the material. Avalanche breakdown is due to electron-hole pair formation by ionization similar to Townsend discharges in gases. It is now generally believed that the avalanche mechanism plays the predominant role in collector breakdown. Preliminary measurements of avalanche breakdown indicate that the breakdown voltage is proportional to $N_a^{-0.7}$. The semiconductor surface also contributes to the breakdown characteristics, but in a manner which tends to obscure the actual breakdown. For purposes of this article, the differences between Zener and avalanche breakdown dependence on N_a are minor so, for simplicity, it will be assumed that collector breakdown voltage is proportional to $1/N_a$.

The variation in high-frequency performance with operating point (collector voltage) has been considered. The improvement in high-frequency performance that can be obtained by altering the transistor design will now be considered.

Optimum Transistor Design

In accordance with Equation (2), improved performance can be obtained by designing for a

large geometrical factor (small r_{bb}), G , small collector area (small C_{bc}), A_c , and small base thickness (small C_{be}), W_b . In addition, the semiconductor material can be "doped" more heavily to increase N_a . However, this will cause μ_n and μ_p to decrease and will necessitate a reduction in V_{CE} . If V_{CE} is always adjusted to some fixed fraction of the breakdown voltage, then $N V_{CE}$ will be constant. In this event, relatively pure (e.g. $\sigma_b < 1$ mho per centimeter) semiconductor material should be used since μ_n will then be maximum. This may be better understood by considering that the change in r_{bb} , for different semiconductor conductivities, is exactly counterbalanced by a change in C_{bc} when V_{CE} is readjusted in proportion to the breakdown voltage.

The situation may be considerably different if, in the operation of the transistor, the collector voltage is to be held constant independent of the semiconductor conductivity. In this event the power amplification as given by Equation (2) can be optimized by choosing σ_b so that $(eN_a)^{1/2} \mu_n \mu_p \equiv (\sigma_b \mu_p)^{1/2} \mu_n$ is maximum, keeping in mind that the μ 's are functions of N_a and σ_b . Accordingly, the optimum value of σ_b can be determined by plotting $(\sigma_b \mu_p)^{1/2} \mu_n$ or by satisfying the relation

$$\frac{1}{\sigma_b} + \frac{1}{\mu_p} \frac{\partial \mu_p}{\partial \sigma_b} + \frac{2}{\mu_n} \frac{\partial \mu_n}{\partial \sigma_b} = 0. \quad (4)$$

Similar expressions with n and p subscripts interchanged are applicable for a p-n-p transistor. Equation (4) states that the optimum value of σ_b is such that the sum of the fractional change in base conductivity plus the fractional change in majority carrier mobility plus twice the fractional change in minority carrier mobility is zero. The optimum value of σ_b can be determined if the functional relationship between μ_n and μ_p and σ_b is known or if measured data is available. Thus, in the case of germanium, the optimum σ_b is approximately 8 mhos per centimeter for an n-p-n transistor and 22 mhos per centimeter for a p-n-p transistor.

The design implications of optimum σ_b , when the collector voltage is fixed, can be summarized as follows. The σ_b to be employed is the smallest of the two values determined from (a) the optimum σ_b as given by Equation (4) and (b) the σ_b corresponding to a collector breakdown voltage somewhat larger than the operating collector voltage.

Comparison of N-F-N and P-N-P Transistors Made From The Same Semiconductor Material

If an n-p-n and a p-n-p transistor are made

from the same semiconductor material containing equal densities of impurity atoms, with identical geometries including the same W_b , and the two are operated at the same collector voltage and frequency, then from Equation (2)

$$\frac{\text{P.A.}_{n-p-n} \left[\frac{\mu_p \mu_n}{K} \right]_{p\text{-material}}}{\text{P.A.}_{p-n-p} \left[\frac{\mu_n \mu_p}{K} \right]_{n\text{-material}}} \approx 1. \quad (5)$$

That is, the high-frequency power amplification of the two transistors would be approximately equal. The approximation comes about only because of the relationship between mobility and impurity density, but is quite valid for germanium even with relatively large impurity densities (with conductivities of around 1 mho per centimeter, the accuracy is within 2 per cent).

If, instead of equal impurity densities, they have equal conductivities of the base material, then

$$\frac{\text{P.A.}_{n-p-n} \left[\frac{(\mu_p)^{1/2} \mu_n}{K} \right]_{p\text{-material}}}{\text{P.A.}_{p-n-p} \left[\frac{(\mu_n)^{1/2} \mu_p}{K} \right]_{n\text{-material}}} \approx b^{1/2} \quad (6)$$

where b is the ratio of electron to hole mobility in intrinsic material. The $b^{1/2}$ result ($2.06^{1/2} = 1.43$ for germanium and $2.4^{1/2} = 1.55$ for silicon), although exact only for small conductivities approaching that of intrinsic material, is still approximately correct for relatively large conductivities. Thus, for 1 mho per centimeter germanium, the more exact evaluation is 1.34.

The optimum value of σ_b forms a somewhat better basis for comparing n-p-n and p-n-p transistors. This comparison can be carried out when values for minority and majority carrier mobilities as a function of σ_b are available. For germanium when σ_b is optimum, the $\text{P.A.}_{n-p-n}/\text{P.A.}_{p-n-p}$ ratio is 0.95.

The comparisons above are for equal collector voltages. If the collector voltages are adjusted in proportion to the breakdown voltages, then in all cases the ratio is that given by Equation (5) so that the two transistors have approximately equal high-frequency power amplifications.

Comparison of Transistors Made From Different Semiconductor Materials

According to Equation (2), the power amplification of an n-p-n transistor is proportional to $\left[\frac{N_a V_{CE}}{K} \right]^{1/2} \mu_p \mu_n$. Consider two n-p-n transistors made of different semiconductor materials with the same impurity densities,

identical geometries including the same W_b , and operating at the same d-c collector voltage and frequency. In order for the first semiconductor to be superior to the second, it is necessary

that the $\frac{\mu_p \mu_n}{K^{1/2}}$ factor of the former be larger than that of the latter. Similarly, if instead of the same impurity densities, the same base conductivities are used, the appropriate factor is $\left[\frac{\mu_p}{K_e} \right]^{1/2} \mu_n$.

If the collector voltages are adjusted to the same proportion of their respective collector breakdown voltages, the appropriate comparison factor is $\mu_p \mu_n M$ independent of the base conductivities. M is a factor, dependent upon the material, which would be equal to E_z if the collector breakdown were due to a Zener mechanism.

In order to compare p-n-p transistors it is only necessary to interchange the p and n subscripts in the above factors. It is important to remember that although interchanging subscripts does not alter the form of some of the factors, the numbers substituted will generally be different when considering "doped" semiconductors. The numbers should be those of the majority and minority mobilities in the base material used.

It is noted that the comparison factor changes, depending upon the basis of comparison. Generally, detailed theoretical or measured data concerning minority and majority carrier mobilities in a semiconductor is needed before transistors of different semiconductor materials can be compared analytically. As a convenient basis

of comparison, a factor of $\frac{\mu_p \mu_n}{K^{1/2}}$ for the intrinsic material can be used as a figure of merit. A few values of this factor are tabulated in Table 1. It is important to note here that the mobilities used are drift mobilities. When drift mobility data is not available, rough comparisons can be made using mobility data obtained by other methods. However, it should be understood that these comparisons may not be highly significant in so far as transistor operation is concerned.

Further Discussion

It was mentioned that W_b is a function of the collector voltage and that this must be considered when W_b is small. W_b decreases with larger collector voltages so that the improvement in power amplification should be somewhat greater than that predicted by Equation (2). In so far as this equation is concerned, the power amplification should vary inversely as W_b^2 . In the derivation of Equation (1), the output self-conductance term, g_{ce} , (see Figure 1a) was

neglected. This term is inversely proportional to W_b and may no longer be negligible when W_b is very small. The modified expression for the power amplification including ϵ_{ce} is

$$P.A. \approx \frac{\epsilon_m}{4\omega^2 r_{bb'} C_{b'e}^2 \left[\frac{C_{b'c}}{C_{b'e}} + \frac{\epsilon_{ce}}{\epsilon_m} \right]}$$

Therefore, when ϵ_{ce} dominates the effect of $C_{b'c}$, the power amplification should vary at an even faster rate than formerly, namely inversely proportional to W_b^3 .

If constructional techniques should be developed such that $r_{bb'} \rightarrow 0$, then both $C_{b'e}$ and $C_{b'c}$ could be "tuned out" with suitable circuits. In this event, the maximum high-frequency performance of the transistor would be limited by the transit time of the minority carriers through the base, and the drift mobility of the minority carriers would be of primary importance.

Modified methods of junction transistor construction^{8,9} will alter some of the results, but generally drift mobilities of both carriers will still be important. In all cases it is desirable to make the base width as small as possible, to use a most favorable geometry including small junction areas, to use a base material whose conductivity is optimum, and to operate at a large collector-to-emitter voltage.

Table I - Semiconductor Figure of Merit

Material	μ_p	μ_n	K_e	$\frac{\mu_p \mu_n}{K_e^{1/2}}$
Germanium ⁵	1900	3900	16	1.85×10^6
Silicon ⁶	500	1200	12	0.17×10^6
90% Ge-10% Si Alloy ⁷	900 est.	1300	15.6 est.	0.30×10^6

References

1. L. J. Giacoletto, "The Study and Design of Alloyed-Junction Transistors," 1954 National Convention Record of the I.R.E., Part 3-Electron Devices and Component Parts, pp. 99-103, and id., "Study of P-N-P Alloy Junction Transistor from D-C through Medium Frequencies," RCA Review, Vol. 15, pp. 506-562, December, 1954.
2. When W_b is very small, or the collector voltage very large, the dependence of W_b upon the collector voltage may have to be considered.
3. C. Zener, "A Theory of the Electrical Breakdown of Solid Dielectrics," Proc. Roy. Soc. (London), Vol. 145A, pp. 523-529, July, 1934.
4. K. G. McKay, "Avalanche Breakdown in Silicon," Phys. Rev., Vol. 94, pp. 877-884, May 15, 1954.
5. M. B. Prince, "Drift Mobilities in Semiconductors I. Ge," Phys. Rev., Vol. 93, pp. 681-687, November 1, 1953.
6. M. B. Prince, "Drift Mobilities in Semiconductors II Si," Phys. Rev., Vol. 93, pp. 1204-1206, March 15, 1954.
7. S. M. Christian and E. R. Johnson, "Energy Gap and Mobility Measurements on Ge-Si Alloys," Session IV-A, Conference on Semiconductor Device Research, Minneapolis, Minn., June 28-30, 1954.
8. H. Krömer, "Der Drift Transistor," Die Naturwissenschaften, Vol. 40, No. 22, pp. 578-579, 1953. See also id., "Zur Theorie des Diffusions und des Drifttransistors," Archiv der Elektrischen Übertragung, Vol. 8, Part I, pp. 203-228, May, 1954; Part II, pp. 363-369, August, 1954; Part III, pp. 499-504, November, 1954.
9. J. M. Early, "P-N-I-P and N-P-I-N Junction Transistor Triodes," Bell Sys. Tech. Jour., Vol. 33, pp. 517-533, May, 1954.

CHARACTERISTICS AND SOME APPLICATIONS OF FUSED JUNCTION PNP
GERMANIUM TRANSISTORS FOR HIGH FREQUENCY USE

R. D. Greene
Raytheon Manufacturing Company
Receiving and Cathode Ray Tube Operations
Newton, Mass.

Summary

The high frequency behavior of fused junction transistors is largely determined by the equivalent circuit parameters - extrinsic base resistance, collector capacitance, and input diffusion capacitance. These factors are inter-related in terms of the physical properties of the transistor. Maximum safe collector voltage is also a function of the transistor physical properties in such a way that the problem of high frequency transistor design becomes one of compromise.

By reducing these limitations to a practical minimum a high frequency fused junction transistor has been designed which has alpha cutoff frequencies up to 30 mc. These units are currently being made on a production basis.

Some circuit applications in which these units have proven useful are broadcast receivers, video amplifiers and high speed switching circuits.

Introduction

When transistors were first introduced on the commercial market practical applications for these devices were largely restricted to the low frequency field. Initial transistor designs were characterized by poor frequency response among other things. The inherent attractions of low power dissipation, miniature size, and long life, in such applications as broadcast receivers, computers, and telemeters, however, has prompted intense development work on transistors of extended frequency range. Transistor tetrodes and triode units with basically new concepts have been announced for use in the medium frequency range.

The object of this paper is to describe the properties and some uses of a conventional fused junction transistor design which has been refined to extend the alpha cutoff frequency to about 30 mc. The techniques involved in commercial production of this device have been developed to the point where these units are available in production quantities. It is therefore considered

worthwhile to discuss some of the properties and applications of this unit.

Design Considerations

In the study of the high frequency behavior of fused junction transistors some form of equivalent circuit is now generally considered most accurate. For this discussion the circuit of figure I will be used¹. For this configuration the approximate expression for maximum high frequency power gain has been shown* to be;

$$G_p = \frac{Q}{KT} \cdot \frac{I_e}{16 \pi^2 F^2 r_{bb} C_{be} C_{tr}} \quad (1)$$

where Q is electronic charge
K is Boltsmanns constant
T is temperature (degrees Kelvin)

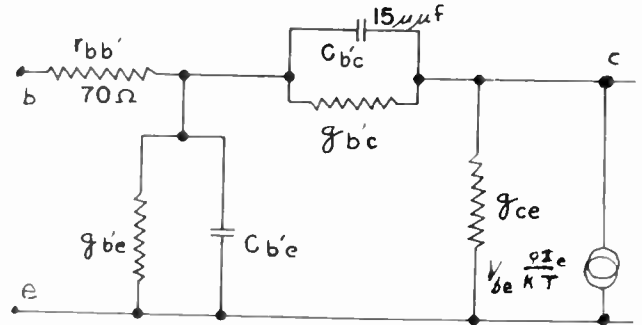


FIGURE I

Π Equivalent Circuit

* The equivalent circuit and equation 1 are essentially those of L. J. Giacoletto. "Study & Design of Alloyed Junction Transistors" Part III 1954 Convention Record IRE.

If we make the assumption that electron and hole mobilities in the base region are constant the transistor parameters r_{bb} C_{be} C_{bc} may be expressed as follows in terms of 1st order design parameters.

$$r_{bb} = \frac{A}{\sigma} \quad \text{where } A = \text{geometry constant}$$

$$\sigma = \text{base conductivity} \quad (2)$$

$$C_{be} \sim W^2 I_e \quad W = \text{effective base width} \quad (3)$$

$$C_{bc} \sim a_c \sqrt{\frac{K_e \sigma}{V_{ce}}} \quad a_c = \text{collector area} \quad (4)$$

$$K_e = \text{dielectric constant of base}$$

$$V_{ce} = \text{collector-emitter voltage}$$

Since the gain of the transistor is inversely proportional to each of the parameters (see eq. 1) the following inferences may be made:

1. The base width should be kept to a practical minimum for a minimum C_{be} .
2. The geometry of the base tab should be that which will make r_{bb} a minimum. In practice this means minimum distance between the active region and the point where base lead is joined to chip.
3. The collector dot size should be kept to a practical minimum for minimum C_{bc} .
4. Since the extrinsic base resistance decreases directly with increasing conductivity and collector capacitance increases only as the square root of the conductivity, the conductivity should obviously be increased by doping for over-all gain benefit. The practical limit to this turns out to be voltage breakdown as explained below;

There are two breakdown phenomena to consider as limits to the maximum voltage which can safely be applied to a transistor. Avalanche breakdown and the so called "punch through" effect². We will explain avalanche first:

Reverse bias applied to the collector-base diode of a transistor extends the space charge or carrier free region at the junction into the base. Because of the relatively heavy collector doping in a fused junction transistor virtually all of this space charge region grows out into the base - and all of the applied potential drop is across this space charge dimension. Minority carriers diffusing across the base are swept up by the po-

tential gradient in this area and are accelerated to a velocity proportional to the square root of collector bias voltage. In a manner somewhat similar to secondary emission effects the accelerated minority carriers generate electron hole pairs by collision and increase the effective current gain of the transistor. This effect increases with voltage to a point, known as avalanche breakdown- V_A , where the collector current increases without bounds for further voltage increase. V_A is inversely proportional to conductivity and therefore constitutes a practical limit on the base conductivity. As an example, for a base chip of practical dimensions, which is doped enough to give an r_{bb} of 70 ohms, V_A will be 35-40 volts.

The second phenomena, known as punch through, is a direct result of the growth of the space charge region mentioned above. As collector bias is increased this carrier free region grows out into the base, decreasing the effective base width of the transistor. At some critical voltage² $V_p = \sigma/2\epsilon_c \cdot W^2$ Min, the space charge region touches the emitter junction. Beyond this point there is no transistor action because there is effectively no base region for minority carrier diffusion. Punch through voltage is inversely proportional to conductivity but directly proportional to the square of base width and is therefore a limit on the practical minimum of base width.

Taking the above items into consideration a conclusion would be to choose an arbitrary voltage maximum, decide upon practical physical dimensions for production, and dope the base region accordingly. The CK760 series is a commercially available fused junction transistor which has been designed with consideration of these compromises. Typical values for this unit would be as follows;

$$r_{bb} \simeq 70 \text{ ohms}$$

$$C_{bc} \simeq \frac{34.5}{\sqrt{V_{ce}}} \text{ uuf}$$

$$C_{be} \simeq 500 I_e \text{ uuf}$$

Practical Voltage Limit

For a typical high frequency fused junction transistor with $f_{\alpha_{c0}} = 10 \text{ MC}$ avalanche breakdown V_A will be on the order of 40 volts and punch through V_p will be about 30 volts. The actual voltage limit for the average grounded emitter circuit case is neither of these but is a combination of the two effects known as collector-emitter breakdown, $V_{\alpha_m}^2$. Referring to figure II it is seen that the collector current for the case where $R_1 = \infty R_2 = \infty$ will be given by $I_c = \frac{I_{c0}}{1-\alpha}$.

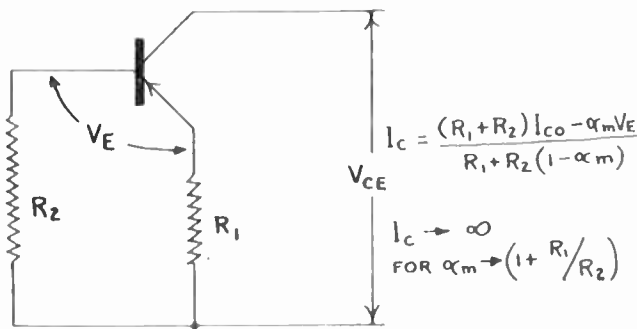


FIGURE 11

Test Circuit For Collector Emitter Breakdown As A Function Of Circuit Impedances.

It was mentioned above that multiplication effects in the space charge region increased gradually to the point V_A . If we define the multiplication factor as m then

$$I_C = \frac{I_{CO}}{1 - \alpha m} \quad (5)$$

This expression will go to infinity for $\alpha m \rightarrow 1$. In practice, αm will go to 15-20 volts below V_A , depending on the punch through and the low voltage current gain of the transistor. At all times $V_{\alpha m}$ will be below or just at V_p because the space charge widening causes an increase in α which is proportional to the decrease in effective base width.

As an aid in circuit design for maximum voltage consider figure 11 for the case of finite values of R_1 and R_2 . For this case I_C is seen to be:

$$I_C = \frac{(R_1 + R_2) I_{CO} - \alpha_m V_E}{R_1 + R_2 (1 - \alpha_m)} \quad (6)$$

In this equation I_C goes to infinity for $\alpha m \rightarrow (1 + R_1/R_2)$. It is here seen that maximum voltage is defined to some extent by the circuit impedances and by distortion requirements. Typical distributions of V_A , V_p , and $V_{\alpha m}$ as a function of alpha cutoff frequency are given for Raytheon high frequency transistors in figure 111.

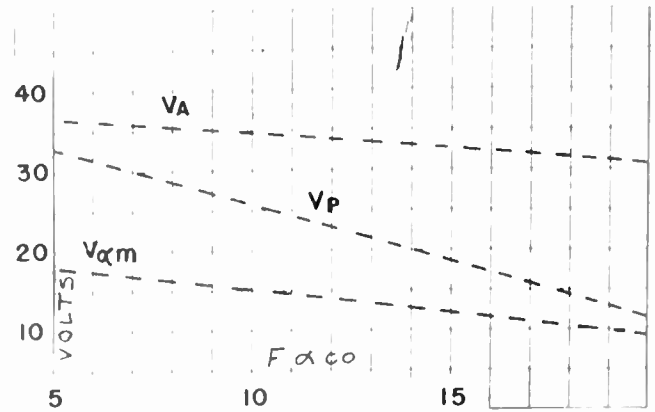


FIGURE 111

Voltage Breakdown Phenomena As A Function Of Alpha Cutoff Frequency.

Circuit Applications

Narrow Band Amplifiers

Figure IV is a schematic of a 455KC-60 DB transistor IF strip³ employing Raytheon type CK760 fused junction transistors. The IF cans for this strip are single tuned and tapped at the primary for an approximate impedance ratio of 20,000 ohms to 500 ohms. In this circuit design transistors having an alpha cutoff frequency of 5 mc will give 28 to 30 DB of gain per stage, including 3 DB transformer loss. Class B detection adds an extra 10 DB to off set r.f. filtering losses so total mixer to audio gain is about 60 DB.

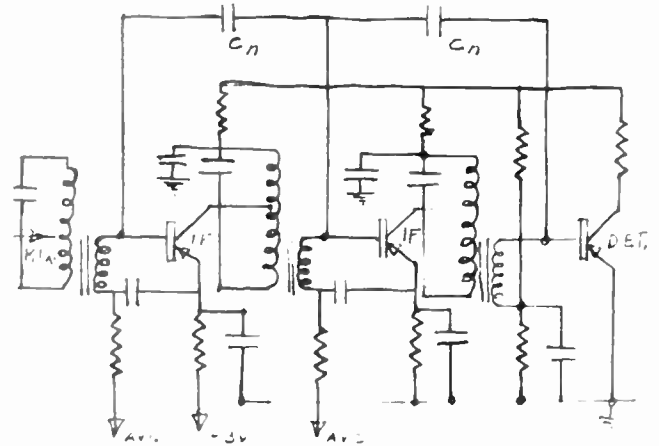


FIGURE IV

NEUTRALIZED I.F. STRIP

One of the design difficulties in medium and high frequency amplifiers of this sort stems from the fact that transistor output is internally connected to the input, and feedback is always present. Referring to figure 1 it is seen that this feedback comes from the collector capacitance, C_{bc} , returning to r_{bb} . The magnitude of this feedback current is approximated by

$\frac{QI_e V_{out}}{KT X_{c_{bc}}}$. We are assuming here that C_{be} is a much lower impedance than C_{bc} .

There are several techniques for neutralizing this feedback, one of the simplest of which is indicated.

Essentially, neutralization in this circuit consists of feeding back a portion of the input from one 1F stage to the input of the previous stage. Because of the presence of r_{bb} , full neutralization is not attainable with this technique. About 140 of the necessary 180 degrees of phase difference is attained however, and this has proven adequate for stable operation. More exact neutralization of the feedback loop is accomplished by addition of the series resistor to compensate for r_{bb} and other effects. This resistor is, for other than laboratory purposes however, considered unnecessary.

For the grounded base configuration, neutralization may be fed back directly from the collector - since input and output currents are approximately in phase. Accurate phase relationships may be obtained in this circuit by forming a bridge network⁴ with C_{cb} and r_b extrinsic as shown in figure V.

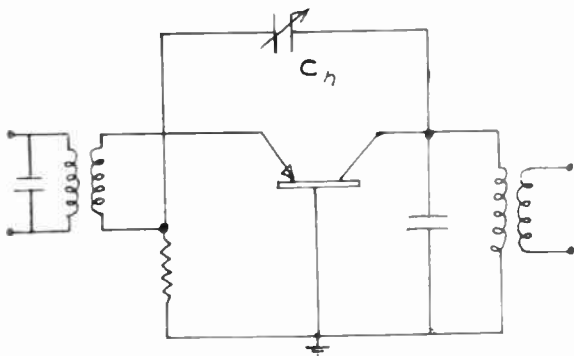


FIGURE V

Narrow Band Neutralized Grounded Base Amplifier

In tuned band pass circuits of analogous type the measured available gain for the grounded emitter configuration, including about 3 DB of transformer loss, is given as a function of frequency in figure VI. It has been established that the common base configuration is more suitable for narrow band amplification at the higher frequencies, partially because it presents less effective output capacitance to the circuit. Narrow band grounded base gain at 5 mc for a transistor with

$f_{\alpha_{co}} = 20$ mc is about 17 DB.

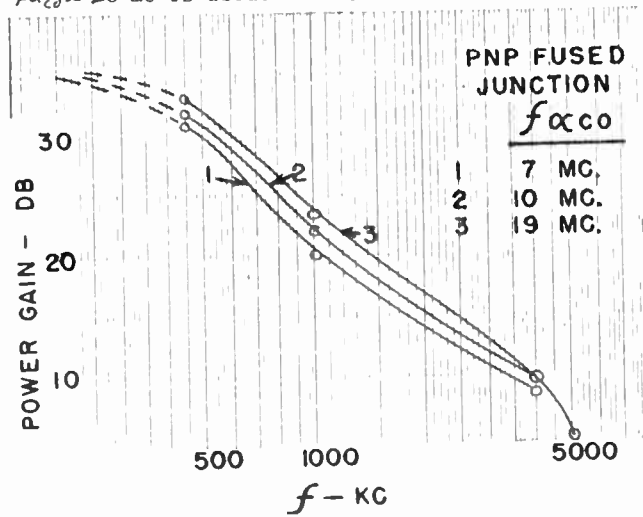


FIGURE VI
Grounded Emitter Stage Gain vs. Frequency
Wide Band Amplifiers

In the design of transistor amplifiers for wide band applications the circuit designer is limited to resistance capacitance coupling because the band width characteristics of coupling transformers are unsuitable. For this case the grounded emitter connection is of most interest, as the grounded base circuit has less than unity current gain and would not be useful for amplifying between equal input and output impedances.

It has been shown⁴ that, for the case where $f_{\alpha_{co}}$ rather than C_c is the limiting factor, the voltage gain band width is

$$G_v \times BW = \frac{\alpha_o}{1+r_b/r_c} \times f_{\alpha_{co}}$$

$$\text{or } G_v \times BW \approx f_{\alpha_{co}}$$

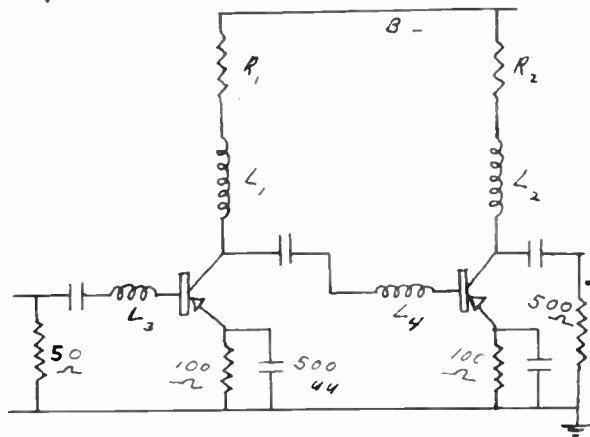


FIGURE VII
Broadband Amplifier

Figure VII shows a circuit diagram of a two stage transistor wide band amplifier on which some experimental measurements have been made. The basic design ideas incorporated into this circuit are entirely analogous those of vacuum tube theory. Each stage load impedance, $R_L + X_{L1}$, shunts a large part of the signal at the lower frequencies but this impedance peaks to a higher value with increasing frequency so that the shunt effect is reduced at the upper frequencies. The major portion of available signal current then feeds into the succeeding amplifier stage. Series chokes, L_3 and L_4 have also been used to tune with the capacitive portion of the input and to split the loading effects of transistor input and output capacitances.

An interesting method of compensation which was tried in this circuit consists of a partially bypassed emitter resistor. The partial bypass introduces an amount of gain degeneration which is a function of frequency. Such a scheme requires no chokes and is useful up to about two megacycles where peaking becomes important.

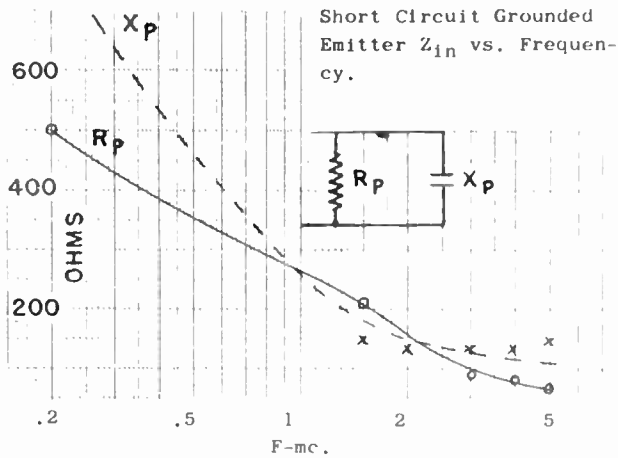


FIGURE VIII

The voltage gain of this circuit referred to equal input and output levels* is about 5 times per stage. The band width is 3-5 mc. Both transistors had measured $f_{\alpha c o}$ of 20 mc - which gives a

* Measured at 1 mc: $Z_{in} \approx r_{bb} + X_L \approx 100$ ohms.

$Z_{out} \approx R_2 R_L / R_2 + R_L \approx 200$ ohms.

Voltage Gain Equals 18 Times.

theoretical band width of 4 mc and fairly good agreement with measurement. The available power gain of this two stage circuit is 18 DB. Similarly, power gains of 10 DB have been obtained for a two stage circuit adjusted to give a band width of 5 mc.

Pulse Operation

On counter and computer circuitry the use of transistors has until recently been severely impeded by the poor transient response of available units. It is, for example, very difficult to get grounded base rise times better than 0.1 microseconds for a standard low frequency transistor without driving the unit well into saturation.

It has been shown⁵ that the small signal rise time for a fused junction transistor may be approximated by:

$$T = \frac{1}{2\pi F} \quad (7)$$

As an example, for a transistor having 10 megacycle α cutoff, rise time would be 0.016 μ sec. Figure IX gives some measured values of rise time under the small signal circuit conditions indicated. A curve calculated from eq 7 is also indicated and shows considerably better response. The apparent discrepancy is mostly a matter of definition, however, because the approximation of equation 7 is defined for $1/e$ or 63% of steady state, whereas measured values were taken between the 10% and 90% points on the slope. For the portion of the curve corresponding to the higher values of alpha cutoff the measurement accuracy was vitiated by equipment as the pulse generator used had a specified rise time of 0.02 microseconds.

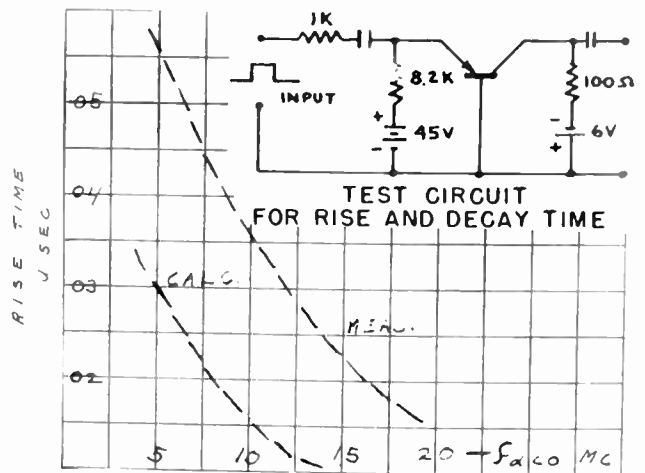


FIGURE IX

Small Signal Rise Time vs. Alpha Cutoff Frequency.

Decay times for this condition were also measured but are not shown in figure IX because they closely coincide, in most cases, with rise time measurements.

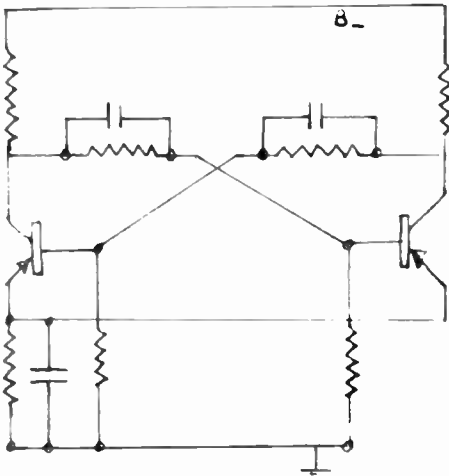


FIGURE X
Typical Multivibrator Circuit.

For the resistance capacitance-coupled multivibrator shown in figure X rise times of 0.2 microseconds were obtained using matched transistors with 8 mc alpha cutoff frequencies. Decay time for this case was 0.3 microseconds. For matched transistors of 17 mc $f_{\alpha_{CO}}$ rise and decay times were 0.1 and 0.2 microseconds respectively.

Conclusion

We have seen how the application of basic principles to fused junction transistor techniques has resulted in a unit having alpha cutoff frequencies up to 30 mc. This unit is useful as a

narrow band amplifier beyond 10 megacycles and has small signal pulse response exceeding 0.02 microseconds. For grounded emitter multivibrator circuits rise times of 0.1 microseconds may be obtained.

Acknowledgements

The author wishes to thank Mr. H. Schenkel, Mr. W. Sheehan and Mr. F. Fisher who performed much of the work described in this report.

References

1. L. J. Giacoletto "The Study and Design of Alloyed Junction Transistors" Part 3 Electron Devices and Component Parts 1954 Convention Record IRE Pages 99-103
2. H. Schenkel and H. Statz "Voltage Punch Through and Avalanche Breakdown and Their Effect On The Maximum Operating Voltages For Junction Transistors" National Electronics Conference Chicago October 6, 1954
3. W. Sheehan and J. H. Ivers "Design of Transistorized High Gain Portable" Electronics March, 1955 Pages 159-161
4. J. B. Angell and F. P. Keiper "Circuit Applications of Surface Barrier Transistors" Proceedings of the IRE Volume 41 #12 December, 1953 Pages 1709-1712
5. J. L. Moll "Large Signal Transient Response of Junction Transistors" Proceedings of the IRE Volume 42 #12 December, 1954 Pages 1773-1783

A MINIATURE PRECISION DELAY LINE

James B. Hickey
Rome Air Development Center
GAFB, Rome, N. Y.

Summary

A lumped constant type delay line having an equivalent "m" derived low-pass filter configuration was developed at Rome Air Development Center, to replace the distributed constant type that failed to meet military temperature stability specifications. The unique construction of the new lumped constant delay line resulted in a miniaturized design with a resulting improvement in the overall space factor. Availability of delay taps at extremely small delay increments gave the new delay line a built-in precision to meet the required delay accuracy tolerance. Additional advantages of the lumped constant delay line over the distributed constant type include temperature stability, reproducibility, and versatility of design.

Introduction

During the past few years the transient delay line has gained prominence as a necessary electronic component for delaying or storing electrical information. When the desired delay time is in the order of microseconds, an electrical network, usually of a low-pass filter configuration, is frequently employed.

The L-C low-pass filter type delay line networks can be divided into the following general classes in accordance with their physical construction:

1. The wire wound distributed constant type with series inductance (L) furnished by a continuous winding and shunt capacity (C) developed between the winding and a grounded shield structure.

2. The lumped constant type employing a discrete inductor and capacitor for each section of the delay network. The delay line described belongs in this category.

The lumped constant delay line was developed at RAIC to replace a wire wound distributed constant type previously developed at RAIC for application in a complex aircraft identification system. Specifications for such a delay line read in part:

1. Sufficient bandwidth for handling $1/2$ microsecond-wide pulses, spaced $1-1/2$ microseconds apart.
2. Capable of total delays in the order of 25 microseconds.
3. Delay accuracy to be held to within plus or minus 0.05 microseconds.

4. Delay accuracy tolerance to be held over a temperature range of minus 50° C. to plus 80° C.

5. Attenuation and space factor to be minimized in the interest of circuit and mechanical designs of airborne components.

Theory

Basic Requirements

The L-C low-pass filter can perform as a delay line and faithfully reproduce impulse voltage waveforms after a desired delay, provided the following minimum conditions are met:

1. Cutoff frequency must be high enough to prevent discrimination against high frequency components of the complex waveform.
2. Phase shift characteristic of the network must increase linearly with frequency.
3. Attenuation characteristic must be independent of frequency within the pass-band and must not be excessive.

Bandwidth. As cutoff frequency of a low-pass filter network varies inversely with the unit delay of each section, the bandwidth requirements dictate the total number of sections required for a given delay and thus effect the bulk or space factor of the delay network.

Phase Characteristic. The "m" derived low-pass filter network can be made to possess a linear phase characteristic by the proper choice of value for the "m" parameter.¹ This value should be in the region of 1.25 to 1.40. In ordinary filter design, a value for the "m" parameter in excess of 1.0 in a series derived filter requires that a negative inductance be inserted in series with the shunt capacitor. This situation is obtained in practice by allowing inductors of adjacent sections of the L-C low-pass network to have positive mutual coupling.²

Figure I-1 shows a single L-C section, Figure I-2 a network of these sections cascaded together with adjacent inductors mutually coupled and Figure I-3 an equivalent network showing the effect of this coupling. The quantities L_k and C_k refer to a prototype constant K filter and the equations shown indicate that the equivalent network is a series "m"-derived filter with "m" greater than 1.0. The equivalence of the two

Circuits shown in Figures I-2 and I-3 can be proved by setting up the Kirchhoff loop equation for any internal loop in each network.³ These equations are identical and are as follows:

$$i_1 [j\omega m - \frac{1}{j\omega C}] + i_2 [j\omega L - \frac{2}{j\omega C}] + i_3 [j\omega m - \frac{1}{j\omega C}] = 0$$

Where i_1 is the current in the preceding loop
 i_2 is the current in the loop in question
 i_3 is the current in the following loop

The coefficient of coupling (k) is related to the "m" parameter by the equation:

$$m^2 = \frac{1+2k}{1-2k}$$

The delay line described in this report has a mutual coupling of 12.5% between adjacent sections. This gives a value of 1.29 for the "m" parameter of the equivalent network. The relation between phase shift (β) in radians and frequency expressed as a percent of the cutoff frequency for the equivalent network, derived from the Campbell's network equations, is given by the equation:⁵

$$\beta = \cos^{-1} \left[1 - \frac{2m^2}{(\omega/\omega_c)^2 - 1 + m^2} \right]$$

A plot of this equation is shown in Figure II for three different values of the "m" parameter. The top curve (A) where "m" = 2.0, shows the phase shift increasing at a decreasing rate with frequency. This condition would result from over-coupling of the adjacent inductors in the actual network. The high frequency components suffer from insufficient delay, resulting in distortion of the voltage waveform. The bottom curve (C) where "m" = 1.0, shows the phase shift increasing at an increasing rate with frequency. This condition results in distortion of the input voltage waveform due to excessive delay of the high frequency components. The center curve (B), where "m" = 1.29, is extremely linear up to 75% of the cutoff frequency and has very little curvature up to 90% of cutoff.

Attenuation: When the series resistance and the shunt conductance of a low-pass filter network are negligible in comparison with series inductance and shunt capacitance, attenuation is expressed by the equation:

$$\alpha = \omega t / 2Q_L$$

By substituting $\frac{\omega L}{R}$ for the coil "Q" it can be seen that attenuation is independent of frequency, as

$$\alpha = \frac{tR}{2L}$$

With time delay, t , equal to \sqrt{LC} and characteristic impedance Z_0 equal to $\sqrt{L/C}$ as in the case of a constant K, the attenuation equation is expressed by⁶

$$\alpha = \frac{R}{2|Z_0|}$$

These two forms of the attenuation equation are of interest because they indicate that to minimize attenuation, the "Q" of the network inductors must be large and/or the characteristic impedance should be as high as possible.

Design Equations

Low-pass constant K filter equations useful in delay line design are:

$$\text{Characteristic impedance } Z_0 = \sqrt{\frac{L_k}{C_k}} \text{ ohms.}$$

$$\text{Time delay per line section } t = \sqrt{L_k C_k} \text{ seconds.}$$

$$\text{Cutoff frequency } f_c = \frac{1}{\pi \sqrt{L_k C_k}} \text{ cycles per second.}$$

$$\text{Attenuation } \alpha = \omega t / 2Q_L = \frac{R}{2|Z_0|} \text{ nepers.}$$

These equations can be applied directly for fairly close approximations, especially if the value for the unit inductance is increased sufficiently to allow for effects of mutual coupling in the "m" derived case. The following equations hold for the "m" derived network and include the effects of mutual coupling between adjacent inductors. Where (k) is the coefficient of coupling between adjacent inductors:

$$\text{Characteristic impedance } Z_0 = \sqrt{(L/C)(1+2k)}$$

$$\text{Cutoff frequency } f_c = \frac{1}{\pi \sqrt{LC(1-2k)}}$$

$$\text{Time delay } t = A \sqrt{LC(1-2k)}$$

The factor A in the time delay equation can be evaluated from the phase shift curves. Since the velocity of propagation v in a filter network is equal to $\frac{2v_0}{\pi}$ and the time delay t is $\frac{t}{v}$, then $t = \frac{t}{v}$. The slope of the phase shift curves given in Figure II is $\frac{\omega t}{\omega_c}$. Thus, this slope is equal to $t\omega_c$. The slope of the phase shift curve where "m" = 1.29 has a constant value of 2.58 throughout its linear portion. The factor A is equal to one-half this slope value.

The equations that apply for the actual network having a mutual coupling of 12.5% ("m" = 1.29) in terms of the unit inductor L and the unit capacitor C are:

$$Z_0 = 1.11 \sqrt{L/C}$$

$$f_c = 1.15 / \pi \sqrt{LC}$$

$$t = 1.12 \sqrt{LC}$$

Development

Figure III shows experimental delay units that represent some of the steps involved in the development of the final design of the delay unit (Figure III-6) starting with the replaced wire wound distributed constant delay unit (Figure III-1). The first step involved building up lumped constant lines employing the standard method of end-coupling the coils (Figure III-2) to check out the required number of sections for a given delay and bandwidth. Ten sections per microsecond delay were tentatively set. This meant that the unit shown in Figure III-2, while occupying more space than the wire wound unit, had only $2/3$ the required delay. From this point, efforts were concentrated on the space factor problem as the new delay line had to replace the old wire wound line physically as well as electrically.

The unit shown in Figure III-3 was constructed to check the feasibility of placing capacitors inside the inductors. Attenuation was increased due to a drop in the coil Q. However, this factor could be offset by keeping the characteristic impedance high which was in line with the requirement of replacing a high impedance wire wound delay line. These units gave encouraging results.

The unit shown in Figure III-4 represents an effort to place more sections in a given space. The results proved very discouraging and the method using end-coupled coils was rejected.

The experimental unit shown in Figure III-5 shows an alternate method employing side coupled coils with capacitor bodies serving as the inductor coil forms. This method resulted in the final design and a complete solution to the space factor problem.

Construction Details

Construction details of the delay unit are shown in Figure IV. The subassembly drawing in Figure IV-1 shows how the delay units are stacked tightly together in three rows. The bottom pig-tail lead of each capacitor passes through a slot in the grounded base plate where it is bent over and secured with solder. The top pig-tail lead of each capacitor serves as a junction terminal for the inductors and becomes an available delay tap between each and every delay unit. A single section is shown in Figure IV-2 with the winding applied directly to the capacitor body. The start lead of the coil is secured to the top pig-tail of the condenser and the finish lead is brought up and attached to the top condenser lead of the adjacent section during

assembly. These connections are illustrated in the expanded sketch of Figure IV-3. This sketch also shows the direction of the current in the winding and the corresponding direction of the mutual magnetic flux linking the adjacent coils. It should be noted that the magnetic polarity of adjacent inductors must be reversed to obtain positive mutual coupling. This reversal is obtained by winding alternate coils in the opposite direction. The proper amount of coupling is fixed by the geometry of the coil form and not by any required spacing of the inductors as in the end-coupled case. This is the optimum space factor as the entire delay network occupies very little more space than is required for the capacitors alone.

The required number of sections per microsecond delay was increased slightly to drop the unit delay per section to 0.097 microseconds. Thus, the desired overall delay accuracy tolerance would be less than the plus or minus 0.05 microseconds required by simply selecting the proper delay tap. This device eliminated the tedious trimming encountered in the manufacture of the wire wound units. Furthermore, the new lumped lines are not sensitive to temperature changes, moisture content, or proximity to the metal case as were the wire wound units.

Design Values. The following are the design values for the lumped constant delay line.

Capacitors - 100 mmf El Menco Silver Mica
CM-15 body.

Inductors - 150 turns of #38 Formex wire
over 11/32 inch length

Average inductance per coil - 77 micro-
henries

Approximate equivalent "m" parameter - 1.29

Approximate coupling between adjacent coils -
12.5%

Approximate characteristic impedance - 980
ohms

Average delay per line section - 0.097 micro-
seconds.

Approximate cutoff frequency - 4.25 mega-
cycles per second.

Approximate space factor - 1.5 microseconds
per cubic inch.

Performance

A direct comparison of three delay line assemblies is shown in Figure V. Figure V-1 shows one of the few lines commercially available at the time of this development. It has a total delay of approximately 8.0 microseconds. This delay line was not designed to handle 1/2 microsecond wide pulses with the required delay accuracy. The delay line shown in Figure V-2 is the replaced wire wound distributed constant type and the delay line shown in Figure V-3 is its replacement, the lumped constant delay type. The latter two delay lines have a total delay of approximately 10.0 microseconds. The lumped constant delay line, made up of two sub-assemblies (Figure IV), is packaged in the same size case as used for the wire wound line. This line could occupy much less space by mounting the sub-assemblies "back to back", thus increasing the thickness only slightly while reducing the width by nearly one-half.

Synoscope traces of a chain of narrow pulses entering and leaving each of these three delay line assemblies give a direct comparison of the performance of the three lines and indicate the satisfactory operation of the lumped constant delay line. Figure VI shows the chain of pulses entering (top trace) and leaving (bottom trace) the 8-microsecond commercial line. These pulses are 1/2 microsecond wide at the mid-amplitude level. The closest spacing is approximately 1-1/2 microseconds from leading edge to leading edge. Output pulses are taken across a 3600 ohm terminating resistor. This set of traces is of additional interest because it gives a good example of pulse-shape distortion due to a non-linear phase characteristic. After only an 8-microsecond delay the high frequency components lag the lower frequencies.

In Figure VII the same chain of pulses can be seen entering and leaving the 10-microsecond wire wound line. In this case the terminating resistor is 3300 ohms. The output pulse shape also suffers slightly from a non-linear phase characteristic that causes the base line to build up within the pulse chain. Additional circuitry was required to combat this non-recovery problem.

Figure VIII shows the chain of pulses entering and leaving the 10-microsecond lumped constant delay line. A 910-ohm resistor was used to terminate this line. Here the output pulse shape is quite symmetrical, indicating a linear phase characteristic. This line has sufficient bandwidth to resolve the closely spaced pulses. It should be noted that there are no reflections along the base line indicating a constant impedance

characteristic. The attenuation indicated by the loss of pulse amplitude, is slightly greater than in the wire wound line, but this is offset by the lack of base line build up and reflections.

Conclusions

The more important advantages obtained with the new lumped constant delay line over the wire wound distributed constant type are:

Space Factor. The lumped constant line gives about 1.5 microseconds per cubic inch as compared to 1.1 microseconds per cubic inch for the wire wound line.

Temperature stability. Employing capacitors having proper temperature characteristics insures a total delay that will not drift with temperature changes.

Availability of delay taps. The top pig-tail lead of each capacitor becomes an available delay tap between each and every delay unit giving delay increments of 0.097 microseconds.

Reproducibility. The delay line has proved to be highly reproducible and at the present time has been in production for over two years.

Versatility of design. A wide range of bandwidth, impedance, and delay can be obtained by proper selection of values for inductance, capacity, and mutual coupling.

References

1. Moskowitz, S., and Racker, J., "Pulse Techniques", Prentice-Hall, Inc., 1951. p. 111
2. Guillemin, E. A., "Communication Networks", John Wiley & Sons, Inc., p. 327.
3. LePage, W. R., and Seely, S., "General Network Analysis", McGraw-Hill Book Company, Inc., p. 102.
4. Lester, J. M., "Transient Delay Line", Electronics, April 1946, p. 147.
5. Russell, F. A., and Padalino, J. J., "Projects For the Study of Electrical Circuits", Vol III, Newark College of Engineering, 1948, p. 56.
6. Everitt, W. L., "Communication Engineering", McGraw-Hill Book Company, Inc., 1937, p. 119.

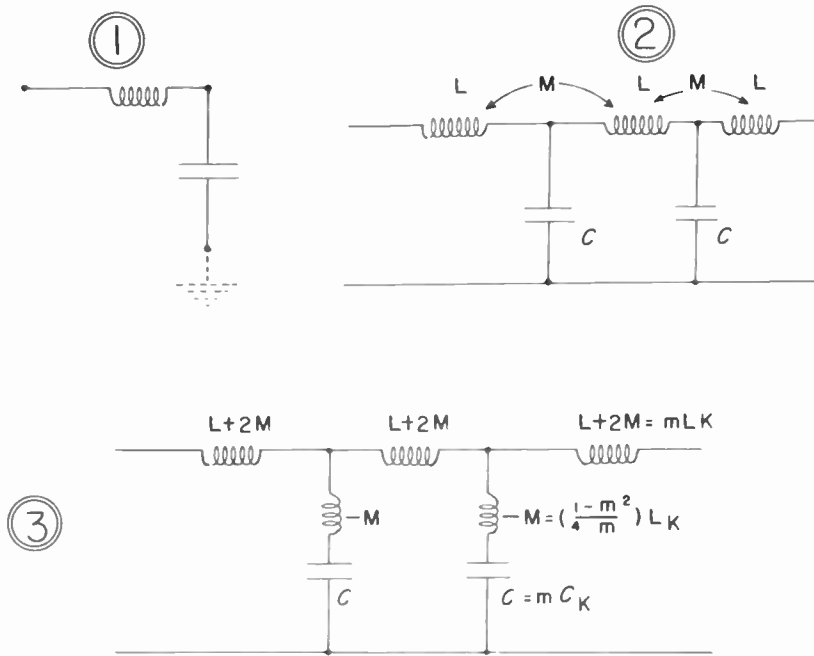


Fig. 1
 (1) Single L-C section. (2) L-C network with coupling. (3) Equivalent "m" derived network.

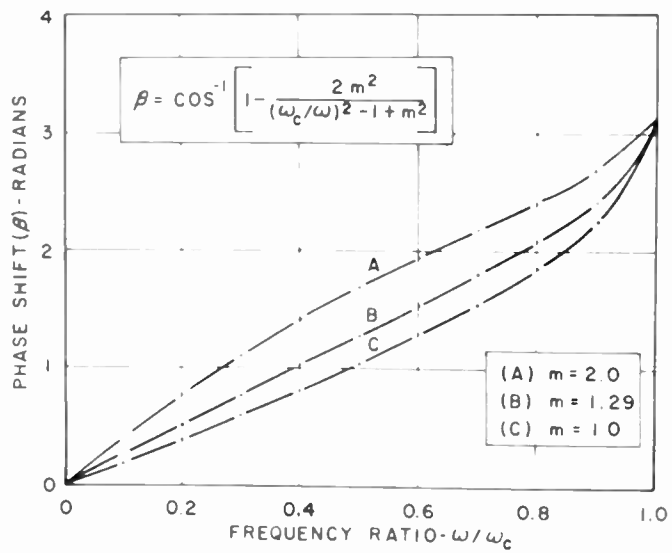


Fig. 2
 Phase shift vs frequency curves.

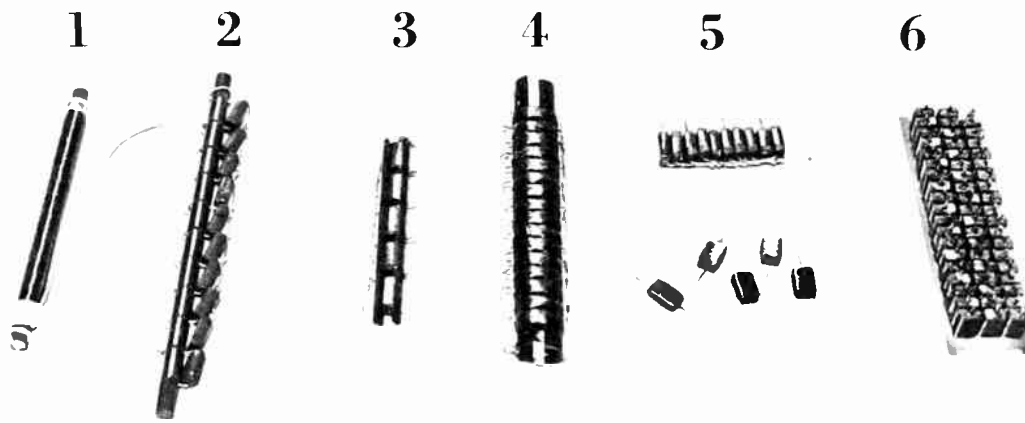


Fig. 3
Experimental delay line units.

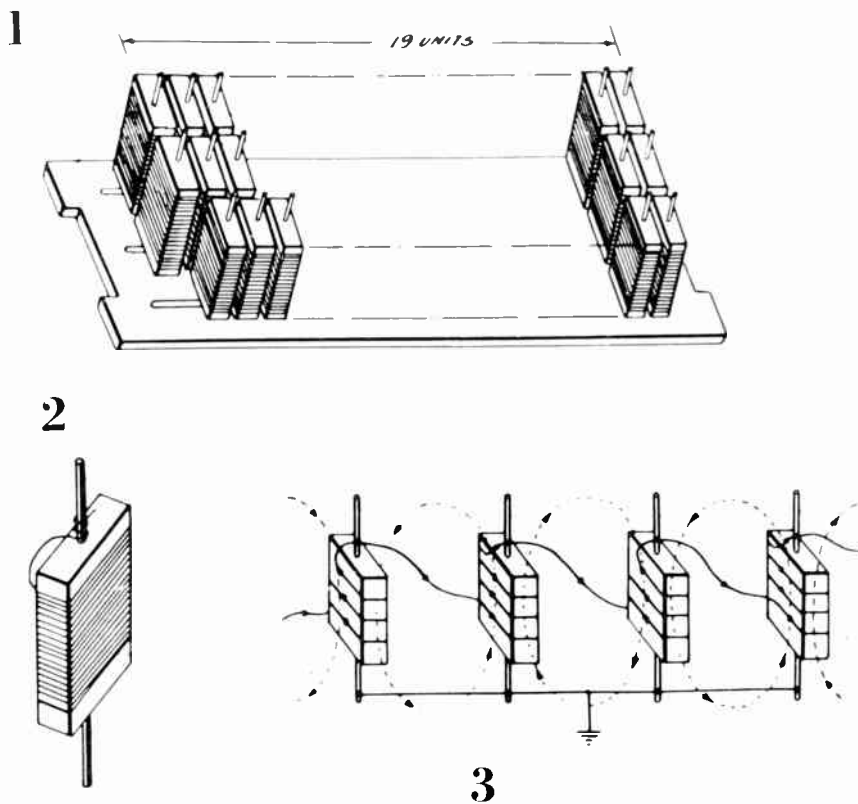


Fig. 4
(1) Sub-assembly details. (2) Single unit.
(3) Connection details.

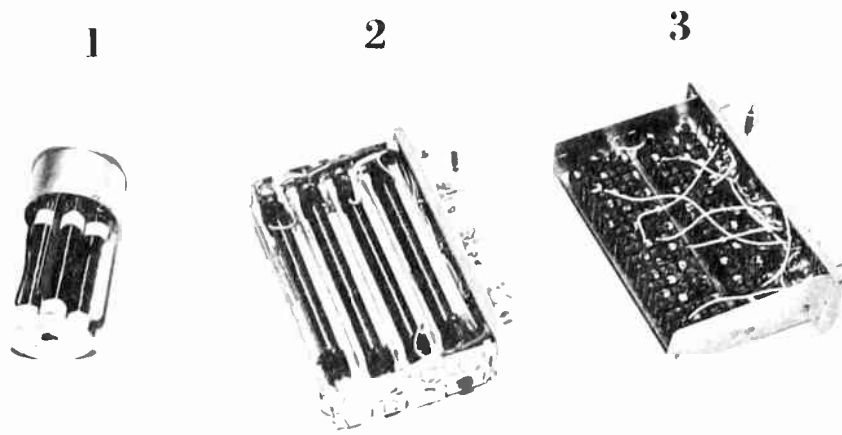


Fig. 5
(1) Commercial distributed constant delay line.
(2) RADC distributed constant delay line. (3) RADC
lumped constant delay line.

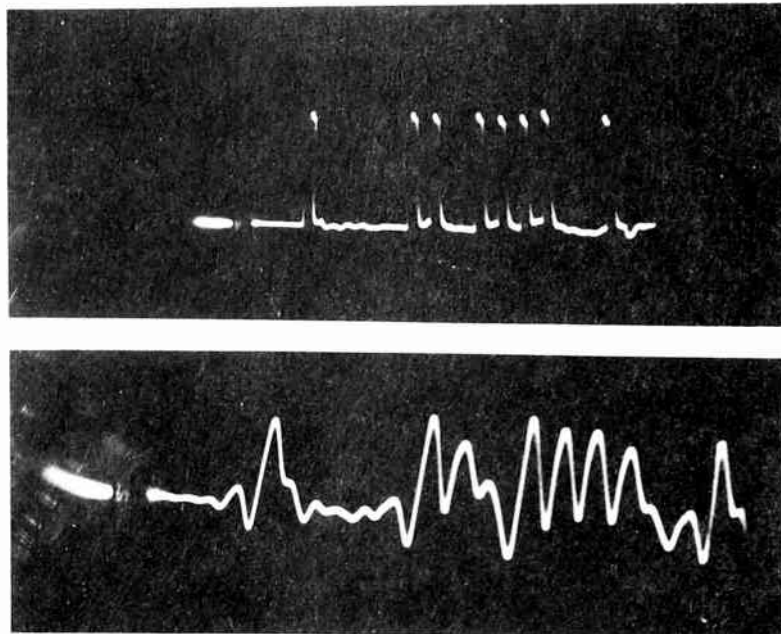


Fig. 6
Input pulses (upper trace) and output pulses
(lower trace) of commercial distributed
constant delay line.

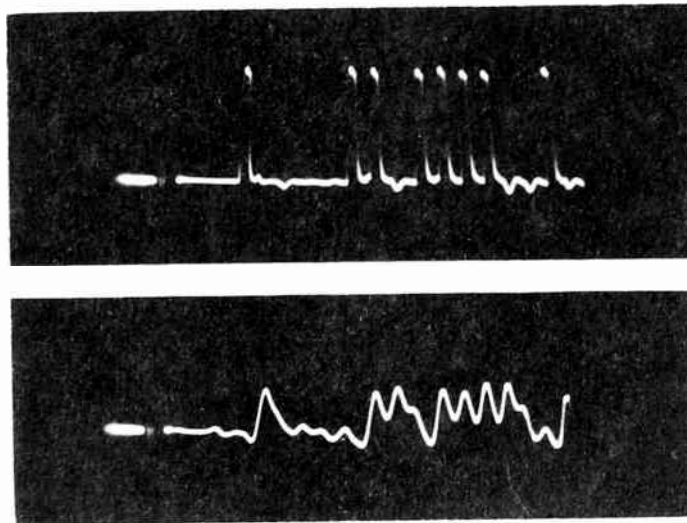


Fig. 7
 Input pulses (upper trace) and output pulses
 (lower trace) of RADC distributed constant
 delay line.

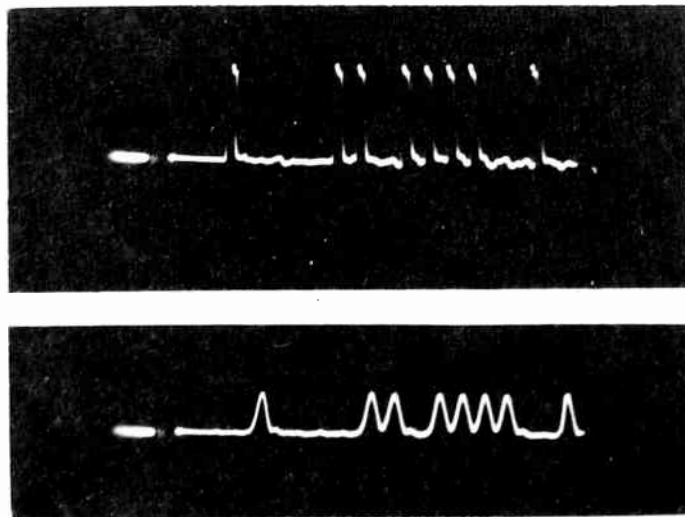


Fig. 8
 Input pulses (upper trace) and output pulses
 (lower trace) of RADC lumped constant
 delay line.

"CRITERIA AND TEST PROCEDURES FOR ELECTROMAGNETIC DELAY LINES"

by Norman Gaw and David Silverman
HELIPOT Corporation, Mountainside, N. J.

The electromagnetic delay line should be thought of as a T or time storage component which might be applied in the same manner as a simple R, L, or C component. Yet, unless properly understood, it could appear to be complex and difficult to apply. The increased application of many new delay line types has caused a measure of confusion among users and manufacturers. Therefore, the intent of this paper is to contribute a common understanding by analysis of distortions, definitions of terminology, and description of test methods. It is hoped that this might instigate the formation of standards for electromagnetic delay lines.

Equivalence of Basic Types

Delay lines are available in a wide variety of shapes and sizes. However, in spite of apparent differences, all electromagnetic delay lines are of two general types as illustrated in figure 1. In the distributed or coaxial type line, the geometry of the two conductors is arranged to take optimum advantages of the delay characteristics of a transmission line. In the lumped line, discrete reactive elements are arranged in the form of a multiple section filter.

Two separate approaches to delay line design have been taken; the first derived from transmission line and the other from filter theory. Yet it can be shown that the properties of a distributed line are approached as the number of sections of a lumped line is increased. Kimbark¹ has shown that a transmission line presents a limit case of filter theory. Therefore, by equivalence, all delay lines may be similarly evaluated and tested.

Distortions Common to Delay Lines

The ultimate in design is to accomplish time delay with complete freedom from distortion. However, since all circuit elements have performance limitations, this is not possible. The best of delay lines, properly applied must necessarily suffer from distortions due to (1) deterioration of rise time and (2) loss of amplitude.

The upper part of fig. 2 shows an ideal pulse (dotted lines) applied to such a line and the resultant stored signal.

In comparing these two curves, note:

- (1) The increase in rise time.
- (2) The decrease of amplitude.

Shortcomings in design and mis-application could lead to other distortions. If many should appear at once, an extreme degradation of signal would result as shown in lower part of fig. 2. In spite of the complex disfiguration, a trained observer could easily distinguish the contribution made by each basic distortion, illustrated in fig. 3:

Phase Distortion: Characterized in the

- (a) under-equalized state by a leading ring.
- (b) over-equalized state by a lagging ring.

Both suffer rounding of pulse leading edge. Under-equalization refers to a decrease of delay at the higher frequencies. Too much delay compensation results in over-equalization.

Input - Output Coupling: Characterized by distortions occurring at one delay time preceding and one delay time lagging the pulse rise. These are due to inter-coupling of the higher frequency portions of both applied and delayed signals.

Discontinuity: Characterized by wave-shape irregularities occurring within two delay periods after the pulse rise. These are due to non-uniformities in the construction of the line.

Mismatch: Characterized by an abrupt change in step level occurring two delay periods after pulse rise. This effect is due to incorrect termination. The curves indicate the separate effects due to resistive and reactive mismatch.

The manufacturer strives to minimize all distortions, but is often required to compromise certain qualities to affect a savings in size and cost. As with any other component, the manufacturers specifications indicate the extent of such compromise.

Delay Line Terminology

In order to fully evaluate the specifications, the language must be

understood. Certain terminology is most often used throughout the industry:

(a) Time delay is the time in which an electrical signal is stored by a system or component. Pulse delay is measured at the half amplitude point of the leading edge of the input and output pulses.

$$T = \sqrt{LC} \quad \text{Where: } T = \text{total delay}$$

L = total inductance
C = total capacitance

(b) Phase shift is a measure of delay at a given frequency.

$$\phi = 360 Tf \quad \text{Where: } \phi = \text{phase shift in degrees.}$$

T = total delay in microseconds.
f = frequency in megacycles.

(c) Temperature Coefficient of Time Delay is expressed as the decimal value of total delay change per degree C.

(d) Phase distortion is the change of signal waveshape due to non-equal delay of its various frequency components.

(e) Phase equalization refers to the methods which are employed to compensate for phase distortion.

(f) Linearity is the time deviation from the desired value to which a tapped or variable delay line may be set. This is usually expressed as a total delay.

(g) Pulse width is the time duration of a pulse signal and is measured between the half amplitude points of the leading and trailing edges. (see fig. 2)

(h) Rise time is the time in which a unit step changes from its initial to final amplitude level and is measured at the 10% to 90% point. (see fig. 2)

(i) Bandwidth is the band of frequencies which a delay line attenuates uniformly or within 3 decibels of equality.

(j) Insertion loss^I is the inverse ratio of the power received by receiving circuit directly connected to a source of power, to the power received by the same circuit when an additional 4-terminal network is inserted between it and the source.

(k) Characteristic impedance^I - which is (1) the input impedance of a line of infinite length, or (2) the input

impedance of a finite line terminated in an impedance of such value as to make the input impedance equal to the termination impedance.

$$Z = \sqrt{\frac{L}{C}} \quad \text{Where: } Z = \text{characteristic impedance.}$$

L = inductance/unit lgth.
C = capacity/unit lgth.

(l) Matching refers to the termination of the line in its characteristic impedance and to the adjustment of the signal source impedance to equal the characteristic impedance of the line.

(m) Standing wave ratio refers to the change of rms voltage or current at various points along the line caused by reflections due to improper matching. It is defined as the ratio of the max. to min. rms value of this voltage or current.

(n) Amplitude distortion refers to the change of signal waveshape to the non-equal attenuation of its various frequency components.

Test Methods

The theory underlying delay line test procedures is rather simple, but elaborate precautions are sometimes required to obtain conclusive accurate results.

High frequency measurements normally require some special care.² In addition, to minimizing distortion, special precautions must be taken regarding the manner in which the delay line is employed in test circuitry regarding:

1. Proper impedance matching,
2. Decrease of loading effect, both resistive and reactive, particularly in a variable or tapped delay line, and
3. Isolation and decoupling between those portions of the test setup which, because of the delay line, are not in phase.

Either pulse or sinusoidal testing may be used to supply comprehensive test information, with each offering particular advantages:

1. Pulse techniques are most often used to determine rise time, pulse delay, distortion, pulse attenuation, and characteristic impedance.

2. Sinusoidal techniques will more readily yield bandwidth and phase response. Greater accuracy may be achieved in the measurement of delay and delay linearity at a particular frequency.

Pulse Testing

Fig. 4 illustrates a pulse testing setup: A high quality pulse or a square wave generator output is coupled through an impedance matching network to the input of a delay line. A suitable high frequency oscillograph may be used to observe the pulse waveshape, providing the amplifier (or deflection plates) into which the signal is fed has relatively low input capacitance and high input impedance.

Reflections will distort the input pulse shape if the delay line is not properly matched. By adjustment of termination to minimize this reflection, the characteristic impedance may be determined and measured.

Fig. 5 illustrates how, by multiple exposure on a single print, the following is recorded:

1. pulse input
2. pulse output
3. sweep timing markers

Some delay line manufacturers will, upon request, supply photographs of this type with their delay lines. From these photographs, delay time can be obtained by comparison with a known frequency of the timing marker.

Input and output rise time may similarly be measured. Delay line rise time may then be obtained by use of the following equation:

$$Tr_{\text{delay line}} = \sqrt{(Tr_{\text{output}})^2 - (Tr_{\text{input}})^2}$$

Where: Tr = rise time

By comparison of the amplitudes of the input and output pulses, the attenuation is obtained as follows:

$$\text{Attenuation} = \frac{V_{\text{in}} - V_{\text{out}}}{V_{\text{in}}}$$

Where: V_{in} = Input pulse amplitude
 V_{out} = Output pulse amplitude

Distortions, if present, may be readily analyzed. Pulse delay may be easily measured to within $\pm 5\%$. Depending on the quality and stability of the test equipment, this accuracy may be extended to $\pm 2\%$.

Sinusoidal Testing

Fig. 6 illustrates a sinusoidal test setup. A calibrated signal generator is fed through a matching network to the input of a properly terminated delay line. A lissajou pattern is used to compare the phase relation between the input and output.

To compensate for phase shift introduced by the measuring oscillograph, a phase equalizing network is normally required. This may be a delay line and may be adjusted to obtain zero closure when the switch is thrown to the input position.

When the switch is returned to the output, the lissajou pattern will give an indication of phase shift introduced by the delay line. A measurement of the lowest frequency which effects an identical closure of the pattern yields the time delay for 360° of phase shift. Effectively, time delay equals the period of this frequency.

As frequency is increased, successive identical closures will be obtained, the periods of these closure frequencies will correspond to sub-multiples of time delay. Phase linearity can then be determined, but the number of points that can be taken is limited by delay line response and over-all time delay.

Accuracy of phase shift measurements is largely dependent upon the accuracy to which the frequency may be determined. Other factors also contribute to error and require special precautions to insure:

1. Freedom from coupling between measured points,
2. Freedom from harmonic distortion, and
3. Adequate resolution of the lissajou closure reading.

A similar test setup employs high frequency voltmeters at input and output in place of the oscillograph. Bandwidth is obtained by plotting the ratio of output to input voltage as frequency is varied.

SUMMARY

All delay lines, irrespective of size or design, may be tested and evaluated by similar procedures. Distortions which may appear, fall into clearly defined

groups and can easily be recognized. Understanding of existing terminology and basic test procedures will aid in the selection of delay lines most suited for particular applications.

Delay lines over the past few years have become established as a new component field. Not too far back, the user was required to design and build delay lines for a specific application. Today, there is a wide selection, not only in types or sizes of delay lines, but in quality and performance as well, which have been brought about by the entrance of many new manufacturers into the field. There are many new applications which have been made practical with the improvement of quality and precision.

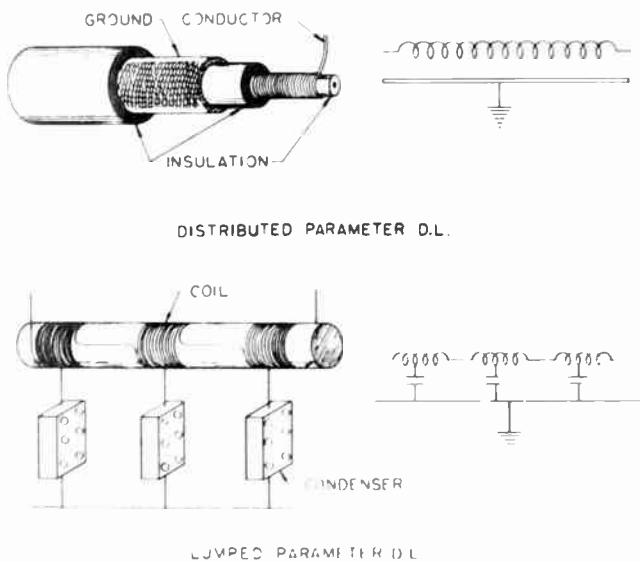


FIGURE 1

The users contributions is of utmost importance towards the continuing advancement and this is to be encouraged by the manufacturer. Because cooperation must be based on comprehension, this paper has been presented to contribute to general understanding with the hope that it would lead to establishment of firm standards of quality, terminology and testing.

References

1. E. W. Kimbark "Electrical Transmission of Power and Signals", Wiley, 1949.
2. M. B. Kline, "Techniques in Pulse Measurements". The Oscillographer, Vol. 14, Nos. 2, 3.

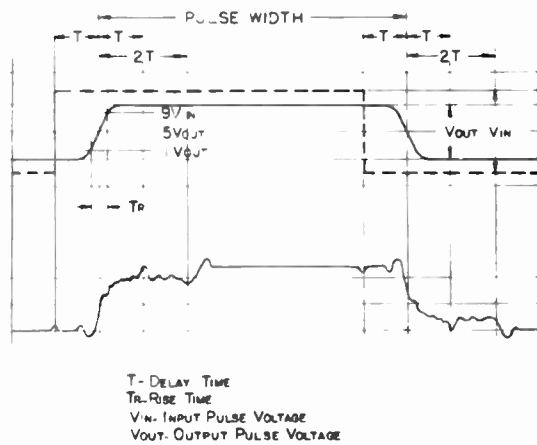


FIGURE-2

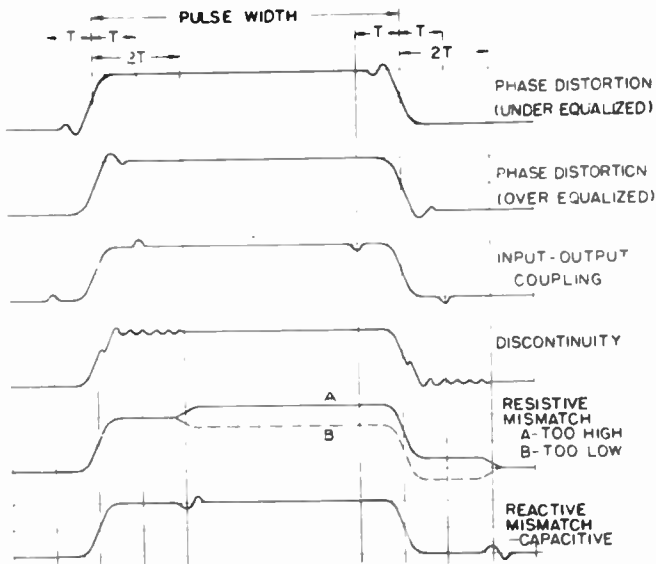


FIGURE-3

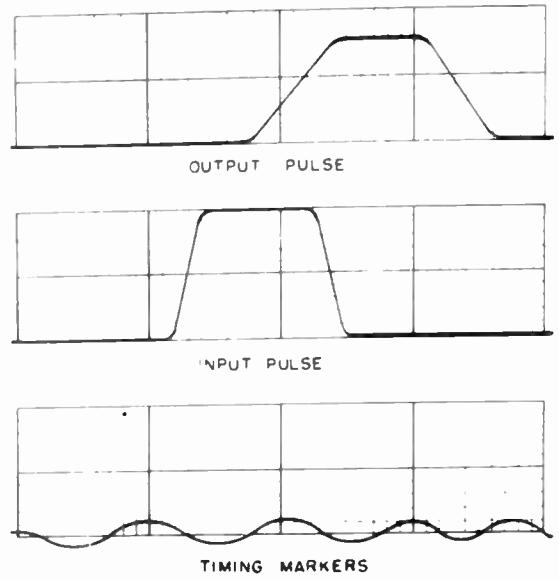


FIGURE-5

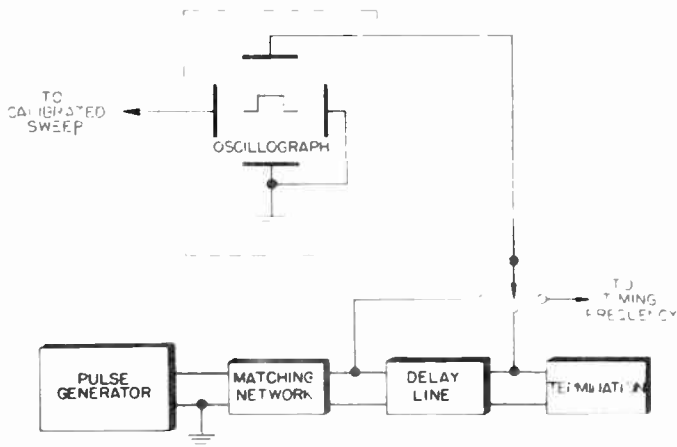


FIGURE-4

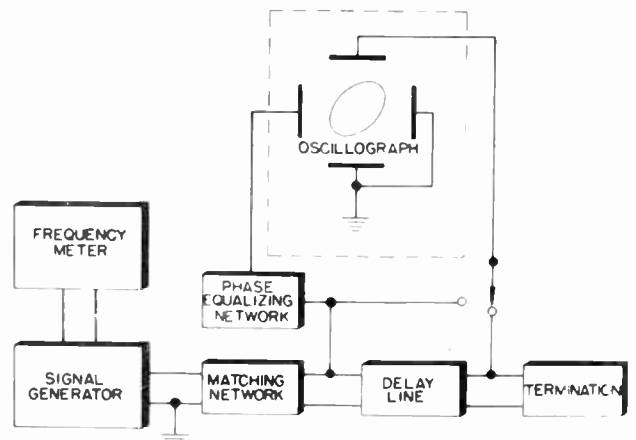


FIGURE-6

"EVOLUTION OF SELENIUM RECTIFIER VOLTAGE RATINGS"

Norman F. Bechtold
Signal Corps Engineering Laboratories
Fort Monmouth, N. J.

Summary

Prior to World War II, selenium rectifier plates were rated at 14 to 16 rms volts per plate. Accelerated wartime use and further development of barrier layer materials resulted in increase of this rating to 26 volts. Military miniaturization needs caused postwar developmental effort to be initially directed toward higher voltage plates. The initial result of a planned program for development of 120 volt selenium plates is a standard line of 40 volt plates available in all common sizes for stacking into any possible circuit configuration. Subsequent use and further test of these items has made it apparent that a multiplicity of advantages are offered through their use; more than 30,000 hours of operational life data have been obtained on experimental samples. For power applications, higher voltage ratings can be utilized to diminish the effect of slightly higher forward resistance by requiring less series plates. Increased efficiency is attained by virtue of the fact that lower reverse losses are evident through use of the 40 volt plates. These characteristics have been used to advantage in a number of magnetic amplifier applications where, generally, the slightly higher forward resistance does not materially affect the operation. Under derated (reverse) conditions, it has been proven that 40-volt selenium plates provide superior characteristics to other available types up to 65°C. Further improvement of production techniques and materials have led to recent development of 60 volt (rms) selenium rectifier plates, development models of which have exhibited superior initial reverse resistance characteristics. Additional data are offered to indicate proposed ratings, current-voltage characteristics, temperature derating factors, and operational life. It is apparent that further improvement in uniformity of production techniques will make these 60-volt selenium plates a marketable item in the near future. In addition, further advancement of this voltage rating will be contingent upon resolution of barrier layer stability problems. Intensified effort in this field by the Services and Industry will provide a marked contribution to the military miniaturization program.

Introduction

Remember 'way back when a selenium rectifier was a "cure-all" for power rectification problems? Recent introduction of the "wonder drugs" of germanium and silicon have begun to bring to light some of the deficiencies and limitations associated with selenium, along with somewhat premature claims for the recently introduced devices. In this respect, it is the intent of this paper to

present to the radio engineering profession a background of accomplishments in selenium plate voltage ratings, in hope that all available power rectifier types may be weighted equally with consideration to the market of the future.

Background

Non-linear conduction characteristics of selenium cells were first discovered by Adams and Day in 1876, and their work was continued by Siemens in 1877, and in 1883 Fritts fabricated selenium cells for which resistance ratios of over 250 to 1 were obtained with reverse voltage ratings of about 8 volts. Further development of these types was deferred, however, in favor of photocells, electrolytic rectifiers, and crystal detectors, until the first commercial selenium rectifier was introduced in 1924¹. By virtue of improved crystallization techniques and purer selenium, cell voltage ratings had by this time been increased to 10 to 12 volts. For approximately 10 years no advancement was made in ratings until artificial barriers were first applied in the mid 1930's, and voltage ratings were increased to about 14-16 volts. A progression toward 18 volts had been achieved by 1940 and accelerated wartime development of material and techniques had further increased ratings to 26 volts by the end of World War II.

The selenium rectifier plate as we know it today, therefore, evolved from the crude laboratory sample of about 70 years ago to the versatile mainstay of most commercial and military power rectification systems. As with most electronic parts, its initial development was slow, and did not "come into its own" until wartime exigency hastened its development.

For those of you who are not familiar with the makeup and action of a selenium rectifier plate, a brief discussion is presented herewith. Figure I is a sectioned view of a selenium plate, the chief constituents of which are a metallic base plate, selenium layer, barrier layer and counter-electrode. Halogen "impurities" (Bromine, Iodine, Chlorine) are inoculated into the selenium in optimum amounts to influence the effects of crystallization. The base plate, preferably etched aluminum, provides a support for a layer of β type (crystalline) selenium which is formed through heat treatment of amorphous selenium under specific conditions. A natural barrier is formed at the surface of the selenium by this process and is supplemented (for higher reverse resistance) by application of an artificial barrier of organic compounds. An electron producing metal (cadmium-

bismuth alloy) counter-electrode is sprayed onto this barrier. A forming process consisting of application of a pulsating dc voltage then stabilizes the barrier layer and burns out any selenium "hot spots" of accumulated electrons. Within the rectifying mechanism thus formed, conventional current flows freely from the selenium to the counter-electrode while it is substantially blocked from flowing in the opposite direction². Because so many variables are involved in production of this device, extreme care must be taken in control of each production parameter. Techniques have now been improved to the point where a high current, high voltage, or high temperature cell can be manufactured by modification of specific materials and processes.

The data to be presented herein applies to the quality-type (industrial) selenium rectifiers manufactured in conformance with stringent military specifications. Although they are more reliable and more expensive than the standard radio-quality stacks with which Radio Engineers are more familiar, manufacturing processes of the two are similar, and advantages in size and cost gained for one type can easily be applied to the other. It should be pointed out that "radio plates" are formed to 40-45 volts, and are subjected to more rapid deterioration than the 40 volt "industrial plates" discussed in this paper. It is apparent that production problems for a responsive yield increase directly with required minimum life. The 60 volt plates discussed herein have not been made in any production quantities to date, but it is conceivable that modified versions may be marketable as a radio quality item in the near future. At their present rate of development, silicon and/or germanium rectifiers may supplant selenium rectifiers in many applications since they offer a significant advantage in the size factor category. On the other hand, although a silicon or germanium rectifier can do the normal radio or television job in one-half the space that a present 6-plate selenium stack occupies, it is unlikely that they will compete on a cost-per basis for many years. Decreases in component cost for the near future must then naturally result only from miniaturization of the selenium stack, since production processes on these present items are now at minimum cost. In this respect, consider the possibility that a 3-plate stack of higher voltage selenium plates might replace this 6-plate stack. An estimated ratio of individual plate price is 1.5/1, due to longer production periods necessary for high voltage plates. The price advantage to be gained would therefore be

$$\frac{3 \times 1.5}{6 \times 1} = \frac{4.5}{6} = 0.75$$

and the advantage gained would be a 25% decrease in cost of each rectifier unit. Bear in mind, then, that the facts to be presented may be indirectly applicable to your own cost reduction problems.

40 Volt Plates

Fulfillment of military miniaturization needs necessitated that postwar rectifier develop-

mental effort be initially directed toward higher voltage selenium plates. A composite picture of the overall Signal Corps plan for progression of selenium plate ratings is demonstrated in Figure 2. The advantages to be derived from fulfillment, or only partial fulfillment, of these goals are readily apparent. The initial goal of a comprehensive development program was a reproducible selenium rectifier plate rated at 40 volts rms. It was necessary to refine production techniques for a few existent laboratory models and to improve artificial barriers in order to accomplish the goal. As a direct result, a standard line of 40 volt plates are available in all common sizes for stacking into any possible circuit configuration. Data pertinent to manufacturing processes, ratings, and characteristics of these plates are already covered in a general manner in previous publications³, so further discussion of this development will be limited to specific application advantages.

It might be applicable to mention at this time that there have been indications that aging characteristics are adversely affected by increases in selenium cell voltage ratings. Figure 3 demonstrates that 33 and 40 volt cells age progressively more rapidly than 26 volt cells⁴. It should be pointed out that this information was compiled on early high voltage cells, and does not apply to improved aging characteristics achieved in later developments. Qualitatively, however, it is indicative of the relative capabilities of each cell type; the faster aging rate is apparently brought about by stresses placed upon barrier materials by both lengthy forming periods and high operating voltages. Interpretation of these data cannot be realistic, however, without clarification of the criteria for "aging". End of life for a metallic rectifier is consistently defined as that point at which the forward resistance (voltage drop) has increased by 100%. Dependent upon general application, satisfactory life may fall anywhere in the range from 50 hours to 50,000 hours. Under varying conditions of operation, 26 volt cells can be applied at rated voltage throughout this entire life range - from minimum current densities for 50,000 hours to maximum current densities for 50 hours. On the other hand, experience has shown that life expectancy for 40 volt cells at equivalent current densities and rated voltage is considerably less. Especially promising results recently compiled (Figure 4) indicate that over 30,000 hours of reliable life has been achieved for development models of 40 volt selenium plates at room temperatures.

I would like at this time to elaborate upon a few of the advantages to be gained through use of these 40 volt cells in some general applications. A curve of resistance-voltage characteristics of 26v, 40v, and 60v selenium rectifiers is offered for comparison in Figure 5. Note that due to increased barrier resistance, conductivity in both the reverse and forward directions has been decreased. Consequently, as cell voltage rating has been increased due to decreased reverse conductivity, forward resistance has in turn

increased. In spite of this apparent deficiency in per plate forward characteristics, a more efficient and better regulated unit is effected through overall decreased internal resistance from less series plates. Since efficiency is also affected by reverse losses, Figure 6 is offered to demonstrate that lower reverse losses are also achieved through use of the 40 volt plates.

Consider, for example, a single phase 30 volt rms input application requiring a forward current of 3 amperes dc into a purely resistive load. For conformance with Signal Corps standards, a 4" x 4" plate would be required to effectively deliver the dc load current in a full wave application. For the purposes of this discussion, let us consider that a choice must be made between 26 volt plates and 40 volt plates. For a 4-1-1 configuration (a single phase bridge having four arms with one plate in series and one plate in parallel per arm) of 40 volt plates, reference to Figure 6 indicates that an rms leakage current of approximately 15 ma can be expected at 30 volts. Since it is necessary to utilize two 26 volt plates in series per arm for this application, 15 volts would be impressed across each series plate in a 4-2-1 configuration. It is apparent that a leakage current of over 30 ma will flow under this condition. It is evident, therefore, from a leakage standpoint at room temperature, that the 4-1-1 40 volt plate stack is superior to the 4-2-1 26 volt plate stack by a ratio of 2 to 1. The relative slopes of the two curves indicate that at lower operating voltages the superiority of the 40 volt plate is even more pronounced in this leakage category.

The effects of temperature on leakage current can be determined from a study of Figure 7. Note that although the 40 volt rectifier is more sensitive to temperature extremes, its reverse leakage is lower than that of a corresponding 26 volt item over the range from -40°C to +80°C. As previously noted, a 2 to 1 advantage is gained for the higher voltage plates at room ambient temperatures.

An additional contributing factor toward power loss and subsequent aging is the forward resistance of each stack. As previously pointed out in the discussion of resistance-voltage characteristics, the forward voltage drop of the 40 volt plate is slightly higher (approx. 20%) than the 26 volt plate. For this 30 volt application under discussion, however, twice as many 26v series plates are required; consequently, the forward voltage drop of the rectifier and power losses related thereto, will be

$$\frac{1+1}{1.2}$$

or 60% greater for the 4-2-1 26 volt stack. This condition will result in a somewhat lower output voltage, poorer regulation, and a greater contribution toward degradation of the stack through aging. No related quantitative comparison can be made for the overall circuit, since the relationship between series and load resistance for each individual circuit will be a factor. The difference in circuit power losses will never be as

great as 60%, but under all circumstances circuit efficiency will be greater for the circuit using 40 volt selenium plates.

It is evident from the above discussion that 40 volt selenium plates are superior to 26 volt plates for this particular application from the aspects of both physical and electrical consideration. It is true that a tailor-made application has been chosen for discussion, whereas others will not make the superiority so apparent; as higher voltages are required, however, the use of the 40 and even 60 volt plates will become progressively more advantageous. Figure 8 indicates the most effective operating areas of the plate ratings under discussion in this paper.

As a further practical demonstration of the benefits to be derived through use of the 40 volt plates, consider its capabilities in a magnetic amplifier application on a comparative basis with some other available rectifying devices⁵. Transfer characteristics have been chosen as a basis for comparison because they are a direct representation of rectifier quality. These control current-load voltage relationships are dependent upon reactor core materials and rectifier forward and reverse characteristics: a high forward resistance results in a lower dc output voltage and corresponding lower gain, while a high reverse leakage current results in a lower slope and decreased sensitivity of the amplifier. In a comparison of transfer characteristics of basic magnetic amplifier circuits, it has been shown that these high voltage selenium plates provide superior gain characteristics to other available types up to +65°C. Figure 9 a,b,c,d demonstrates that a 40 volt stack of approximately half the size of a 26 volt stack is superior for magnetic amplifier circuits. Note that the 30% change in leakage from 25°C to 65°C demonstrated in Figure 7 has not appreciably altered the transfer characteristic for this particular application. Although selected versions of these plates are presently being used commercially for magnetic amplifiers, the above investigation was performed on conventional power items. It is planned that this investigation will continue in order to establish relative long life stability at elevated temperatures.

60 Volt Plates

The next, and most recent, step toward an ultimate goal of 120v plate rating was an attempt to develop a reproducible 70 volt selenium plate. While methods of making satisfactory cells of this rating were not found, a limited number of 60 volt cells were constructed through improved laboratory production techniques and materials. Since production experience and research on the 40 volt development indicated that optimum values had already been found for many of the production parameters, work was conducted using already proven production techniques and equipment wherever feasible. Time was spent mainly on factors which were believed to be critical in developing high voltage cells; namely, the

artificial barrier layer, the front electrode composition, and selenium layer application. A variation of the molten coating process was employed for applying a brominated selenium layer to a nickel plated aluminum base plate. The rapidly cooled selenium layer was pressed under as close control as possible at 180 pounds per square inch and 135°C for ten minutes. After annealing at 219°C for 25 minutes, a three-step process was employed for obtaining an organic artificial barrier layer of polystyrene containing selenium dioxide and diethanol amine on top of a calcium-magnesium inorganic barrier layer. A bismuth-cadmium counter-electrode melting at 145°C was sprayed on to complete the basic cell unit. Electroforming was performed by connecting cells "back-to-back" and applying progressively higher alternate voltage for 50-150 hours.

In the course of the development work, both the pressed powder and the molten coating processes were employed for applying selenium. Various amounts of chlorine, bromine, iodine, and other materials were added to alter the selenium characteristics. Artificial barrier layers containing phenolic resins, nitrocellulose, ethyl cellulose and polystyrene were studied during the course of these experiments. Varying amounts of plasticizers, amines and inorganic materials were added in an effort to develop higher reverse voltages. In an attempt to improve high temperature response, high melting point tin-cadmium alloys were tested as counter-electrodes. Electroforming in oil containing amine additives was attempted, but poor forward conductivity and electroforming breakdowns could not be adequately controlled. Although occasionally various methods yielded cells capable of withstanding up to 80 volts, poor forward conductivity, short operating life, or partial or complete loss of cell batches due to electroforming breakdowns occurred with every method attempted.

In spite of the development obstacles encountered, sufficient rectifier samples rated at 55-60 v per plate and 250 ma/sq. in. of effective area (full wave) have been evaluated and data compiled.

Proposed current and voltage derating curves are typified in Figure 10 over the ambient operating temperature range. At an ambient of 70°C, ratings for a 4-1-1 bridge of 1" x 1" cells are 55v rms input and 100 ma dc output into a resistive load. Temperature limitations of these high voltage plates, coupled with the advantages offered by high temperature selenium cells, make it apparent that use of specific types will be contingent upon individual requirements of each application. Improvement of uniformity in production techniques is necessary before these 60 volt plates can even be considered as a marketable item, since it is apparent that only specially selected presently available cells will be reliable for a maximum period of 5000 hours, and that the probability of failure increases with ambient temperature.

As illustrated previously, the per plate forward voltage drop increases somewhat with reverse voltage rating, and is accompanied by proportionate power losses in the forward direction. It has also been shown how reverse leakage current is less for a higher voltage cell when operated at the same voltage as a lower rated cell. The relative effects of these conditions on cell temperature rise are illustrated in Figure 11. In order to eliminate as many variables as possible, the stacks studied were all operated at the same forward current. The extremely low leakage current associated with the 40 volt item at low voltages (below 26 volts) more than compensates for the increased forward losses, and lower plate temperature and potential longer life are possible for the 40 volt item at the low voltage levels. Sharp increases in leakage of the 40 and 60 volt plates as reverse voltage approaches their respective rated values brings about corresponding total power loss increases. Interpretation of these power losses to cell temperature rise, as noted by experiment, further corroborates the statements made previously that higher voltage cells, when operated at rated values, tend to age more rapidly than lower rated cells. The crossover point between the 40 and 60 volt curves seems to indicate that the latter item is a better (longer life) 40 volt cell than the former; this postulation will be investigated more fully in subsequent studies at the Signal Corps Engineering Laboratories.

Thoughts for the Future

There has been no attempt herein to present an impression that these new 60 volt selenium plates are ready for immediate application as replacement items. On the contrary, they have been difficult and expensive to manufacture in order to meet development specifications, and the production yield has been too low for any practical usage. All that can be said is that characteristics of the better cells are promising, and potentially superior to presently existing counterparts. Although the 70 volt goal of the present work, as established, was proven beyond the current state of the art, a step has been taken in the right direction. Furthermore, no theoretical reason has been found to disprove that usable 70 to 100 volt selenium rectifier plates cannot someday be produced. There are those who say that the problem becomes more formidable as voltage ratings increase; this might be so, but if pictures never lie, let us consider for a moment Figure 12, which depicts the history to date of the evolution of selenium voltage ratings. It would undoubtedly be purely conjecture to predict, after extrapolation of this curve beyond 1955, that 100v cells will be a reality within another 20 years.

There is really nothing more that can be said at this time, except that the indicated trend is certainly worthy of further consideration. The areas for development are large, and the application potentialities speak for

themselves. The challenge is presented to the selenium rectifier manufacturer, not only by the advancements and possibilities discussed herein, but also by the introduction of the germanium and silicon devices as competitors on the open market. It is the opinion of the author that standing of the selenium rectifier on the market of the future depends not upon development in the state of the art, but conversion of this "art" to a "science". Herein lies resolution of either limited or widespread use; not to seek better barrier materials, selenium inoculants and forming techniques through tedious trial and error, but through scientific analysis of constituents and their relative contributions to the action of the semiconducting selenium. Intensified effort in this respect by both the Services and Industry will provide a marked contribution to the military miniaturization program. I leave it up to you, the manufacturer, and you, the user, to make your own appraisal of the future of selenium rectifiers in the competitive power conversion field.

Acknowledgment

The author is indebted to Mr. S. F. Danko of the Signal Corps Engineering Laboratories for his valuable comments offered during preparation of this paper.

References

1. Henisch, H. K.: "Metal Rectifiers", Oxford Press, 1949.
2. Ramsey, G.: "The Selenium Rectifier", Electrical Engineering, December, 1944.
3. Cataldo, J. P.: "Development of 40-Volt Selenium Rectifier Plates", Electrical Manufacturing, May, 1952.
4. Gramels, J.: "Selenium Rectifiers-Factors in Their Application", Bell System Technical Journal, November, 1953.
5. Bechtold, N. F. and Zucchini, M. B.: "Choosing Rectifiers for Magnetic Amplifier Circuits", Electrical Manufacturing, Dec., 1954.
6. Bonner, W. F. and Oliver, F. J.: "Advanced Development in Metallic Rectifiers", Electrical Manufacturing, October, 1951.

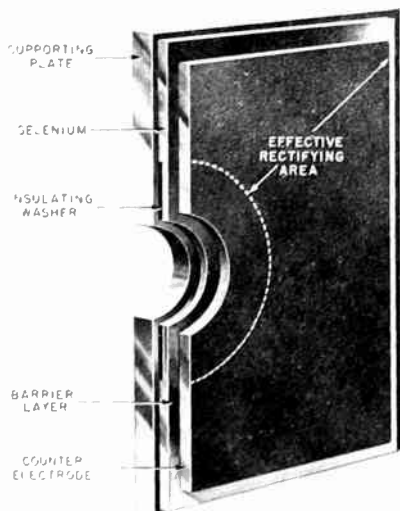


Fig. 1

Selenium Plate Cross-Section.

PROGRESSIVE DEVELOPMENT OF HIGH VOLTAGE SELENIUM RECTIFIER PLATES



EACH FIGURE DEPICTS STACK SIZE NECESSARY FOR A 120 VOLT INPUT APPLICATION

Fig. 2

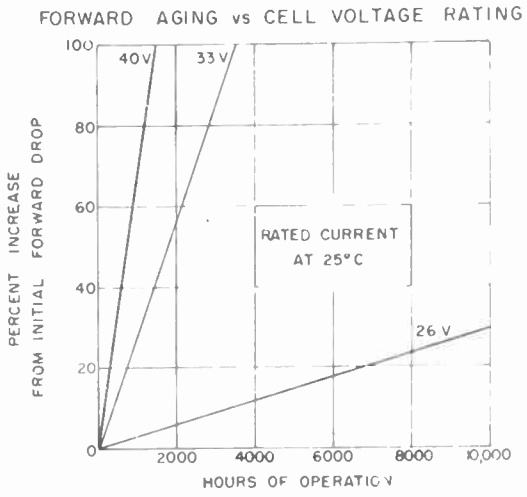


Fig. 3
(Courtesy of Bell Laboratories)

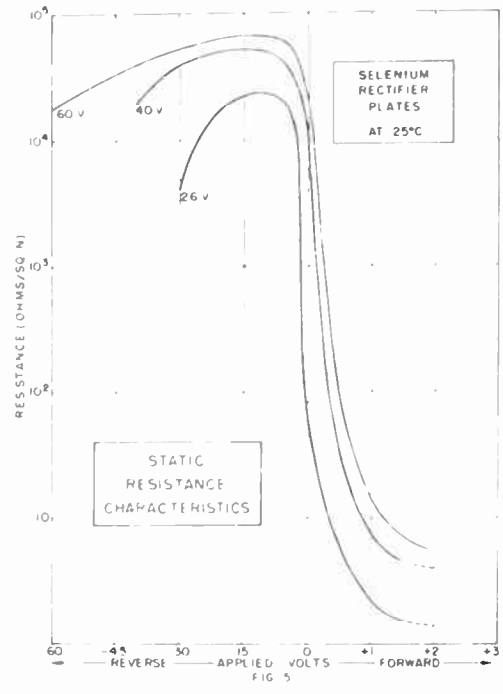


Fig. 5

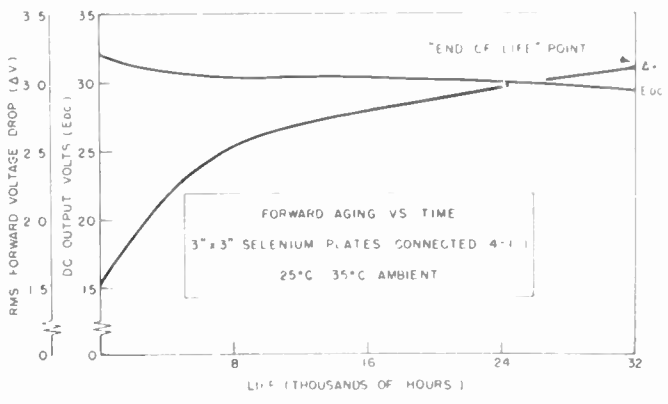


Fig. 4
Life Characteristics of 40 Volt Cells.

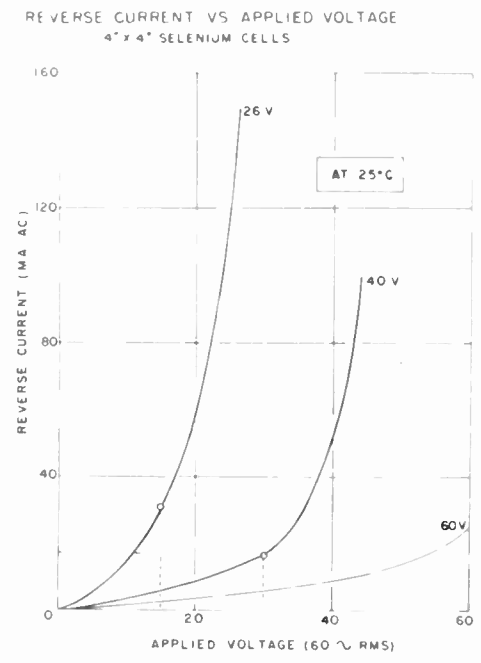


Fig. 6

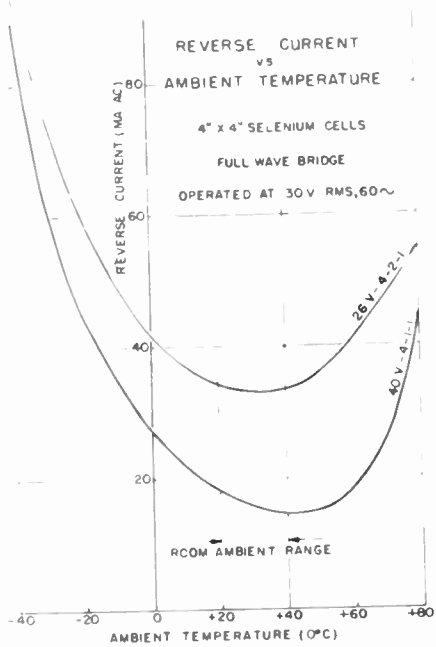


Fig. 7

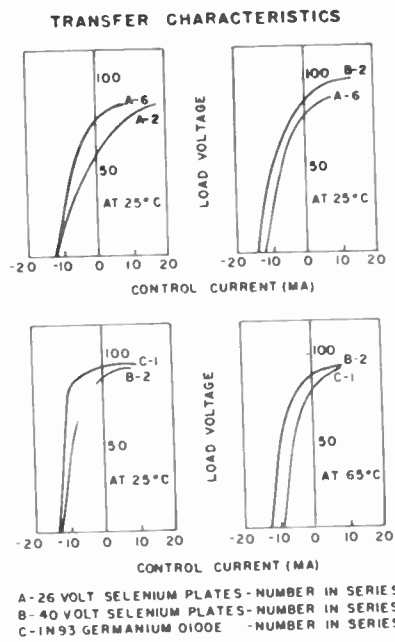


Fig. 9

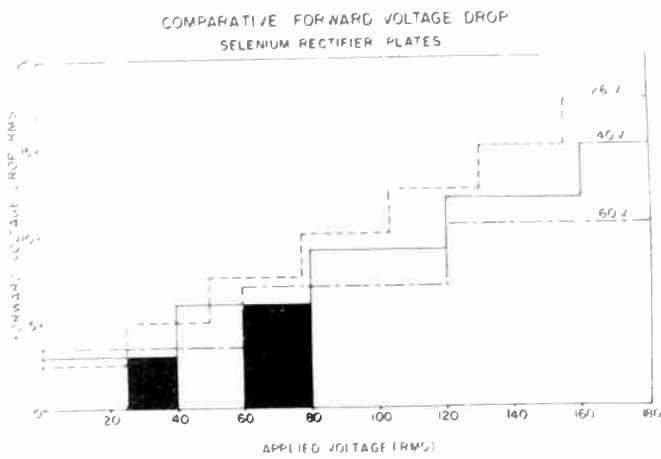


Fig. 8

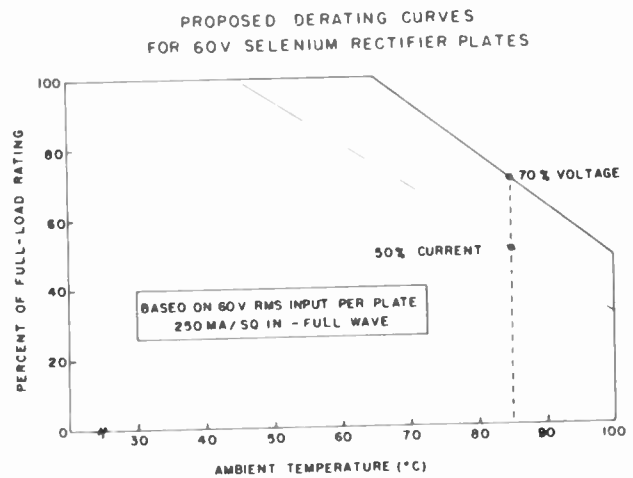


Fig. 10

COMPARATIVE STACK TEMPERATURE RISE
 SELENIUM RECTIFIER PLATES
 (1" x 1" BRIDGE OPERATED AT 220 MA DC)

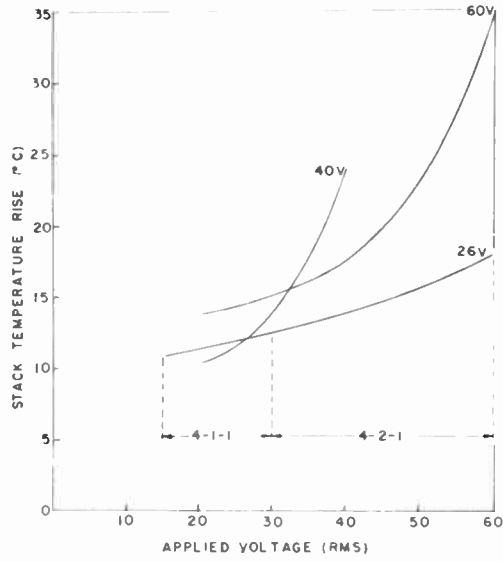


Fig. 11

EVOLUTION OF SELENIUM RECTIFIER VOLTAGE RATINGS

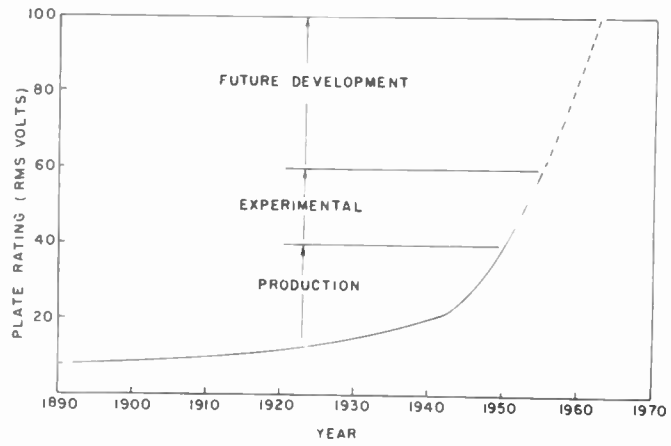


Fig. 12

A PRECISION DEFLECTION YOKE

Harold J. Benzuly
Radio Corporation of America
Camden, New Jersey

Summary

A very important consideration in the registration of multiple images such as required in the present RCA Color Television Camera is the deflection yoke. Complete uniformity between units used together is essential and it is shown how this controlled precision can be easily obtained.

A technique for constructing a deflection coil assembly suitable for use with a camera pick-up tube is described and the results obtained from a unit built for an image-orthicon camera are reported. The objective was to reproduce as closely as possible the electrical characteristics of a conventional wire wound yoke without exceeding the physical size of the standard unit. Preliminary tests in an image-orthicon camera of such a yoke have shown attractive possibilities.

Introduction

One of the most important considerations in the registration of several television images, such as required in the present RCA color television camera, is the deflection yoke. Since misregistration is a degradation of picture quality that is quite apparent and annoying to the viewer, it is imperative that errors in registry at the transmitting end of the system be held within very close limits. In present cameras this is done by providing several registration controls and using carefully constructed deflection components. This paper describes a different approach to the construction of deflection coil assemblies.

Because variations in geometric distortion rather than geometric distortion per se produce misregistration, the emphasis is primarily on uniformity. While any distortion is undesirable, techniques of field-shaping¹ and focus modulation permit compensation for the symmetrical barrel and pin-cushion variety. Furthermore, a certain amount of symmetrical distortion is tolerable providing it is identical in all of the images superimposed so that no color separation occurs. Thus, while accuracy and low distortion are extremely important, precise reproduceability is of paramount concern.

In the camera, distortion can be introduced by optics, tubes or the deflection coil assemblies. But, while the sources of error are known, evaluation of each element's contribution is extremely difficult. The use of high quality optics, carefully adjusted, makes negligible the distor-

tion inserted at this point. Image-orthicons, although made with rigidly controlled accuracy, due to their inherent complexity can contribute some error. However, proper installation and operation reduces nonsymmetrical distortions to a currently irreducible minimum and allows excellent registration to be obtained. Distortions produced in a deflection yoke depend directly on the care and accuracy exercised in its design and manufacture. Thus, the deflection yoke designer, knowing that perfection in his art is not a panacea, is charged with achieving the highest possible precision.

An insight to his problem might be given by a brief description of the procedure used in registering an RCA color camera. Three image-orthicons are used in individual deflection assemblies for the red, blue and green images which have been separated by dichroic mirrors. The two horizontal coils in each yoke (and likewise the vertical coils) are connected in series and the three yokes are then paralleled across the horizontal and vertical output transformers. The green channel has been arbitrarily adopted as the master channel to which the red and blue images are registered. The test pattern normally used consists of wide-spaced horizontal and vertical lines in a grid pattern, a large circle and test wedges, all thin black lines on a white background. In setting up the green channel, first the mechanical rotation of the yoke is adjusted to make the bottom of the raster parallel to the bottom of the optical image. Then size and linearity are set using master controls which operate on the applied deflection voltage waveforms. The red and blue images are then separately registered to the green using rotation, centering, individual size and linearity controls and a "skew" correction adjustment. "Skew" is a term applied to a distortion causing square shapes on the test pattern to appear as rhombic shapes on the television picture. It can be corrected by applying a variable vertical sawtooth of current to the horizontal deflection coils.

Since a common deflection voltage is applied to all three yokes, individual size and linearity controls are obtained from adjustable resistive and reactive elements in series with the deflection coils. These permit compensation for production tolerances.

The deflection obtained from a given deflection yoke is a function of the form-factor and ampere-turns. In the so-called form-factor are

included the effective length, diameter, turns distribution and efficiency parameters. If the two coils comprising a given yoke (both horizontal and vertical) are connected in series, properly oriented with respect to each other and with the axis of deflection and then fed with a perfect sawtooth current, any asymmetry in the magnetic field (barring disturbing external effects) will be due to construction geometry such as the location of turns in the winding? Since the errors in registration with which we are concerned are on the order of a few percent and since, as mentioned earlier, it is quite difficult to isolate such errors for evaluation, the best approach is to tie down accurately the location of the turns so that no variation is permitted. While several methods are available for accurately locating the turns of a deflection coil winding, it is felt that the application of printed circuit techniques, besides achieving a high degree of precision in this respect, can supply several additional advantages as well.

The use of printed coils permits realization of the ultimate in geometric uniformity between units. It suggests a simple method of fabrication suitable for automation techniques. It should result in cost reduction, size reduction and closer tolerances in electrical characteristics than normally obtained. But, most important from the point of view of this paper, a high degree of uniformity in production units should be possible.

The Printed-Circuit Yoke

To explore these possibilities, a deflection yoke for an image-orthicon television camera was constructed entirely from printed circuits. Before describing this printed model, the construction of a conventional yoke will be reviewed.

An image-orthicon deflection yoke is assembled on a long phenolic coil form into which the image-orthicon is inserted. A layer of shield cloth is first wrapped around the form for electrostatic shielding. This cloth consists of thin copper wires woven parallel to each other (in one direction only) through a cloth base. They are all joined together at one end which is grounded. A layer of varnished cloth is then applied for insulation. Next, the horizontal deflection coils, flat wound and preformed are mounted in place. Another layer of varnished cloth, a second layer of shield cloth, more varnished cloth and finally the vertical coils, followed by a last layer of varnished cloth and the iron wire wrap which serves as a return path for the flux.

The coils are wound flat around pins accurately located in a board. They are laid out in six or seven groups of turns, the groups being equally spaced on the ends and approximating a cosine distribution along the major axis. Wooden spacers are provided between groups to maintain their proper relative position. The coils are

then shellacked and formed around a cylinder. A finished horizontal coil is shown in Figure 4.

At the outset it was believed that a printed yoke could be built which would replace directly (mechanically and electrically) the conventional unit. To this end the physical dimensions were predetermined and the electrical parameters set as design objectives. No attempt was made to redesign the standard yoke, but merely to reproduce it using printed coils. Only three different printed patterns were used for the entire yoke, two coil patterns and a shield pattern. The two coil patterns, shown in Figure 1, are mirror-images of one another. The third, to be used in place of the shield cloth referred to earlier, was printed in a continuous strip. A section of this pattern, already formed, is shown in Figure 2.

All patterns were made by an etching process from 2.7 mil copper deposited on a semi-cured melamine glass base material 13 mils thick. The coils have 43 turns per pattern, a conductor width of 10 mils and a minimum turns spacing of 10 mils. The turns are laid out according to a cosine distribution along the major axis and are equally spaced on the ends.

The electrostatic shield pattern consists of 15 mils conductors equally spaced at 60 mils, all joined at one end to a bus 3/16" wide.

The deflection coils were built up to the proper inductance by alternately stacking the two preformed mirror-image patterns and interconnecting them as shown diagrammatically in Figure 3 to provide a continuous current path. Interconnections were made by soldering short pieces of thin copper ribbon between solder pads. An important feature of this scheme is the self-insulating action of the patterns. Consequently no insulating wrappers need be inserted between coils as in the conventional yoke. The two small holes along the center line seen in Figures 1 and 3 are for accurately indexing the patterns while assembling the coils and later for accurately locating the finished coils on the coil form.

Patterns were preformed by strapping them to a mandrel of the proper size, stacked and indexed in the order in which they would be assembled, and subjecting them to a temperature of 320°F for one hour. Figure 4 shows a single, formed coil pattern alongside a completed conventional horizontal coil for comparison.

Experimental Results

The complete deflection yoke (Figure 5) consisting of horizontal and vertical coils and the two layers of electrostatic shielding was assembled by the techniques just described, inserted in a focus coil and operated in a monochrome image-orthicon television camera. Some modifications were made to the driving circuits because the im-

pedance of the printed yoke was somewhat higher than that of its conventional counterpart but its performance was quite acceptable and the results are certainly encouraging. The major shortcoming encountered was the high resistance. This will be discussed later in detail.

Four patterns were stacked and interconnected for each horizontal coil and eight patterns for each vertical coil. The measured inductance of a single pattern was nominally 189 microhenries. The completed horizontal coils measured 2.9 millihenries each in air and about 3.9 millihenries with the iron-wrap in place. DC resistances of these coils were 103 and 97 ohms respectively. The vertical coils had measured DC resistances of 232 ohms and 215 ohms. Matching of the coils with respect to resistance was somewhat restricted by the limited number of patterns available at the time.

In comparison, the conventional wire-wound yoke has horizontal coil inductances of approximately 3.0 millihenries each (with the iron-wrap return-path in place) and D.C. resistances of about 9.5 ohms.

The vertical coils have inductances of approximately 15.5 millihenries and DC resistances of about 18.5 ohms.

The horizontal retrace time for the printed yoke was just over 11 microseconds compared to about 9 microseconds for the wire-wound yoke in this circuit. However the inductance, with which the retrace time varies directly as the square root, is 1.3 times larger in the printed yoke.

The radial build of the printed yoke was .30" compared to .43" for the conventional yoke.

Uniformity of Printed Patterns

Quite a large number of the printed coil patterns had "opens" in the windings when received although most of these were repaired and used. The causes of this poor yield explain to a large extent the exceptionally high resistance of the coils. Figure 6 shows a plot of the individual pattern DC resistances. The ordinate is in ohms and the abscissa refers to successive numbers assigned to each pattern for identification. White circles denote patterns which required repair. Just over half of the points are grouped in a region between 21 and 25 ohms with an average value of 23.1 ohms; the others, for the most part, are scattered. The calculated resistance per pattern based on a .0027" x .010" cross-section of copper and a measured path length of 43.72 ft. was 13.2 ohms with an expected but unknown percentage increase due to undercutting during etching. Figure 7 shows the effects of the undercutting. This is a photomicrograph (magnified 60 times) of the cross-section of three conductors. Two things are obvious from this photograph: a reduction in area due to the

trapezoidal shape and a variation in conductor width due to non-uniformity in drafting for the printing negative. Measurements from four such photographs taken at different sections indicate an average cross-sectional area 40% less than that calculated resulting in an increase in resistance of 67% over the calculated value. This would bring the 13.2 ohms (calculated) up to 22.2 ohms which is within 4% of the mean value of 23.1 ohms mentioned above. Variations in the etching time and the strength of the bath, imperfections in the copper surface and perhaps some poor repairs would also tend to explain the large number of opens and wide range of resistances.

Uniformity of inductance is inherent with this technique. Tolerances of $\pm 1\frac{1}{2}\%$ have been achieved with similar types of coils when care has been exercised in etching.

Evaluation

The fabricating technique used in the construction of this yoke appeared to work out very well. Patterns took to the forming process quite readily, the indexing of patterns was precise and, while perhaps a more elegant method of inter-layer connection might be devised, the method described was quick and relatively easy.

One of the areas open to question is the expected yield from such printed coil patterns. Although those used were made with considerable care on a laboratory rather than a production basis, several limitations were inherent from the start. First, the specification of 10 mil lines and a minimum spacing of 10 mils is impractical from two standpoints; high resistance and difficulty in etching. Secondly, slight imperfections in the copper surface might cause "opens" with such narrow conductors (particularly if they are "necked-down" by undercutting and drafting irregularities) whereas with wider conductors these imperfections would be less effective. The drafting, done to a 4:1 scale, required that the conductor lines (inked by hand) be drawn in two parts, half above and half below a locating center-line. It is obviously very difficult to achieve uniformity by this method and considerable improvement in the final product is to be expected from an improved drafting technique. With allowance made for undercutting and careful control of the etching process it seems reasonable to assume that resistance can be held to within 10% of the calculated value and still produce a very satisfactory yield. Although some required repair, over 50% of the coil patterns printed for the yoke came within a $\pm 10\%$ tolerance in resistance.

The inherently high resistance which is limited presently in one dimension by the .0027" maximum standard copper thickness can be reduced by using wider conductors. The designer has quite a flexible device with which to work since

irregular shapes such as conductors wide along the longitudinal axis and narrowed to reduce the end turn region are quite feasible. Furthermore, the turns distribution, the number of turns per pattern, or the number of patterns stacked can be varied or patterns printed on both sides of the base material might be used. This would, of course, remove the self-insulating property.

Capacity across the coils can be controlled by increasing or decreasing the base material thickness or even changing the material to one with a different dielectric constant. Normal deflection currents should not cause any difficulty with the bond strength, particularly when the coil resistances are reduced to more reasonable values.

Although the end turns cannot be bent up as with wire wound coils, this is not a necessity in many applications.

Conclusions

A deflection yoke for an image-orthicon was built entirely from printed circuits and operated in a television camera. With the exception of resistance (which for the printed circuit model was much higher) the parameters of a conventional wire-wound yoke were quite readily reproduced, including inductances per coil of as much as 16 millihenries. The use of wider conductors, improved drafting techniques and allowances for undercutting will reduce the resistance to an acceptable value. Furthermore, reasonable care in etching should provide good yield from the printed material, correlation between calculated and measured values and close tolerances on electrical characteristics. While the experimental work reported here was rather limited in scope, experience with printed

coils in other sections of RCA indicate that a tolerance of better than 1% in inductance can be realized and better than 10% in resistance.

Because of their inherent precision and low cost and because they provide great flexibility to the designer, permit assembly methods suitable for automation techniques and make possible a reduction in size, printed circuits should find application in the production of deflection yokes for many types of cathode-ray tubes, in particular camera tubes such as the image-orthicon and vidicon.

Acknowledgement

The author is particularly indebted to Dr. O. D. Black of the Physical and Chemical laboratories of RCA Victor who obtained the material, processed the patterns and took the photomicrographs. Also to Mr. S. L. Bendell of the Camera Equipment Advanced Development Group with whom many discussions on deflection circuits were held, to Dr. H. N. Kozanowski, Manager of the Special Projects group for his helpful suggestions and criticisms during the preparation of this manuscript and to Mr. W. J. Poch, Manager of the Broadcast Studio Equipment Engineering Section, at whose suggestion this paper was prepared.

References

1. Soller, Starr, Valley; Cathode Ray Tube Displays (Radiation Laboratory Series, Vol. 22), Mc Graw-Hill Book Co., Inc., 1948; pp. 338-342.
2. Soller et al; op. cit.; pp. 352-355.

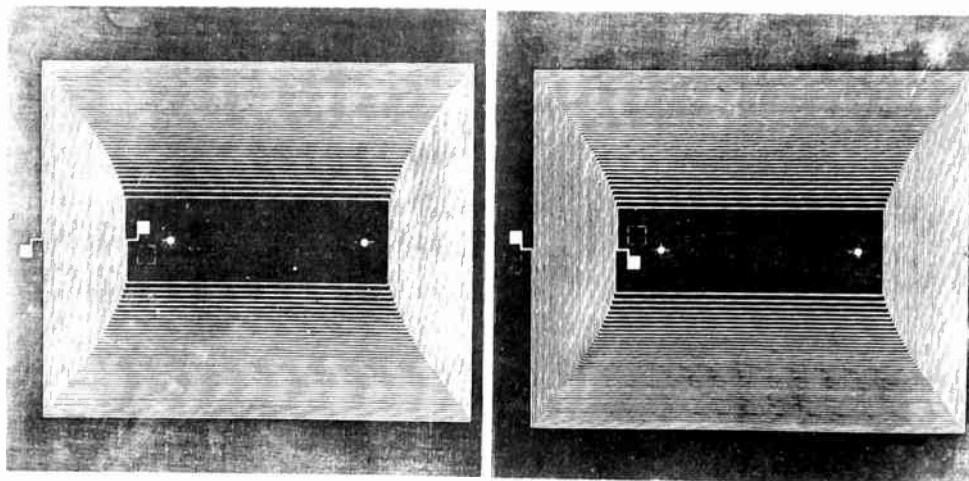


Fig. 1

The two mirror-image coil patterns used for building both the horizontal and vertical deflection coils. Small holes along centerline are for indexing during assembly. Dotted squares near solder tabs are punched out for interconnecting.

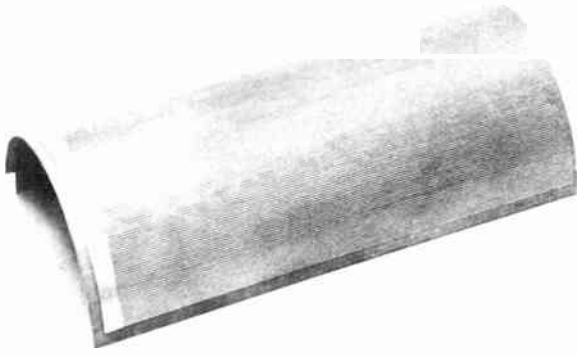


Fig. 2
Section of printed electrostatic shield formed for assembly. Material is melamine glass with .0027" copper. Narrow conductors are 15 mils wide, evenly spaced at 60 mils. The common bus is 3/16 inch wide.

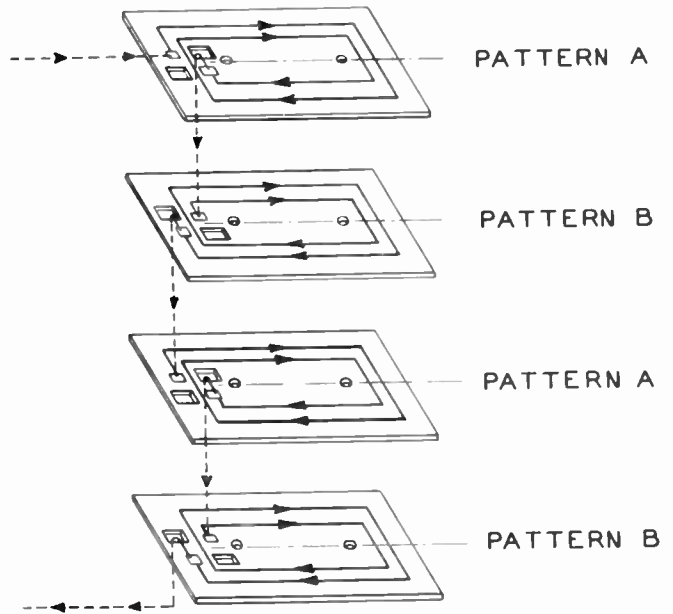


Fig. 3
Exploded view showing method of interconnecting alternately the mirror-image coil patterns. Patterns can be stacked, indexed and formed before assembling.

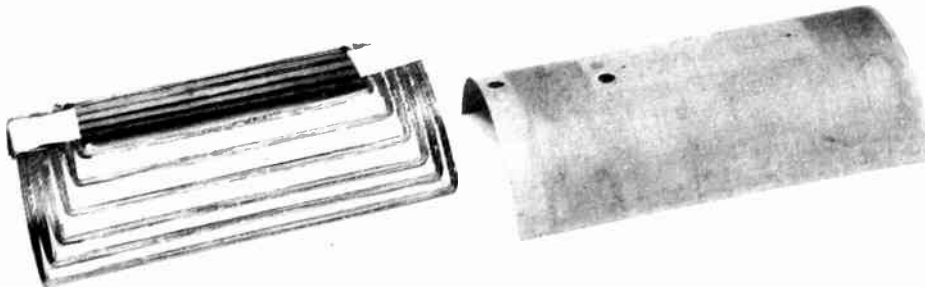


Fig. 4
A single formed, printed coil pattern shown beside a completed horizontal coil made in the conventional manner. The location of individual conductors is precisely fixed with the printed coil.

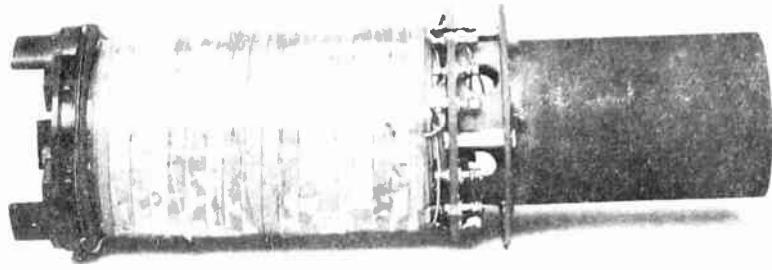


Fig. 5
 Completed printed circuit deflection yoke for image-orthicon television camera. Both horizontal and vertical deflection coils and the electrostatic shields are made of printed circuits. Outer layer is iron-wrap for flux return path.

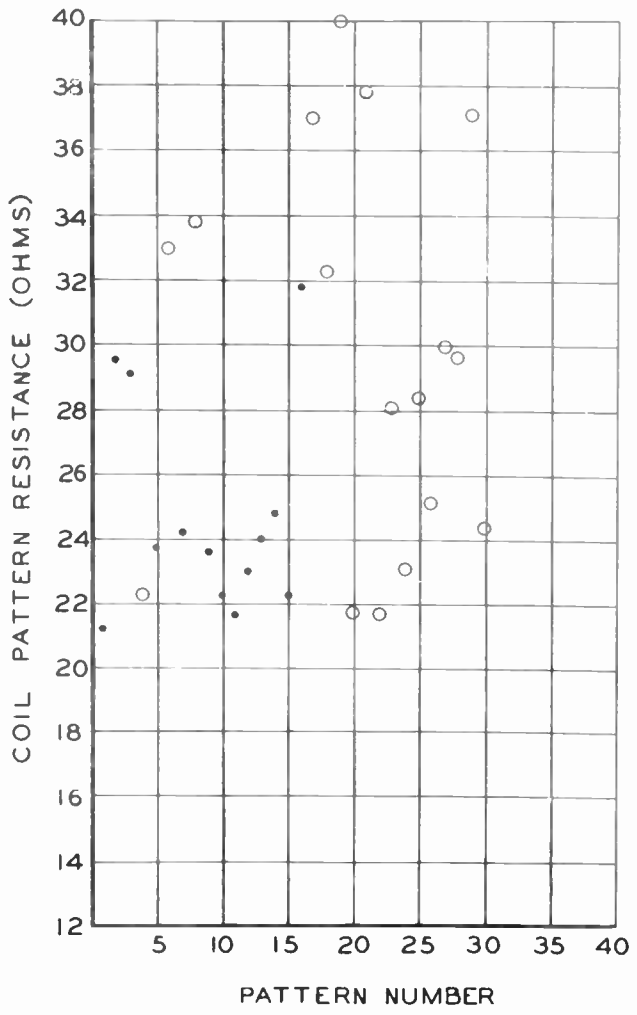


Fig. 6
 Measured resistance of individual coil patterns. White circles indicate repair was necessary.



Fig. 7
 Photomicrograph (magnified 60 times) showing the effects of undercutting. This cross-section of coil pattern conductors also shows line width variation due to drafting.

CERAMIC-TO-METAL SEALS FOR MAGNETRONS

Leo J. Cronin
Raytheon Manufacturing Company
Waltham 54, Mass.

Summary

The contents of this paper have been designed to inform the radio engineer of recent advances in ceramic-to-metal seal designs, particularly as applied to magnetrons.

Problems with reference to insulation and microwave power are outlined. It is shown that many advantages accompanied the change from glass seals to ceramic seals. Briefly these advantages relate to improved assembly techniques, freedom from corona, high temperature resistance, miniaturization and ruggedization. Specific seal designs are considered and illustrated. References are made to ceramic materials throughout the paper in order to provide background material.

Special tests are described with particular reference to mechanical reliability. In a test with high ambient temperature it is shown that seals kept at elevated temperatures (up to 500°C) for prolonged periods maintain their resistance to gas permeability. Seals made about five years ago are still vacuum tight after room temperature shelf life tests. About one half million seals have been made in the past few years for magnetrons.

Introduction

In the design of a magnetron, which is illustrated by Fig. 1, there exists two problems which deserve considerable attention - electrical insulation and transmission of the power generated in the interaction space. For a solution, designers have recently resorted to ceramics and ceramic-to-metal seals. Reference to seals will be taken to mean high temperature seals using solders with melting points in excess of 700°C. Consequently, this definition rules out soft solders, silver and platinum paints and all organic materials. Among other criteria, these seals should maintain a high vacuum at tube processing temperatures of, say, 700°C.

Glass served well in the low power magnetrons of World War II when the power and frequency were mostly below 1 megawatt and 10,000 mc/sec, respectively, but became obsolete with the advent of high power magnetrons. In order to see why glass was inadequate it may be well to consider the design of glass structures.

High Voltage Bushing

Because the anode operates at ground potential, the cathode must be supported by an insu-

lating mechanism. In practice this mechanism becomes an insulator bushing. These bushings must withstand the high anode voltage and accompanying electrical stress which leads to corona, arcing or puncture. They must have high insulating value, low loss, and high dielectric strength. In addition to these electrical requirements, the bushings must be physically strong to support the heavy cathode assembly under conditions of rough handling, shock and vibration.

The high voltage cathode bushing, shown in Fig. 2 as part of an early magnetron, was designed to withstand 90 KV. The total glass length between electrodes was 6 inches. Preliminary analysis for electrical stress and design parameters had been conducted assuming a coaxial structure and using the expression after Peek* which relates the voltage gradient, g_x , to the total voltage, dielectric constants and geometry.

$$g_x = \frac{e}{\pi K_x \left[\frac{\ln \frac{r_2}{r_1}}{K_1} + \frac{\ln \frac{r_3}{r_2}}{K_2} + \frac{\ln \frac{r_x + 1}{r_x}}{K_x} \right]}$$

In an actual test the bushing arced over at 86 KV but showed corona and fluorescent spots on the glass at a lower value. Fig. 3 illustrates the arcing that obtains when the flashover voltage is exceeded. It illustrates very well one of the major disadvantages of a high voltage bushing operating at atmospheric conditions. An additional disadvantage, shown in the picture, is the formation of fluorescent spots on the glass. The punctures that can occur at the seal as a result of overstress are not shown but nevertheless are just as real.

Reduction in size accomplished by going to ceramic bushings and operation under oil is shown in Fig. 4. The diameter has been reduced from 6" to 2" and the length between electrodes from 6" to 1". In addition, the disadvantages of corona, arcs and seal punctures are eliminated.

Output Window

Similar advantages have been obtained with the output window. Designers of magnetrons feel that output window assemblies are a necessary evil. They, of course, would like a window of zero thickness to eliminate electrical losses, facilitate matching, provide a broadbanded output and avoid vacuum problems. Ceramics down to .009" thickness have been tested on the mass spectrometer

* F. W. Peek, Jr. Dielectric Phenomena in High-Voltage Eng. P. 34, 3rd Edition, McGraw Hill.

and were tight. They are too thin, however, to provide adequate strength. Experience has placed the useful thickness between .060" and 0.5" for the majority of seals. Thicker pieces are avoided because of weight, electrical losses, and formation of thermal gradients in processing that lead to cracks.

Just as with ceramics, the lower limit of the metal is set by lack of physical strength. Seals have been made to Kovar up to .100" thick but economics and seal design usually dictate thicknesses between .020" and .050".

A typical window might consist of a ceramic disc 1/8" x 2" sealed to a Kovar cylinder with a .030" wall. Details of processing are available through the Raytheon Patent Office. Electrical details are the responsibility of the magnetron designer. He has to make the ceramic diameter large enough to avoid electrical breakdown which would be manifested by excessive corona or arcing. Sharp points in the ceramic-to-metal seal area should also be avoided.

Other Seals

The magnetron of Fig. 1 contains four ceramic-to-metal seals in its envelope. In addition to the high voltage cathode bushing and output window already described, there are two smaller seals. These other two are merely for low voltage terminals. They can be regarded as small editions of the large bushing and do not represent any particular design problems. The four assemblies contain about 30 linear inches of ceramic-to-metal seal.

A collection of ceramic-to-metal seals is shown in Fig. 5. Among the designs are lead-in seals, cylindrical high and low voltage bushings, flat and cylindrical output assemblies, and some special engineering tests.

Fig. 6 pictures one of the largest seals we have made. The ceramic cylinder is about 8" in diameter and 7" high. This seal is not used specifically for magnetrons but has furnished experience which will be useful in the magnetron field should the need arise.

Advantages

Until the advent of these high temperature seals, it was impossible to design and operate a magnetron with megawatts of power output. The development of the high alumina ceramic body and the Raytheon sealing process allowed among other advantages: 1. ceramic-to-metal vacuum tight seals, 2. ceramic output windows transparent to microwave energy and capable of passing high power (10 megawatts or more), 3. close tolerance assemblies, 4. oxide free assemblies, 5. high temperature processing in hydrogen, 6. multiple simultaneous braze joints, 7. subsequent braze joints closely adjacent, 8. 700°C exhaust temperatures, 9. reduction in over-all magnetron size, 10. more rugged structures, 11. high and

low voltage bushings, lead-ins, and terminals.

Reliability

Incidental to other tests, seals have been subjected to impact shock and vibration tests. Results are available on a ceramic cylinder assembly of 2" diameter which was part of a ten pound cathode-pole assembly. During the vibration test the frequency was varied slowly and uniformly over a frequency range of 10 to 58 cps with a constant acceleration of 10 g. This test was run separately for each of two planes, one plane being parallel to pole axis and the other transverse. The frequency range was traversed in two complete cycles and duration in each plane was five minutes. For the impact test, the assembly was mounted securely to the test platform of the impact shock machine. A series of increasingly harder shocks were applied up to maximum of 100 G for a duration period of 6.5 milliseconds. The ceramics were still good after these tests. It should be emphasized, however, that these tests were not designed to test the seal to failure. Emphasis was on other features such as the strength of the cathode support structure.

In another test of this type, a smaller ceramic cylinder (about 1" C.D. x 1 1/2" long) on an assembly weighing approximately five pounds was subjected to the shock of a heavy hammer falling through 130°, the maximum of the machine. Two assemblies were given 60 blows each without detrimental effect.

Another example of ceramic and seal strength was obtained by exerting compression longitudinally on a ceramic cylinder with .030" Kovar sealed to each end. The Kovar bulged to form a corrugation but the seal was still tight when checked on the mass spectrometer leak detector using helium.

Magnetrons have been caught in the demand for increased quality and reliability which has been asked of electron tubes in general. As components of tubes, ceramic-to-metal seal assemblies have not escaped sharp scrutiny. How do we know they won't leak or break? Will they be dependable under high ambient temperatures? What are the operational or maintenance problems? Will they pass the rigorous tests of thermal shock endurance, stability, fungus resistance and salt spray? These and other questions immediately come to mind when the reliability of an electronic product is considered.

We can say in general that ceramic-to-metal seals, properly made, will pass their requirements with flying colors. In addition, they lend themselves well to the ruggedization and miniaturization programs.

Specifically, we have had seals of both the compression type and lead-in design, which are now over five years old, maintain their original degree of vacuum. These assemblies were brazed, baked out and sealed off with an ionization gage attached. Periodic readings have been taken

through the years with the satisfying results mentioned.

Ceramics, themselves, are very insensitive to external conditions of ambient gases and temperatures. Consequently, by adequately protecting the metal appendages, seal assemblies can be made to withstand all manner of severe climatic conditions.

Ceramics

In order to speed the development of magnetrons and ensure that they will not be delayed for lack of ceramic-metal seal components, we have developed a high alumina body to supplement commercial sources. It has not been feasible to obtain rapid deliveries of experimental ceramics from commercial vendors. On the other hand, with our own facilities, we can start from the blueprint stage and supply finished ceramics within a few days if the need arises.

Fig. 7 illustrates some typical ceramic parts we have fabricated. In general, the larger parts are for ceramic-to-metal seals and the smaller parts are for internal electrical spacers. Spacers may be made of 100% alumina or from the high alumina composition. Various methods of fabrication have contributed to the formation of these shapes. Among the forming methods are - slip casting, dry pressing, hydrostatic pressing, extrusion, injection molding and machining.

A research program has been found necessary to aid development and production facilities. One of the important phases of research are petrographic and metallographic studies of seal cross sections.

Another phase of research involves the use of x-ray diffractometers and the electron microscope. These research tools are beneficial in studies concerning: identification of unknown compounds, determination of crystallite sizes, orientation of crystals, phases and their changes, lattice measurements and many other investigations.

High Ambient Temperature

A simple test was designed to answer the question "will ceramic-to-metal seal assemblies remain vacuum tight at elevated temperatures?" For this test, two standard ceramic cathode bushings were assembled with attached cold cathode vacuum gauges. The ceramic cylinders were $1\frac{1}{2}$ " long by 1" O.D. with a seal at each end, this gave about 6.2 linear inches of ceramic-to-metal braze. To serve as a control and also check leakage through metal, two similar assemblies were made but the ceramics were omitted. That is, cups entirely of Kovar were brazed to the cold cathode gauge in place of the ceramic-metal assembly.

These four assemblies were sealed onto a pumping system and baked out at 450°C for $1\frac{1}{2}$ hours. The liquid nitrogen trap was filled and the units sealed off with a vacuum of better than 5×10^{-7} mm of Hg. The four were then placed in an oven

and baked continually at $250 \pm 15^\circ\text{C}$. The vacuum readings varied slightly from day to day but at the end of 2,357 hours they were all better than 7×10^{-7} mm of Hg.

Following the test at 250°C the temperature was raised to 400°C and held for 709 hours. At the end of this time, the temperature was further increased to 500°C and held for 528 hours. Readings at the end of all these tests were all better than 6×10^{-7} mm of Hg. These conditions far exceed what would be required in actual service, of course, but the results provide useful experimental information. The total time at elevated temperatures was 3,594 hours. Tests were terminated only for lack of space.

Vacuum gauge readings given above were at the indicated temperatures. Four months later the assemblies were taken off the shelf and a set of readings taken at room temperature. The vacuum on all was still better than 9×10^{-7} mm of Hg.

These special tests of accelerated life tests, vibration, impact shock, high ambient temperature, and vacuum checks represent a few of the measures taken to insure a quality product. Many routine and quality control tests are also instituted and maintained to ensure built-in quality on the assembly line.

Production

Results of the transition period from laboratory to mass production were very gratifying. The first seal put into production was the RK-6002 magnetron output window. Of the first 2000 pieces there were only a few leakers for a yield of over 99%. Since then, many varied shapes and problems have been encountered. Production yield has had its ups and downs in common with all manufacturing industries. But the over-all results have been very satisfactory.

Seals have been used in production magnetrons such as the QK-221, QK-172, RK-6002, QK-241, QK-358, QK-338, QK-428, RK-6410, RK-6406 and RK-6402. Some of these tubes used as many as four seal assemblies per tube - output window, high voltage bushing, cathode bushing and getter bushing.

About one half million ceramic-to-metal seals have been made at Raytheon for high power magnetrons - tubes which might never have been built without the advent of ceramic-to-metal seals.

It has not been possible to cover all details of ceramic-to-metal seals in this brief talk. However, it is planned to cover other phases in a talk to be given next April at the annual meeting of the American Ceramic Society.

Acknowledgment

This work was performed in the Raytheon Microwave and Power Tube Operations managed by Dr. P. L. Spencer. Innumerable individuals contributed to this large program to make it the success that

it is. Particular thanks go to members of the Techniques Dept., Production Dept. and the Magne-

tron Development Lab. for their many contributions.



Fig. 1
Five Megawatt Pulse Magnetron.

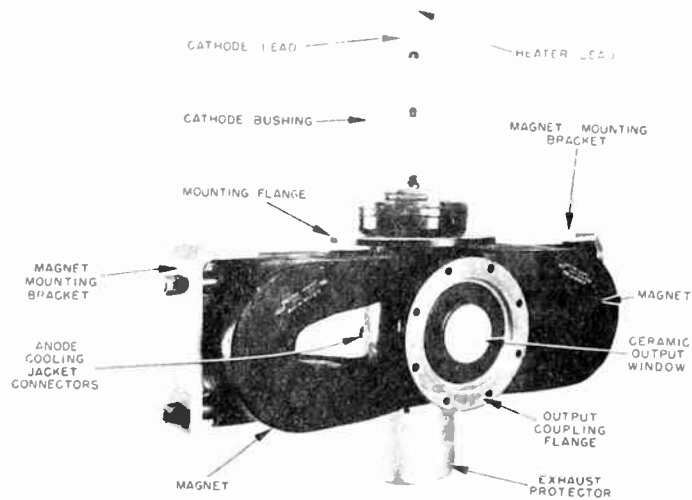


Fig. 2
Packaged QK-169C Magnetron.

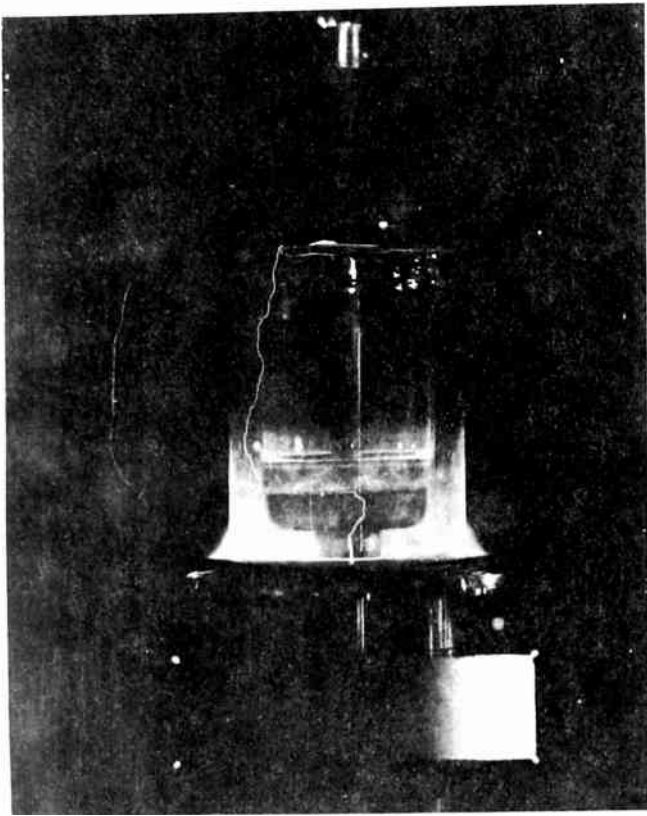


Fig. 3
Arc-Over Tests on QK-169 Cathode Bushing.

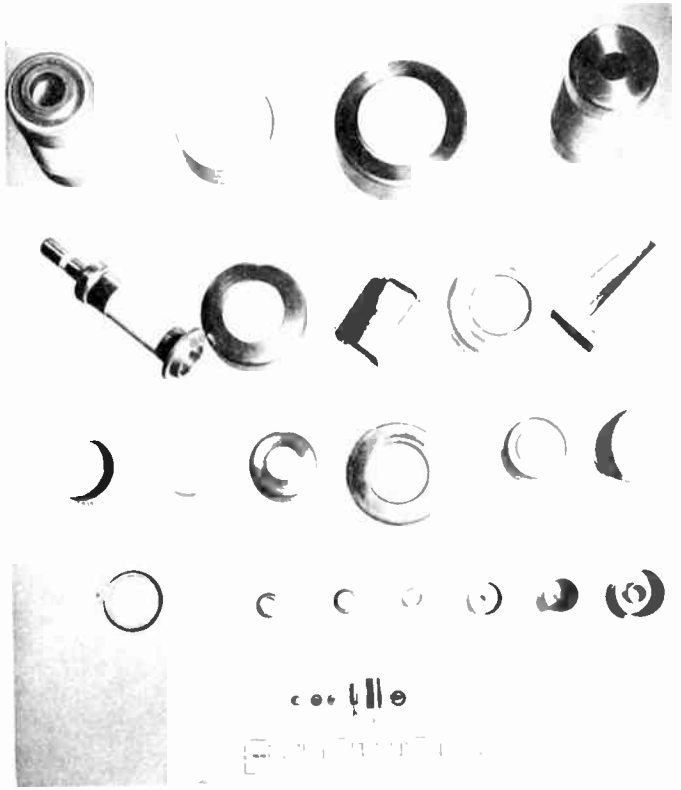


Fig. 5
Collection of Seals.

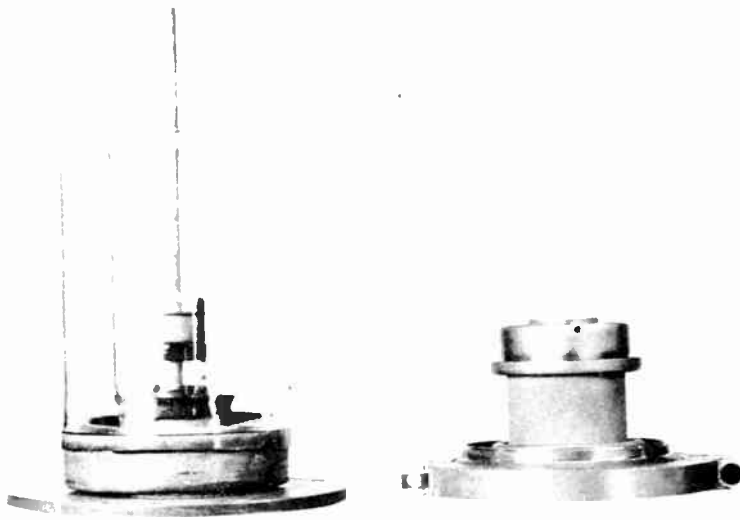


Fig. 4
Comparison of Glass and Ceramic High Voltage Bushing.



Fig. 6
Large Seal.

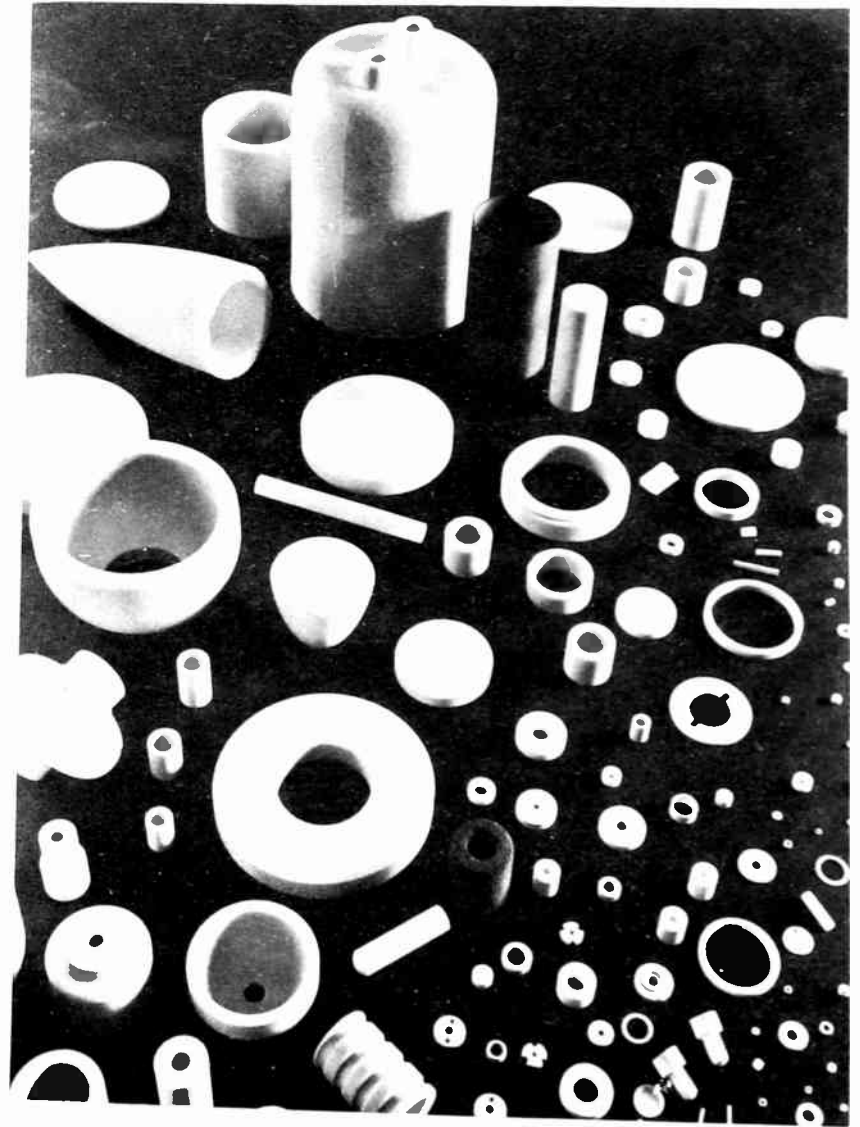


Fig. 7
Selection of Ceramic Articles.



